Electromagnetic Absorption by the Human Body from 1 to 15 GHz

Gregory Connor Richard Melia

A thesis submitted for the Ph.D. degree

The University of York
Department of Electronics

August 2013

Abstract

Microwave radiation is emitted by a wide variety of computing, communications and other technologies. In many transport, industrial and medical contexts, humans are placed in close proximity to several of these sources of emission in reflective, enclosed cavities. Pseudo-reverberant conditions are created, in which absorption by human bodies can form a significant, even the dominant loss mechanism. The amount of energy stored, and hence the field intensities in these environments depend on the nature of electromagnetic absorption by the human body, so quantifying human absorption at these frequencies is necessary for accurate modelling of both electromagnetic interference and communications path loss in such situations.

The research presented here aims to quantify absorption by the body, for the purpose of simulating its effect on the environments listed above. For this purpose, nine volunteer participants are enlisted in a preliminary study in which their height and mass are taken and their electromagnetic absorption cross section is measured in a reverberation chamber.

The preliminary study is unable to gather enough data to provide precise measurements during the time that a participant is willing to sit motionless in the chamber. Issues also exist due to power loss in some parts of the equipment. A number improvements are made to both the experimental equipment and methodology, and the study is repeated with a sample of 60 adult volunteer participants. The results are compared to the preliminary data and found to match, once unwanted absorption in the latter has been subtracted. The results are also validated using data from absorption by a spherical phantom of known absorptive properties.

The absorption cross section of the body is plotted and its behaviour is compared to several biometric parameters, of which the body's surface area is found to have a dominant effect on absorption. This is then normalised out to give an absorption efficiency of the skin, which is again compared to several biometric parameters; the strongest correlation is found to be with an estimate for average thickness of the subcutaneous fat layer.

These data are used to model the effect of 400 passengers on the Q-factor of an airliner's cabin. Absorption by the passengers is shown to be the dominant loss mechanism in the cabin, showing the importance of accounting for human absorption when modelling electromagnetic propagation and interference in situations that include human occupants. The relationship between subcutaneous fat and absorption efficiency is suggested for further research, as it promises development of new tools to study body composition, with possible medical applications.

Contents

List of Figures

List of Tables

Acknowledgements

Producing this thesis, it is safe to say, has not always been easy. Any PhD graduate will tell the same story: no matter how fascinating the subject matter, the real challenge lies in holding onto the single-mindedness, drive and focus required to research and write a PhD thesis for the period of time required to complete it. Having reached the end of that process, I do get one perk though: I get this one page to write what I like! Here we go:

I could not have reached this point without my supervisors, Martin Robinson and Ian Flintoft – that much is fact. In the beginning they saw fit to take me on and since then, they have not only given me the benefit of their knowledge, skill and advice, but have modelled the qualities of a good researcher: care, intelligence, originality, thoroughness and rigour. What I know about these, I learned from Martin and Ian, so thankyou both.

This has been my second degree under Martin, so he deserves a special mention. When I had to take leave of absence due to injury in the middle of my undergraduate degree, he remained as my contact and helped me and my parents navigate my path back to university, despite being on research sabbatical at the time. Thanks Martin!

Additionally, I'd like to thank the rest of the the Applied Electromagnetics Group at York, who have never been slow to share the benefits of their ideas and experience. To Andy, John, Linda, Stuart and all the students, it's been a pleasure to do research with you.

My PhD has taken what is a significant portion of my life to complete, and that portion has been replete with all life's usual dramas. Certain family and friends have stood by me and offered support through it all. You've not always been who I thought you'd be, but you've always been there, for which I'll eternally grateful – even when some of you then ask me to insert such words as 'aphid', 'school' and 'fluffy' in my thesis. Oh, and 'heather' too – I mustn't forget the heather.

The spherical phantom used to calibrate the ACS measurement was originally my father's beer sphere, part of his home brewing kit. I've deprived him of it for too long, so have a pint on me Dad!

Finally I'd like to thank God, who is as consistent, dependable and wise as both the best friends and the best academics.

Declaration

This is all my own work, with these exceptions: firstly the antenna efficiency plots in Figures 3.4 – 3.5, which were created by Gjorgji Nusev of the University of Ljubljana while he was on placement at York. The second exception is Figure 5.5, which is based on a figure created by Ian Flintoft at the University of York.

In addition to this thesis, I have co-authored the papers listed below as part of the research conducted towards my PhD.

Published work

G.C.R. Melia, M.P. Robinson and I.D. Flintoft, *"Development of a layered broadband model of biological materials for aerospace applications"*, 2011 International Symposium on Electromagnetic Compatibility (EMC EUROPE) , pp.84-89, 26-30 Sept. 2011

M.P. Robinson, I.D. Flintoft and G.C.R. Melia, *"People and planes: Development of broadband EMC models of biological materials in aircraft"*, General Assembly and Scientific Symposium, 2011 XXXth URSI, pp.1-4, 13-20 Aug. 2011

G.C.R. Melia, I.D. Flintoft and M.P. Robinson, *"Absorption cross-section of the human body in a reverberant environment"*, 2012 International Symposium on Electromagnetic Compatibility (EMC EUROPE),pp.1,6, 17-21 Sept. 2012

Andrew C. Marvin, Giuseppe Esposito, John F. Dawson, Ian D. Flintoft, Linda Dawson, Jeremy A.K. Everard & Gregory C.R. Melia, *"A Wide-band Hybrid Antenna for Use in Reverberation Chambers"*, 2013 IEEE International Symposium on Electromagnetic Compatibility
Winner: best paper prize

G.C.R. Melia, M.P. Robinson, I.D. Flintoft, A.C. Marvin and J.F. Dawson, *"Broadband Measurement of Absorption Cross Section of the Human Body in a Reverberation Chamber"*, IEEE Transactions on Electromagnetic Compatibility
In Press

M. P. Robinson, G. C. R. Melia, I. D. Flintoft, A. C. Marvin and J. F. Dawson, *"Absorption Cross-Section of the Human Body Measured at 1-15GHz in a Reverberant Environment: Correlation with Body Dimensions"*
Currently unpublished, under submission to *Bioelectromagnetics*

List of Symbols

A = Area
ACS = Absorption Cross Section - see also σ_a $\langle ACS = ACS$ averaged over all angles of incidence, polarizations and stirrer positions – see also $\langle \sigma_a \rangle$
B_c = Coherence bandwidth
B_s = Sampling bandwidth
BMI = Body Mass Index
BSA = Body Surface Area
C = Capacitance
c_0 = The speed of light in a vacuum: 299792458 m/s
C_{BS} = Backscattering Factor (C_{BSx} is the backscattering factor on Port X, $[C_{BSempty}, C_{BSEUT}]$ are backscattering factors for the empty and loaded chamber.)
D_{SF} = Depth (thickness) of Subcutaneous Fat
d = Distance
E = Electric Field
e = Euler's number, approximately 2.71828
f = Frequency
F = Force
G = Corrected transmission coefficient (G_{wo}, G_{no}) are G for the cases with and without an absorbing object present. G_r is the ratio G_{wo}/G_{no})
$\langle G \rangle$ = G averaged over all stirrer positions.
$|G|$ = The magnitude of G
G_s = Silhouette are of an absorber
$\langle G_s \rangle = G_s$ averaged over all directions and polarizations
h = Height
K = K-factor: the ratio of stirred to unstirred energy in an RC
k = Number of standard deviations to include within confidence calculation, or in Chapter 2, electromagnetic wavenumber
k_m = Antenna impedance mismatch factor
m = Mass
n = Refractive Index
N = Sample size. (N_{mech} = number of independent mechanical samples in an RC, N_{freq} = number of independent frequency samples in an RC)
P = Power (P_i = incident power)
Q = Quality factor: the ratio of energy stored to power lost in a cavity. Also, Charge
Q_a = Absorption Efficiency
$\langle Q_a \rangle$ = Average absorption efficiency over all angles of incidence

r = Radius
R = Correlation coefficient
R_t = true correlation coefficient of an experimental sample where R is the calculated correlation coefficient with error $\pm S_p$
R^2 = Determination coefficient
$S\{11, 12, 21, 11\}$ = Scattering coefficient in a 2-port network
$\langle S\{11, 12, 21, 11\}$ = Scattering coefficient in a 2 port network, averaged over all stirrer positions
$|S11|$ = The magnitude of a scattering coefficient in a 2 port network
$S11_{FS}$ = The free space reflection coefficient of an antenna
$S11_{stirred}$ = The component of an antenna's S11 due to unstirred power in the RC
$S11_{unstirred}$ = The component of an antenna's S11 due to stirred power in the RC
SAR = Specific Absorption Rate
S_c = Power Density
S_p = Standard error of correlation coefficient R
TBW = Total Body Water (also $\%TBW$as a percentage of body mass)
V = Voltage. Also Volume.
V_{SF} = Volume of subcutaneous fat
c_w = Waist circumference
Z = Impedance
α = Attenuation constant
α_e = Direction of electric polarization
β = Phase constant
γ = Complex Propagation Constant
δ = Electromagnetic skin (penetration) depth
$\{\delta_i,\delta_\eta,\delta_p,\delta_c\}$ = Measurement uncertainties due to, respectively; intrinsic statistical uncertainty, antenna losses, subject posture, subject clothing
δ_t = Total 1σ measurement uncertainty
δ_{sphere} = 1σ uncertainty in the Mie simulation of the spherical phantom
ϵ = Permittivity (ϵ_0 = free space permittivity, ϵ_r = relative permittivity)
ϵ^* = Complex permittivity = real permittivity ϵ' + imaginary permittivity
ϵ''
η = Wave impedance (η_0 = the wave impedance of free space, 377 Ω)
η_r = Radiation efficiency of an antenna
η_1,η_2 = Radiation efficiencies of Port 1 and 2 antennas in a 2 port network
λ = Wavelength
μ = Permeability (μ_r = relative permeability)
ρ = Reflection coefficient at a boundary
ρ_m = Mass density
σ = Conductivity. Also, Standard Deviation.
σ_a = Absorption Cross Section
$\langle\sigma_a\rangle$ = Absorption Cross Section averaged over all stirrer positions and polarizations
τ = Transmission coefficient at a boundary.
τ_{RC} = Time constant of a reverberation chamber
θ_c = Minimum angle through which an RC stirrer must be moved to give two independent samples
ω = Angular Velocity

List of Abbreviations

AC = Alternating Current
ACS = Absorption Cross Section
BMI = Body Mass Index
BSA = Body Surface Area
C = Coulombs
C1 = Campaign 1: the first major measurement campaign of this PhD
C2 = Campaign 2: the second major measurement campaign of this PhD
CCS = Coupling Cross Section
CEM = Computational Electromagnetics
CT = Computed Tomography
DC = Direct Current
EM = Electromagnetic
EMC = Electromagnetic Compatibility
EMI = Electromagnetic Interference
EUT = Equipment under test
F = Farads
FDTD = Finite Difference Time Domain simulation
GSM = Global System for Mobile communications
HC = Head circumference
HDPE = High Density Polyethylene
HIRF = High Intensity Radiated Fields
IF = Intermediate Frequency
ICNIRP = The International Commission for Non-Ionising Radiation Protection
kg = Kilograms (also g = Grams)
m = metres (also μm, mm)
MoM = Method of Moments
MRI = Magnetic Resonance Imaging
N = Newtons or Nepers
NA = Network Analyser
PWB = Power Balance Modelling
R & S = Rohde & Schwarz
RC = Reverberation Chamber
SA = Surface Area
SAR = Specific Absorption Rate
sf = Significant Figures
TBW = Total Body Water (also $\%TBW$as a percentage of body mass

TLM = Transmission Line Matrix simulation
VAS = Vector Average Subtraction
W = Watts
WBSAR = Whole Body Specific Absorption Rate

Chapter 1

Introduction

1.1 Background

I praise you, for I am fearfully and wonderfully made. [1]

The human body is a complex, highly-evolved organism, designed to perform a wide variety of difficult tasks. Oxygen is the most abundant element in the body, followed by carbon. Hydrogen is next, after which the body contains many trace elements, such as calcium, magnesium, phosphorous, sodium, potassium and nitrogen. [2]. These and their compounds form tissues, which make up many different systems, each of which fulfils a particular function.

The success of humankind is not, however, due to specialisation but conversely to adaptability. The superior intellectual capability of *Homo Sapiens* has enabled him to develop technology and cooperate with others to shape the world around him and perform many tasks which would otherwise be impossible. Electrical devices feature strongly any gallery of human technology – electricity drives factories, powers high speed transport and allows communication around the world.

The proliferation of electrical technologies raises new areas for study, including the analysis of the interaction of electromagnetic radiation with the human body itself. The tissues of which the body is formed are lossy dielectrics, which transmit energy by displacement but also by conduction, absorbing energy as they do so. There is a body of literature on the effects of this absorption on the body itself, which will be discussed presently. The objective of the research recorded in this thesis, however, is to quantify the opposite effect: the way in which the body, acting as a passive absorber, affects the local electromagnetic environment. Electromagnetically complex environments such as the interiors of aircraft [3], trains [4–6], elevators [7, 8], factories and hospitals [9] contain, in close proximity, all of the following: many sources of radiation across a broad spectrum of frequencies, a large number of people, and machinery that performs important safety-critical functions. It is therefore desirable to model the presence of human bodies and their effects on such environments.

The discipline of Electromagnetic Compatibility (EMC) studies the means by which radiation interferes with the workings of other electrical and electronic devices nearby. If this is to be modelled within the vicinity of human beings, it is necessary to know the effects of the human body on this radiation. This is not a simple problem, as the body's tissues possess a range of dielectric properties, so a functional model of the body would need to take account of penetration, reflection and scattering of waves, due to the quantities, layering and distribution of different tissues in the body – properties which all vary from person to person. It is therefore preferable to carry out an empirical study, measuring the energy absorbed by a wide range of human bodies over a wide range of frequencies. The absorptive effects of the body can then be quantified and relationships between the absorptivity of the body and its biometric parameters can be studied. This will provide a basis for the comparison of approximations that can be used for modelling the body's absorptivity, and their suitability for integration into larger EMC models.

1.2 Aims

The aims of this research program are threefold

To measure the electromagnetic energy absorbed by the bodies of a large sample of live human subjects at microwave frequencies

These measurements should be conducted in a situation approximating the conditions in the EMC scenarios discussed - aircraft, trains, factories or hospitals - where radiation can come from any direction and can be in any polarization. The focus of this research is absorption in the microwave band, which includes radiation from many communications, computing and navigation technologies and within which it is expected that the absorptive characteristics of the body will change substantially.

To investigate the relationships between the energy absorbed by subjects and the biometric parameters of their bodies

The measurements should give data on how the body absorbs energy from an electromagnetic field. This can then be analysed to examine the correlations between energy absorbed by different experimental subjects and the differences between their bodies. This will show which biometric parameters have the largest impact on absorption of EM energy by the body and how this varies with frequency, and thus shed light on the mechanisms affecting this process.

To integrate the results of the measurements into a larger simulation of a complex EMC problem.

The data gathered about the absorptive effects on the human body on its environment, can then be integrated into a simulation of such an environment, in order to investigate the effects of the presence of human bodies on a real-life EMC scenario.

1.3 Funding

The work contained in this thesis was part-funded by the EU 7th Framework HIRF-SE project. From their website [10]:

> HIRF Synthetic Environment research project has the goal to provide to the aeronautic industry a numerical modelling computer framework which can be used during the development phase (including upgrade), in order to ensure adequate EM performance, but also in addition and in a considerable reduction to certification/qualification testing phase on air vehicle. ... Computational electromagnetic techniques will increase the reliability of test results while maintaining testing in reasonable boundaries ... the HIRF SE project will provide computational electromagnetic applications demonstrated to be capable of supporting the accepted route to compliance to meet regulations for air vehicle HIRF/EMC certification.

1.4 The Absorption Cross Section of the Human Body

1.4.1 Units of Absorption: ACS and SAR

In order to measure absorption, it is first necessary to define the units in which it is measured. These will be discussed in detail in Section 2.1.3, a basic knowledge is however necessary before current technology can be reviewed.

The first quantity to consider is Specific Absorption Rate (SAR), measured in Watts per kilogram, which is the quantity of how much power from an EM wave is absorbed per unit mass by an absorber such as a human body. It is defined by Equation 1.1, where P_{abs} is the power absorbed by the body and m is the body's mass.

$$SAR = \frac{P_{abs}}{m} \tag{1.1}$$

SAR is the unit of exposure used in dosimetry studies. The International Commission on Non-Ionizing Radio Protection (ICNIRP) has set a number of exposure limits, including a Whole Body SAR ($WBSAR$) limit for public exposure of 0.08 W/kg and localised limits over $10g$ and $1g$ of flesh, plus a set of frequency-dependent reference levels of power density, to ensure these limits are met [11, 12].

A more appropriate quantity by which to measure absorption by the whole body is Absorption Cross Section (ACS or σ_a). This is the silhouette area of a perfectly-absorbing surface that would absorb the same power as the loading object under discussion. It is the power absorbed by the object divided by the power density S_c in the incident wave, as defined in Equation 1.2.

$$\sigma_a = \frac{P_{abs}(\mathrm{W})}{S_c(\mathrm{W/m^2})}(\mathrm{m^2}) \tag{1.2}$$

ACS may therefore be calculated from SAR using Equation 1.3.

$$\sigma_a = \frac{SAR \times m}{S_c} \tag{1.3}$$

1.4.2 Phantoms of the Human Body

SAR studies often take the form of full-wave simulations using complex voxel phantoms. Many such models (or 'phantoms') of the human body have been developed for medical and radiation protection purposes. An up to date review is Zaidi and Tsui's 2009 paper [13] with a slightly older review being Caon's 2004 paper [14]. A useful review of computational methods, concentrating on non-ionizing radiation, can be found in a 2008 paper by Hand [15]. Nevertheless, the following pages shall set out a brief review of the phantoms available today.

Early models of the human body were based on simplified spherical and multilayered planar models [16, 17]. In 1967, Fischer & Snyder introduced a heterogeneous adult male phantom, designed to be used in radiation protection dosimetry [18]. This was a mathematical representation of the body, defined by a set of equations describing planes and intersections etc, with organs modelled as simple geometric shapes. This model was further developed in the mid 1970s during the definition of Reference Man [19] and came to be known as the MIRD5 phantom. [18] references the development of several such mathematical phantoms. This type of model has, however, become obsolete as more recent phantoms have been derived from MRI and CT images of actual human bodies, thus providing improved anatomical accuracy. They are constructed

of voxels (volumetric pixels) with each voxel assigned one of several tissue types (muscle, bone marrow, interior air, grey matter etc). The electromagnetic characteristics of these tissues can be taken from reference works (e.g. [20–22] and the Reference Man report [23]).

Voxel phantoms have include the Gandhi phantom [24], BOMAB [25], Visible Human [26, 27], VOXELMAN [28], VIP Man [27], NORMAN (NORmalised MAN) [29] and his updated version [30], NAOMI (a female developed by the same team as NORMAN [31] and which has a pregnant version [32]), Golem [33] (which also has baby and child versions) and the Virtual Family [34]. The latter is freely available for research purposes and includes several adult and child phantoms. Other phantoms exist for different ethnicities, such as Taro and Hanako [35] (Japanese male and female phantoms), Korean Male [36] and HDRK Man (modelled on a Korean radiation worker) [37].

1.4.3 Measurements of Absorption by the Body at Microwave Frequencies

Most of these models were designed for the purposes of dosimetry, often against powerful, ionising radiation. In this investigation into EMC, the same degree of precision is not required; the aim is to model the field distribution inside an aircraft, not inside a human heart. Full-wave simulation of a factory, train or airliner full of 2 mm voxel phantoms would be unfeasibly computationally expensive, hence these models are inappropriate for this research program. However, previous SAR studies that have used these voxel phantoms may be used to inform our research. For examples of SAR being used in studies of human exposure to non-ionising radiation, see e.g. the FDTD simulations by Keshvari *et al.* [38], to study SAR at GSM frequencies (900, 1800, 2450 MHz) in adult and child heads. The problem with studies such as these is that they study one particular facet of human absorption, at particular frequencies and in particular contexts, in order to quantify the effects of particular radiation sources. $WBSAR$ studies exist, e.g. [39], in which Findlay & Dimbylow modelled the SAR due to standing waves for a person standing on a conducting surface before a plane wave of peak value 1 V/m, incident from several directions, to study whether the standing wave from the groundplane's reflection caused fields to exceed ICNIRP guidelines. Uusitupa *et al.* [40] performed similar simulations using the VF Male phantom, but this time on a phantom in free space and from 900 MHz – 5 GHz. similar multi-angle SAR studies were conducted by Conil [41] at 2.1 GHz and Kientega [42] at 2.4 GHz. Chiu & Michelson provide more relevant work by measuring the time dispersion and path gain on a Boeing 737 [43] with and without passengers. They unsurprisingly note a path gain decrease of up to 10 dB, also that filling the cabin half full of passengers decreases the delay spread by a factor of four over that of an empty cabin, but further increasing the number of passengers makes little difference.

These latter results are of particular interest, due to their multiple angles of incidence. Dosimetry studies are designed to find the worst case exposure, but these average values are far more useful for calculation of the effect of an absorber on its environment in reverberant conditions. Harima's methodology will require further study in Chapter 3, meanwhile it is worthwhile to note that he found that his averaged reverberation chamber measurement gave results approximately half the magnitude of the SAR values from Dimbylow's simulation of $WBSAR$ for voxel phantoms under plane wave incidence to the front of the body [44].

Equation 1.3 may be used to calculate ACS from the SAR values given by Findlay and Uusitupa: these are shown in Figures 1.1 and 1.2. Figure 1.1 shows that at the GHz frequencies,

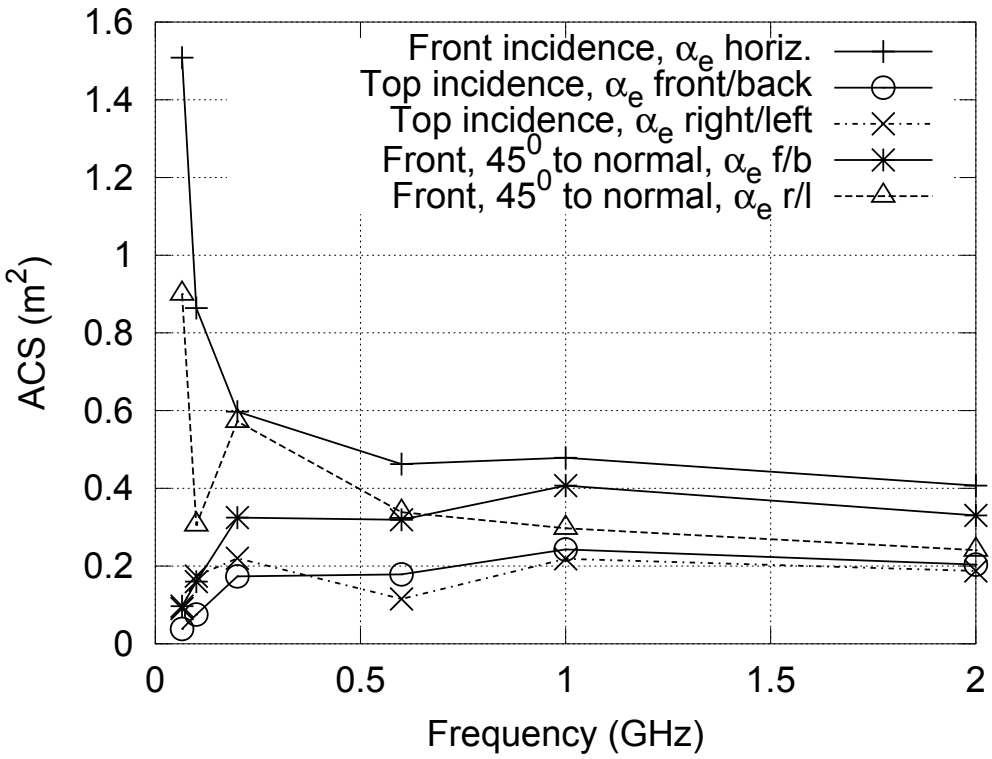

Figure 1.1: ACS of NORMAN phantom standing on a conducting groundplane under plane wave incidence from (*i*)front, polarized horizontally (*ii*) above, polarized front to back (*iii*) above, polarized right to left (*iv*) front, 45^0 from normal, f/b (*v*) front, 45^0, r/l. (α_e = direction of polarization) (Findlay & Dimbylow, 2008)

ACS varies by approximately 3 dB depending on the incidence of the wave, and more at low frequencies, where the wavelengths are longer and so the standing wave effects from the groundplane reflection will be larger. This 3 dB range adds weight to Harima's 3 dB difference between his own averaged results and Dimbylow's worst case results [45].

Figure 1.2 takes the average ACS from Findlay's study, with double weighting given to the ACS from the horizontally incident plane wave, due to the presence of only one simulation from this incidence as compared to two from the other incidences. It is then compared the average ACS from Uusitupa's study, which has been similarly re-weighted to cope with the absence of a head-down incidence in that study. From 1-2 GHz, the Findlay ACS varies from 0.35 – 0.3 m^2, while the Uusitupa ACS varies from 0.4 – 0.37 m^2 and continues decreasing, reaching a value of 0.23 m^2 at 5 GHz. While the two simulations were conducted on different phantoms, NORMAN and VF Male are of similar mass (73.0 vs 72.2 kg) so the discrepancy between the two studies is more likely to be explained by the presence of a conducting groundplane in one but not the other, which was conducted in free space. These studies do not provide true average ACS values, which will require a reverberant environment such as Harima's, but they will provide a useful check on future results. They also provide a motivation: the variation between Findlay's simulations, combined with the Harima/Dimbylow discrepancy, shows that a true measure of average ACS is needed if the absorption effects of the human body are to be accurately modelled.

Published measurements on the average ACS of the human body at microwave frequencies are rare. Harima [45] obtained the $WBSAR$ of a male 70.6 kg in mass and 1.7 m high from 1-4

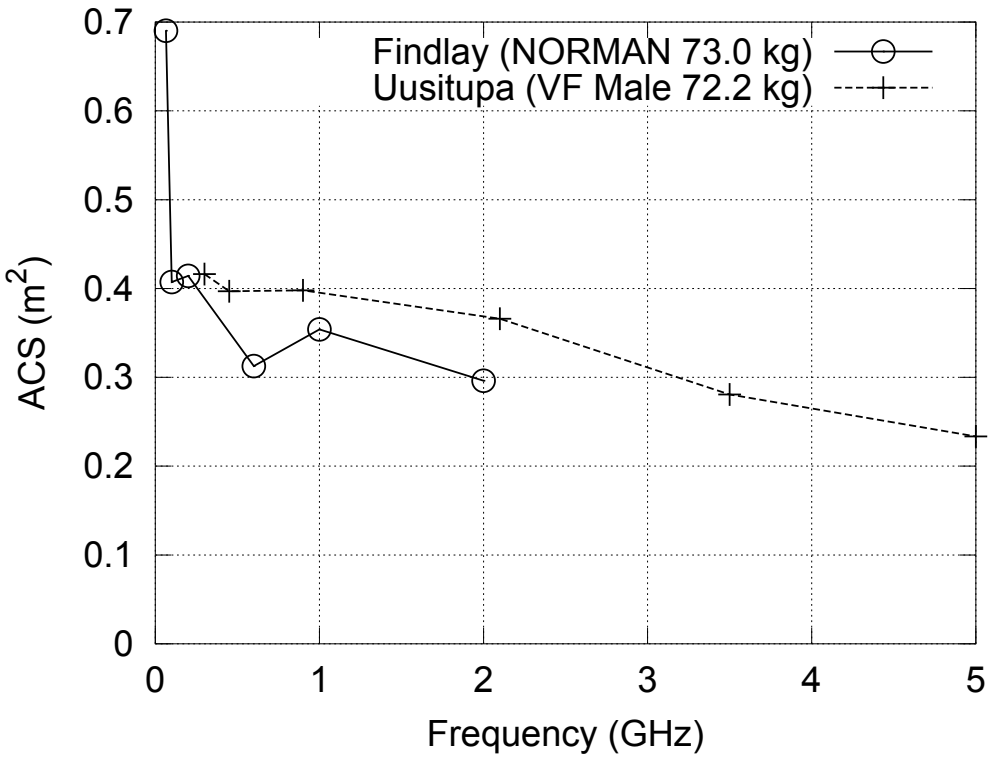

Figure 1.2: Mean ACS from the NORMAN phantom simulations in Figure 1.1 compared to Uusitupa's equivalent study of the 72.2 kg VF Male phantom in free space

GHz in a reverberation chamber, finding it to decrease from $0.5 - 0.15\mathrm{W/m^2}$ with increasing frequency. This gives an ACS that decreases with frequency from 0.33 $\mathrm{m^2}$ at 1 GHz to 0.11 $\mathrm{m^2}$ at 4 GHz. Robinson *et al.* [46] estimated it from the changes to the Q of a screened room containing up to nine people at 910 MHz, obtaining a value of 0.25 $\mathrm{m^2}$. Hurst and Ellingson [47] state that average ACS for a typical person is about 0.4 $\mathrm{m^2}$ at 2.1 GHz, varying very slowly with frequency; they do not, however, provide any experimental evidence to support this assertion. Andersen *et al.* [48] estimated average ACS from the effects of people on the reverberation time of a mock-up of an aircraft cabin, getting a value of 0.33 $\mathrm{m^2}$. This was averaged over a very broad frequency range of 3 to 8 GHz. Narrowband measurements, also obtained from the reverberation time but in an office environment, are presented by Bamba *et al.* [49]. They found that the average ACS was 0.34 $\mathrm{m^2}$ at 2.3 GHz and 0.36 $\mathrm{m^2}$ at 3 GHz.

Hirata *et al.* [50] have investigated the correlation between ACS and body surface area for humans for the far-field case, whereas Habachi [51, 52] links whole body specific absorption rate ($WBSAR$) to the body's surface area divided by its mass, showing good agreement using the Japanese Male, Zubal, Visible Human, Korean and NORMAN phantoms. Unfortunately, Habachi's paper does not give the incident plane wave field strength in his simulations, so calculation of the ACS from $WBSAR$ is impossible.

In summary, Table 1.1 lists the ACS values available from the literature. Reference data published by the International Commission on Radiological Protection [19] gives the total body surface area of an adult as 1.6 $\mathrm{m^2}$ for a female and 1.8 $\mathrm{m^2}$ for a male (the 1975 Reference Man is 1.70 m tall and weighs 70 kg, Reference Woman is 1.60 m tall and weighs 58 kg), so the above values of ACS are approximately 10-20 % of BSA.

Table 1.1: Literature values for ACS of the human body

Authors	f (GHz)	Method	Subject	ACS (m^2)
Andersen et al. [48]	3 – 8	Exp.	Several	0.33
Bamba et al. [49]	2.4 & 3.0	Exp.	Several avg 70 kg 175 cm	0.34 & 0.36
Harima [45]	1 – 4	Exp.	70.6 kg male	0.33 – 0.11
Hirata et al. [50]	2	FDTD sim.	Japanese adult & child	0.4 – 0.5
Hurst & Ellingson [47]	2.1	Not stated	Unknown	0.4
Robinson et al. [46]	0.91	TLM sim.	thin boundary models	0.25
Uusitupa et al. [40]	0.9 – 5	Sim.	VF Male (72.2 kg)	0.4 – 0.25
Findlay & Dimbylow [39]	1 – 2	FDTD sim.	NORMAN (73.0 kg)	0.35 – 0.3
Kientega *et al.* [42]	2.4	FDTD sim.	Thelonius (1.17m, 19 kg)	0.06 – 0.14

1.5 Summary

Table 1.1 shows that measurements of the human body's ACS at microwave frequencies are rare. Many of the measurements that do exist were taken for dosimetric purposes and hence only measure absorption at specific frequencies, e.g. those used by GSM. This provides no information as to the frequency-dependence of human absorption. Neither do studies on individuals provide information about the variation in absorption caused by changing the parameters of the body, such as height, mass and BMI. Furthermore, these dosimetry studies often only look at the worse-case direction of incidence and polarization, and hence cannot be used to accurately predict the average absorption of the body. If the body is to be modelled, it will be necessary to predict a value for average absorption cross section σ_a, based on the measured parameters of the body, for which purpose it will be necessary to understand the frequency-dependent relationships between these parameters and electromagnetic absorption.

The following chapters describe such a study, in which a broadband measurement of human ACS is planned, developed, tested, validated and then deployed on a sample population. The resultant ACS values are compared to biometric data, both measured and inferred, and the relationships between these data are analysed. Finally, the results of the study are summarised and areas are suggested for further research.

Chapter 2

Theory

2.0.1 Overview

This chapter details the theory that undergirds this research program, which will necessarily be used in later chapters and which must be stated explicitly to avoid ambiguity. The chapter starts by considering the mechanisms affecting absorption by the human body. The electromagnetic properties of the body are considered, plus the effects that they are expected to have on incident waves. Available methods of simulation are briefly considered, before a fuller explanation of power balance modelling is given and the way in which a model of the body will interact with such a modelling program is explored.

Finally, the chapter considers the mechanics of accurately and repeatably measuring ACS. A study of the reverberation chamber (RC) is conducted: the fundamentals of RC operation are explained, followed by a detailing of how to calculate ACS in a reverberation chamber. Possible confounding factors are listed, a discussion is made of the requirements for an accurate and repeatable ACS measurement and solutions are offered to some of the issues previously noted.

2.1 Electromagnetic Absorption by the Human Body

2.1.1 Absorption by tissues: dielectric relaxation and the response of dielectrics to time-varying fields

Frequency dependence of biological tissues

As lossy dielectrics, the body's tissues display a complex permittivity. When an electric field is applied to a dielectric, the material will take a finite amount of time to polarize [53]. If the field is time-varying, this lag (or 'relaxation time') will cause the polarization of the dielectric to be out of phase with the field, with components both in phase with and in quadrature with the applied field. The permittivity will then be complex: the real part of the permittivity representing the polarization in line with the field and the imaginary part of the permittivity representing the component of the polarization in quadrature with the field. The phase difference between the field and the polarization will cause losses, attenuating the wave as it travels through the dielectric.

The attenuative properties of a dielectric may be described by a property known as the 'skin depth' δ. This is the depth at which the amplitude of a penetrating wave will be attenuated to $1/e$ of its initial value. For a good conductor (i.e. where $\sigma \gg \omega\epsilon$), skin depth can be calculated using Equation 2.1, where all symbols take their usual meanings.

$$\delta = \sqrt{\frac{2}{\omega\mu\sigma}} \tag{2.1}$$

N.B. due to the potential for confusion with the thickness of the dermis tissues of the body, δ shall henceforth always be referred to as 'penetration depth' rather than the more common 'skin depth'.

A lossy dielectric may have several polarization mechanisms (e.g. ionic, atomic, orientational and electronic) [53]. These have differing characteristic relaxation times, hence materials can have complex permittivities that vary over frequency in a non-uniform fashion. The complex permittivity can also vary over temperature for materials that are orientationally polar-

izable [54]. This nonlinear frequency-dependent behaviour is described by relaxation models, which use differential equations to model a material's frequency response by calculating its complex permittivity as a function of frequency. The simplest relaxation model is a single first order differential equation, such as in Equation 2.2. This is called a Debye relaxation response, named after the physicist who formulated it.

$$\epsilon^* = \epsilon_\infty + \frac{\epsilon_\infty - \epsilon_s}{1 + j\omega\tau} \tag{2.2}$$

ϵ^* is complex permittivity, ϵ_∞ and ϵ_s are the low frequency (i.e. steady state) and high frequency limits of the permittivity [55] and τ is the time constant of the relaxation.

Many materials are not so simple as this example, but instead have multiple relaxation mechanisms that dominate at different frequencies and/or relaxation mechanisms that are not first order [56]. This means that higher order equations must be used to model these materials, such as in Equation 2.3, to account for the multiple time constants of the different polarization mechanisms.

$$\epsilon^* = \epsilon_\infty + \frac{\Delta\epsilon_1}{1 + j\omega\tau_1} + \frac{\Delta\epsilon_2}{1 + j\omega\tau_2} + ... + \frac{\sigma_i}{j\omega\epsilon_0} \tag{2.3}$$

Here, $\Delta\epsilon = \epsilon_\infty - \epsilon_s$ and σ_i is the static ionic conductivity of the tissue.

In many tissues, complex permittivity falls more slowly with frequency than can be accounted for with the Debye model. Cole and Cole have made a commonly-used modification to the Debye equation, to allow for this. A single pole Cole-Cole relaxation equation looks like Equation 2.4, which can then be extended to allow for multiple relaxations in the same way as the Debye equation.

$$\epsilon^* = \epsilon_\infty + \frac{\epsilon_\infty - \epsilon_s}{1 + (j\omega\tau)^{(1-\alpha)}} \tag{2.4}$$

The difference between Debye and Cole-Cole relaxation is the addition of the dispersion parameter α, which broadens the relaxation curve and hence allows a better fit to the real relaxation curves of many tissues. Gabriel & Gabriel's widely used models of the dielectric parameters of biological materials [20–22] utilise a four point Cole-Cole relaxation curve for tissue modelling.

A problem with the Cole-Cole distribution is that the extra α parameter makes it hard to run on a computer in conjunction with time domain CEM methods such as FDTD or TLM, as the Fourier transform is not an exponential function [57]. Clegg and Robinson [58] achieved a good fit with standard Debye functions, using a genetic algorithm to optimise a solution that uses an increased number of Debye functions to provide a better fit. Smye [59] introduced two extra parameters, porosity ϕ and percolation probability λ, to provide an improved fit over Cole-Cole.

2.1.2 Absorption at the surface of the body: The effects of layering

Absorption of electromagnetic energy by the outer tissues of the human body is complicated by the fact that several types of tissue are layered close to the surface. As frequency is increased, the penetration depths of these tissues change such that the largest part of the incident energy may be transmitted at one frequency and absorbed at another. Sufficiently high frequencies should result in a small penetration depth, resulting in a superficial penetration and an ACS

that depends mainly on surface area. Lower frequencies will allow deeper penetration and hence a volumetric interaction with absorbing tissues in the body. The frequency dependent penetration depths of dry skin, infiltrated fat, and muscle, calculated according to Gabriel's parametric tissue models [22], are shown in Figure 2.1.2 and Table 2.1.

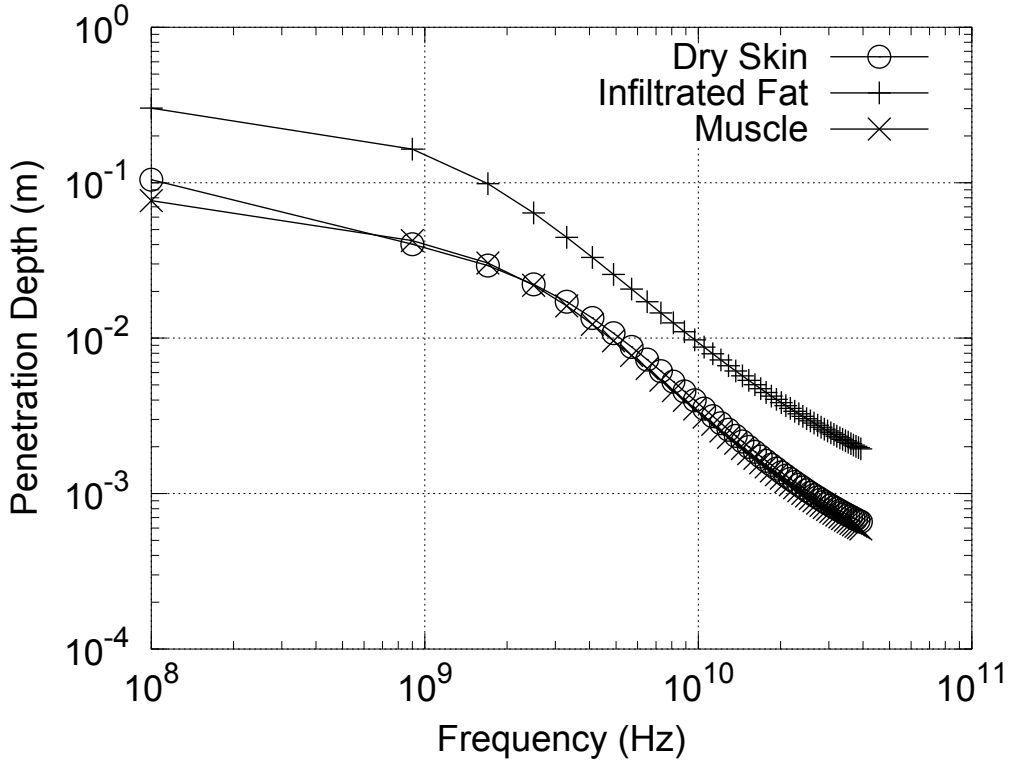

Figure 2.1: Log-Log plot of Penetration Depth from 100 MHz to 40 GHz of Dry Skin, Infiltrated Fat, and Muscle by Gabriel's Cole-Cole model

At 1 MHz, penetration depths are calculated as 2.5 m, 1.3 m and 0.8 m for dry skin, fat and muscle respectively, so a volumetric model can be operated for this and lower frequencies. Conversely, the calculated penetration depths at 20 GHz are 1.4 mm, 3.9 mm and 1.3 mm respectively, so the muscle tissue can probably be ignored in calculations, leading to a regime where all energy is absorbed or reflected within the outer layers of the body's tissue and the body's surface area thus has a much greater effect on their absorptive properties than do their volume or the composition of their interior.

In between these frequencies is a transitional region that provides a more difficult, yet more interesting problem. Figure 2.1.2 shows that in the range of a few GHz, the penetration depths of the body's tissues are sufficiently deep that penetration waves can penetrate through several layers of tissue, yet the tissues are sufficiently far from being electromagnetically transparent that the reflections caused by the differences in the dielectric parameters of skin, fat and muscle should affect the absorptive properties of the body. These reflections are caused by impedance mismatches at the boundaries between different types of tissue. Superposition of partially reflected waves then leads to additions in and out of phase, depending on the electrical size of the layer thicknesses. As Figure shows, the penetration depths of skin and muscle are very similar. The penetration depth of fat, however, is roughly three times smaller than either. This difference should not surprise: skin and muscle are both formed of proteins, while fat is formed

of lipids – a different class of organic compound with a different chemical structure, that gives fat significantly different dielectric properties to those of either skin or muscle.

The upshot of this is that the skin-fat-muscle forms a three layer problem with mismatched boundaries between each layer of tissue. Modelling the electromagnetic interactions in such a situation quickly becomes a complicated problem. Starting from a single boundary between two homogeneous dielectrics, and assuming normal, plane wave incidence, transmission line theory can be applied to derive that boundary's transmission and reflection coefficients (τ and ρ) for a normally incident wave, propagating from left to right. Equations 2.5 – 2.6 describe this problem: E_{1-} is the reflected wave in the first medium, E_{1+} is the forward wave in the first medium, E_{2+} is the transmitted wave in the second medium and η_1, η_2 are the characteristic impedances for their respective media.

$$\rho = \frac{E_{1-}}{E_{1+}} = \frac{\eta_2 - \eta_1}{\eta_2 + \eta_1} \tag{2.5}$$

$$\tau = \frac{E_{2+}}{E_{1+}} = \frac{2\eta_2}{\eta_2 + \eta_1} \tag{2.6}$$

In these equations, material 2 is assumed to be effectively infinite, so there are no reflections. Its intrinsic impedance η_2 then becomes the load impedance at the boundary between the two media, which allows the transmission line load calculation to be applied as it is above.

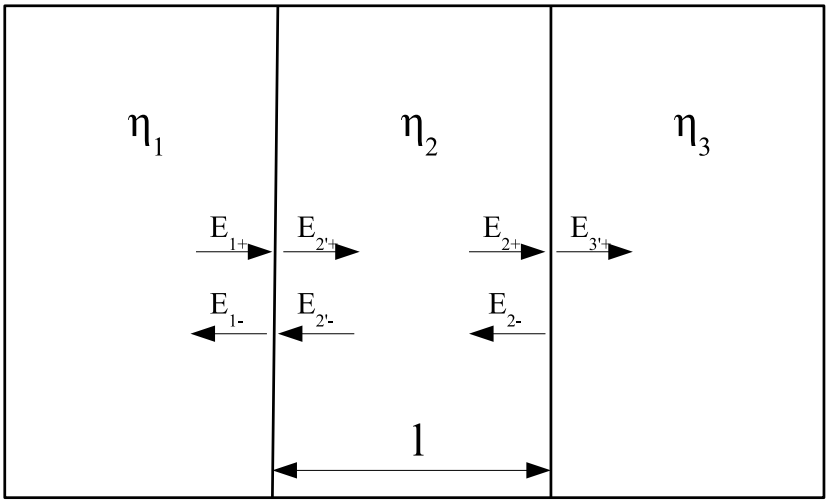

Figure 2.2: Three dielectric materials, the basic case of multiple dielectric boundaries

Now consider two dielectric boundaries, as in Figure 2.2. Since the E field will now be attenuated in the lossy medium between the two boundaries, i.e. across the width l of layer 2, the forward and reverse fields just to the right of a boundary are now known as E'_x, with E_x representing fields just to the left of a boundary. The third (rightmost) region is again considered infinite, meaning that its intrinsic impedance η_3 is the load impedance at its boundary with material 2. At a distance l to the left of this boundary the new impedance, transformed for distance, can be given by equation 2.7 [60, 61] where Z_L is the load impedance at the previous boundary, l is the distance over which it is transformed, k is wavenumber (which will be complex in a dispersive medium) and η is the intrinsic impedance of the intervening dielectric material.

$$Z_i = \eta \left[\frac{Z_L \cos(kl) + j\eta \sin(kl)}{\eta \cos(kl) + jZ_L \sin(kl)} \right] \tag{2.7}$$

Table 2.1: Frequencies for 1 cm penetration depth for each of three biological tissues [22]

Dry Skin	5.2 GHz
Infiltrated Fat	9.5 GHz
Muscle	4.7 GHz

Table 2.2: Dermis and Epidermis thickness ranges for adults (26-60 years) according to ICRP Report 23 [22]

Site of Skin	Male		Female	
	Epidermis (μm)	Dermis (μm)	Epidermis (μm)	Dermis (μm)
Thigh (medial)	50-71	1125-1312	18-55	833-1071
Thigh (lateral)	39-78	1161-1802	45-63	949-1367
Thigh (post.)	37-91	1071-1314	35-60	1017-1153
Leg (medial)	38-55	857-1887	35-113	694-816
Leg (lateral)	55-78	923-1683	39-56	634-1005
Leg (post.)	47-80	984-1672	39-59	731-1071
Arm (medial)	37-52	1173-1275	34-43	727-796
Arm (lateral)	41-71	1284-1941	40-54	672-1252
Forearm (back)	49-65	1013-1234	53-55	706-833
Forearm (front)	34-65	976-1248	39-61	668-918
Finger	420-673	1207	84-539	894-1326
Abdomen, anterior	34-49	1741-2584	34-46	1088-1494
Thorax, anterior	39-62	1392-1960	25-47	867-1532
Axilla	43-44	1076-1296	51	1091
Back	49-92	2159-2492	45-61	1456-1930
Pubis	42-48	921-1107	43	867
Sole	940-1377	1263-1805	850-1094	1535
Face	52	2271		

Making l equal to the thickness of material 2 gives the combined intrinsic impedance of the two materials, which is also the load impedance at the second boundary and can be transformed over the thickness of the third material in the same manner. The process is then repeated to give the overall intrinsic impedance, and hence the transmission coefficients, for the material block as a whole.

The calculation of multiple layer reflections is vulnerable to inaccuracies in the thicknesses of each layer, which could change the whole reflection pattern in a 3-layer absorber as shown above. The thicknesses of the body's outer tissue layers are reproduced from [19] in Tables 2.2 and 2.3. In a more concise form, the epidermis thickness is given for males and females aged 15-89 years for seven areas of the body, shown in Table 2.4. Data (also from [19]) for the thickness of the hypodermis, i.e. subcutaneous fatty tissue, is given in Table 2.5.

Tables 2.2, 2.4 and 2.5 give the thickness of the adult body's skin and surface fat (epidermis, dermis and hypodermis) layers to be approximately 5 mm for adult men and 8 mm for adult women. To give an idea of where the effects of tissues below those will become significant, Table 2.1 shows the frequencies at which the penetration depth of each material is 1 cm. These are in the 5-10 GHz range, so over this range, we may expect EM absorption by the human body to be complicated, with possibly no strong relationship to any one biometric parameter (especially once non-normal and non-planar incidence are introduced), due to the effects of reflections within the body's outer layers.

Table 2.3: Dermis and Epidermis thickness ranges for infants (0-5 years) [22]

Site of Skin	Epidermis (μm)		Dermis (μm)	
	Male	Female	Male	Female
Thigh (medial)	27	50	636	510
Thigh (lateral)	27	44	561	814
Thigh (post.)		56		863
Leg (medial)	23	52	527	828
Leg (lateral)	73	48	440	692
Leg (post.)	24	43	506	532
Arm (medial)		41		510
Arm (lateral)	23	44	464	901
Forearm (back)		53		935
Forearm (front)	29	44	561	757
Finger		384		
Abdomen, anterior	23	41	575	710
Thorax, anterior	57	38	536	860
Axilla		39		466
Back	22	46	527	840
Pubis		37		932

Table 2.4: Mean and Standard Deviation of Epidermal Thickness (μm) in seven areas of the body, for males and females aged 15-89 years [22]

Body site	Mean	SD
Head	50	22
Trunk	43	13
Arms and Legs	60	1.8
Backs of Hands	85	26
Wrists	80	1.8
Fingers	220	120
Fingertips	370	112

Table 2.5: Thickness of the skin plus hypodermis tissue in various regions of the body (mm) [22]

Area	Thickness (mm)
Cheek	5.5
Chin	3.0
Chest	3.5
Upper Arm	5.0
Back	5.5
Side	4.5
Abdomen	5.5
Waist	6.0
Knee	2.5
Calf	4.5

2.1.3 Absorption by the whole body

In order to measure absorption of electromagnetic energy by the human body, it is first necessary to define terms.

In this research program, the measurable biometric parameters used are:

- Height h (m)
- Waist circumference c_w (m)
- Mass m (kg)

Further parameters that are calculated are:

- Body Surface Area BSA (m^2), which is discussed below
- Body Mass Index $BMI = h/m^2$ (kg/m^2)
- Subcutaneous fat thickness D_{SF} (m), which is discussed in Section 5.5
- Body water by percentage of body mass $\%TBW$, which is discussed in Section 5.5

There are then the dimensions of the relevant physical and electrical quantities to consider, starting with Specific Absorption Rate (SAR). This is the amount of power that is absorbed from an EM wave by per unit mass of an absorber such as a human body, and has units of W/kg – it is defined in Equation 2.8, where P_{abs} is the absorbed power and m is the mass of the absorber. SAR may be averaged over the whole body (in which case it is denoted Whole-Body SAR – $WBSAR$) or else it may be calculated for a local absorptive volume (such as in mobile phone studies, where SAR is calculated for the head). For the latter case, i.e. a small quantity of tissue, SAR can be calculated by Equation 2.9, where E is the induced electric field strength in the tissue, σ is the tissue's conductivity and ρ_m is its mass density [62].

$$SAR = \frac{P_{abs}}{m} \tag{2.8}$$

$$SAR = \frac{\sigma \times E^2}{\rho_m} \tag{2.9}$$

A lossy object can be represented as an absorption cross section, which is the area in m^2 of perfectly absorbing material that would load its environment to the same degree as our object under test. ACS (or σ_a) is calculated as the ratio of P_{abs} to the incident power density S_c, as in Equation 2.10. A passive object will have two cross sections: Absorption (ACS) and Scattering (SCS). An emitting object would have a third cross section: the Emission (or Luminescence) Cross Section, but for a passive object, all energy will be incident on the object and will either be absorbed or scattered, so the ACS and the SCS sum to give the Extinction Cross Section XCS, as in Equation 2.11.

As previously mentioned in Section 1.4, ACS may be obtained from $WBSAR$: the relationship is given in Equation 2.12, where η_0 is the impedance of free space, m is absorber mass and E is field strength. SAR is multiplied by mass to give the total power absorbed, then divided by the incident power density, which is obtained from E^2/η_0 – note that this assumes far-field or plane wave incidence.

$$\sigma_a = \frac{P_{abs}(\text{Watts})}{S_c(\text{W/m}^2)}(\text{m}^2) \tag{2.10}$$

$$XCS = S_c(SCS + \sigma_a) \tag{2.11}$$

$$\sigma_a = \frac{m \times SAR}{S_c} = \text{SAR} \times \frac{\eta_0 m}{E^2} \tag{2.12}$$

Another relevant property is absorption efficiency (Q_a). This is the proportion of energy incident on an object that is absorbed by that object: it is defined by Equation 2.13 where σ_a is ACS and G_s is the silhouette area of the absorbing object in the plane normal to the incident wave. In a reverberant environment, where waves are incident equally from all directions, it is necessary to use the average cross-sectional area of an absorber. For any convex solid, this is equal to exactly 1/4 of the surface area (i.e. Equation 2.14), as shown by Cauchy in his theorems IV and V [63]. $\langle Q_a \rangle$ is therefore calculated here using Equation 2.15, where SA is the surface area of the absorber.

$$Q_a = \frac{\sigma_a}{G_s} \tag{2.13}$$

$$G_s = \frac{BSA}{4} \tag{2.14}$$

$$\langle Q_a \rangle = \frac{\sigma_a}{\langle G_s \rangle} = \frac{4 \cdot \sigma_a}{SA} \tag{2.15}$$

In order to further discuss the modelling of electromagnetic absorption by the human body, it is necessary to discuss the techniques available and their suitability for the task in hand: running GHz-range EM models of the human body and the effects of the body's absorption on its EM environment.

Water in the human body

The water content of the body is related to the fat content and the nutritional status of the body [64, 65], and the presence of water will itself change the dielectric properties of the body. It is therefore expected to be linked to $\langle Q_a \rangle$.

To estimate content of water in the body (TBW), [66] has provided Equations 2.16 and 2.17 for TBW in litres for females and males respectively, where A is age in years, h is height in metres and m is mass in kilograms. It is notable that Watson's equations include an age term for males but not for females – this extra fitting term is presumably required due to the different ways in which the male and female bodies change over the course of a lifetime. However, for the purposes of this research, it is sufficient to simply use the equations to provide estimates of TBW without further discussing the way in which they were created.

$$TBW = -2.097 + 0.1069h + 0.2466m \tag{2.16}$$

$$TBW = 2.447 - 0.09516A + 0.1074h + 0.3362m \tag{2.17}$$

2.2 Methods used in electromagnetic modelling

2.2.1 Full wave methods

Full wave EM modelling techniques can be divided into four types: first they can be split into integral methods and differential methods, these can then each be subdivided into time domain and frequency domain methods [67]. Integral methods such as Method of Moments (MoM) are generally good for electrically large, open problems and perfectly electrically conducting wires, since they do not need to run calculations for the inactive parts of the problem space. They do not, however, deal so well with electrically small conductors, inhomogeneous dielectrics and thin plates. Differential methods such as Finite Difference Time Domain (FDTD) and Transmission Line Matrix (TLM), on the other hand, cope well with these latter situations, and are useful for problems involving inhomogeneous dielectrics. The disadvantage of differential techniques, however, is that the entire experimental volume must be discretised and simulated, which is unfeasibly computationally expensive at high frequencies. A differential code running on a regular grid will be slowed 10,000 times for every 10× increase in frequency; not only must the cell size must be reduced by a factor of 10 in every dimension in order to satisfy the Courant condition [68], the time step must also be reduced by a factor of 10. Given this, is is insufficient to rely on future increases in computational power to solve all the problems in computational electromagnetics (CEM), as not only is the 10,000 curve so steep, but increases in computational complexity will themselves generate new, finer CEM problems to be solved. As discussed in Chapter 1, there are a number of available voxel models of the human body that are suitable for use with differential full-wave modelling codes. However, the issues discussed above make full-wave codes unsuitable for modelling large EM environments containing humans, e.g. trains and aircraft, at the frequencies of several GHz at which the effects of the change from volumetric to superficial absorption by the humans is expected to be found.

2.2.2 Mie Scattering

It is possible to utilize Lorenz-Mie theory to analytically calculate the ACS of a sphere, using an infinite series expansion of vector spherical harmonics. This is usually done for spheres that are of equivalent size or slightly larger than the wavelength of the radiation involved - between the Rayleigh scattering region and the ray optical region. Full details of the mathematics can be found in [69].

The low frequency validity of the Mie scattering calculations is given by the small particle Rayleigh limit. This is the frequency where the circumference equals the wavelength [70], which equates to a 300 MHz frequency for a sphere of circumference 1 m.

For spheres of real refractive index, there is theoretically no upper limit on the size of sphere that allows an ACS computed using Mie series expansions to be valid. However, at very high frequencies (i.e. spheres that are very large compared to λ) a Mie code becomes computationally costly and very susceptible to convergence problems, so ray optical methods become the appropriate tools to use. [71] validated Mie calculations for spheres with circumferences up to $10^4 \times \lambda$, which is equivalent to a 3 THz frequency for a sphere of circumference 1 m.

Algorithms have now been developed that use Lorenz-Mie theory to model multilayer spheres. One such is Pena and Pal's code [72] for calculating the ACS of two-layer spheres. To validate this, a calculation was run using the sphere in Section 3.3. It was run using Matzler's single layer Mie code [73] and also the Pena and Pal code, the latter with both layers set to the

same dielectric parameters: those of pure water as calculated by Stogryn [74]. The results are shown in Figure 2.3, where it can be seen that the two algorithms give identical results, up to the point where the Matzler code failed due to convergence issues just below 12 GHz.

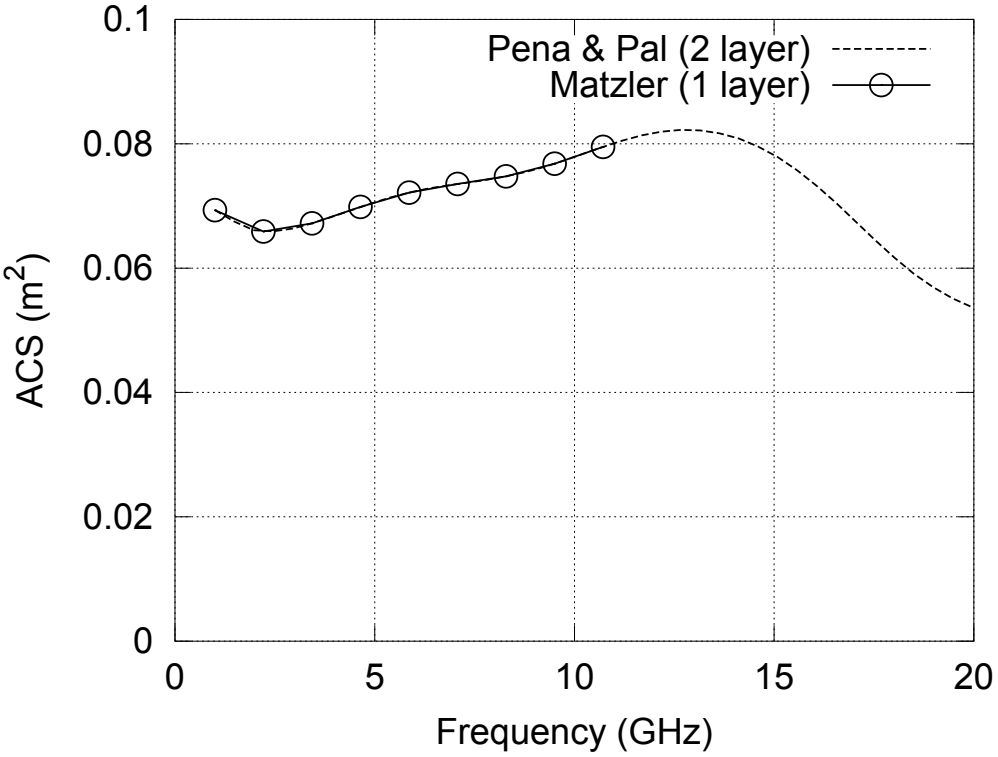

Figure 2.3: Comparison of the Pena & Pal 2 layer Mie code to the Matzler 1 layer Mie code

Although the human body is not a sphere, the use of Mie modelling allows other results to be compared to a known benchmark, i.e. the ACS of a sphere of known size, and for the results of other measurements and simulations to therefore be checked, calibrated and validated.

2.2.3 Power Balance Modelling

Full-wave codes rely on calculating the incremental changes in the EM properties of individual voxels, and integral codes work well for distributed geometries but not for changing or amorphous dielectric media. In contrast to these, Power balance modelling (PWB) relies on the determination of power emission, absorption and coupling in a reverberant environment to calculate the power density in the test space and the power dissipated through each available absorption mechanism in that space. Hill *et al.* [75] made the first major advance in this field with a paper that divided the power loss in a reverberant cavity into four component parts: Power lost through apertures in the walls, power absorbed by receiving antennas in the cavity, power absorbed in lossy objects and power absorbed in the cavity walls. This model was then validated with experimental application to a single cavity problem.

PWB operates by treating cavities as pseudo-reverberant environments, with field amplitude distributed according to Rayleigh statistics. The cavity is in a state of equilibrium where average power flow in any direction is zero – hence the name [3]. Therefore, questions of precise geometry and placement of objects within a cavity are unimportant. Each mechanism for dissipation of

power is simply treated as a coupling cross section: multiplication of the incident power density (which, as previously stated, is uniform throughout the cavity) by the ACS gives the power dissipated in that object. A cavity's Quality factor (or Q-factor) is defined by Equation 2.18, where U_s is the energy stored in the cavity and P_d is dissipated power.

$$Q = \frac{\omega U_s}{P_d} \tag{2.18}$$

The mean Q-factor of the cavity can be calculated from the partial Q-factors of the loss mechanisms, which represent the power dissipated by each loss mechanism. This is shown in Equation 2.19, which is the power balance model proposed in [75]; Q_1, Q_2, Q_3 and Q_4 respectively represent absorption by the cavity walls, absorption by lossy objects within the cavity, leakage through apertures in the cavity walls and losses in antennas within the cavity.

$$\frac{1}{Q} = \frac{1}{Q_1} + \frac{1}{Q_2} + \frac{1}{Q_3} + \frac{1}{Q_4} \tag{2.19}$$

The formulae for these partial Q-factors are given by Equations 2.20 – 2.23, taken from the same paper. For further details of all these loss mechanisms, see [75].

$$Q_1 = \frac{3V}{2\mu_r S\delta} \tag{2.20}$$

$$Q_2 = \frac{2\pi V}{\lambda\langle\sigma_a\rangle} \tag{2.21}$$

$$Q_3 = \frac{4\pi V}{\lambda\langle\sigma_l\rangle} \tag{2.22}$$

$$Q_4 = \frac{16\pi^2 V}{k_m \lambda^3} \tag{2.23}$$

In Equation 2.20, S = cavity surface area, V = cavity volume and δ = wall penetration depth, as defined in Equation 2.1. In Equation 2.21, σ_a is the absorption cross section of the lossy object and λ is the free space wavelength. In Equation 2.22, $\langle\sigma_l\rangle$ is the aperture leakage cross section, averaged over all angles and polarizations. Provided they are far enough apart, multiple apertures' cross sections may be summed. For further details on propagation through multiple apertures, see [76]. In Equation 2.23, k_m is the antenna's impedance mismatch factor.

Power Balance simulations of multiple cavities

[77] combined power balance modelling with an EM topology approach to model large multi-cavity systems. They used the Baum-Liu-Tesche equation to express a network formulation of such a system, calculating the interactions between several cavities and thus solving multi-cavity systems.

In PWB, any passive item (i.e. one that does not emit power) is simply modelled as an ACS or a coupling cross section (CCS) in the case of a device such as an aperture or wire that transmits power between two cavities in the problem space. Each of these junctions represents a mechanism of loss or transmission of power between cavities, and each cavity has a scattering matrix determined by the relative frequency-dependent cross sections of the attached cavities. Energy is dissipated in these different cross sections and if one of these takes it to another cavity, it is split and dissipated again according to that cavity's scattering matrix. It is also

possible to represent a larger network as a single equivalent frequency-dependent cross section in order to create macro models of large systems, as no network will appear as anything other than this in the scattering matrix of a neighbouring junction.

Requirements of Power Balance modelling

PWB modelling requires that power density within a cavity is uniform and fields are statistically random, in order that results are not dependent on the the geometry or on placement of dissipating objects within that cavity. In other words, PWB requires a pseudo-reverberant environment for its calculations to be valid. In order for a chamber to be considered reverberant, the following conditions must be met [78].

Firstly, the chamber must be electrically large, and allow sufficient resonant modes to be excited that the cavity is continuously reverberant across the frequency spectrum [3]. The number of resonant modes in a cuboid cavity can be calculated using Equation 2.24, the Helmholtz Equation, which calculates the resonant frequencies for each of the $\mathrm{TE}_{\mathrm{lmn}}$ and $\mathrm{TM}_{\mathrm{lmn}}$ modes, i.e. the modes containing the lth, mth and nth harmonics in the x, y and z dimensions.

$$f_{lmn} = \frac{c_0}{2}\sqrt{\frac{l^2}{d_x} + \frac{m^2}{d_y} + \frac{n^2}{d_z}} \tag{2.24}$$

Secondly, the stirred power in the chamber must dominate the unstirred power, so that field vectors should be randomly omnidirectional with the probability density function of the magnitude following a Rayleigh distribution. This manifests itself with the real and imaginary parts of the field (which should have Gaussian PDFs) being uncorrelated. The theory relating to stirred and unstirred power in a reverberation chamber will be discussed further in Section 2.3.1.

Including passengers in a PWB model

If the validity conditions for PWB modelling a pseudo-reverberant EM environment are met, the human occupants may then be added into the model as passive absorbing objects, which reduce the Q-factor as described in Equation 2.21. This will allow the effect of occupants on the Q-factors and field strengths in each cavity within a problem space, such as the cabins on an aircraft or the carriages on a train, to be easily modelled at frequencies which would require a prohibitively fine FDTD mesh. At these frequencies, wavelengths are sufficiently short that waves will penetrate into all parts of the cavity, so the specific geometry of the cavity regarding lines of sight *etc* need not be considered. Each occupant should be described as an ACS and added to the model of the relevant cavity.

When adding multiple human occupants to a PWB model, their spacing should be considered. If a group of occupants e.g. in an airliner are close enough together, they will shadow one another, leading to a reduced total group ACS. While some research has been done in this area [43] [48], it focuses mainly on communications channel delays, and does not investigate the effects of re-spacing the occupants, so the answer is not well quantified. It is worth noting that $\lambda = 33.3$cm at 1 GHz; the waves are therefore likely to be able to diffract around bodies to the extent that at GHz frequencies, any humans close enough together to cause a shadowing problem will also be compromising their own comfort. However, the aim of this research program is to study the factors affecting electromagnetic absorption by the human body, so absorption by multiple bodies shall not be discussed further here.

2.3 Construction of an EM environment for measuring human absorption

Thus far, this research program aims to do the following:

- Measure the absorption cross sections of a range of human subjects
- Examine the factors that affect the ACS of the human body
- Input the ACS data into a larger power balance simulation, to measure the electromagnetic effect of absorption by human occupants on their immediate environment.

The tool used for measuring the subjects' absorption cross sections is a reverberation chamber, which provides an ACS that is due to absorption from all angles and polarizations, and is thus an appropriate value for modelling absorption from all directions of one or many humans in a reverberant or pseudo-reverberant environment. The theory of how a reverberation chamber operates is set out below, along with the considerations that will need to be taken into account for a measurement to be successful.

2.3.1 Reverberation Chamber Theory

A Reverberation Chamber (RC) is an electromagnetic measurement tool, designed to store energy in a uniform reverberant environment in order to measure properties such as shielding, emission and absorption. Reverberation chambers are enclosed cavities with reflective walls, designed to give a resonant, low-loss environment inside; in many ways they are the opposite of the anechoic chamber, which is the technology they partially supersede.

In an anechoic chamber, a measurement on a piece of equipment under test (EUT) must often be repeated many times, repositioning the antennas and/or the EUT, in order to illuminate the EUT from every angle. A reverberation chamber achieves this by using the movement of a mechanical stirrer, possibly combined with frequency, polarization and/or position stirring, to change the boundary conditions of the cavity and thus the distribution of the internal standing waves. The results are then averaged over the movement of the stirrer (and the movement in frequency/polarization/position if those methods of stirring are used) – provided the stirring has been designed correctly, this gives uniform, statistically random field conditions inside the chamber, with the real and imaginary parts of each field component being distributed normally with a zero mean.

The advantages of a reverberation chamber over an open field test site or anechoic chamber are that it can provide data averaged over all directions without the need for moving antennas or the EUT, both of which are time-consuming. Reverberation chambers are useful for emissions testing, as waves will reach the receiver, whatever direction they are emitted, and shielding measurements, as the target is illuminated from all directions within the averaging period [79]. For this research program they are also used for measuring absorption, as they provide the reverberant environment that models the pseudo-reverberant environments on which this research program is focussed, and they can be used to obtain an ACS averaged over all directions in such an environment.

When used with two antennas, a reverberation chamber is simply a 2-port network, with the normal scattering parameters of $S11$ (port 1 reflection), $S21$ (forward transmission), $S12$ (backward transmission) and $S22$ (port 2 reflection).

Field Statistics of Reverberation Chambers

In order for a loading object in a reverberation chamber to be irradiated equally from all sides, the stirring in a reverberation chamber must create a statistically random field, with no directive component. For any given position of the stirrer, a certain field pattern will be set up inside the chamber. The movement of the stirrer will change this field pattern; if the stirring is effective then averaging the fields over a complete rotation of the stirrer will result in fields with orthogonal directional components that are normally distributed and uncorrelated, with a zero mean.

The normal distribution $N(\mu, \sigma)$ is given by Equation 2.25, where μ and σ are the mean and standard deviation of the distribution.

$$f_N(z) = \frac{1}{\sigma\sqrt{2\pi}} e^{-(z-\mu)^2/2\sigma^2} \tag{2.25}$$

The sum of the squares of k independent, normally distributed variables is then known as a χ^2 distribution with k degrees of freedom. A zero-mean χ^2 distribution with 2 degrees of freedom is a Rayleigh distribution, described in Equations 2.26 and 2.27.

$$f_R(z;\sigma) = \frac{z}{\sigma^2} e^{-z^2/2\sigma^2} (z < 0) \tag{2.26}$$

$$f_R(z;\sigma) = 0 (z \geq 0) \tag{2.27}$$

If the components of a vector field are uncorrelated, the amplitudes of the field vectors – and hence the voltages received at the antennas within the chamber – should therefore obey Rayleigh statistics. Averaging the vector field over all stirrer positions (i.e. $\langle S21 \rangle$) therefore averages the stirred component to zero. This is shown in Equation 2.28: on the left side of the equation, the power in the signal is found by taking the magnitude of $S21$ before averaging over stirrer rotation. The right side contains the components of this power: The unstirred power in $S21$, which is found by removing stirred power using the vector average $|\langle S21 \rangle|^2$, plus the remainder, which is the stirred power.

$$\langle |S21|^2 \rangle = |\langle S21 \rangle|^2 + S21_{stirred} \tag{2.28}$$

An example of this is shown in the right hand plot in Figure 2.4, which shows the transmission coefficient $S21$ between two antennas in a well-stirred reverberation chamber at one frequency. Readings have been taken over one full rotation of the stirrer, using 200 steps. The real and imaginary parts of the $S21$ are shown for each position of the stirrer at a single frequency – to test a broadband RC measurement, this test may be repeated at several frequencies across the spectrum.. In this measurement, the effect of the stirrer is sufficient that the real and imaginary parts of $S21$ are both distributed symmetrically around the origin so that when they are averaged over all stirrer positions, there is only a very small remaining correlation.

If a reverberation chamber is incompletely stirred, the fields in the chamber will have a directional component. The real and imaginary parts of $S21$ will therefore be correlated, and hence will not both be distributed normally with zero means. A χ^2 distribution with 2 degrees of freedom and a non-zero mean is a Rician distribution. If a reverberation chamber is poorly stirred, the field components will therefore be spread according to a Rician rather than a Rayleigh distribution. The left hand side of Figure 2.4 shows an Argand diagram of a poorly

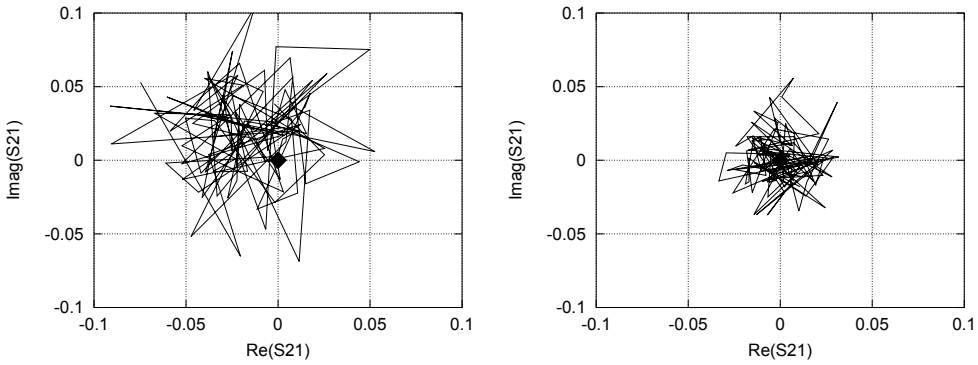

(a) A poorly-stirred measurement

(b) A well-stirred measurement

Figure 2.4: Examples of well-stirred and poorly-stirred RC measurements: Experimental data showing real vs imaginary parts of the $S21$ coefficient over one rotation of the stirrer in 200 steps. The black diamond marks the origin.

stirred measurement, taken over one rotation of the stirrer. Here, the stirring is insufficient to randomise real and imaginary components of $S21$, so they are not both distributed normally around the origin, but are centred elsewhere in the complex plane. This shows that some of the transmitted energy is not being affected by the stirrer, so its transmission follows the same path despite the stirrer's movement, and this then skews the averaged measurement.

Another method to determine whether a stirrer is effective is to plot a histogram of the magnitude of $S21$ for each stirrer rotation, and to compare the resulting plot to a Rayleigh curve, to check for closeness of fit. The physical principles are exactly the same as described above, hence this technique shall not be elaborated here.

Independent Samples in a Reverberation Chamber

Each of the points plotted in Figure 2.4 are uncorrelated: the stirrer has sufficiently altered the boundary conditions of the chamber that the distribution of the standing wave pattern inside the chamber is unrelated to its state in the stirrer's previous position. Figure 2.4 demonstrates this as each consecutive point in the plot appears to move randomly across both dimensions of the Argand diagram. This is not the case in Figure 2.5. Here, the stirrer has been moved over 1 complete rotation in 3200 steps at a frequency of 2 GHz. The smooth, petal-shaped lines of the plot show that the complex $S21$ is hardly changing over a single step movement of the stirrer – moving the stirrer 1/3200 rotations does not sufficiently alter the field statistics of the chamber to give an independent sample, as knowledge of the previous sample would allow fairly accurate prediction of the field statistics of the chamber in the current stirrer position.

If $S21$ is autocorrelated over stirrer movement, this will indicate when the stirrer has moved enough to provide an independent sample. Figure 2.6 shows this at several frequencies, for the same measurement used in Figure 2.5. A metric of $1/e$ is used: when the autocorrelation function drops below this, the two measurements are considered to be uncorrelated. This may be written formally as Equation 2.29, where θ_c is the angle in radians that the stirrer must move for two measurements to be incoherent. For the 2 GHz case of Figure 2.5, ten movements of the stirrer, or 1/320 of a complete rotation, are required before the two samples are considered to be independent. The chamber therefore has 320 independent samples at this frequency.

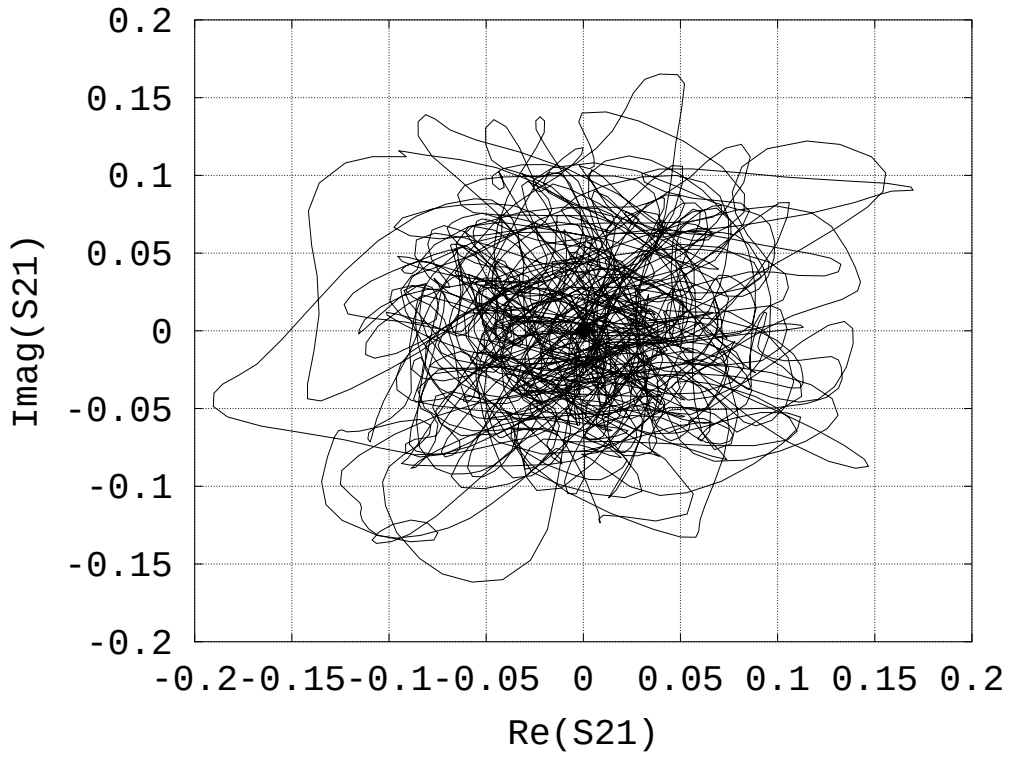

Figure 2.5: Over-stirring the Reverberation Chamber: Experimental data showing real vs imaginary parts of $S21$ over 1 stirrer rotation in 3200 steps at 2 GHz

$$N_{mech} = \frac{2\pi}{\theta_c} \tag{2.29}$$

The effectiveness of the stirrer can be seen to increase with frequency, as smaller movements of the stirrer are required to give an independent sample in the chamber. Below a certain frequency, the stirrer will become unusably ineffective. The chamber itself will stop resonating as frequency is decreased: the operation of a reverberation chamber must be operated in the region where enough modes resonate close enough together that the chamber is continuously resonant across changing frequency. The York chamber has dimensions of 4.70 m x 3.00 m x 2.37 m; a calculation using the Helmholtz equation indicates that it has over 60 modes below a frequency of 200 MHz. At 200 MHz it has also been found to support over 50 independent samples, indicating that the stirrer sufficiently changes the boundary conditions of the chamber to provide independent measurements at this frequency [80]. The York chamber is shown from the inside in Figure 2.7, where the stirrer is clearly visible in the shot.

Frequency Stirring

It is also possible to obtain independent samples in a reverberation chamber by changing frequency: as the wavelength of the stimulus is changed, reflections from the walls and stirrer will occur at a different phase, so the standing wave pattern in the chamber will change. A stirring effect may therefore be obtained by averaging over a frequency window of chosen bandwidth to either side of the frequency point of interest.

The number of available frequency samples is obtained in the same way as for mechanical samples: the stirrer is held static and the $S21$ is autocorrelated over frequency. The frequency

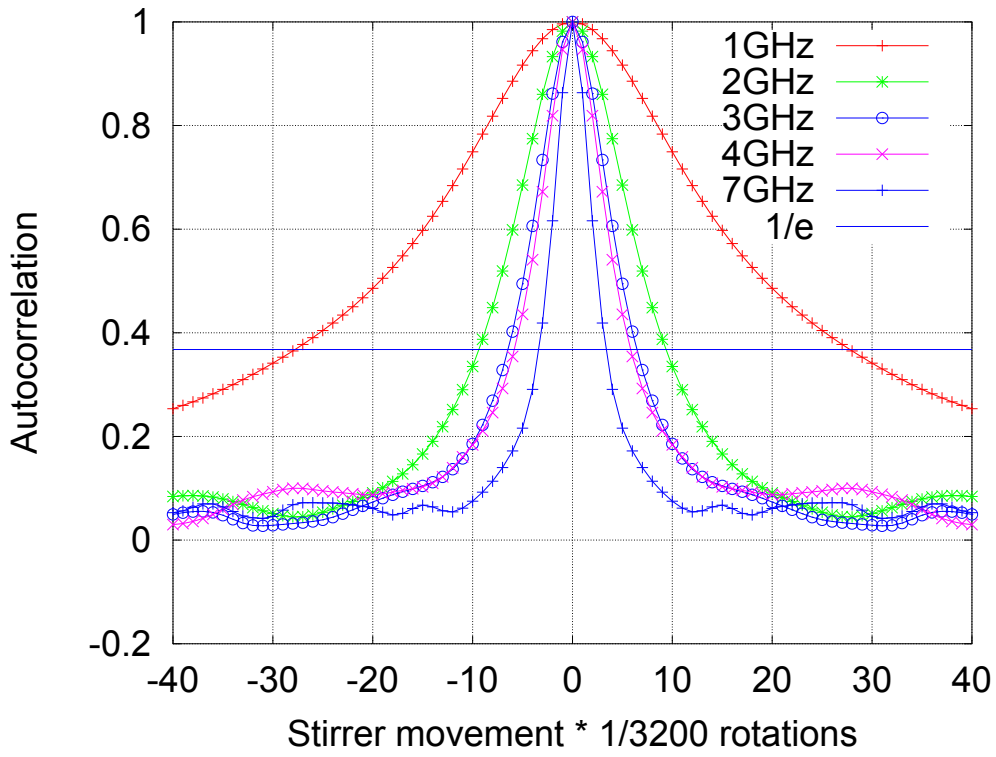

Figure 2.6: Autocorrelation of S21 over stirrer movement, to find the nuber of available independent samples in the York reverberation chamber

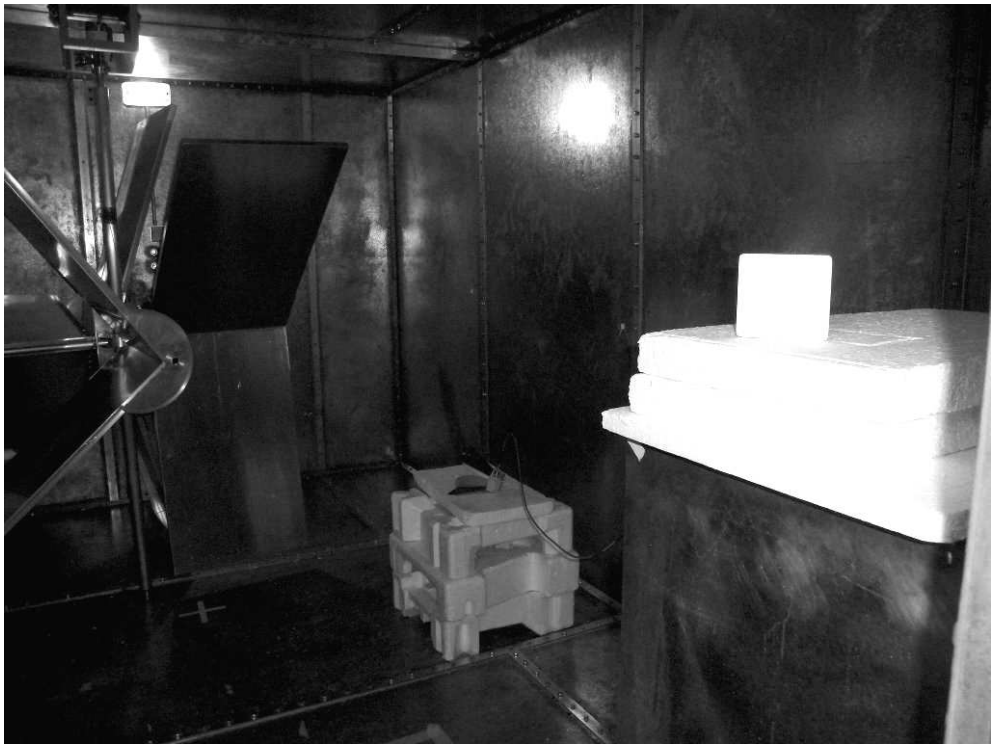

Figure 2.7: The York reverberation chamber: The stirrer is visible on the left of shot, one antenna points into the stirrer on its right, the other antenna is pointing at the camera. The York RC is an adapted secure communications room from a British foreign embassy.

shift required to provide an independent sample is that at which the autocorrelation function falls below the $1/e$ metric [81, 82]. This is then known as the coherence bandwidth B_c. For a given frequency stirring window size Δf, the number of available frequency samples N_{freq} is given in Equation 2.30, where C_{freq} is a constant of approximately unity, which equates the measured number of independent samples in the room with the approximation given by $\Delta f / B_c$. Note that this is the number of available frequency stirring positions; these will not all be used unless the sampling bandwidth B_s, which is the bandwidth between measured frequency points, is equal to or smaller than B_c, otherwise Equation 2.31 applies.

$$N_{freq} = C_{freq} \frac{\Delta f}{B_c} \ (B_s \leq B_c) \tag{2.30}$$

$$N_{freq} = C_{freq} \frac{\Delta f}{B_s} \ (B_s \geq B_c) \tag{2.31}$$

The total number of independent samples N_{ind} in a measurement is then the product of N_{mech} and N_{freq}, as in Equation 2.32.

$$N_{ind} = N_{mech} \times N_{freq} \tag{2.32}$$

Calculating the Q-factor of a Reverberation Chamber

From Hill [75], the Q-factor of a cavity is defined by Equation 2.33, where U_s is the total energy stored in the cavity and P_d is the power dissipated in the cavity.

$$Q = \frac{\omega \times U_s}{P_d} \tag{2.33}$$

For an individual resonant mode, Q can be obtained by taking the resonance bandwidth of that mode, as in Equation 2.34. Note that here, Δf is not the same as the Δf in Equation 2.31 where it represents the frequency stirring window size: here it is the 3 dB bandwidth of an individual resonant mode.

$$Q = \frac{\Delta f}{f} \tag{2.34}$$

However, in the statistical region in which reverberation chambers operate, these resonant peaks run into each other, so this is impossible. It is possible to approximate Q from the ratio of the volume filled by the stirrer to the volume of the chamber [82], as in Equation 2.35, where V is the volume of the reverberation chamber, V_s is the volume occupied by the stirrer and C_{mech} is once again a constant of the order of unity, equivalent to C_{freq} in frequency stirring.

$$N_{ind} = C_{mech} \frac{QV_s}{V} \tag{2.35}$$

Also from [82], it is possible to obtain Q from the coherence bandwidth of the chamber, as in Equation 2.36.

$$Q \approx \frac{f}{B_c} \tag{2.36}$$

From [83], Q can be obtained from $\langle S21 \rangle$ by Equation 2.37

$$Q = \frac{16 \times V \times \pi^2}{\lambda^3} \times \langle |S21|^2 \rangle \tag{2.37}$$

2.3.2 Calculating Absorption Cross Section

ACS can now be calculated from the change in Q when a loading object is inserted into the chamber. Varying the partial Q due to absorbers while holding all other partial Q factors constant in Hill's power balance equation (Equation 2.19) gives Equation 2.38.

$$\Delta Q_2 = \frac{-1}{({Q_{EUT}}^{-1} - {Q_{empty}}^{-1})} \tag{2.38}$$

Recall the formula for Q_2 (Equation 2.21) and rearrange to give ACS:

$$\langle \sigma_a \rangle = \frac{2\pi V}{Q_2 \lambda} \tag{2.39}$$

The change in Q_2, the term for partial Q due to the loading object is then given by Equation 2.40, assuming a previously empty chamber.

$$\frac{1}{Q_2} = \frac{\lambda \langle \sigma_a \rangle}{2\pi V} \tag{2.40}$$

Substituting into Hill's full power balance equation (Eq. 2.19) gives the total change in chamber Q due to the insertion of a load with average ACS $\langle \sigma_a \rangle$

$$\frac{1}{\Delta Q} = Q_1 + Q_2 + Q_3 + Q_4 = 0 + \frac{2\pi V}{\lambda \langle \sigma_a \rangle} + 0 + 0 \tag{2.41}$$

Substitute into Equation 2.37, which relates Q to $\langle |S21|^2 \rangle$

$$\frac{2\pi V}{\lambda \langle \sigma_a \rangle} = \frac{16 \times V \times \pi^2}{\lambda^3} \cdot \Delta \langle |S21|^2 \rangle \tag{2.42}$$

Cancelling gives Equation 2.43, which allows calculation of average ACS $\langle \sigma_a \rangle$ of a load, from the change $\Delta \langle |S21|^2 \rangle$ in the chamber's transmission coefficient when the load is inserted.

$$\langle \sigma_a \rangle = \frac{\lambda^2}{8\pi} \cdot \frac{1}{\Delta \langle |S21|^2 \rangle} \tag{2.43}$$

Calculating ACS with reflections at ports

Equation 2.43 assumes perfect transmission throughout the system. Realistically this is not the case: reflections due to impedance mismatches in cables and connectors will occur at both ports. Equation 2.44 divides the power averaged transmission coefficient $\langle |S21|^2 \rangle$ by the vector averaged reflection coefficients, to cancel the effects of these reflections [83]. The ACS equation (2.43), then becomes Equation 2.45, where G_{wo} is the chamber transmission coefficient $\langle |S21_{EUT}|^2 \rangle$ of the loaded chamber, corrected using Equation 2.44 to remove the effects of port reflections. Similarly, G_{no} is the unloaded chamber transmission coefficient $\langle |S21_{empty}|^2 \rangle$ corrected in the same manner, and G_r is the ratio of these two quantities: $G_r = G_{no}/G_{wo}$.

To measure ACS, it is therefore necessary to record the $S11$, $S21$ and $S12$ for both the unloaded and loaded chambers, to apply Equation 2.44 to transform $S21_{wo}$ and $S21_{no}$ to G_{wo} and G_{no}, and then to extract $\langle \sigma_a \rangle$ from the difference between the two G-factors using Equation 2.45.

$$\langle G \rangle = \frac{\langle |S21|^2 \rangle}{(1 - |\langle S11 \rangle|^2)(1 - |\langle S22 \rangle|^2)} \tag{2.44}$$

$$\langle \sigma_a \rangle = \frac{\lambda^2}{8\pi} \cdot \frac{1}{G_{no}} (G_r - 1) \tag{2.45}$$

Accuracy of the ACS calculation

Carlberg [83] has provided an error analysis of this ACS measurement technique, which is as follows:

Assuming they are independent, small errors ($\delta G/G$) in G_{no} and G_{wo} will add in quadrature to give a relative error $\delta G_r/G_r = \sqrt{2}\delta G/G$

The error in ACS is then given by Equation 2.46

$$\frac{\delta\langle \sigma_a \rangle}{\langle \sigma_a \rangle} = \frac{\sqrt{2}G_r}{G_r - 1} \frac{\delta G}{G} \tag{2.46}$$

The error in G may be determined by Equation 2.47, where k is the number of standard deviations in the error (and hence determines the confidence level, e.g. $k = 1$ would give 68 % confidence) and N is the number of independent samples over which the result is averaged.

$$\frac{\delta G}{G} = \frac{k}{\sqrt{N}} \tag{2.47}$$

It is important to note that the $\sqrt{2}G_r/(G_r - 1)$ term will amplify the errors for even a small error δG. This will be especially so if G_r is close to 1, i.e. if the effect of loading the cavity is small, so G_{wo} is proportionally not much smaller than G_{no}. The less energy absorbed by the EUT, the less G_{wo} will be attenuated compared to G_{no} and thus the larger the confidence interval of $\langle \sigma_a \rangle$.

2.3.3 Unstirred energy in a Reverberation Chamber

In any real reverberation chamber, some energy is going to be transmitted directly from transmitter to receiver, without interacting with the stirrer. This energy will consequently travel the same path between ports for multiple or all measurements, rather than being scattered differently every time the stirrer moves, and thus will skew the measurements taken in the chamber. This energy has found a *direct path* from transmitter to receiver, and adds a Rician component to the otherwise Rayleigh environment in the chamber.

Measuring K-Factor

The unstirred energy in a reverberation chamber can be quantified using the Rician K-factor, which is defined in Equation 2.48 [81].

$$K = \frac{\mathrm{P}_{\mathrm{direct}}}{\mathrm{P}_{\mathrm{stirred}}} \tag{2.48}$$

K may be calculated by Equation 2.49

$$K = \frac{|\langle S21 \rangle|^2}{\langle |S21 - \langle S21 \rangle|^2 \rangle} \tag{2.49}$$

The vector average operation in the numerator removes the stirred component of $S21$, therefore the numerator contains the unstirred transmitted power. In the denominator, the unstirred component of S21 (i.e. the vector averaged $\langle S21 \rangle$, where the stirred power has been

averaged out) is subtracted, so the denominator contains only the stirred power in S21. Divided, they therefore give K, the ratio of unstirred to stirred power in the measurement.

Vector Average Subtraction

As discussed above, the presence of a direct (i.e. unstirred) transmission of energy between the ports of a reverberation chamber will give a Rician distribution of field vectors, i.e. a distribution with normal components in two degrees of freedom, not centred on the origin. This means that there is a correlation between the field components, so the EUT will not be illuminated equally from all sides and at all points in the chamber.

To correct this, a vector average is taken of the complex $S21$. This gives the mean value of $S21$ over all stirrer positions at a particular frequency, which would be zero were the fields properly (i.e. Rayleigh) distributed around the origin. Subtracting this mean value from each of the individual values of $S21$, as in Equation 2.50, will re-centre both the real and the imaginary components of the distribution around 0. Some correlation between $Re(S21)$ and $Im(S21)$ may still remain if the shape of the distributions of the orthogonal components is non-Gaussian, however the vector average subtraction procedure does remove the non-centredness of the $S21$ distribution, and therefore greatly reduces the correlation between the real and imaginary components of $S21$. As the non-zero mean is caused by the presence of unstirred Rician energy, the vector average subtraction operation has removed this effect of the unstirred energy, and can be said to have improved the stirring in the chamber.

$$\langle |S21_{corrected}|^2 \rangle = \langle |S21_i - \langle S21 \rangle|^2 \rangle \tag{2.50}$$

In the complex plane, it can be visualised as Figure 2.8: the vector average of the complex $S21$ in 200 stirrer positions is subtracted individually from each individual $S21$, to re-centre the distribution of $S21$ around the origin in both the real and imaginary axes. Correct field statistics have been restored by removing the directive effect of the unstirred energy in the chamber. Removing this component of the energy at this point will then propagate through the calculation, so the effects of unstirred energy are not included when using Equations 2.44 and 2.45 to calculate $\langle G \rangle$ and $\langle ACS \rangle$ – the change in average ACS due to the presence of unstirred energy in the chamber will then be removed.

This can be tested by comparing the proportional change in ACS when vector average subtraction is applied, to the size of the Rician K-factor. Once data has been gathered, this test will be applied in Section 3.6.

2.3.4 Coherent Backscattering in a Reverberation Chamber

It has been claimed [84] that in a reverberation chamber, the antenna backscattering factor C_{BS} is always 2:

$$C_{BS} = \frac{\langle |S11 - \langle S11 \rangle|^2 \rangle}{\langle |S21|^2 \rangle} = 2 \tag{2.51}$$

The theory states that in a well stirred reverberation chamber, the stirred component of $\langle S11 \rangle$ contains double the power of the stirred component of $\langle S21 \rangle$ (and the same applies to $\langle S22 \rangle$ and $\langle S12 \rangle$ *mutatis mutandis*) because of what is known as the 'glory effect', where the ray paths from the transmitting antenna to the stirrer and back again deliver twice the power of paths from one antenna to the other via the stirrer, due to each ray adding in phase with its outgoing ray. This effect is then known as the coherent backscattering effect. The

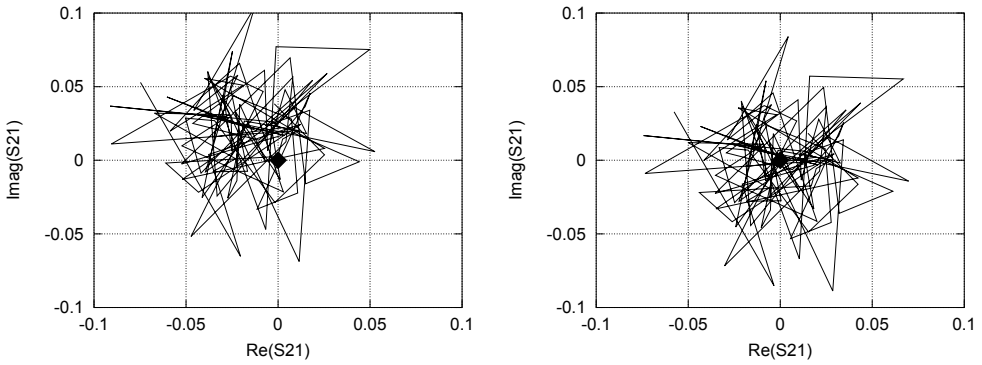

(a) A poorly-stirred measurement

(b) The same measurement after subtracting $\langle S21 \rangle$

Figure 2.8: A visual example of vector average subtraction. The vector mean $\langle S21 \rangle$ of the 200 points is subtracted individually from each point, to centre the real and imaginary distributions of $S21$ around the origin

backscattering factor C_{BS}, which is the ratio of the stirred power in $S11$ to the stirred $S21$, will therefore always, according to this theory, be 2.

There are three components to $S11$: as shown in Equation 2.52. $S11_{FS}$ is the reflection from the antenna mismatch, $S11_{stirred}$ is energy that leaves the antenna and re-enters it again after interaction with the stirrer and $S11_{unstirred}$ leaves and re-enters the antenna without interaction with the stirrer.

$$S11 = S11_{unstirred} + S11_{stirred} + S11_{FS} \tag{2.52}$$

In a well-stirred chamber $S11_{unstirred}$ is assumed to be small. The vector average $\langle S11 \rangle$ will average $S11_{stirred}$ to zero, hence $\langle |S11 - \langle S11 \rangle|^2 \rangle$ removes only $S11_{FS}$ from the $S11$ parameter, leaving the stirred energy component remaining. This should then be twice the stirred component of $\langle S21 \rangle$. If this is correct, it would then be possible to measure σ_a using only one antenna, by doubling $S11_{stirred}$ to find $S21_{stirred}$. This is further investigated in Section 3.4.4.

2.3.5 Antenna Efficiency

The radiation efficiency η_r of a transmitting antenna is defined by Equation 2.53, where P_r is the power radiated from the antenna, P is the total power delivered to the antenna from the port (after mismatch losses) and P_l is the power lost in the antenna [85]. This may also be applied to receving antennas, in which case $\eta_r = P/P_{Rx}$, where P is the power at the terminals of the antenna and P_{Rx} is the power received by the antenna.

$$\eta_r = \frac{P_r}{P} = \frac{P_r}{P + P_l} \tag{2.53}$$

A measurement of the transmission between two antennas in a reverberation chamber will therefore include the product of both antennas' efficiencies. As the efficiencies are frequency-dependent, they may distort the frequency-dependent properties such as ACS. In order to remove the effects of the efficiencies from the true measurement of chamber transmission, it is necessary to divide by both efficiencies as shown in Equation 2.54, which can be rearranged to give the product of the two antenna efficiencies, as shown in Equation 2.55.

$$G = \frac{\langle |S21|^2 \rangle}{(1 - |\langle S11 \rangle|^2)\eta_1(1 - |\langle S22 \rangle|^2)\eta_2} \tag{2.54}$$

$$\eta_1\eta_2 = \frac{\langle |S21|^2 \rangle}{G(1 - |\langle S11 \rangle|^2)(1 - |\langle S22 \rangle|^2)} \tag{2.55}$$

Unfortunately, antenna efficiency is a notoriously hard property to measure, as it is impossible to obtain a value of P_r or P_{Rx} that has passed through one antenna once, and which therefore includes the effects of only one efficiency. If an antenna of known efficiency is available, it is possible to measure the efficiency of an antenna under test (AUT) using the reference antenna and measuring the power transmitted between these two antennas, as shown in Equation 2.56. P_{AUT} is the power measured at the terminals of the (receiving) antenna under test and P_{REF} is the power measured at the terminals of the (transmitting) reference antenna. It is also possible to measure efficiency using the Wheeler Cap method, where a AUT is placed below a conducting hemispherical 'cap' and its input impedance is measured with and without the cap [86].

$$\eta_{AUT} = \eta_{REF}\frac{P_{AUT}}{P_{REF}} \tag{2.56}$$

In a reverberation chamber, methods have been proposed [87,88] for measuring the efficiencies of one and two antennas. However, these methods rely on assumptions about the chamber backscattering factor at each antenna C_{BS1}, C_{BS2}, which are stated in Section 2.3.4 but which are shown in Section 3.4.4 to be inaccurate. Efficiency can however be measured using three antennas, in which case three efficiency products are found, one between each pair of antennas. The products η_1,η_2,η_3 may then be divided as in Equations 2.57 and 2.58 to give the relative efficiency of each individual antenna. The chamber time constant τ_{RC} must then be measured in order to discover the absolute efficiencies of the antennas. This is a lengthy process, as the frequency domain antenna measurements must be transformed into the time domain using an inverse Fourier transform to obtain the chamber time constant τ_{RC}. The smaller τ_{RC}, the finer the frequency resolution needed to detect this in the inverse Fourier transform, and hence the slower the frequency domain measurements will be.

$$\frac{\eta_1\eta_3}{\eta_2\eta_3} = \frac{\eta_1}{\eta_2} \Rightarrow \eta_1\eta_2\frac{\eta_1\eta_3}{\eta_2\eta_3} = {\eta_1}^2 \tag{2.57}$$

$$\eta_1 = \sqrt{(\frac{\eta_1\eta_3}{\eta_2\eta_3})\eta_1\eta_2} \quad \eta_2 = \sqrt{(\frac{\eta_2\eta_3}{\eta_1\eta_3})\eta_1\eta_2} \quad \eta_3 = \sqrt{(\frac{\eta_1\eta_3}{\eta_1\eta_2})\eta_2\eta_3} \tag{2.58}$$

2.4 Summary

In this chapter, all the theory necessary for taking measurements of absorption by the human body has been presented. The key outcomes are that at microwave frequencies, absorption by the body within a larger EMC environment may be appropriately simulated as an absorption cross section within a power balance model. A measurement of absorption cross section may be taken within a reverberation chamber; the methodology for such a measurement is designed, tested, improved and validated in Chapter 3. This methodology is then used to gather measurements of human ACS, which are presented in Chapter 4 and analysed in Chapter 5.

Chapter 3

Development of a Methodology for Measuring ACS

3.1 Overview

The theory for measurement of average ACS in a reverberant environment has been described in Chapter 2. This chapter describes the development of a methodology for taking measurements in the York reverberation chamber. This has dimensions 4.70 m x 3.00 m x 2.37 m and a lowest usable frequency (LUF) of 200 MHz [80].

3.2 Measurement of Absorption Cross Section in a Reverberation Chamber: Initial method

Initial measurements of average ACS were carried out in accordance with the methods described in [83]. These were conducted by measuring the drop in transmission between two antennas in the York reverberation chamber when it was loaded with a human subject. The antennas were two double ridged waveguide horns: an ETS-Lindgren 3115 and an ETS-Lindgren 3117. These were connected to an Agilent ENA E5071B vector network analyzer through N-type bulkhead connectors in the chamber wall, and placed as is shown in Figures 3.1 and 3.2. A full 2-port calibration was performed at the connectors on the antenna ports. The network analyzer (NA) used a 6 dBm stimulus, which was the highest that the NA would provide without amplification and which kept the worst-case $WBSAR$ well within exposure guidelines [11]. The NA's intermediate frequency bandwidth was set to 70 kHz.

Frequency sweeps were made using 1601 points, spaced at 5 MHz intervals from 1 GHz to 8.5 GHz. This frequency step was chosen as the reverberation chamber (RC) was known to lose coherence within 5 MHz across the frequencies of interest, so all frequency samples would be independent. 5 MHz was also chosen to provide a suitable compromise between measurement time and measurement resolution.

The equipment was arranged in the reverberation chamber as shown in Figures 3.1 – 3.3. In order to eliminate direct path, the port 1 antenna was aimed at the stirrer, while the port 2 antenna was pointed at a chamber wall at approximately 45 degrees. This gave a measured K factor of typically 0.03, rising to 0.1 at the lowest frequencies in the loaded chamber and with spikes of up to 0.15.

Normalized transmission factors were then calculated and σ_a was then calculated using Equation 2.45. Frequency stirring was applied using a window size of 20 points, i.e. 100 MHz. This window size was chosen as an acceptable compromise, providing additional 'stirring' to the existing mechanical stirring, without being so large as to obscure any resonances or other features of the measurement. As such, 100 MHz can be taken to be the frequency resolution of these results.

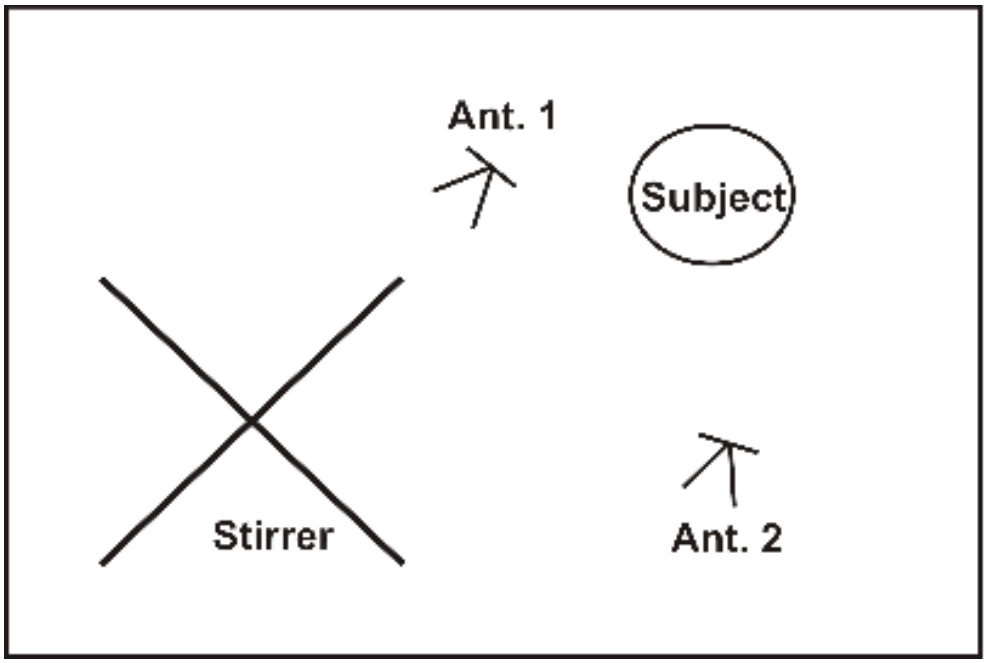

Figure 3.1: Equipment placement in the Reverberation Chamber during Campaign 1 measurements

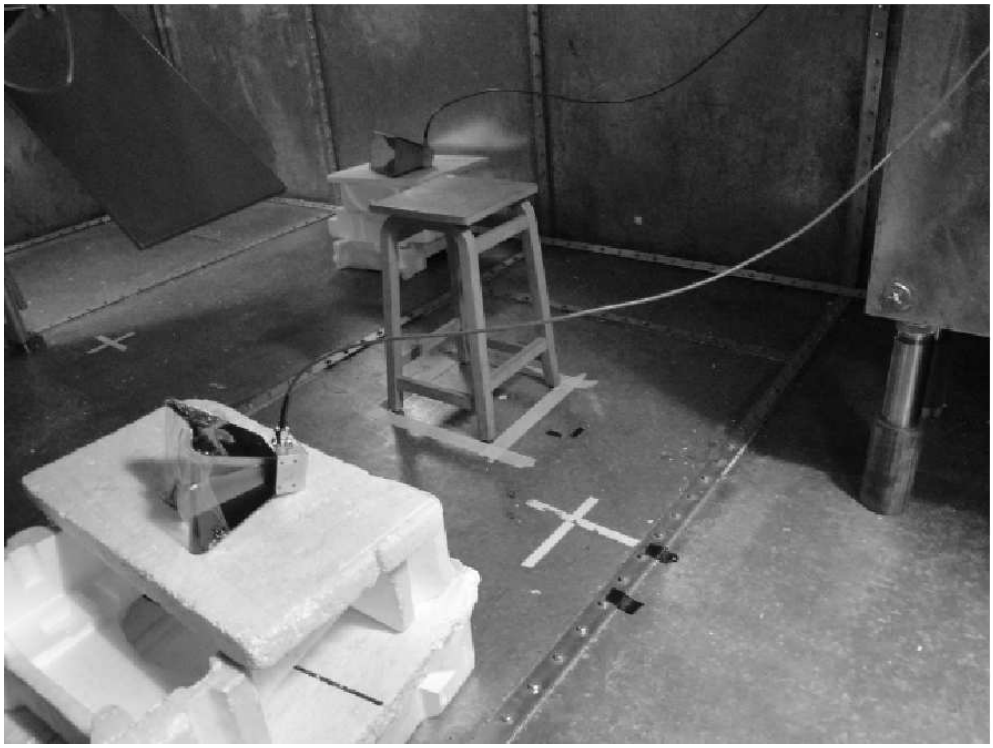

Figure 3.2: Equipment placement in the Reverberation Chamber during Campaign 1 measurements

Figure 3.3: Initial method: Experimenter in the Reverberation Chamber

3.2.1 Accounting for the radiation efficiencies of the antennas

As discussed in Section 2.3.5, a two-antenna ACS measurement will include the product of the antennas' radiation efficiencies. To obtain accurate data, it is therefore necessary to measure the radiation efficiencies of the antennas used in ACS measurement. Unfortunately, η_r is a notoriously hard property to measure. Gjorji Nusev, of the University of Ljubljana, attempted measurements of the York antennas using a two-antenna method; his results are shown in Figures 3.4 and 3.5. Notable about the results is that they are different for the two different measurements; other measurements were tried, but were extremely time consuming and calculations gave impossible efficiencies of over 100 %, indicating that something was wrong with the measurement. These measurements are still not reliable enough to take on a point-by-point basis, so it was decided to assign a flat radiation efficiency of 95 % to each antenna, which is a value supported by these and also by other measurements [87]. Further investigation into antenna efficiency would be useful, but its time-consuming nature makes it a low priority for this study - especially given that the horn antennas' relatively high efficiencies will not make large differences to ACS calculation, and that errors due to antenna efficiency will have the same effect on the ACS values of all subjects measured, hence the differences in average ACS between subjects will be preserved.

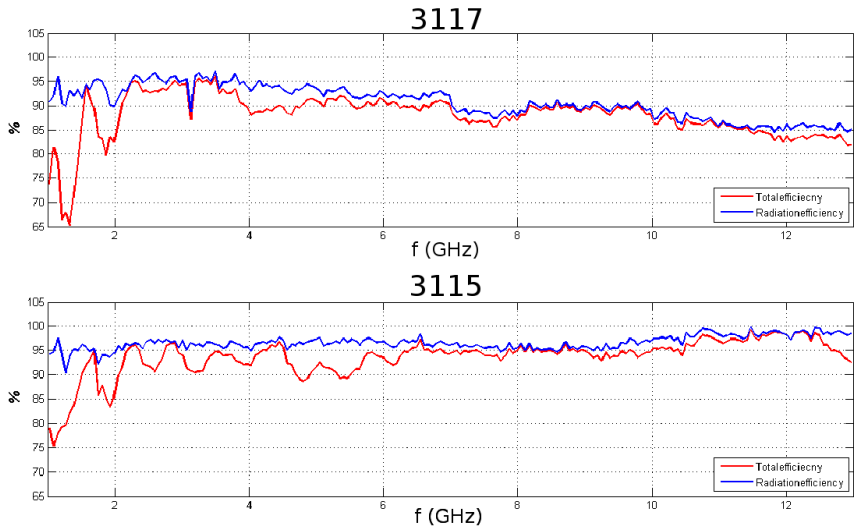

Figure 3.4: Radiation efficiency of the ETS-Lindgren 3115 and 3117 horn antennas, measured by G. Nusev

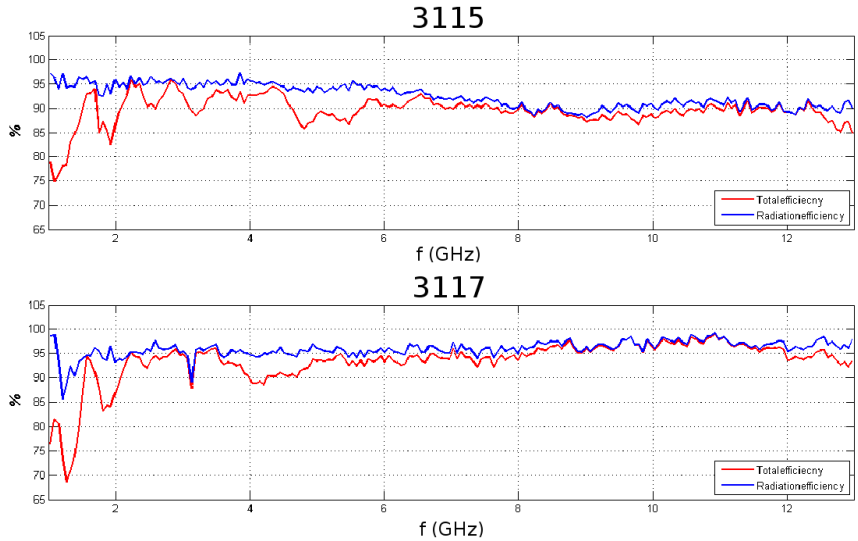

Figure 3.5: Radiation efficiency of the ETS-Lindgren 3115 and 3117 horn antennas: another measurement by G. Nusev

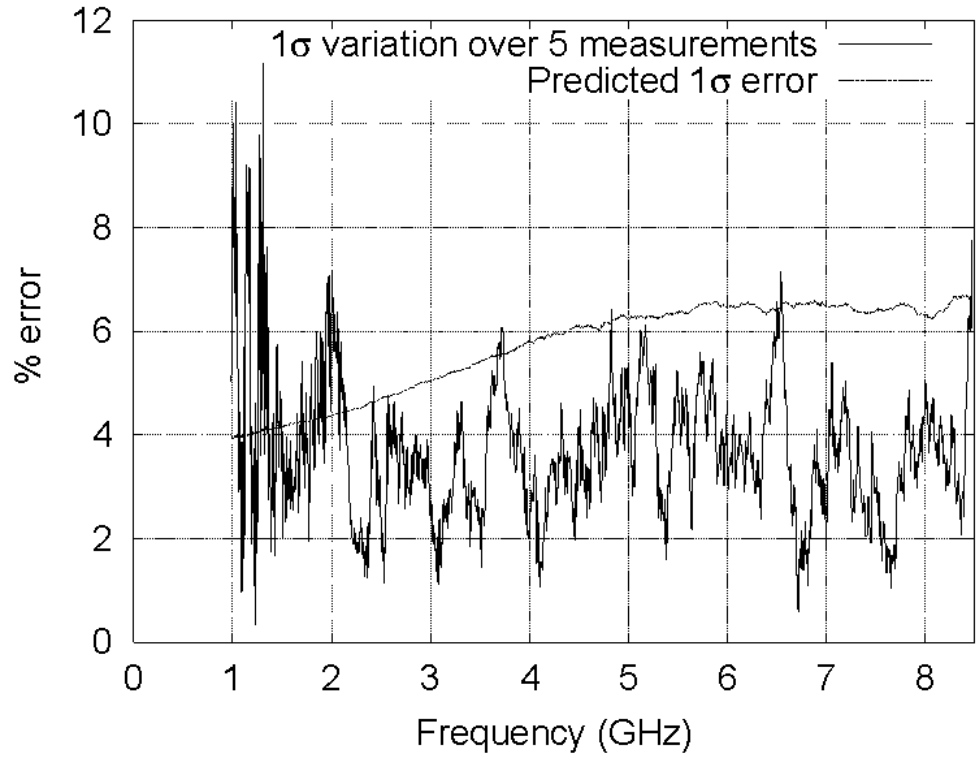

Figure 3.6: Actual 1σ error in $\langle ACS \rangle$ versus averaged theoretical statistical 1σ error in five measurements of the experimenter, with five different calibrations

3.2.2 Removal of unstirred energy using vector average subtraction

In order to eliminate any Rician component of $\langle |S21|^2 \rangle$, i.e. any unstirred power that remained due to imperfect stirring of the chamber, the vector average subtraction described in Section 2.3.3 was applied, i.e. $S21$ was vector averaged over all stirrer positions and this value was then subtracted from each individual measurement of $S21$ before the power average was taken. The resulting change in $< |S21|^2 >$ was as large as 15 % at the low end of the frequency range, but reduced to between 5 % and 10 % by 3 GHz, apart from one region around 5 GHz where it again spiked to 15 %. This is consistent with stirring being more effective at higher frequencies.

3.2.3 Achievable accuracy of the initial ACS measurement

The confidence interval of these measurements can be calculated using the theory in Section 2.3.1. Figure 3.6 shows the mean of the calculated 1σ confidence bands for five measurements of the experimenter, plotted alongside the actual standard deviation of the five measurements. The measured values match well with the theory above 2 GHz (remembering that this is a statistical value, not an exact calculation, and also that 5 data points will not accurately describe a normal distribution), but from 1-2 GHz there is some extra source of error, not accounted for by the theory and which is possibly due to noise in the reverberation chamber that is not then removed by the averaging calculation, or problems with the equipment at lower frequencies. However, over most of the frequency range, the measurement is accurate within its predicted 6-7 % confidence band.

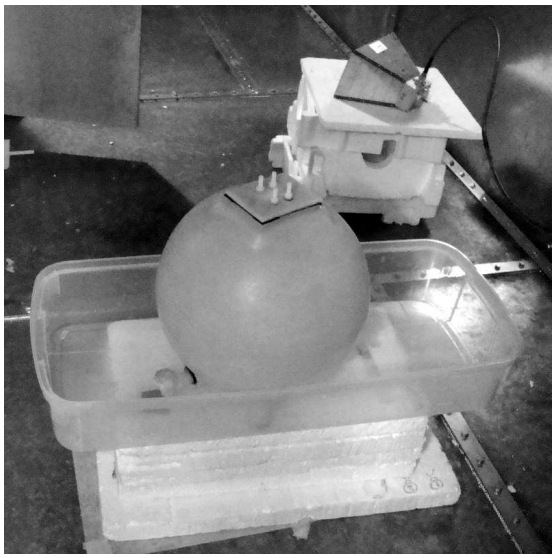

Figure 3.7: The spherical phantom used to validate the ACS measurement

3.3 Validation of the ACS measurement using a spherical phantom

The ACS measurement was validated using the spherical container shown in Figure 3.7, manufactured by Hambleton Bard and originally used for storing home-brew beer under pressure. As the ACS of a two-layer spherical object can be calculated analytically using two-layer Mie codes (as discussed in Section 2.2.2, this sphere could be used as a calibration object: its ACS could be measured in the reverberation chamber and compared to the Mie calculation. The sphere was manufactured of High Density Polyethylene (HDPE) and was 38 cm in diameter. The lid was made of steel with a gasket: this was replaced with a piece of nylon and a hand-cut rubber gasket. The phantom was filled with deionised water, the frequency-dependent dielectric properties of which were calculated from Stogryn's formula for pure water at 293 Kelvin [74]. The HDPE shell was given a flat frequency response of $\epsilon_r = 2.35$, $\tan(\delta) = 10^{-4}$, based on [89].

3.3.1 Error analysis of the Mie sphere calculation

Errors could be introduced to the Mie calculation of the spherical phantom's ACS due to: measurement errors of the sphere shell's thickness, measurement errors in the sphere's volume, inaccuracy in the sphere's volume due to its imperfectly spherical shape, inaccuracy of the inner layer's dielectric properties due either to inaccuracies in the Stogryn formula or to imperfections in the water, or inaccuracies in the outer layer's dielectric properties due to material variation (HDPE is not a well-defined material).

The shell's thickness was measured using a pair of Vernier calipers, which gave a reading of 4 mm. An attempt was made to measure the same property using an echo sounder, but no meaningful results were achieved. The measurement was taken on the flange around the opening at the top of the sphere; the manufacturing process might have left the curved sides of the sphere a different thickness. An error of ± 0.5mm was therefore assigned to this property. Figure 3.8 shows how the result of the two-layer Mie calculation varies when the shell's thickness is varied from 3 mm – 6 mm and Figure 3.9 shows the percentage error in the calculation generated by

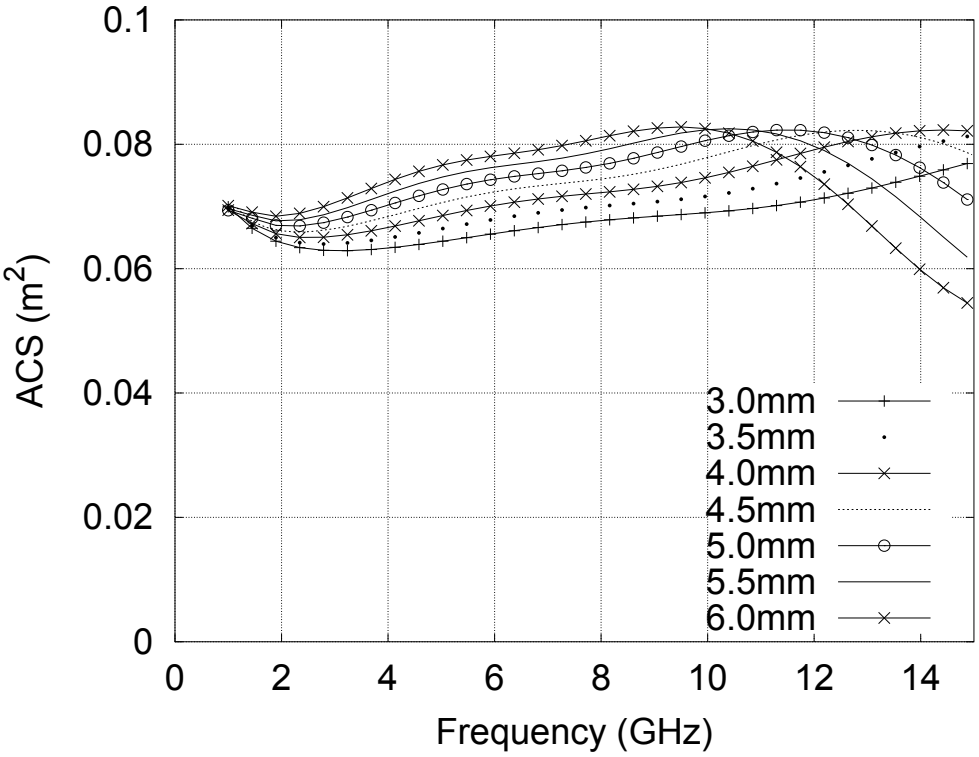

Figure 3.8: Variation in the two-layer Mie calculation of spherical phantom ACS for varying shell thickness

a ±0.5mm variation in the shell thickness.

The volume of the sphere was calculated by measuring the diameter of the sphere with a metre rule and reading to the nearest centimetre marking. A ±5mm error is therefore assigned to this property. The results of varying the sphere's diameter by ±5mm are shown in Figure 3.10.

The deionised water used to fill the sphere was taken from a lab-grade Millipore purifier. The dielectric properties of water have been well-researched and Stogryn's results have been confirmed to within tenths of a percentage point [90], therefore a ±0.5 % error is assigned to both the permittivity and conductivity. The results of varying these are shown in Figure 3.11.

It is notable that in Figures 3.10 and 3.11, ACS appears to change far more with changing sphere size and water permittivity at 1GHz than it does over the rest of the frequency range. However, not that the plotted results in these figures are percentage changes: the large change due to a 1 % ϵ_r variation at 1GHz in Figure 3.11 is still a change in ACS of less than 1%. These are not plotting errors: they do appear in the Mie simulations. This may either be due to an instability in the Mie code or a resonance in the sphere at 1 GHz, though it should be recalled that at this frequency, the size of the sphere approaches the Rayleigh small particle limit of validity for the Mie approximation. Given that it is also at the very bottom of the measured frequency range, at the point where the ACS measurement is least accurate, a full explanation is unlikely to be found for this feature, so it shall not be considered further.

HDPE is a less well-defined material than deionised water. Therefore, a ±5 % error is assigned to both the permittivity and conductivity of the outer layer. The results of varying these are shown in Figure 3.12.

From Figures 3.8 – 3.12, an ACS error bound can be set of 5 % for errors due to shell

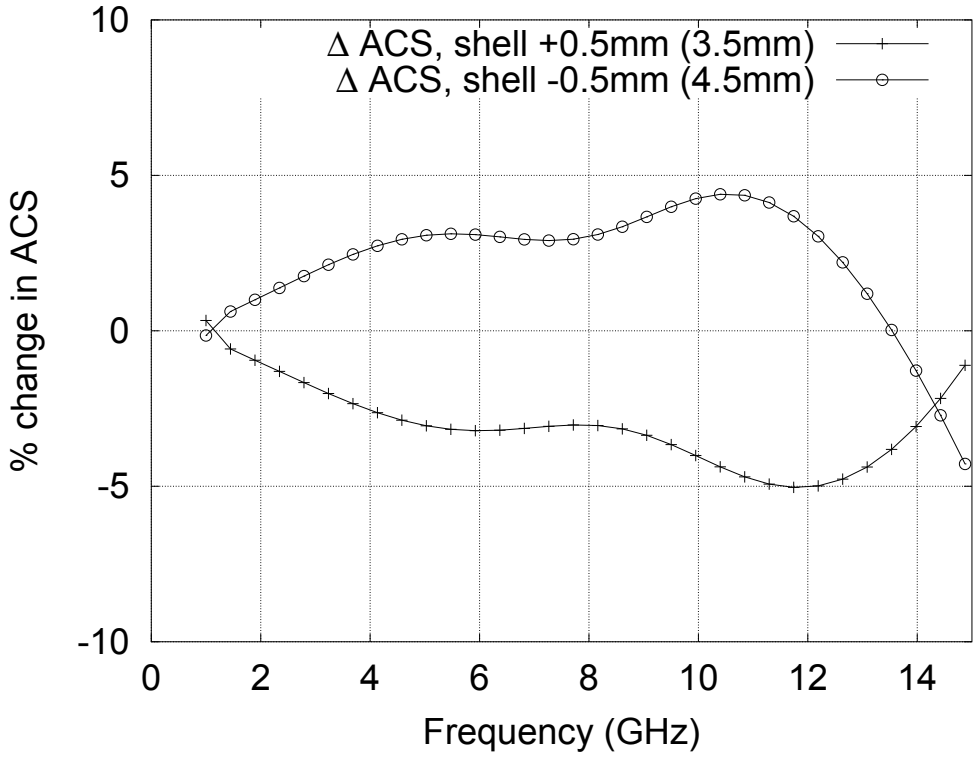

Figure 3.9: Percentage variation in the two-layer Mie calculation of spherical phantom for a ±0.5mm variation in HDPE shell thickness

thickness, 3 % for errors due to the size of the sphere, 1 % due to errors in the inner (water) layer's dielectric parameters and 4 % due to errors in the outer (HDPE) layer's dielectric parameters. To these, add a 5 % error to account for errors in the volume due to imperfections in the sphere's shape. Equation 3.1 adds the errors in quadrature, giving a total 1σ confidence interval δ_{sphere} of ±9 % for the two-layer Mie calculation of the spherical phantom's ACS.

$$\sqrt{0.05^2 + 0.03^2 + 0.01^2 + 0.04^2 + 0.05^2} = \delta_{sphere} = 0.09(1\text{sf}) \tag{3.1}$$

3.3.2 Comparison of a measurement of the spherical phantom's ACS to a two-layer Mie simulation

It is now possible to plot a two-layer Mie calculation of the spherical phantom's ACS vs a measurement. Figure 3.13 uses a measurement from February 17th 2012 for this purpose. The measurement was taken using the standard Campaign 1 measurement setup. Error bars are included on the plot for the ±9% confidence interval on the calculated value. Recall that the statistical accuracy of the measured value is just under 7 %, as shown in Figure 3.6. The current figure shows that the measurement and simulation fall within each other's confidence values, so can be said to agree. The shape of the measurement may give cause for concern, as it appears, while still within the confidence limit of the simulation, to be sloping downwards at high frequency. This point will be better informed by extension of the frequency range and improvement of the measurement accuracy, both of which are implemented in Section 3.4.

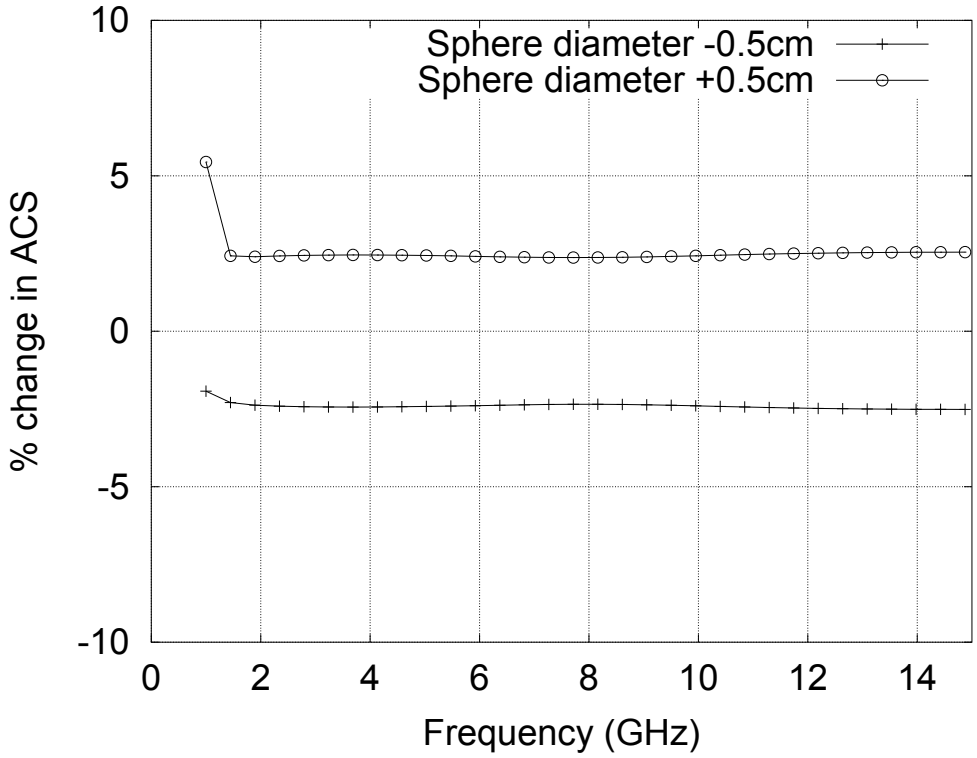

Figure 3.10: Percentage variation in the two-layer Mie calculation of spherical phantom ACS for a $\pm$5mm variation in sphere diameter

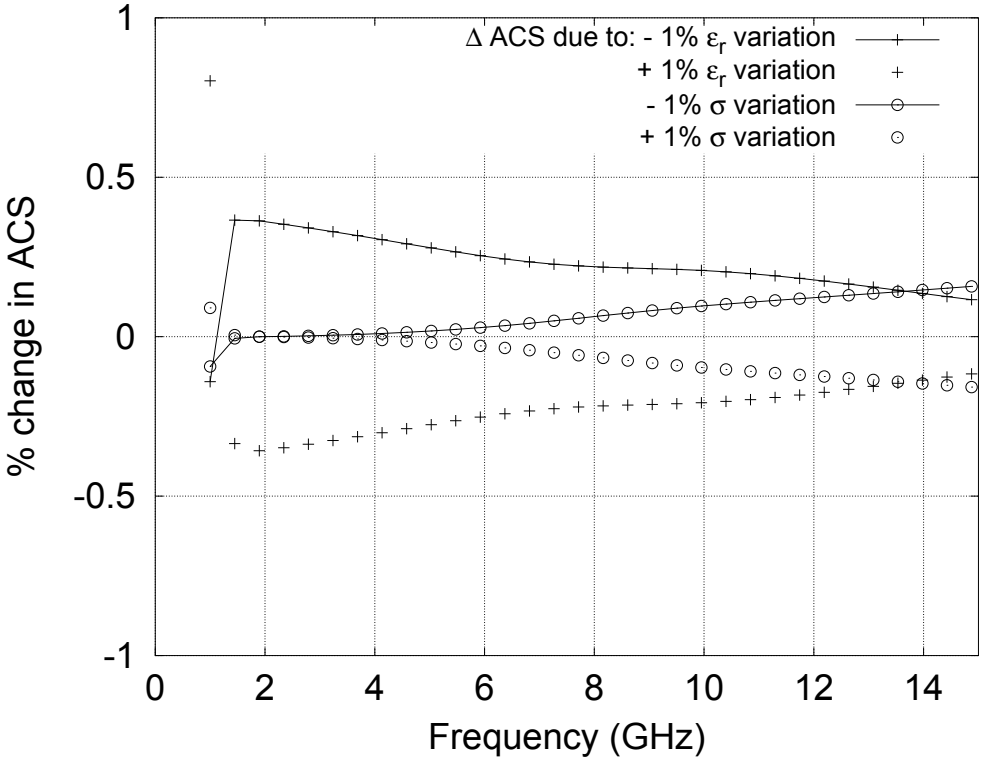

Figure 3.11: Percentage variation in the two-layer Mie calculation of spherical phantom ACS for a $\pm$1 % variation in inner layer (deionised water) permittivity and conductivity

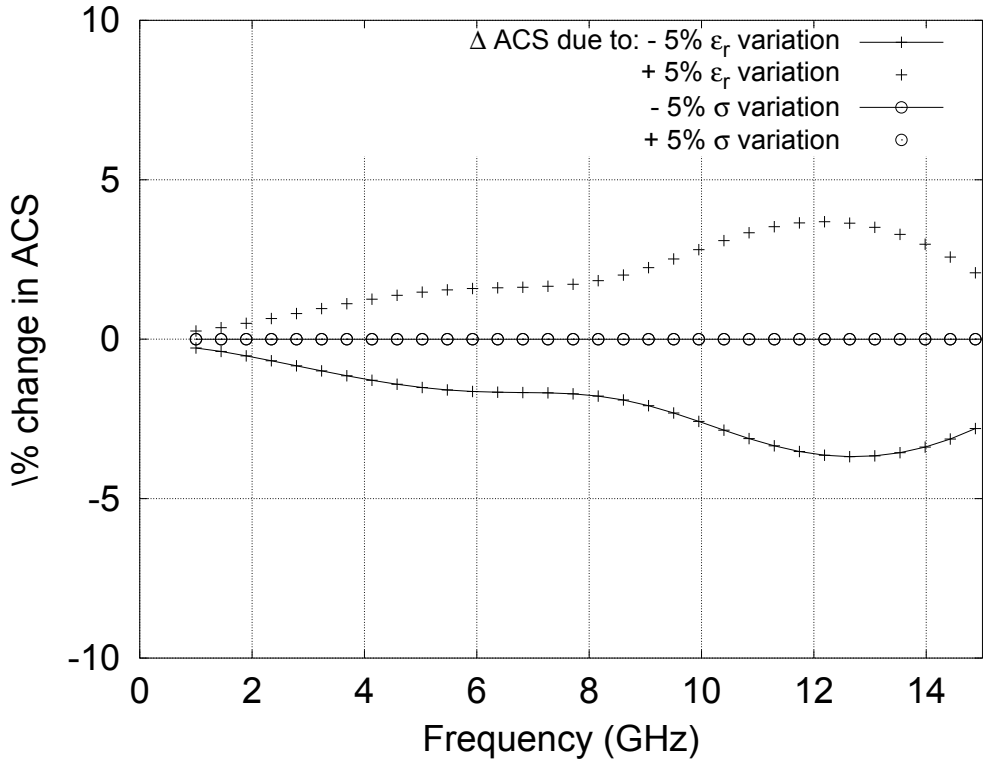

Figure 3.12: Percentage variation in the two-layer Mie calculation of spherical phantom ACS for ± 5 % variation in outer layer (HDPE) permittivity and conductivity

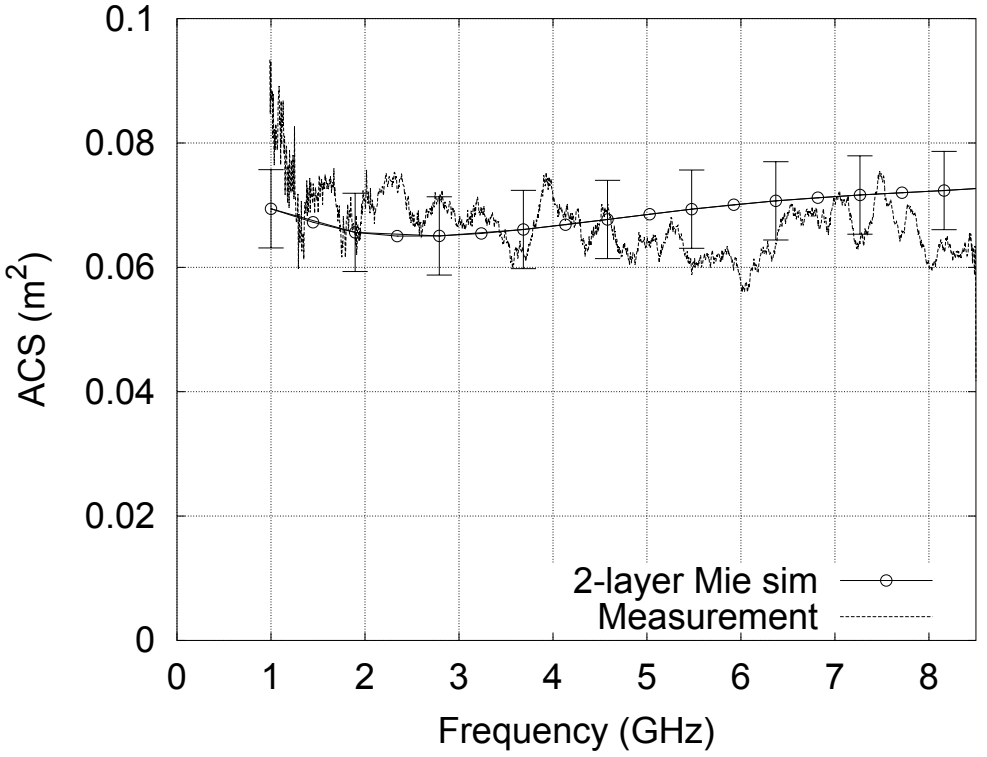

Figure 3.13: Simulation vs measurement of the spherical phantom ACS, using the initial measurement methodology. The two-layer Mie simulation has error bars corresponding to ± 9 %, which is the confidence limit of the simulation

3.4 Improvement and Optimisation of the Human ACS Measurement

At this point, a method has successfully been developed for measuring average ACS in the York chamber. It utilizes a stepped measurement technique, frequency stirring and the methodology provided by Carlberg *et al.* It was successfully deployed for the first measurement campaign of this thesis (C1), found in Section 4.2. However, the measurement technique has several problems. Ignoring systematic errors, the measurement is only accurate to within 7 %, due to the limited quantity of data that is gathered. A brief look at Chapter 4 will show that this is more than the difference in average ACS between many of the subjects measured, so the current technique is unable to distinguish between subjects of even remotely similar physiology. One solution would be to improve the statistical accuracy of the measurement by gathering more data. However, doing this using the C1 technique would be infeasible, as the measurement currently takes 15 minutes to run for each of the loaded and unloaded cases. As the measurement requires a human subject to remain almost motionless in the chamber, increasing the measurement time would discourage volunteers. Measurement speed must first be increased, so that more data can be gathered and the statistical accuracy of the results can hence be improved.

In addition to the statistical accuracy of the measurement, comparison to the Mie simulation of the spherical phantom in Figure 3.13 suggests the possibility of systematic errors in the upper part of the frequency range. These could possibly be due to the relatively high proportion of unstirred energy (the K-factor) of this measurement, which currently varies between 0.03 and 0.15. Improving the stirring of the measurement can only prove beneficial. Extending the frequency range upwards would also better inform this observation, in addition to the obvious benefit of observing the quantities under investigation across a wider range of frequencies. The speed, accuracy, stirring and frequency range of the measurement are all targets for improvement.

3.4.1 Equipment

Before the second measurement campaign (C2) was started, a new network analyser was purchased. This was a Rohde & Schwarz ZVB20 vector network analyser, capable of measurements from 10 MHz – 20 GHz

The Rohde & Schwarz datasheet [91] recommends that the ZVB20 be switched on 30 minutes prior to calibration and use, after at least three hours stored at the experimental ambient temperature. These conditions were followed for all measurements using this NA.

3.4.2 Continuous stirring

The C1 methodology utilised stepped stirring, in which the stirrer was moved between measurements, then held static while the NA performs a frequency sweep. This is time-consuming, as the stirrer must be accellerated and then allowed to settle between measurements. It is faster to move the stirrer at a constant speed while continuously sweeping the NA over frequency.

Figure 3.15 shows two measurements of the spherical phantom, one using the C1 measurement technique and the other using continuous stirring. The second measurement uses 800 NA sweeps over one full rotation of the mechanical stirrer, a 5 MHz frequency step and a 100 MHz frequency stirring window, giving 20 frequency samples - the same as the stepped measurement. The continuously stirred measurement takes 8 minutes to run and the measured average ACS

stays visibly closer to the two-layer Mie result than does the stepped measurement, indicating improved stirring. The improvement in the stirring will be quantified in Section 3.4.3; for now, it is enough to observe that increasing the number of mechanical stirrer positions has resulted in improved results that are consistent with the simulation, which shows that more samples are available in the chamber than were utilised in the C1 measurement technique.

3.4.3 Optimisation

The previous set of live RC measurements had the problem that in order to extract sufficient information to provide an accurate average ACS measurement, it was necessary to run the measurement for longer than anyone was prepared to remain static in the chamber. The measurement has been accelerated through the use of continuous mechanical stirring and at this point in the development of the human ACS measurement, it uses 800 NA sweeps over one full rotation of the mechanical stirrer, a 5 MHz frequency step and a 100 MHz frequency stirring window, giving 20 frequency samples. The measurement can be further improved by optimising the measurement technique to utilise the reverberation chamber's full capabilities, in order to gather the maximum possible amount of data, *in the right places*, in the shortest amount of time.

Properties over which we have control are:

- The speed of the stirrer
- The number of sweeps taken by the NA (i.e. the number of mechanical stirrer positions)
- The speed (up to its maximum) at which the NA sweeps over frequency
- The NA's IF bandwidth, which limits its maximum sweep speed
- The frequency step size of the sweeps
- The size of the frequency stirring window. However, an overly large window could smooth genuine features of the data.

Properties over which we do not have control:

- The number of independent samples available from the chamber - this varies over frequency, and is linked to the chamber's Q-factor.
- The Q-factor of the chamber. This can be reduced by loading the chamber with extra absorbers. It will also be reduced when the chamber is loaded by a human subject, so care must be taken to make calculations for this case, rather than for the empty case.

Equipment considerations

Network Analyser IF Bandwidth

The maximum bandwidth on the ZVB20 is 500 kHz. Using the 800 position measurement, only a few seconds were saved by setting the analyser to this value, so the next setting of 100 kHz was chosen for use for further measurements.

Equipment placement

Shortening the cables between the network analyser and the antennas would allow the NA to sweep faster, as individual pulses spend less time passing through the cables. The antennas were

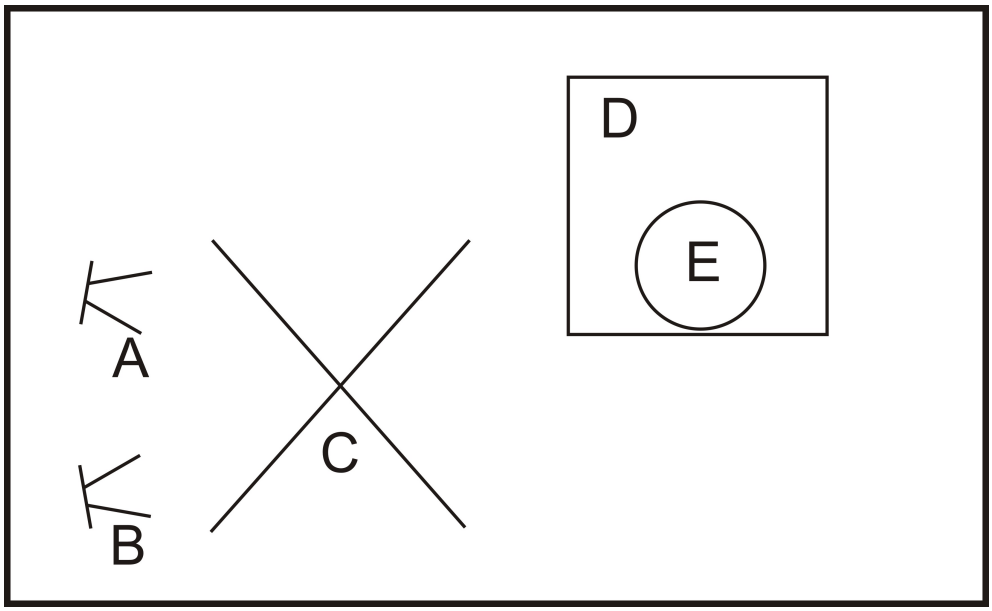

Figure 3.14: Equipment setup in the reverberation chamber for Campaign 2 measurements. Horn antennas A and B are on short cables, placed next to the bulkheads on the wall and facing into the stirrer C, on the opposite side from the subject E, who sits on the polystyrene block D.

therefore moved to the positions shown in Figure 3.14. Cables were routed through bulkheads in the chamber wall on the left in the diagram, opposite to the bulkheads used in the previous setup. This new setup allowed a total of 5 m of cabling to be used: two 1 m and two 1.5 m cables, one of each both inside and outside the chamber.

Additionally, this new positioning allowed the two antennas (which are also cross-polarized) to be pointed directly into the stirrer. This should stir the energy in the chamber better than the setup used in Campaign 1, which is shown in Figure 3.1. The effect on the stirring of this change in antenna position will be investigated in Section 3.6.3.

Optimising Accuracy

The equations in Section 2.3.1 show that there is a trade-off between measurement speed and achievable accuracy. The use of more mechanical stirring will increase accuracy, but will also increase measurement time. This could be reduced by an increased frequency stirring window, but frequency resolution would be lost in the process. The time penalty of extra mechanical stirring could also be offset by increasing the frequency step size, at the cost - again - of decreased frequency resolution. This latter technique may additionally attenuate the effectiveness of the frequency stirring: this is discussed in Section 3.4.3.

Optimising Frequency Stirring

Measurements were taken from 500 MHz - 15 GHz in 5 MHz steps, in the empty chamber and with the spherical phantom present. These measurements were continuously stirred, with sweeps taken over 800 stirrer positions. The $S21$ was then autocorrelated over stirrer positions at 1, 4, 7, 11 and 14 GHz, and was correlated over 1 GHz ranges centred around each of these frequency points for the averaged $\langle |S21|^2 \rangle$.

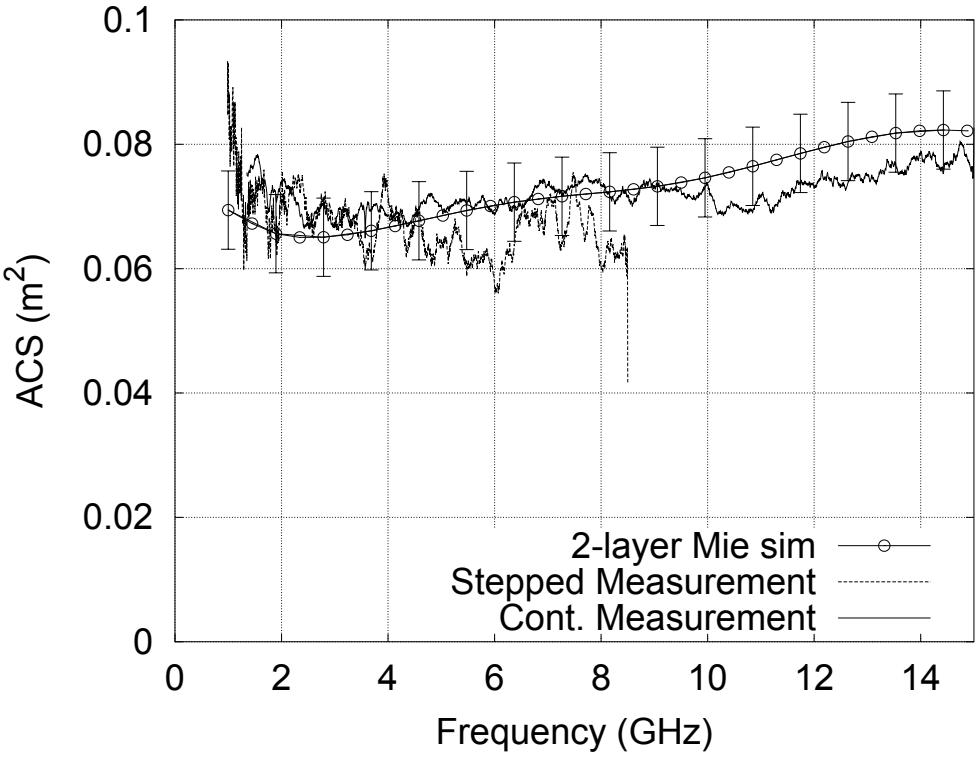

Figure 3.15: Spherical phantom $\langle ACS \rangle$, measured using stepped and continuous stirring

To check that changes in the frequency stirring had no impact on the effectiveness of the mechanical stirring, the data was then downsampled to give one frequency point every 10 MHz and the $S21$ was once again autocorrelated over stirrer movement. Figure 3.16 shows the correlation over stirrer movement for the 5 MHz case. When the data was downsampled, the equivalent graph was identical to Figure 3.16, indicating that as predicted, a decrease in frequency resolution does not affect the number of independent mechanical positions available in the chamber. Frequency and mechanical stirring can therefore be optimised independently.

Figures **??** and 3.18 show the autocorrelations of the same data over frequency, for the original and the downsampled data. They show that coherence is lost within 5 MHz and 10 MHz respectively, i.e. the first frequency step in both cases. The number of available frequency samples has therefore remained the same; the coherence bandwidth is less than 5 MHz for the empty chamber and each frequency point provides an independent sample, so the number of samples used is equal to the number of frequency points within the stirring window. The frequency stirring could be improved (i.e. more samples could be collected) by narrowing the frequency resolution of the measurement.

Widening the frequency step

This would increase the speed of the measurement. It would, however, proportionately reduce the number of samples available in any given window used for frequency stirring, requiring a larger window to be used to maintain accuracy - this larger window could then obscure features of the measurement. Reducing measurement time by increasing the frequency step would allow the use of more frequency sweeps (i.e. more mechanical samples) for a given measurement time. However, Table 3.1, which gives the total number of independent samples in a measurement

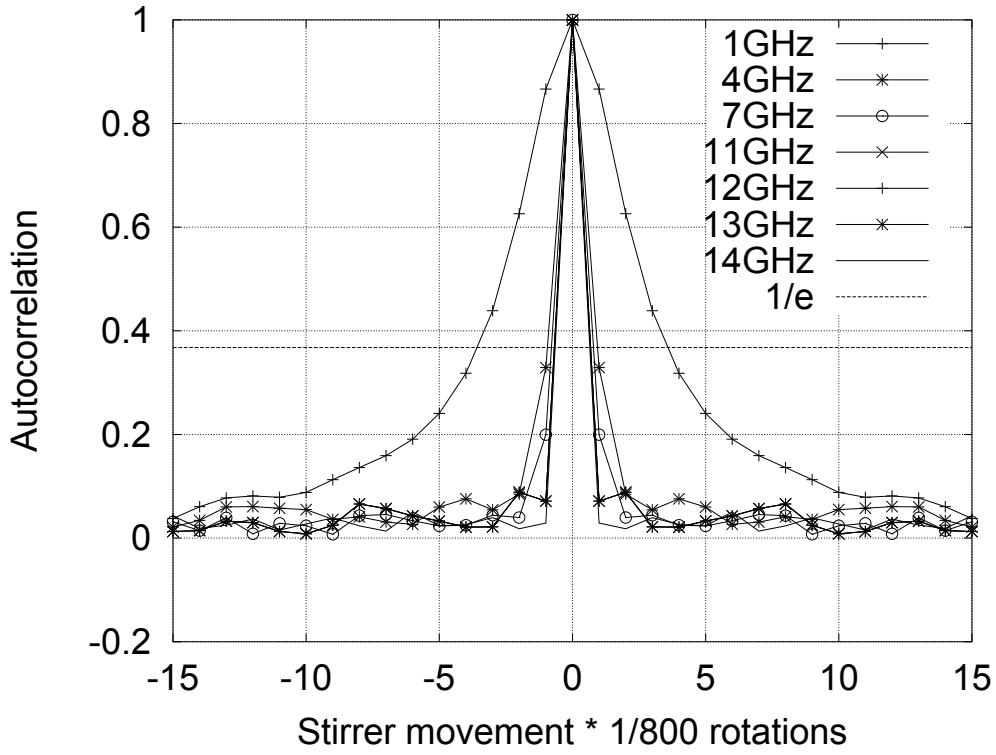

Figure 3.16: Autocorrelation over stirrer movement, empty chamber, 5 MHz steps

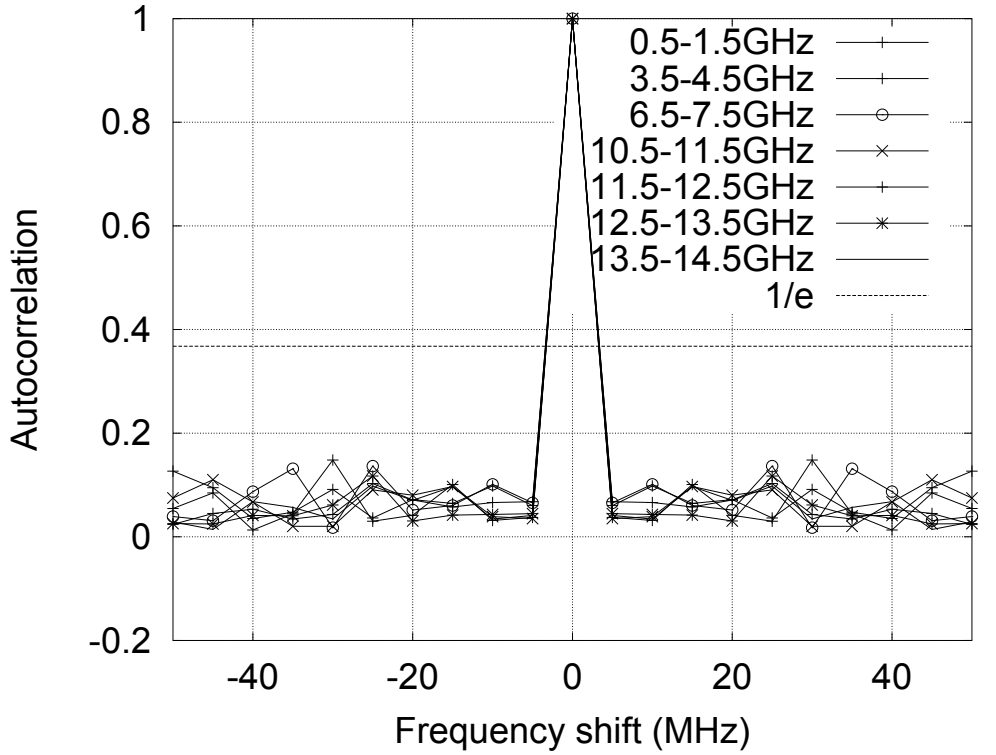

Figure 3.17: Autocorrelation over frequency, empty chamber, 5 MHz steps

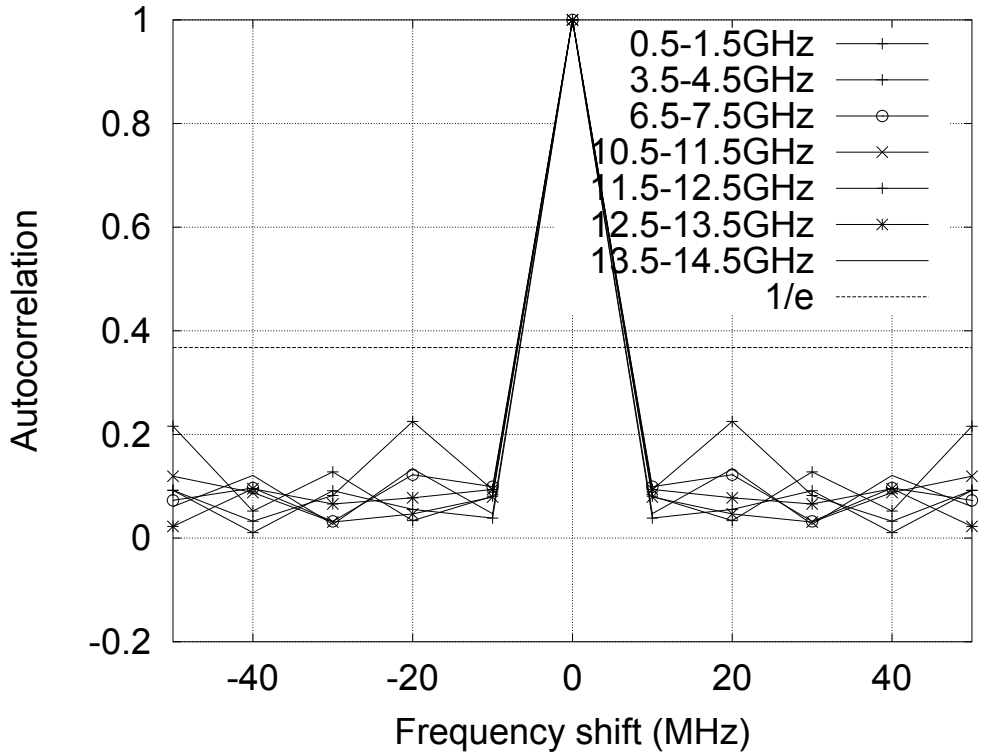

Figure 3.18: Autocorrelation over frequency, empty chamber, 10 MHz steps

Table 3.1: Total independent samples in an 800 mechanical position, 100 MHz frequency window measurement, where 6400 steps = 1 complete rotation of the stirrer

f(GHz)	Steps to incoherence	Available mech samples	Freq samples	Total
1	25	115	20	2300
2	15	320	20	6400
3	9	457	20	9140
4	8	640	20	12800
7	5	800	20	16000

with 800 mechanical stirrer steps and a 100 MHz frequency window, shows that this would only be useful in the upper part of the frequency range, where there are more independent samples available: at 1 GHz there are only 115 available mechanical samples, so all the information available from mechanical stirring is currently being extracted from the chamber. Broadening the frequency step would, by reducing the effectiveness of the frequency stirring, reduce the amount of information extracted at the low end of the range, where there is least available and it is therefore most necessary that all available information be collected.

Narrowing the frequency step

It would be possible to gain extra frequency samples by using a finer frequency resolution, although this would increase the NA's sweep time. It is necessary to determine the minimum frequency step that will give an independent sample at all points across the frequency range. Reducing the frequency step to a finer level would be pointless, but reducing it to this level will provide extra independent samples across the entire spectrum. The frequency stirring will then be maximally efficient at extracting information, allowing the measurement time to be reduced

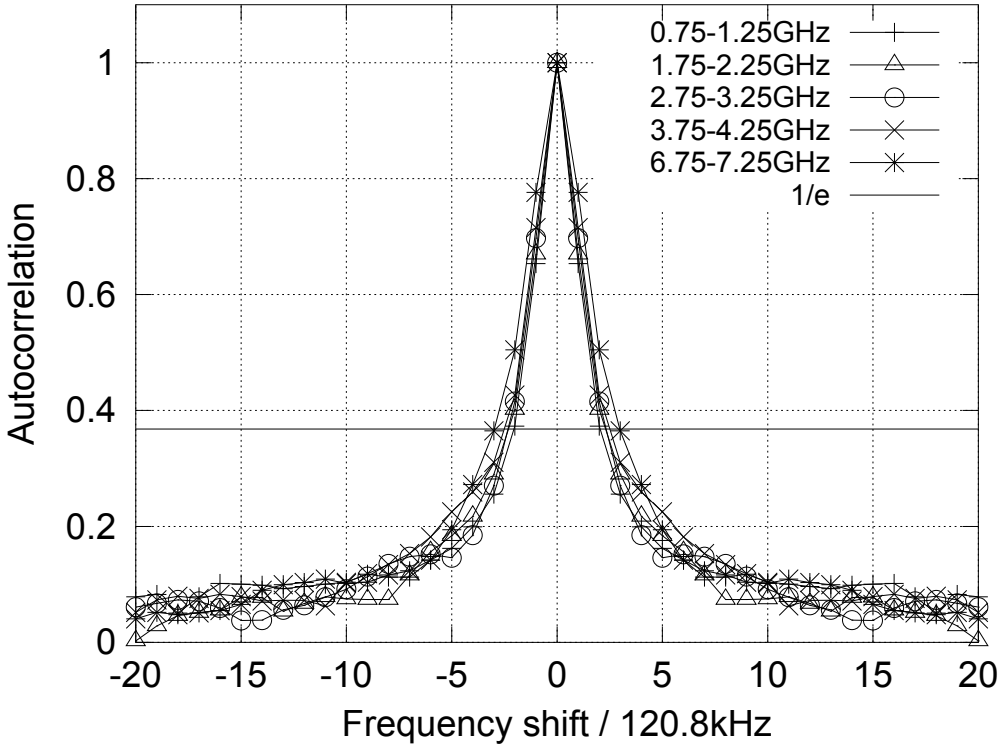

Figure 3.19: Autocorrelation over frequency in steps of 120.8 kHz (empty chamber)

by using fewer mechanical samples - an experimental strategy which will remove mechanical information only at the high frequencies where more independent samples available than are needed, but not at the low frequencies where all the available information must be gathered.

In order to find the coherence bandwidth of the chamber, sweeps were taken with the same setup as before but with a frequency resolution of 120.8 kHz - the finest that could be achieved while fitting a 1-15 GHz frequency range into two sweeps of the NA. Data was taken for the empty chamber, for the chamber loaded with the spherical phantom and for the chamber loaded with the experimenter. Autocorrelations are shown in Figures 3.19, 3.20 and 3.21. These show that frequency stirring has so far been under-utilised, as the chamber would support a far narrower frequency step than 5 MHz, and hence far more frequency samples than are utilised in a measurement with a 5 MHz step. However, it is also apparent that the number of independent samples in the empty chamber is not the limiting factor: that is the number of independent positions in the loaded chamber, which is attenuated as the chamber's Q is lowered. At 1 GHz, the coherence bandwidth increases to 1.61 MHz when loaded by the experimenter. However, as the experimenter's average ACS was lower than that of some subjects that were measured in previous experiments, 2 MHz would be a sensible frequency step, which would collect nearly all of the information from the loaded chamber while not wasting time by measuring coherent frequency points.

These figures give a fine enough frequency resolution to allow inference of the chamber's coherence bandwidth. These inferred coherence bandwidths are shown for each case in Table 3.2, along with the respective Q-factors calculated using Equation 2.36.

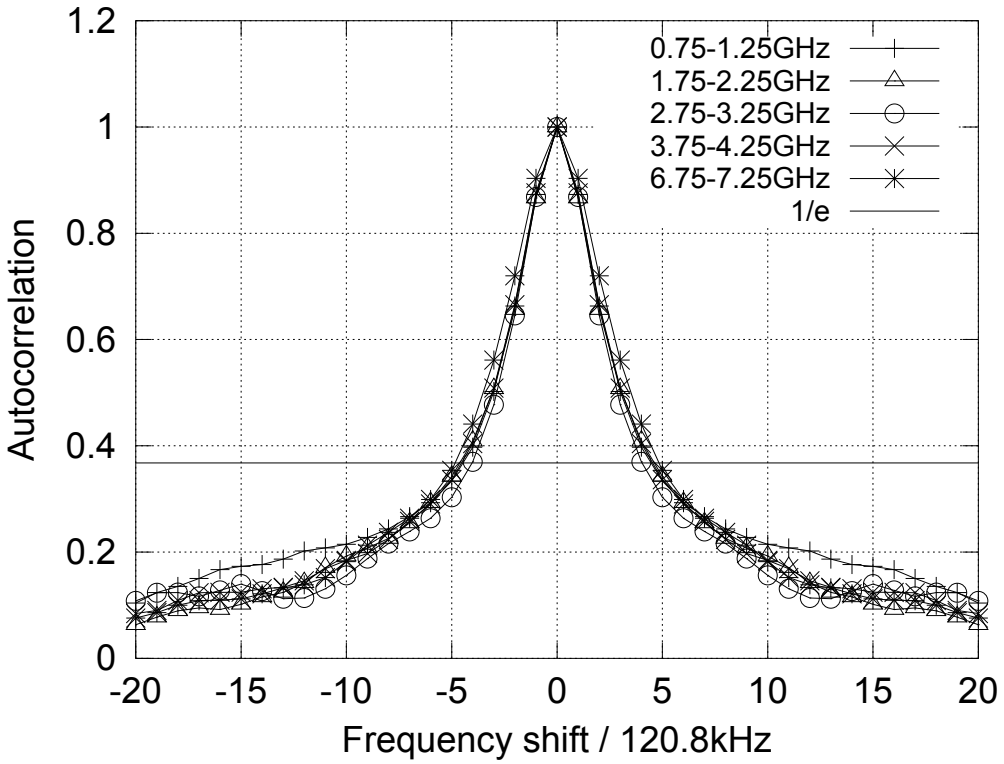

Figure 3.20: Autocorrelation over frequency in steps of 120.8 kHz (spherical phantom)

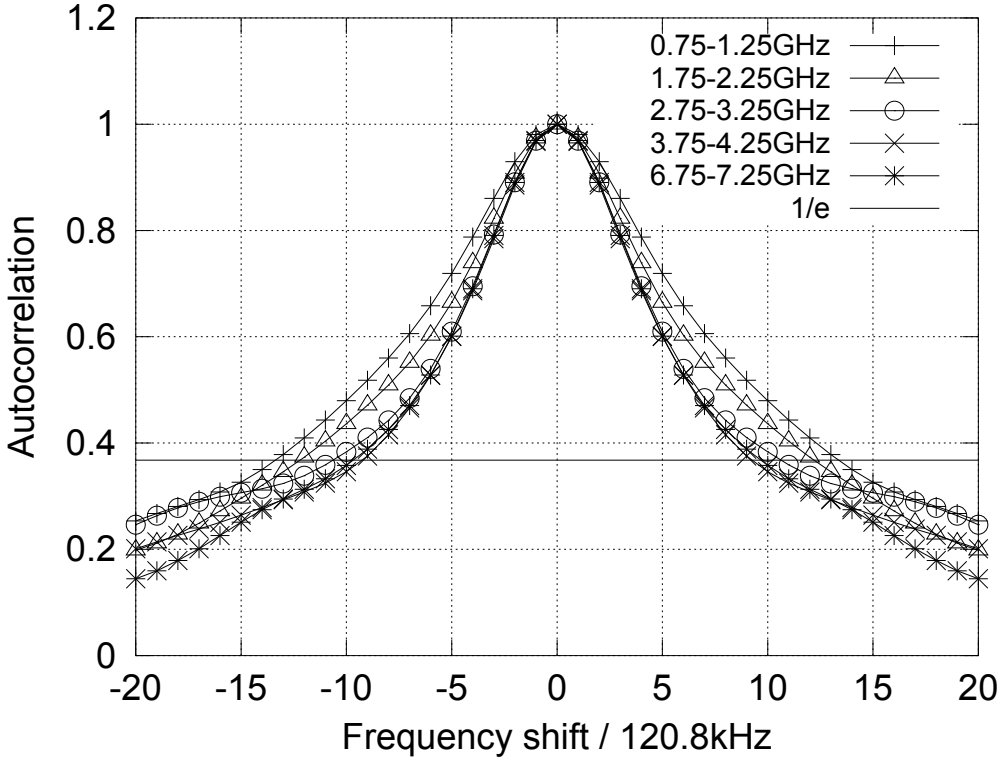

Figure 3.21: Autocorrelation over frequency in steps of 120.8 kHz (72 kg human subject)

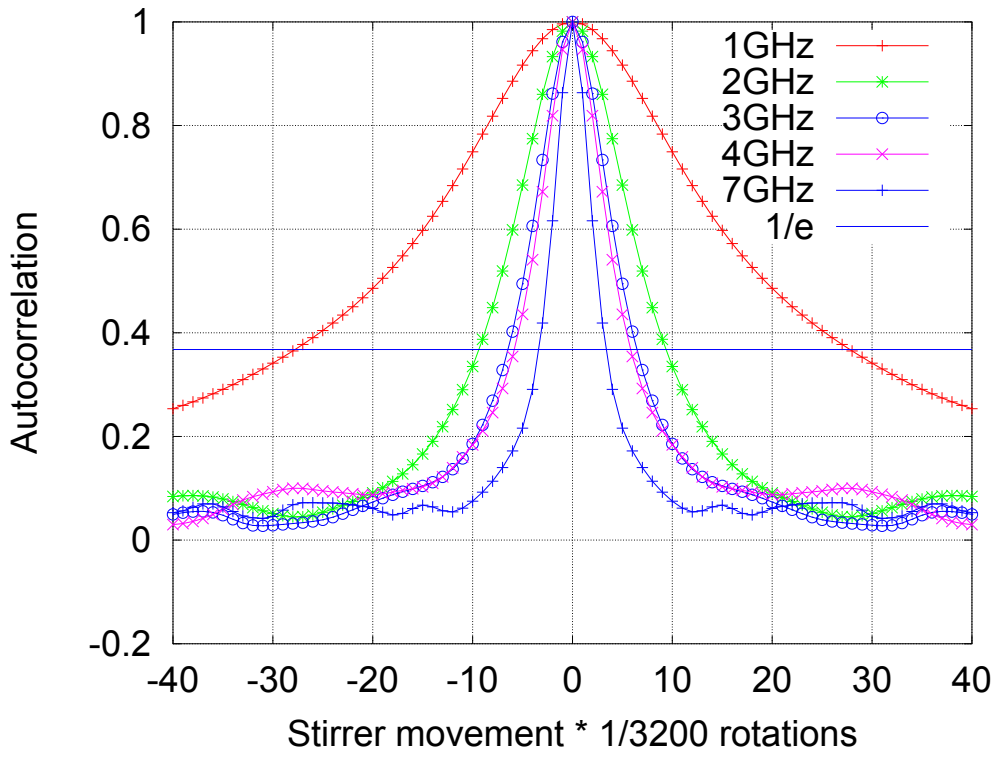

Figure 3.22: Autocorrelation over 1 full rotation of the stirrer, in 3200 steps (Reproduced from Figure 2.6

Optimising Mechanical Stirring

If $1/e$ is used as the threshold of coherence, Figure 3.16 shows that transmitted signals become incoherent after only one movement of the stirrer (1/800 rotations), at all frequencies except the lower end of the frequency range. In order to give more detail, the 3200 stirrer position measurement from Campaign 1 was autocorrelated. The results are shown in Figure 3.22. The number of steps required to lose coherence, and therefore the number of mechanical samples available in the chamber, are shown in Table 3.3. This shows that the number of independent samples supported by the chamber (plotted in Figure 3.23) increases with frequency – no data was computed above 7 GHz as the available 1280 samples are already more than sufficient. Only 115 samples are available at 1 GHz so taking a greater number of mechanical samples will only improve the measurement at higher frequencies. Measurement time has already been extended by narrowing the frequency resolution to 2 MHz from 5 MHz, as the NA now has to perform 2.5 times as many sweeps as before. In order to minimise measurement time, the number of mechanical samples taken should be kept low, at a level that will improve the measurement across the whole spectrum: to this end, the NA will be swept 300 times over the stirrer's rotation. This will provide 300 independent samples across all but the very bottom of the spectrum, will keep measurement time down (300 sweeps of the NA take less than 8 minutes, which is considered to be acceptable) and will, when combined with the 2 MHz frequency resolution, provide the total number of independent samples shown in Figure 3.24.

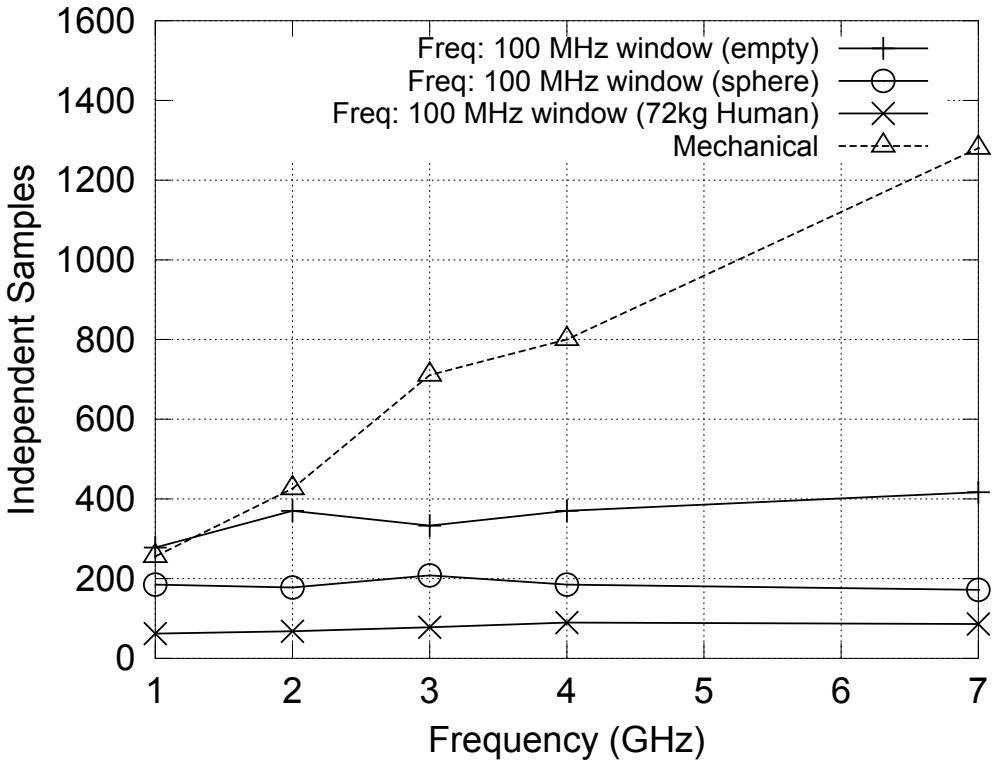

Figure 3.23: Independent samples available in RC

Table 3.2: Coherence Bandwidth B_c in the reverberation chamber: loaded and unloaded. Calculated from Figures **??** – **??**

	Empty		Spherical Phantom		72kg Human	
f (GHz)	B_c (kHz)	Q	B_c (kHz)	Q	B_c (kHz)	Q
1	360	2780	540	1850	1610	620
2	270	7410	560	3570	1470	1360
3	300	10000	480	6250	1280	2340
4	270	14800	540	7410	1110	3600
7	240	29200	580	12100	1160	6030

Table 3.3: Independent stirrer positions in the empty reverberation chamber

f (GHz)	Steps to incoherence	Available mech samples
1	15/6400	115
2	15/6400	320
3	9/6400	457
4	8/6400	640
7	5/6400	800

Validating the optimised measurement technique

Based on the data in the previous sections, the measurement technique intended for use in the second campaign of human measurements therefore uses continuous stirring, 300 mechanical samples, a 100 MHz frequency window and a 2 MHz frequency step. Taking the data from Table 3.3, the mechanical positions are modelled as rising from 115 at 1 GHz, where the limiting factor is the number of independent samples supported by the chamber, at a rate of 0.4 samples per 2 MHz step (at which rate it would reach 315 at 2 GHz) until it reaches 300 mechanical samples,

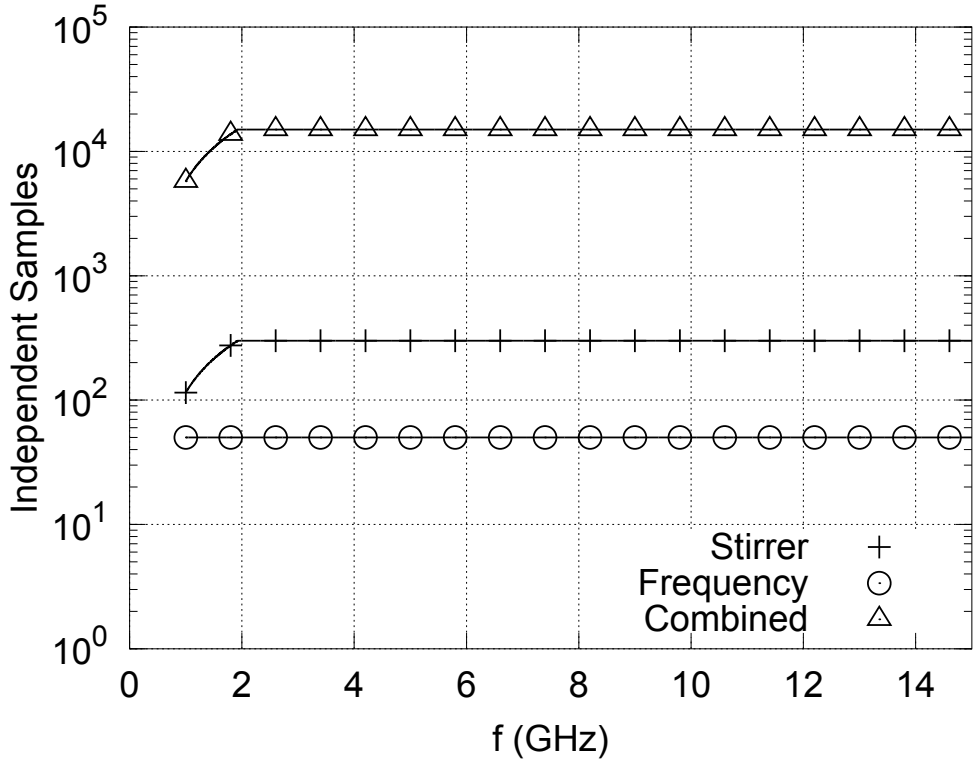

Figure 3.24: Total independent samples in final $\langle ACS \rangle$ measurement setup

at which level it stays for the rest of the frequency range. Figure 3.24 plots this alongside the constant value of 50 frequency samples (100 MHz window, 2 MHz step) to show the total number of independent samples in the final measurement, which is 15000 across most of the frequency range.

The spherical phantom was measured five times using a single calibration and also five times, re-calibrating the NA each time. Figures 3.25 and 3.26 show the calculated ACS of the phantom for each of these measurements. The variation between measurements is similar between the two plots, which shows that the calibration of the system is reliably repeatable.

Figure 3.27 then shows the theoretical 1σ error that should be seen in the five re-calibrated measurements, as calculated by Equation 2.46. This is the statistical confidence interval of the measurements, and does not include systematic or other measurement errors. Comparing this to the actual σ value of the five measurements will show whether any unknown errors are causing additional deviation.

Figure 3.28 makes this comparison. As can be seen, the standard deviation between the five measurement is comparable to the confidence band, but stays within it at all points except at 9.2 and 13.6 GHz. Note that the smaller values for the measured σ are to be expected - if five properties vary randomly within a band, they will sometimes randomly be close together. Neither are the two spikes worrying: the error value is a standard deviation not a limit.

Figure 3.28 gives two crucial pieces of information. Firstly, the errors are behaving as the theory predicts. This means that there are no significant additional sources of error, and that the errors seen are under control. Secondly, it shows us the value of the errors for the new standard measurement. Across most of the frequency range, the statistical errors show σ of $2.6 - 2.8$ %. This compares to the initial experiments where $\sigma = 6.5\%$ above 4 GHz.

This measurement setup (300 sweeps, 100 MHz freq. stirring window, 2 MHz step size, 100 kHz IF BW, equipment placed as in Figure 3.14), which takes 7 minutes 40 seconds to run, and gives results to within a statistical confidence band of 2.6-2.8 %, has been designed as the optimised ACS measurement for human measurements. This setup is used for the second campaign of live measurements, recorded in the next chapter.

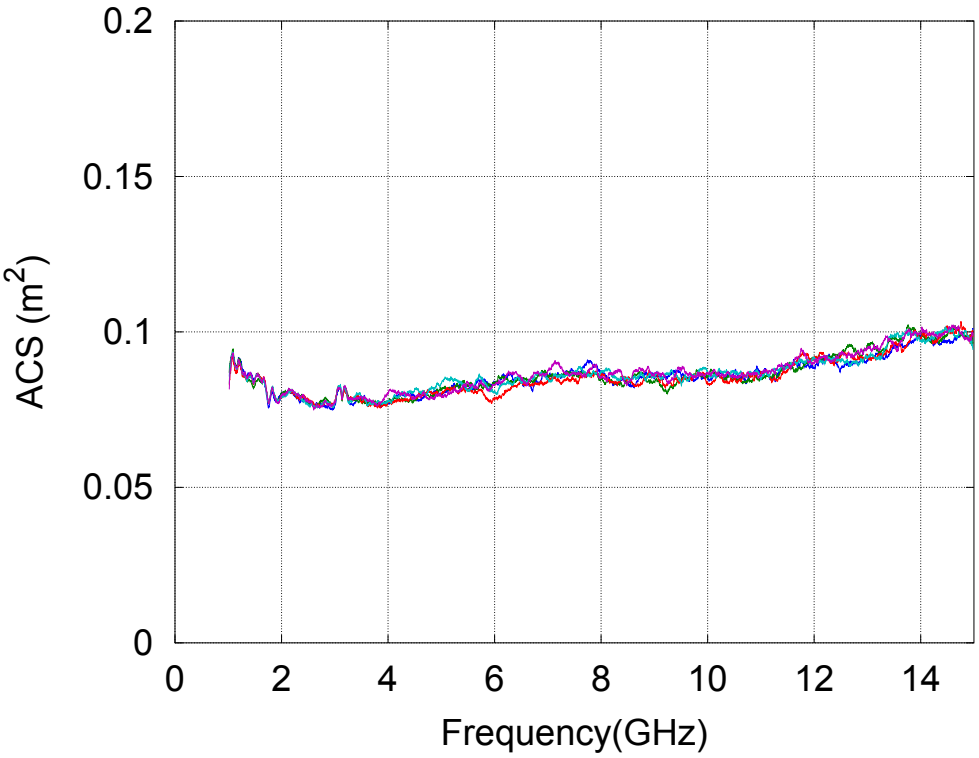

Figure 3.25: Spherical Phantom $\langle ACS \rangle$ from five measurements using the same calibration

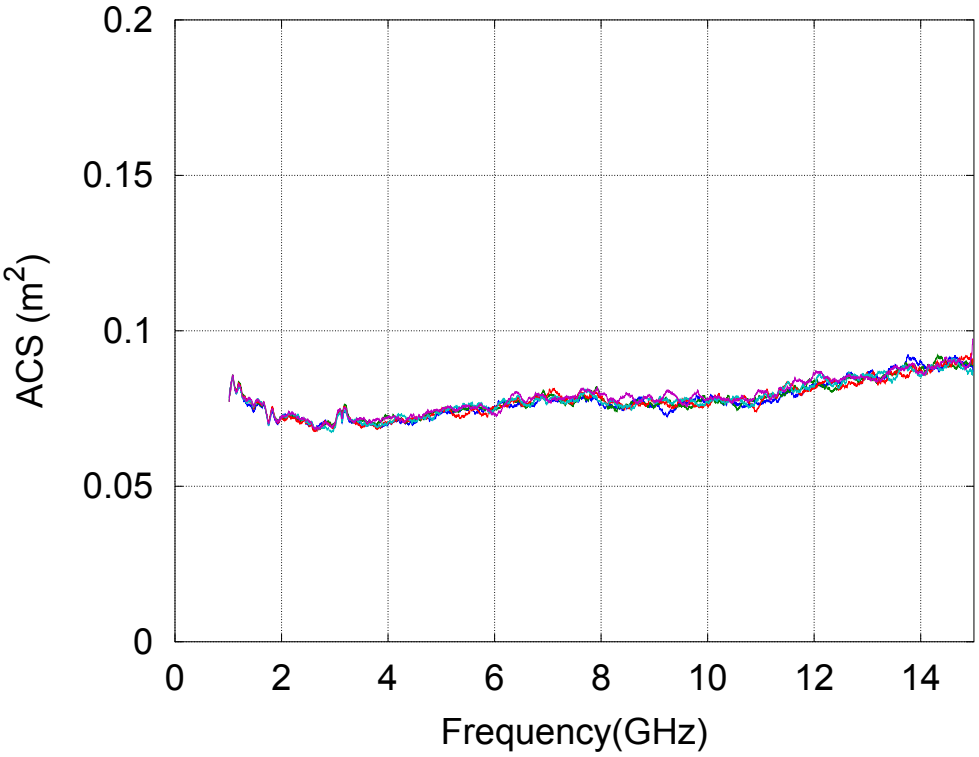

Figure 3.26: Spherical Phantom $\langle ACS \rangle$ from five measurements using five separate calibrations

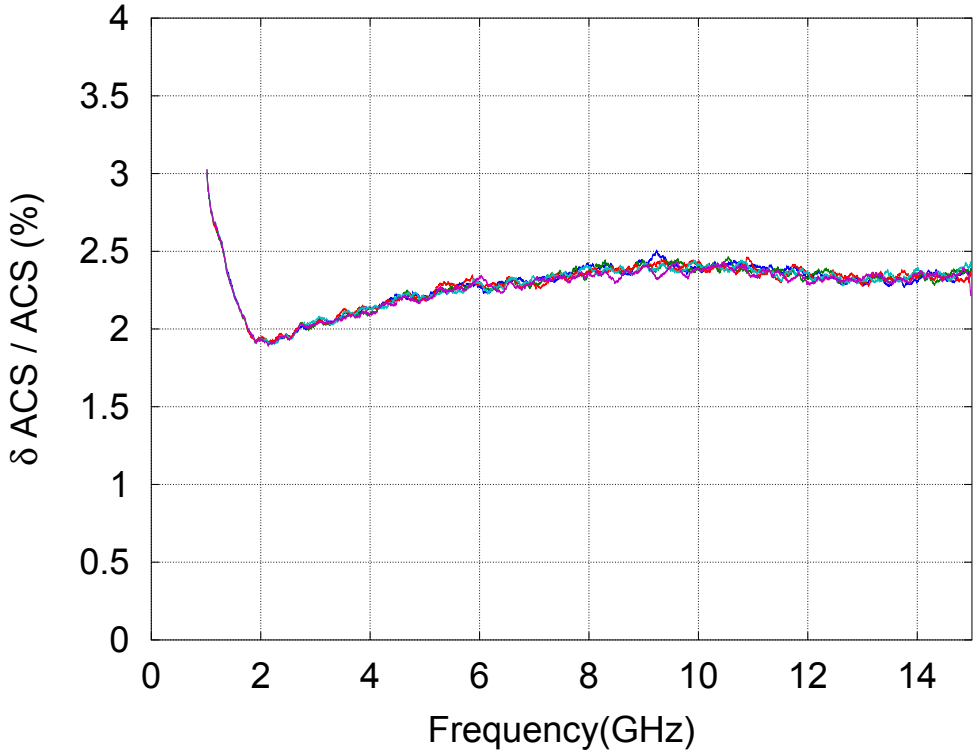

Figure 3.27: Theoretical 1σ statistical error in five sphere measurements with five different calibrations

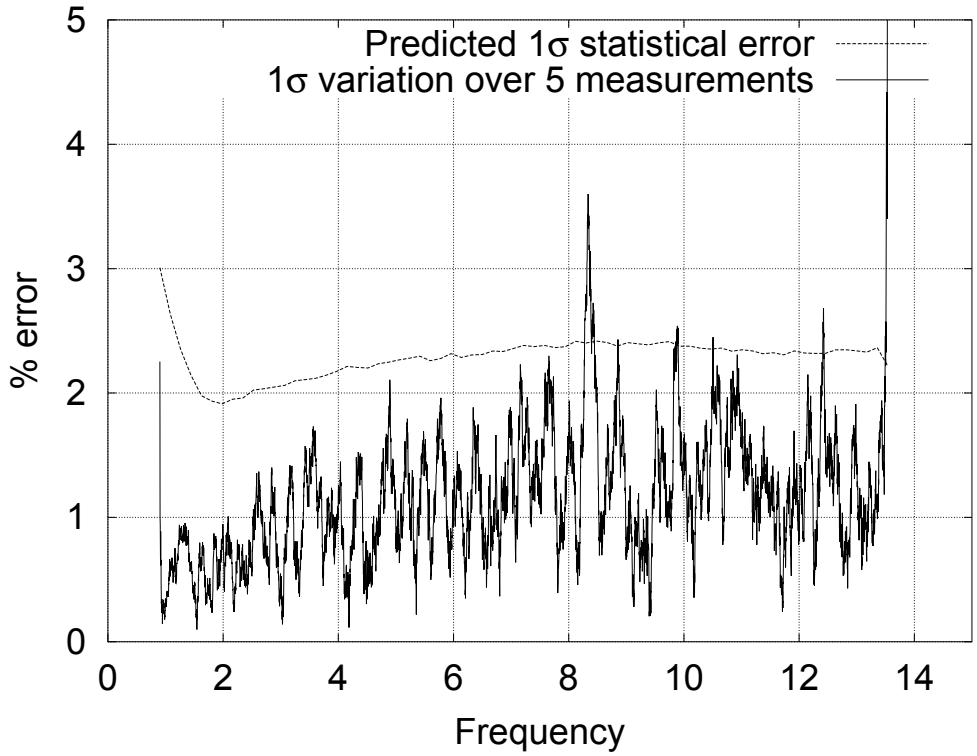

Figure 3.28: Actual 1σ error in $\langle ACS \rangle$ versus averaged theoretical statistical 1σ error in five sphere measurements with five different calibrations

3.4.4 Measurement using one antenna

If measurements could be taken using only one antenna, it would provide several advantages over a two antenna measurement:

- Only one set of cables would be required and only one port of the NA would need to be calibrated – thus providing a simpler experimental setup that would be less vulnerable to calibration errors.
- Use of one antenna would reduce the uncertainties in ACS due to uncertainties in antenna efficiency.
- A one port measurement could be taken in half the time of the current measurement, in which the NA sweeps over both ports.

It should be possible to take ACS measurements using only one antenna, by utilizing the coherent backscattering effect. This is described in Section 2.3.4 but briefly, it states that the stirred power in a reflection coefficient at any given antenna will be twice the stirred power in the chamber transmission coefficient [84]. If this description is accurate, it should be possible to obtain a virtual $\langle |S21|^2 \rangle$ (and therefore to measure ACS) from a measurement that utilises only one antenna, by halving the stirred component of that antenna's reflection coefficient, i.e. $\langle |S11 - \langle S11 \rangle|^2 \rangle$.

Investigating the constancy of the Backscattering Factor

If ACS is to be measured using one antenna, it is necessary to test whether $\langle|S11 - \langle S11\rangle|^2\rangle = 2 \times \langle|S21|^2\rangle$ over all frequencies of interest. For this purpose, a two port S parameter measurement was taken in the empty York reverberation chamber. This measurement used a Q-par Angus WBH1-18S horn antenna on Port 1 and the ETS Lindgren 3117 horn on Port 2. The measurement was continuously stirred, 1200 samples were taken over one complete rotation of the stirrer, which took 6400 seconds. Data was taken using the ZVB20 NA with a 10 kHZ IF bandwidth, a 15 dBm stimulus power and a 5 MHz frequency step. The Port 2 (3117) antenna was pointed into the stirrer and the Port 1 (Q-par) antenna was aimed at the door at roughly 45^0 in order to prevent direct reflections. The setup is shown in Figure 3.29.

The result of this measurement is plotted in Figure 3.30,where $\langle C_{BS1}\rangle$ is near the 3 dB value that is predicted by the theory in [84] and discussed in Section 2.3.4, but $\langle C_{BS2}\rangle$ is well above 3 dB, rising to nearly 6 dB at 15 GHz. Figure 3.30 shows that, relative to the transmitted power reflected power formed a larger component of the power absorbed in the Port 2 antenna than in the Port 1 antenna in both measurements. One possible explanation for this is that the antenna on Port 1 may have a significant dielectric loss associated with its casing (see Figure 3.29 – this is the white antenna on the right, facing the camera). It can be derived that $\langle|S21|^2\rangle$ includes the product of the two antenna efficiencies $\eta_1\eta_2$. The equivalent products for $\langle|S11|^2\rangle$ and $\langle|S22|^2\rangle$ will be η_1^2 and η_2^2. Therefore, the effects of high losses in the Port 1 antenna would be seen in the transmission parts (i.e. the denominators) of both backscattering factors as (there is an n_1 term in both denominators – see Equations 3.2 and 3.3, which are derived from Equation 2.55), but only in the reflection part (i.e. the numerator) of C_{BS1}, as this is the only equation to contain n_1^2 in the numerator (Equation 3.2).

$$C_{BS1} = \frac{\langle|S11|^2\rangle\eta_1^2}{\langle|S21|^2\rangle\eta_1\eta_2} \tag{3.2}$$

$$C_{BS2} = \frac{\langle|S22|^2\rangle\eta_2^2}{\langle|S12|^2\rangle\eta_2\eta_1} \tag{3.3}$$

It must be concluded that, *contra* Ladbury *et al.* [84], the backscattering factor in a reverberation chamber does not necessarily equal 2, or any value close to 2, especially at frequencies of several GHz where C_{BS1} and C_{BS2} diverged. The backscattering factors cannot therefore be used individually to provide a one antenna method for measuring ACS. However, the antenna efficiencies cancel in the product of the two backscattering factors, as shown in Equations 3.4 and 3.5, so if the variations in the backscattering factors are solely due to the antennas' efficiencies, the product of the two factors should be 4. $\sqrt{C_{BS1}C_{BS2}}$ is shown in Figure 3.31.

$$\frac{\langle|S11|^2\rangle\eta_1^2}{\langle|S21|^2\rangle\eta_1\eta_2} \times \frac{\langle|S22|^2\rangle\eta_2^2}{\langle|S12|^2\rangle\eta_2\eta_1} = \frac{\langle|S11|^2\rangle\langle|S22|^2\rangle\eta_1^2\eta_2^2}{\langle|S21|^2\rangle\langle|S12|^2\rangle\eta_1\eta_2\eta_1\eta_2} \tag{3.4}$$

$$\frac{\langle|S11|^2\rangle}{\langle|S21|^2\rangle}\frac{\langle|S22|^2\rangle}{\langle|12|^2\rangle} = C_{BS1}C_{BS2} \tag{3.5}$$

Equations 3.4 and 3.5 give the product of the two backscattering factors. In Figure 3.31 the square root of this product is taken, to give an average value of the two factors. If the theory in [84] is correct, this should equal 2.

In Figure 3.31, the ratio of (the stirred components of) reflected and transmitted energy is now clearly much nearer 2 than in the previous plots, although this result does not show the

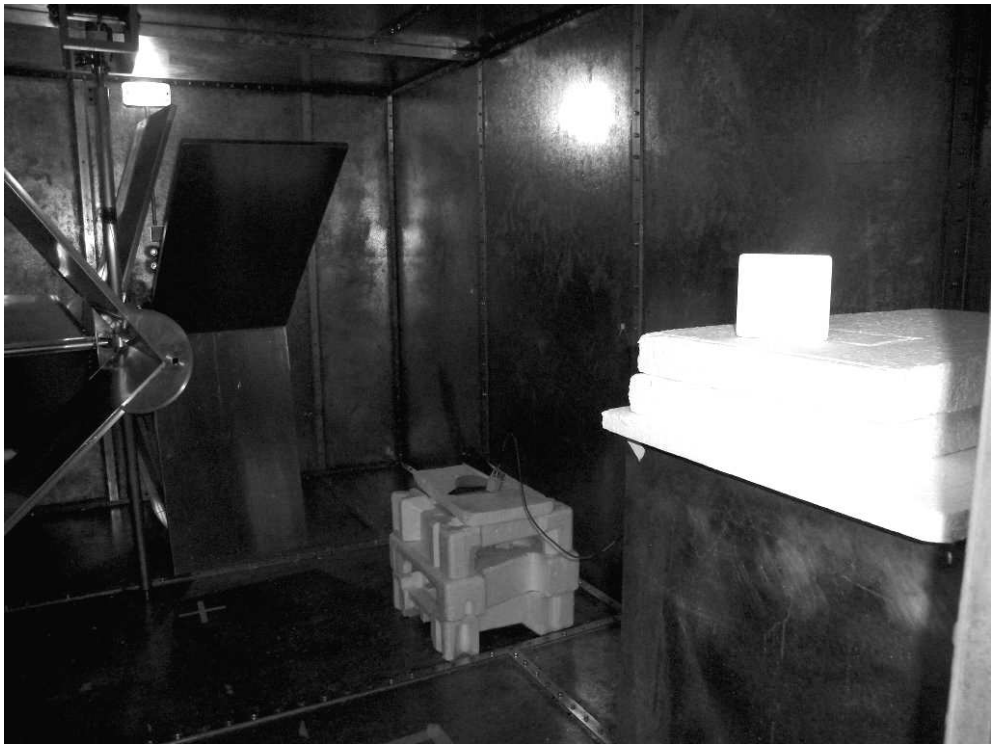

Figure 3.29: Measurement setup for the backscattering experiment. Antenna 1 is on the right, pointing towards the camera and Antenna 2 is at the other end of the chamber, pointing into the stirrer.

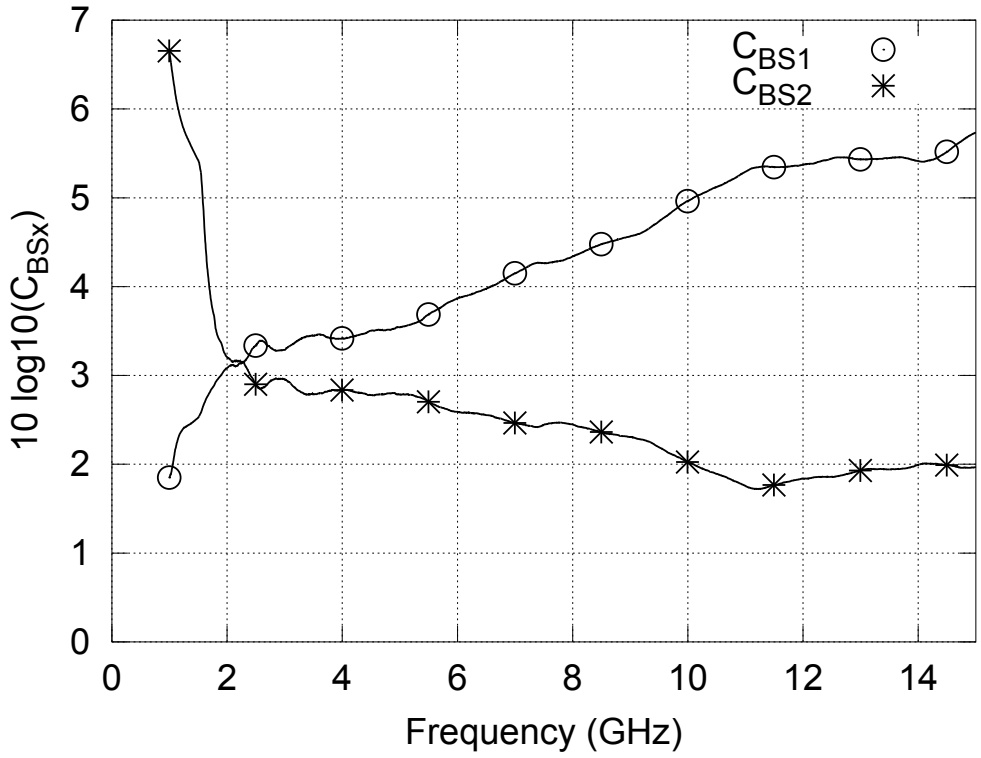

Figure 3.30: Backscattering factor, i.e. ratio of reflected to transmitted (stirred) energy, at both ports

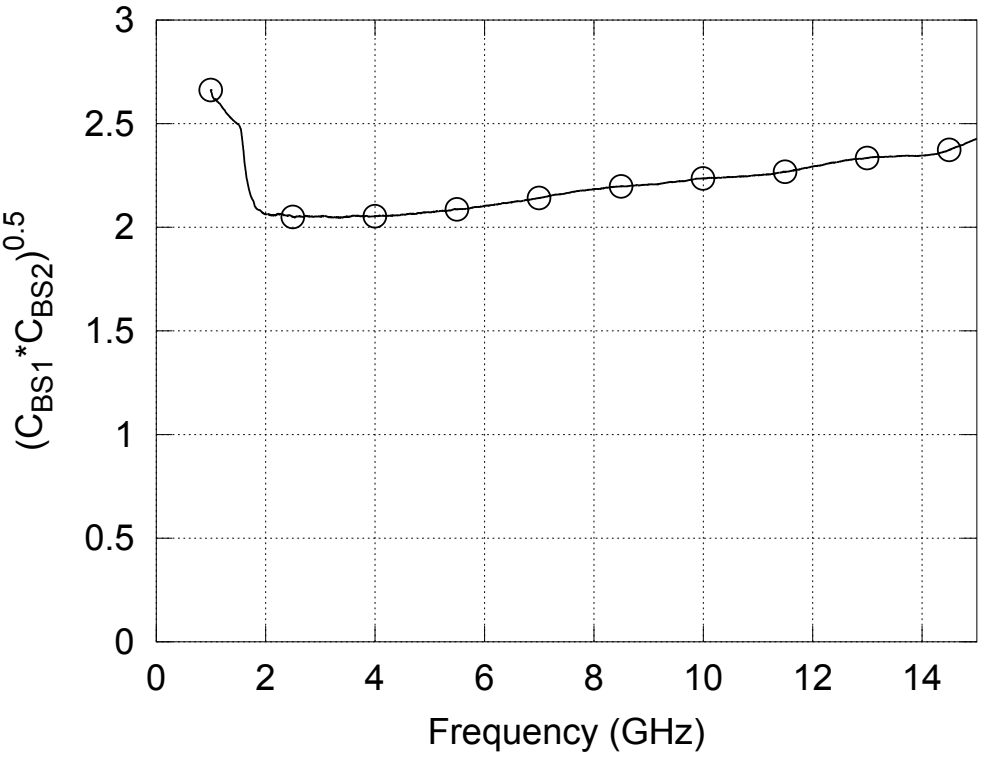

Figure 3.31: Root Product of (stirred components of) reflection coefficient divided by transmission coefficient, at both ports

individual results for the two ports. However, C_{BS} clearly does not equal 2 sufficiently closely to be used as a simple scaling factor to find $S21_{stirred}$ from $S11_{stirred}$: we have shown that this is not the case, and that C_{BS} varies with frequency, with antenna position and possibly also with antenna design. Average ACS has been successfully measured with one antenna by observing the change in the time constant of the chamber as it is loaded, after calibrating C_{BS} using a second antenna, which is not then used during ACS measurement [92]. However, this technique requires a very fine frequency resolution (the cited authors use 50 kHz) in order to obtain adequate resolution in the time-domain data that is output by the inverse Fourier transform, which makes the technique far too time-consuming for broadband measurements, especially on live subjects. However, the antenna calibration technique could be applied to our measurement, so long as C_{BS} remains constant when the chamber is loaded. A methodology would look like the following:

- Assemble and calibrate two antennas in RC
- Use Port 2 antenna to measure C_{BS}, the Port 1 backscattering coefficient
- Leave antennas exactly in place
- Take human measurements, using Port 1 antenna
- Divide $S11_{stirred}$ by C_{BS1} to give $S21_{stirred}$
- Calculate $\langle ACS \rangle$ as with the 2 antenna measurement

This method still requires two antennas to be used during calibration, therefore introducing inaccuracies due to the efficiency (if unknown) and calibration of the Port 2 antenna However it has advantages over a two antenna measurement. These are that it allows increased speed of measurement and reduced uncertainties due to the equipment calibration, both because a one antenna measurement allows the use of very little cabling: only two short cables are needed, one for inside the chamber and one for outside. However, this method will only work if the backscattering factor remains constant when the chamber is loaded.

Measurements

A measurement was taken to observe how the backscattering factor was altered by a human presence in the chamber, under conditions as close as possible to those eventually used for the final human measurements. This measurement was designed to mimic as closely as possible the setup for the C2 measurements on human subjects: it therefore used the 3115 and 3117 antennas, both pointed directly into the stirrer. A 10 MHz frequency step was used, and a 100 kHz IF bandwidth. 800 samples were taken over 1 rotation of the stirrer, which took slightly under 15 minutes. The experimenter, also the subject, wore jeans and a t-shirt, weighed 73.0 kg including these and was seated on the wooden stool.

Sweeps were taken of $S22$ and $S12$, allowing for a two antenna ACS measurement using the $\langle|S12|^2\rangle$ and the free space reflection coefficients, a one antenna measurement using the 3117 antenna (on Port 2) and the 3115 antenna to calibrate, and a calculation of the backscattering factor for both the empty and the loaded chambers.

Results

Figure 3.32 shows the change in backscattering factor due to the loading of the chamber with a human subject. Figure 3.33 shows the changes in the stirred components of the reflection coefficients due to the loading of the chamber with a human subject. Figure 3.34 shows the ACS calculated with the 2 port (continuously stirred) method and the 1 port method. The latter calculation is done using both the backscattering coefficients for both the empty and the EUT cases.

Figure 3.32 shows that the backscattering factor is substantially increased - up to a maximum of 35% - when the human subject is in the reverberation chamber. Figure 3.33 bears this out: the stirred component of $\langle|S12|^2\rangle$ (the denominator in the backscattering ratio) is attenuated by more than the stirred component of $\langle|S22|^2\rangle$ (the numerator) when the subject is added, whereas this ratio should remain constant (i.e. the top and bottom pairs of lines should remain parallel) if the backscattering factor were unaffected by the addition of the subject.

It has now been shown that the backscattering coefficient C_{BS} is not only dependent upon the precise chamber setup such as the location of the antennas, but also upon the loading of the reverberation chamber. To find how greatly the change in backscattering affected the ACS calculation, this was performed on the same data using firstly the two port method (including both free space reflection measurements), secondly the one port method but using the empty chamber backscattering coefficient $C_{BSempty}$ for both the empty and the EUT calculations, and thirdly using the one port method and the loaded chamber backscattering coefficient C_{BSEUT}. Results are shown in Figure 3.34.

This graph shows that the change in the backscattering coefficient has a substantial effect on the calculated average ACS values, which remain close up to around 4 GHz but then diverge

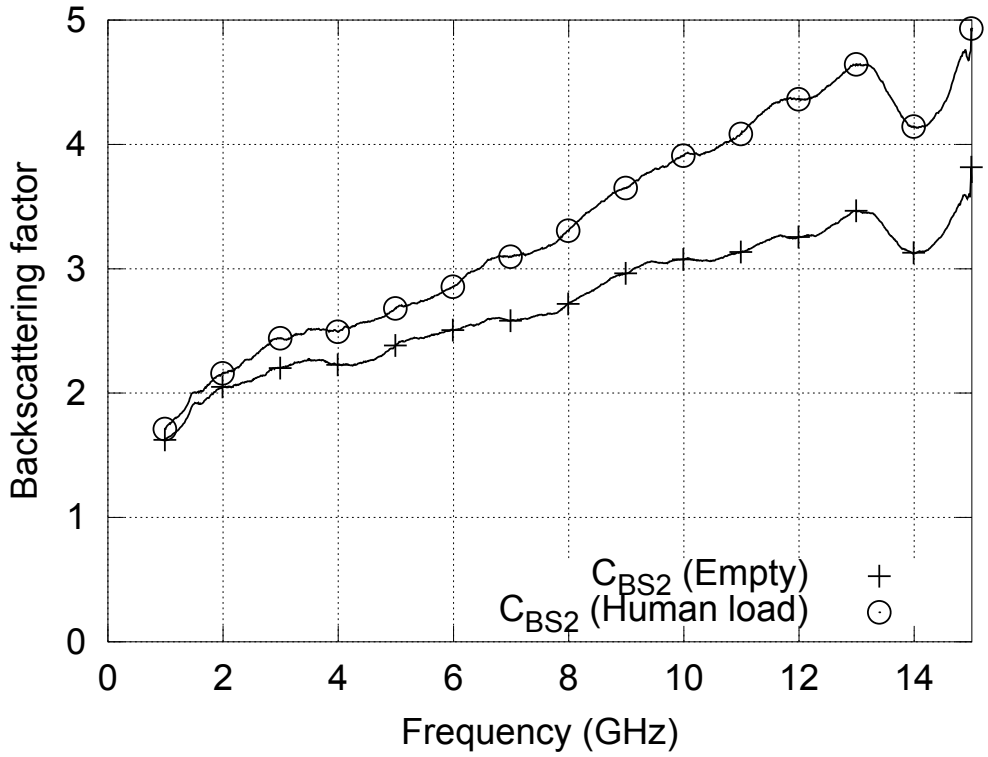

Figure 3.32: Chamber backscattering factor C_{BS2}, showing the effect of loading the chamber with a human subject

markedly as the C_{BS} values also diverge. This is because of Equation 3.6

$$\langle \sigma_a \rangle \propto \frac{1}{G_{wo}} - \frac{1}{G_{no}} \tag{3.6}$$

For both the loaded and unloaded cases, $G = S21_{stirred}$ once $S21_{unstirred}$ and $S21_{FS}$ have respectively been removed by vector average subtraction and reflection coefficient division. Therefore, we calculate G by $G = S22/BS$ and the relationship becomes Equation 3.7 if the $C_{BSempty}$ is used for both cases, and Equation 3.8 C_{BSEUT} is used for both cases.

$$\langle \sigma_a \rangle \propto \frac{C_{BSempty}}{S22EUT} - \frac{C_{BSEUT}}{S22empty} \tag{3.7}$$

$$\langle \sigma_a \rangle \propto \frac{C_{BSEUT}}{S22EUT} - \frac{C_{BSEUT}}{S22empty} \tag{3.8}$$

Consider that C_{BSEUT} is larger than $C_{BSempty}$; if $C_{BSempty}$ is used for both cases, a correct fraction is subtracted from a fraction that is too small, while if C_{BSEUT} is used for both cases, a fraction that is too large is subtracted from a correct fraction. Figure 3.34 is therefore correct in showing that average ACS is too small in both calculations, compared to the two port method.

Conclusions

It is not at this moment feasible to use the coherent backscattering effect as a tool to measure average ACS in a reverberation chamber using only one antenna by reconstructing $S21_{stirred}$ from $S11_{stirred}$. That would require the coefficient C_{BS} to remain constant when the chamber

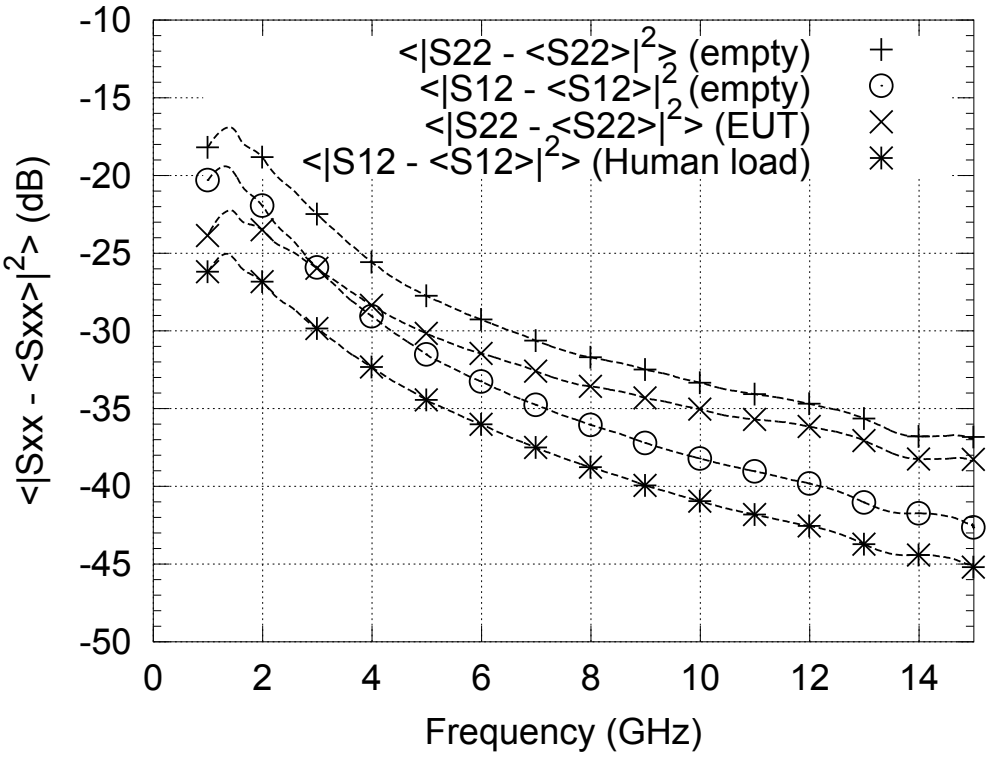

Figure 3.33: Stirred components of the S parameter components of C_{BS2}, showing the effect of loading the chamber with a human subject

is loaded. C_{BS} does not remain constant, but increases with decreasing chamber Q.

This does, however, suggest another method for measuring ACS. If C_{BS} is indeed related to chamber Q, it will be possible to measure Q and therefore ACS by measuring the change in C_{BS} as the chamber is loaded. However, this measurement has proved to be extremely sensitive to chamber setup, which makes it also unfeasible for ACS measurement. The relationship between coherent backscattering and Q could, however, make an interesting further study.

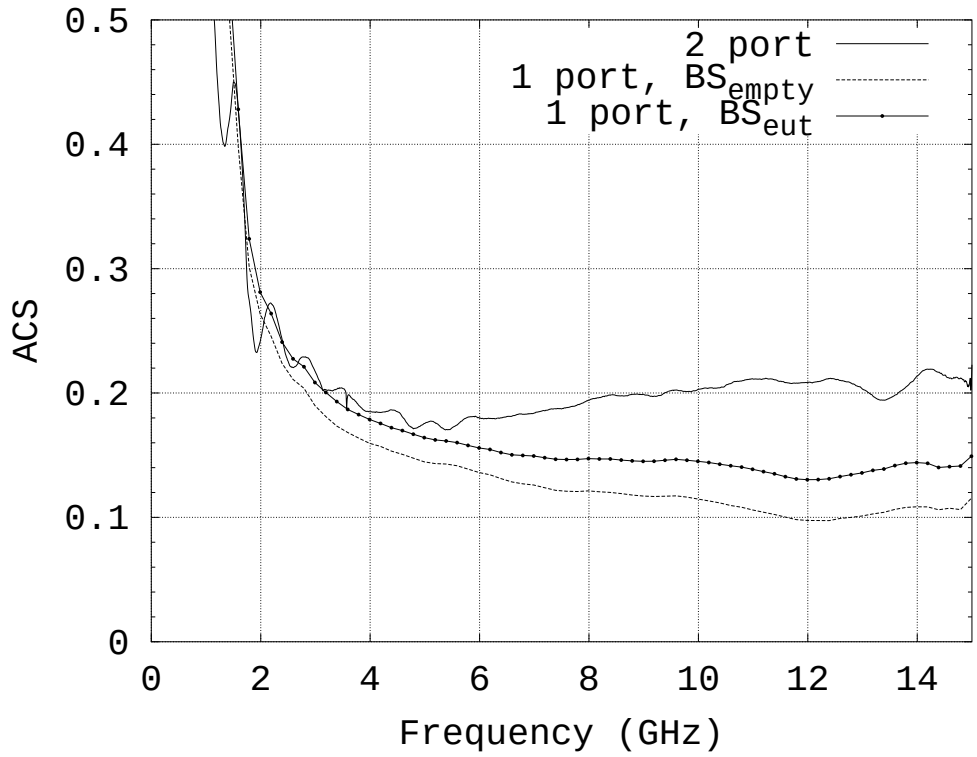

Figure 3.34: Experimenter's $\langle ACS \rangle$, calculated using 2 port method, 1 port method with $C_{BSempty}$ and 1 port method with C_{BSEUT}

3.5 Finalised methodology for measuring ACS

The finalised method uses two antennas to measure ACS, as the investigations into measurement with one antenna did not prove fruitful. The method is the one described in Section 3.4.3, i.e. the optimised version of the two-antenna method. The calculated statistical uncertainty in the measurement is 2.6-2.8 %, which has been validated by measurements, as shown in Figure 3.28. It is now necessary to compute the uncertainty due to systematic, measurement and calculation errors.

Testing the finalised method against the multilayer sphere model

The new methodology that has been developed can now be tested by using it to measure the average ACS of the spherical phantom and comparing those results to simulations using the multilayer Mie model. The results of this comparison are shown in Figure 3.36.

The measurement has some unusual features from 7-11 GHz, which have not been reproduced and which are therefore regarded as systematic errors caused by inaccuracies in the calibration. This emphasises that the continuous measurement method is more prone to calibration errors than the C1 measurement, because while previously the $|\langle S11 \rangle|^2$ and $|\langle S22 \rangle|^2$ measurements were taken at measurement time (and hence with the same calibration) and were then factored out, $|\langle S11 \rangle|^2$ and $|\langle S22 \rangle|^2$ are now taken from the free space antenna measurements, which are taken using a differently calibrated machine. Correct calibration of the NA is therefore important when using the finalised ACS measurement.

Apart from the systematics, however, the measurement behaves as predicted and as simu-

lated. It can be taken in under 8 minutes and, notwithstanding an increased reliance over the initial stepped method on an accurate calibration, provides accurate measurement of average ACS. This is therefore the final method of average ACS measurement, which will be used for the second measurement campaign.

3.5.1 Uncertainty in the estimation of the surface area of the human body

The surface area of the human body (BSA) is an important property to discover, as it is expected to have a significant effect on the body's ACS at high frequencies – this is discussed further in chapters 4 and 5. BSA is, however, a difficult property to estimate or measure, due to the structural complexity of the body. If we wish to investigate correlations between ACS and BSA, it will however be necessary to do one of these things. Measurement of the surface area of the population required for this experiment would be sufficiently difficult and time consuming to be unfeasible, so it will therefore be necessary to estimate the surface area of subjects' bodies. A number of empirically-derived formulae exist for this purpose, mainly using subject height and mass as input variables. Others do exist, such Takai and Shimaguchi's equation (Equation 3.9) that also uses head circumference (HC) [93]. Their equation has, however, been found to be an inaccurate estimator of BSA [94], and so is not used here. Tikuisis *et al.* [94] found the Takai & Shimaguchi equation to provide a worse fit to their data than any of the other estimators they tested.

$$BSA = 617m^{2/3} + 0.2453h^2 + 0.6825HC^2 - 2142 \tag{3.9}$$

A frequently-used estimator is the Dubois & Dubois equation, shown in Equation 3.10,

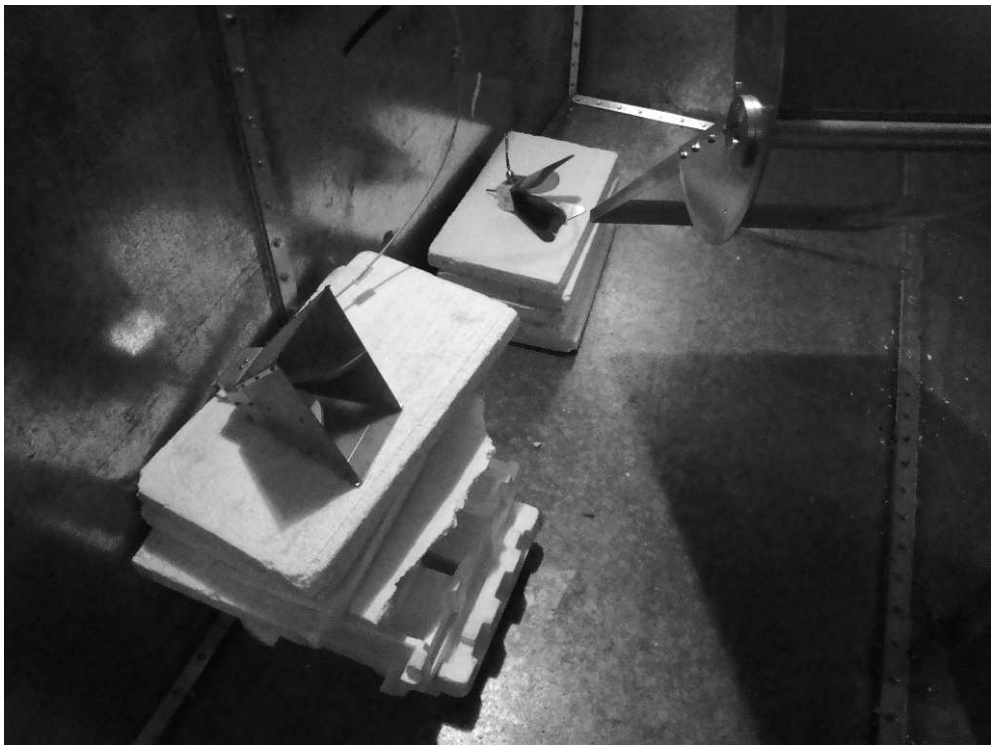

Figure 3.35: Antenna position for the finalised ACS measurement

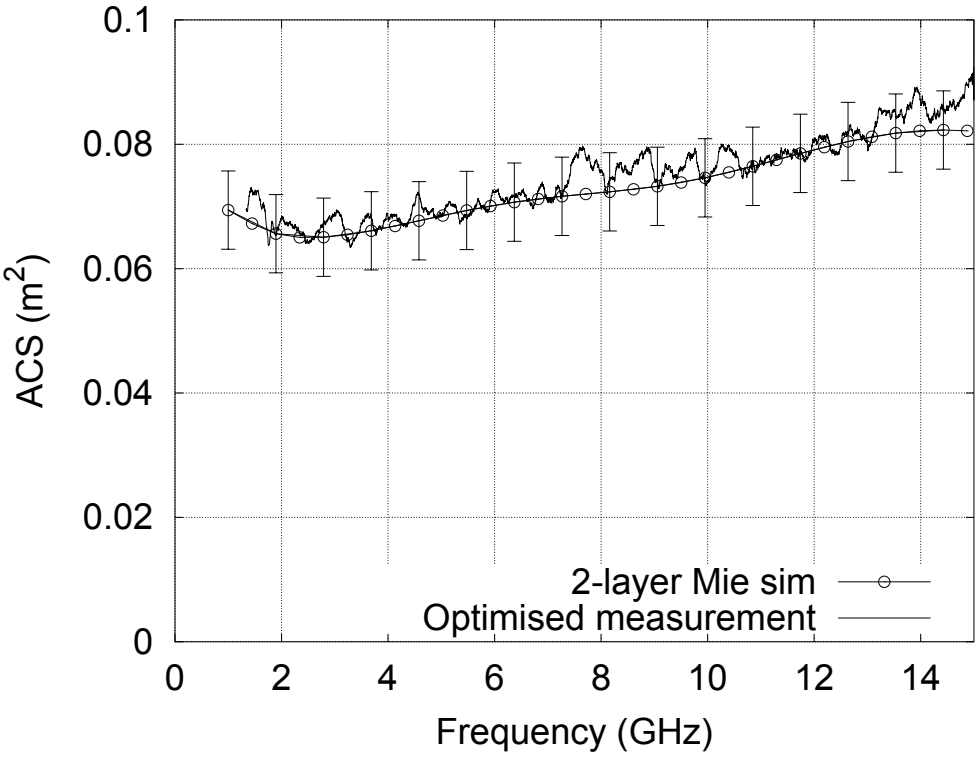

Figure 3.36: Spherical phantom $\langle ACS \rangle$, measured with the finalised method and computed with the multilayer sphere model

where h = height (m), m = mass (kg) and BSA is measured in m^2. Dubois & Dubois derived their equation from regressing surface area values for nine subjects, which they measured by mapping their bodies with paper moulds. [95].

$$BSA = (71.84 \cdot m^{0.425} \cdot h^{0.725})/10000 \tag{3.10}$$

In 1978, Haycock *et al.* calculated BSA using 34 measurements on each of 81 subjects and thus derived Equation 3.11 [96].

$$BSA = 0.024265 \cdot m^{0.5378} \cdot (100h)^{0.3964} \tag{3.11}$$

Mosteller 1987 derived a simplified formula, shown in Equation 3.12. It was designed to be easily calculable in practical situations, and similar concerns exist as with the Dubois formula: that it under- or over-estimates BSA for unusually light or heavy people [97].

$$BSA = \frac{(m \cdot 100h)}{3600^{0.5}} \tag{3.12}$$

Yu *et al.* derived a formula from 3D body scans of 3951 Chinese adults [98]. However, as only one of the subjects in our experiment was Chinese, this formula shall not be investigated further.

Bailey 1996 [99] recommend the formula derived by Gehan and George [100], shown in Equation 3.13, which was derived from measurements of 401 subjects from a previous study by Boyd in 1935 [101].

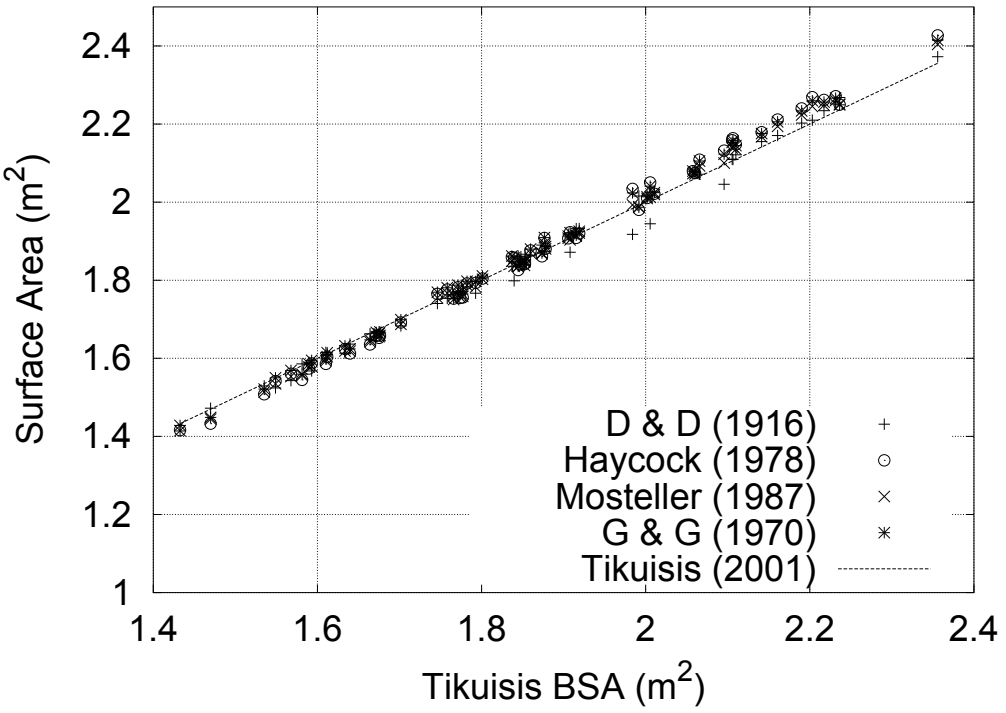

Figure 3.37: Five estimates of Body Surface Area of experimental subjects

$$\ln(BSA) = 0.422\ln(100h) + 0.515\ln(m) - 3.751 \tag{3.13}$$

In 2001, Tikuisis *et al.* used a Cyberware 3D body scanner to scan 395 men and 246 women, representing a broad range of the North American adult population with the exception of senior citizens and individuals over 2 m in height (due to the h limitation of the scanning apparatus) [94]. They found that previous BSA equations tended to overpredict BSA with increasing body size. They generated separate BSA equations for adult men and women, which are shown in Equations 3.14 and 3.15 respectively.

$$BSA_{male} = \frac{128.1}{10000} \cdot m^{0.44} \cdot (100h)^{0.60} \tag{3.14}$$

$$BSA_{female} = \frac{147.4}{10000} \cdot m^{0.47} \cdot (100h)^{0.55} \tag{3.15}$$

To compare these five formulae for estimating BSA, Figure 3.37 plots their estimates of each of the 60 volunteer subjects in the Campaign 2 ACS experiment. This figure shows that they mostly give good agreement but when there is an outlier, it is usually the BSA value predicted by the Dubois & Dubois equation. While these are all estimates – no actual BSA measurements have been taken – the good agreement given by the other four estimates in these cases, combined with the fact that the Dubois & Dubois equation was derived from data from only nine subjects, suggests that it should not be used for making accurate estimates of BSA.

A more accurate indicator of the agreement between BSA estimators is given by Figure 3.38, which shows the standard deviation of the five estimated BSA values for each subject. These are as low as 0.2% and are below 1% for all but 9 subjects. this data is plotted as a

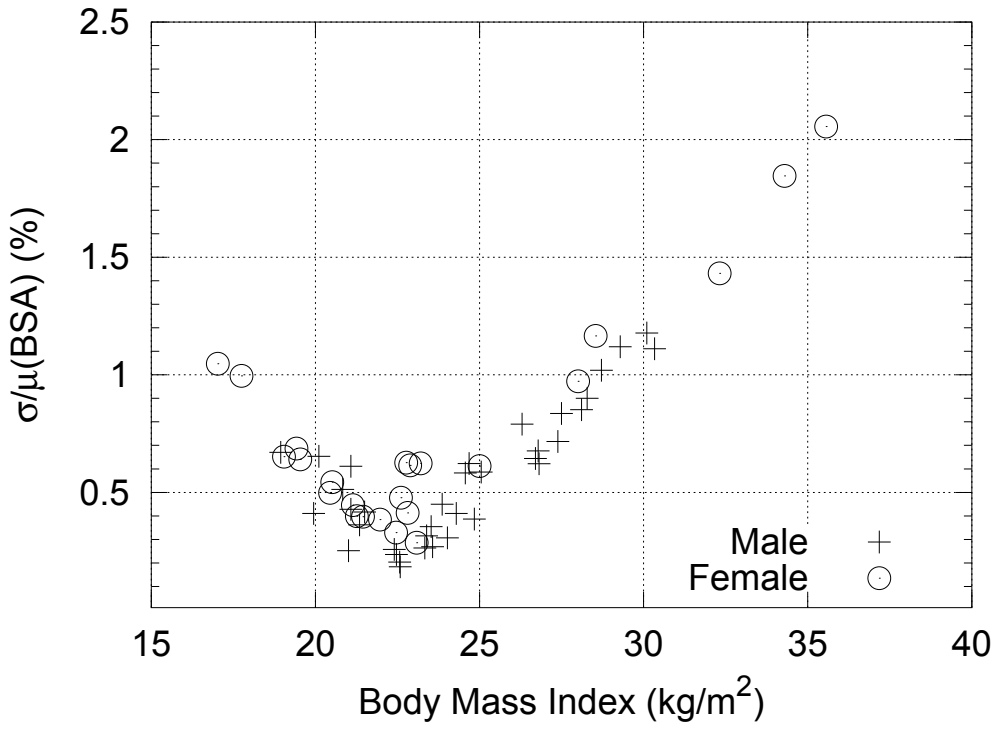

Figure 3.38: Standard deviation of BSA values generated by five estimating equations, plotted vs BMI for 60 subjects

Table 3.4: Errors produced by BSA estimation formulae

	n	RMS % error
Dubois + Dubois	9	1.56
Gehan + George	130	1.48
Haycock	81	2.71
Mosteller	0	2.03
Tikuisis	641	1.26

function of Body Mass Index (BMI), which is defined as a subject's mass (kg) divided by their height (m) squared. The three subjects with the highest BMI, Subjects 65, 39 and 63, also have the widest spread of estimated BSA values, with $\sigma = 2.06\%, 1.85\%, 1.43\%$ respectively. Figure 3.38 shows that the five formulae do not accurately estimate BSA for people with both very high and very low BMI, while showing good agreement for people with a more normal build - although it should be borne in mind that the experimental population had slightly lower BMI than the British population as a whole. The surface area of the human body is of course likely to change with age, but the good agreement between the five predictor formulae gives some indication that this can be adequately accounted for by the changes in height and mass – if people with the same height and mass showed a wider variation in BSA, the sample populations used to create the five equations could be expected to show more variance in BSA and hence the formulae would give a wider spread of results.

Table 3.4 is taken from [94] and shows the sample size n used to generate each BSA estimator and the RMS percentage error of predictions from that sample. Note that Mosteller's formula was presented theoretically, without any example fits.

The Tikuisis formulae were created from the largest database (the Civilian American and European Surface Anthropometry Resource (CAESAR) database, which is composed of 395 men and 246 women and is designed to be a representative sample of the populations of North America and Europe). The formulae show the smallest RMS error compared to that database. For these reasons, the Tikuisis formulae shall henceforth be used to calculate our subjects' BSA, and results shall be given a 2 % confidence limit.

3.5.2 Errors due to losses in the antennas

The antennas have each been assigned a flat efficiency of 95 %, which was a best estimate from the measurements in Section 3.2.1, informed by other measurements of similar antennas. However, these are not precise results; in Holloway's measurements [87] the horn antennas' efficiency varies from 93-99 %. Therefore, a ±4% uncertainty is assigned to each antenna's efficiency. The ACS is a function of the product of the two efficiencies, therefore they can be added in quadrature. As two different models of antenna are used, their efficiencies will not be identical, so the uncertainties due to each antenna add in quadrature.

$$\delta_{\eta 1 \eta 2} = \sqrt{\delta_{\eta 1}^2 + \delta_{\eta 2}^2} = \sqrt{0.04^2 + 0.04^2} = 0.056 \tag{3.16}$$

Therefore, variation in the antenna efficiencies could account for a ±6% uncertainty in the results.

3.5.3 Errors due to subject position within the reverberation chamber

To achieve maximum (and hence consistent) loading, an absorber in a reverberation chamber should be placed entirely within the stirred volume of the chamber, with all sides of the absorber fully exposed [102]. The spherical phantom was placed 1.50 m from the near wall and 0.60 m from the right hand wall (viewed from the door). $\langle S21 \rangle$ was measured using the finalised method. This was then repeated with the phantom moved to 1.20 m and then 1.80 m from the right hand wall. The three results were used to calculate the sphere's ACS, with the results shown in Figure 3.39. The standard deviation of the three measurements is shown in Figure 3.40.

The variation in Figure 3.40 can be compared with the predicted statistical variation shown in Figure 3.28. It can be seen that the variation between the different positional measurements is within the bounds expected from purely statistical variation, so the measurement may therefore be declared position-independent, which agrees with the theory for the stirred volume of a well-stirred reverberation chamber.

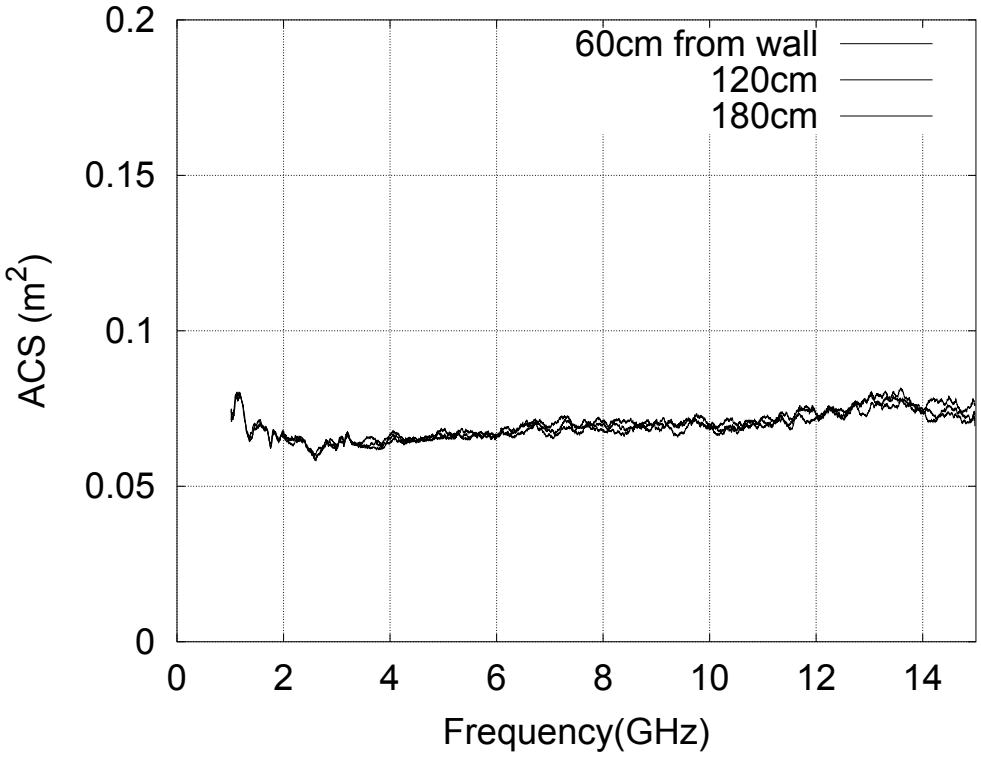

Figure 3.39: Spherical Phantom $\langle ACS \rangle$, varying position within the reverberation chamber

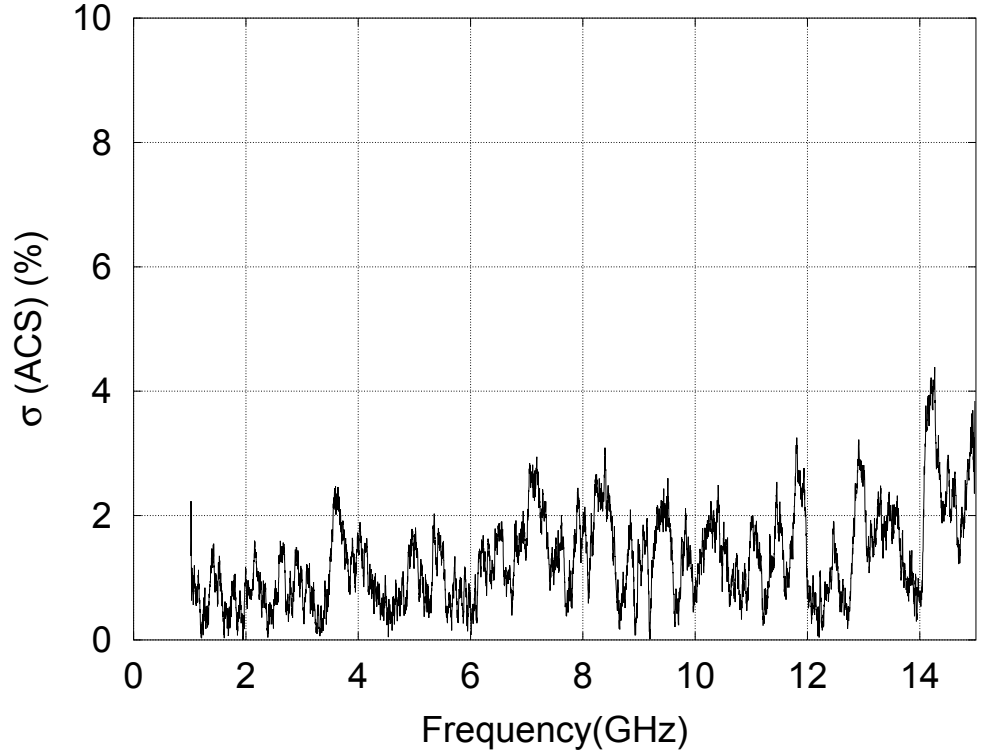

Figure 3.40: Standard Deviation of spherical phantom $\langle ACS \rangle$, varying position within the reverberation chamber

3.5.4 Errors due to subject posture

In certain postures, parts of the body will shadow others - such as the insides of the arms - reducing the exposed surface area of the subject. This will not affect any volumetric absorption mechanisms but it will confound any superficial absorption, which is expected to dominate at high frequencies. It is therefore necessary to control for subject posture. To do this, measurements were taken, using the finalised methodology, of the experimenter in three different postures. The three positions are shown in Figure 3.41; the 'foetal' and 'star' positions were designed to envelope the effects of posture by providing maximum and minimum exposed surface area, while the 'seated' position was designed to be that adopted by subjects in the main *ACS* experiment. Note the presence of the polypropylene chair and board in Figure 3.41, as the impedance of the polypropylene may have had an absorptive and/or matching effect.

The results of the posture measurements are shown in Figures 3.42 and 3.43. Both changes in posture make a measurable difference in average *ACS* (i.e. above the statistical resolution of 2.6-2.8 % shown in Figure 3.28): moving from the seated to the foetal position reduces average *ACS* by 20-24 % across the whole frequency range, with a mean change of -21.5 %. The effect of moving from the seated to the star position is less pronounced and more variable: average *ACS* increases by between 4 % and 17 %, mean 9.2 %. Based on these results, subjects should be told to remain seated with their hands on their laps, as in the seated posture in these measurements, and to remain still if possible for the duration of the measurement. Unless a subject wishes to deliberately confound the measurement, it is safe to assume that nobody will make such a drastic change in posture as either of these. Therefore, a ±5% uncertainty is assigned to differences in subject posture.

3.5.5 Errors due to subject clothing

Clothing, depending on the material, a subject's clothes could absorb energy and/or act as a matching layer to their body. To control for this, three measurements were taken on the experimenter using the finalised *ACS* method. In the first, he wore only his underpants. In the second, he additionally wore cotton jeans, socks and t-shirt and a polyester 'fleece' sweater (this measurement was used as the 'seated' measurement in Section 3.5.4). In the third, he additionally wore training shoes and a Royal Marines No. 5 dress jacket with metal buttons. Subject mass was 72.0 kg in underpants, 73.1 kg in jeans and sweater and 75.4 kg in coat and shoes; the subject did not eat or go to the toilet between measurements.

Figures 3.44 and 3.45 show the results of these measurements. Removing the subject's

Figure 3.41: Seated, star and foetal postures. Note that the experimenter's shoes and watch were removed during the measurements.

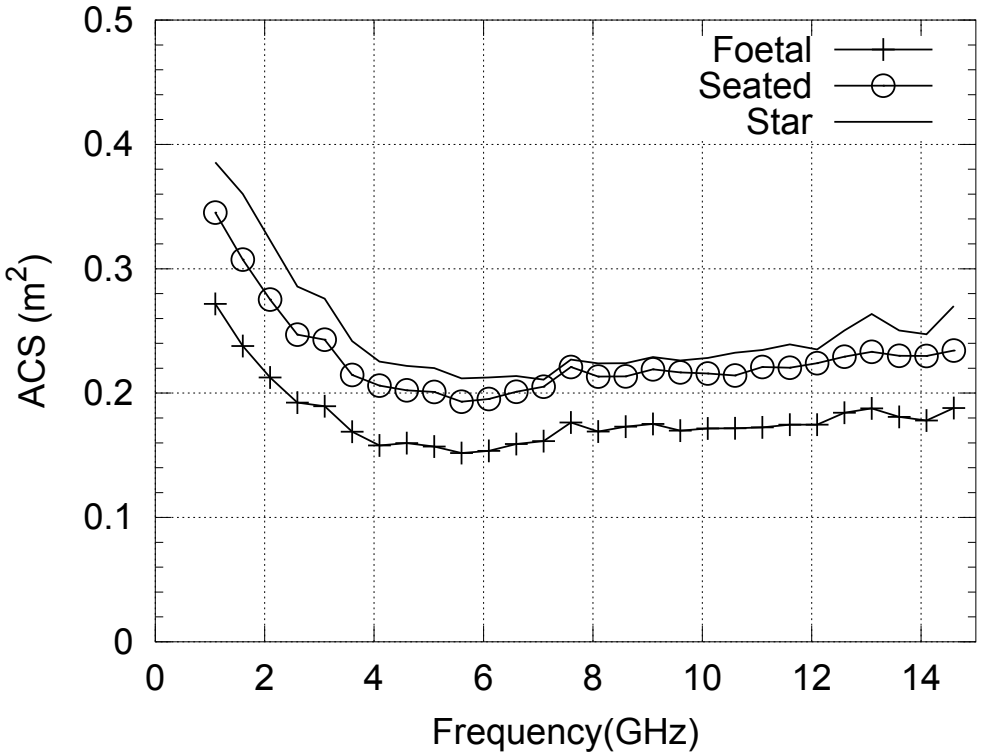

Figure 3.42: $\langle ACS \rangle$ of experimenter in three different postures

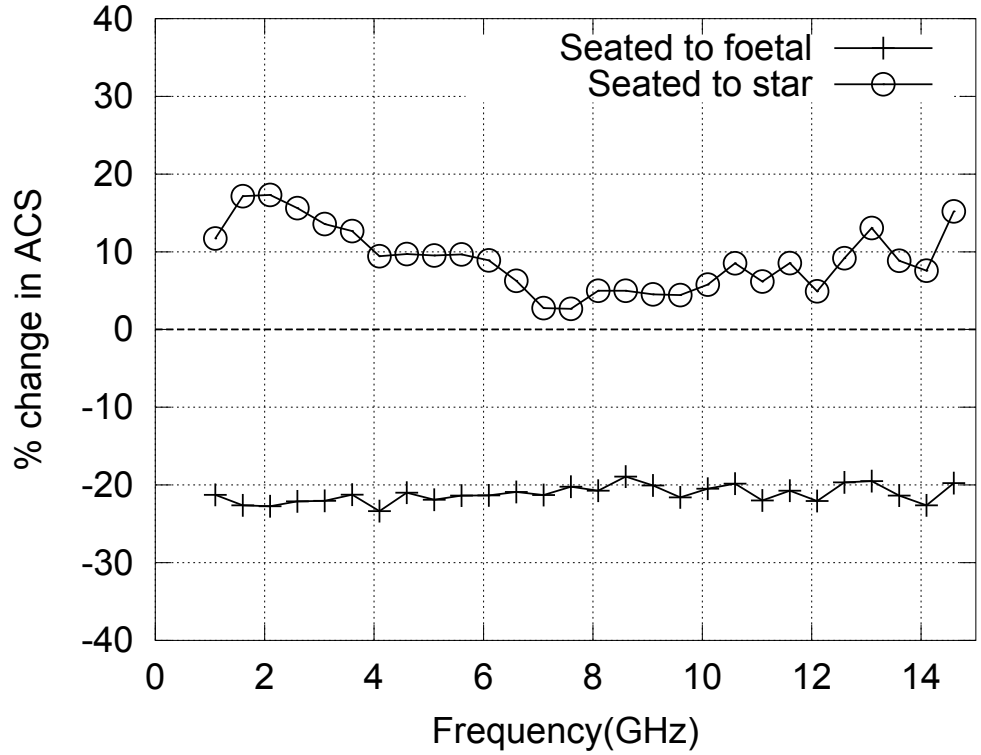

Figure 3.43: Percentage change in $\langle ACS \rangle$ when the subject moves from the seated position to the foetal and star positions

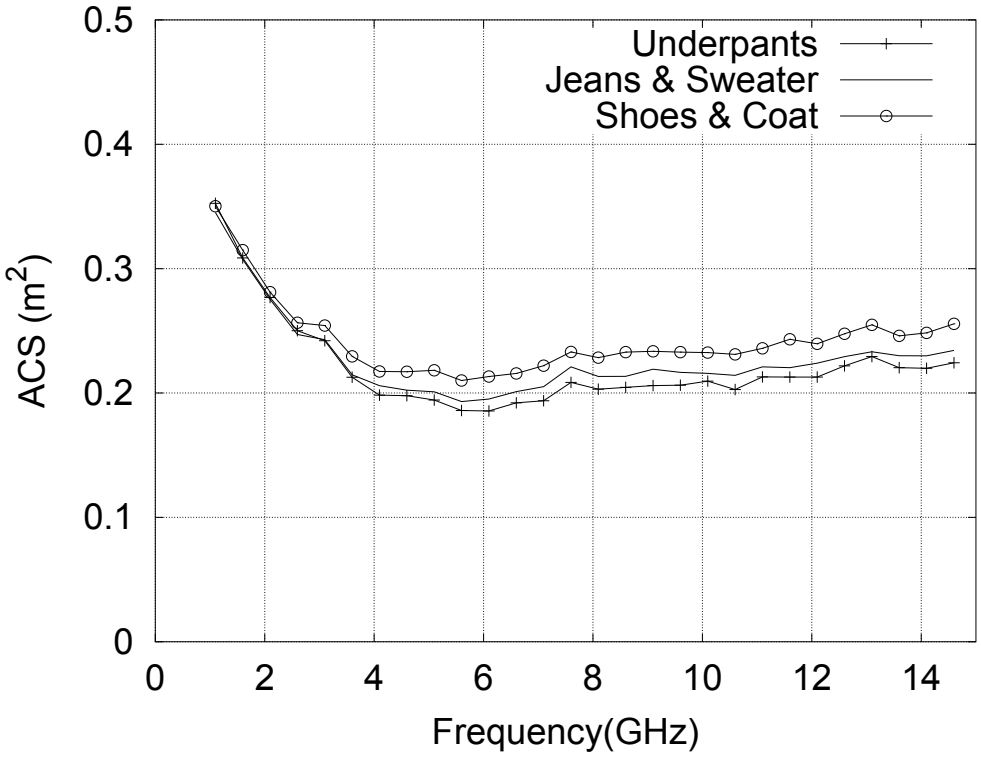

Figure 3.44: ACS of experimenter dressed in three different levels of clothing: underpants, + t-shirt, jeans and sweater, + shoes and coat

inner clothing and measuring his average ACS in his underpants does not give a significant ΔACS until 4 GHz, and maximally reaches 5.5 %. The difference in average ACS due to the experimenter putting on his shoes and coat over his indoor clothing, meanwhile, becomes significant below 3 GHz and is maximally 10.5 %.

While these measurements would ideally be conducted on naked subjects, this would raise issues of ethics clearance and also of subject recruitment. It is felt that a good compromise is to proceed by asking subjects to come for measurement in a single layer of cotton clothing, which will keep both the material and the bulk of clothing as constant between subjects as is feasible. As the differences in clothing will be less than between the underpants and jeans/sweater measurements in this study, where the difference reached 5.5 %, a $\pm 2\%$ uncertainty in average ACS is assigned to differences between subjects' clothing in the main study.

3.5.6 Error analysis of the optimised measurement technique

Uncertainties have been identified in the results of measurements taken using the optimised measurement technique, due to various mechanisms:

- Intrinsic statistical uncertainty $\delta_i = 2.6$ %
- Antenna losses $\delta_\eta = 6$ %
- Subject posture $\delta_p = 5$ %
- Subject clothing $\delta_c = 2$ %

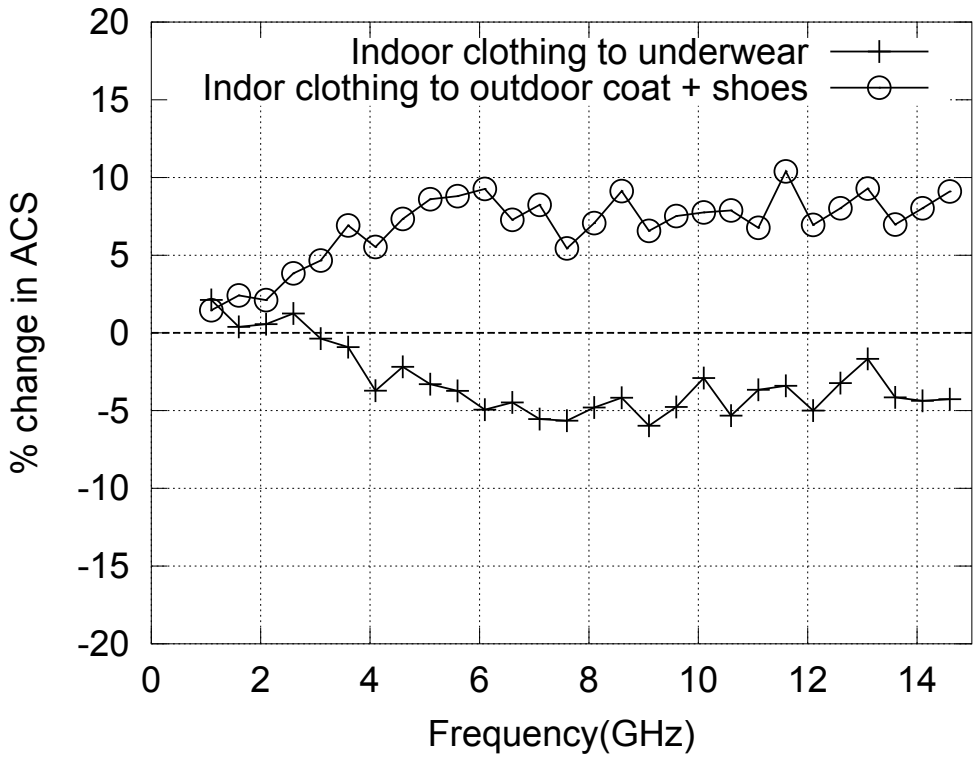

Figure 3.45: $\Delta\langle ACS\rangle$ between experimenter wearing underpants, t-shirt jeans + sweater, and full outdoor clothes (shoes, jeans, t-shirt, sweater and coat)

Therefore, the uncertainty in the ACS measurement is:

$$\delta_t = \sqrt{{\delta_i}^2 + {\delta_\eta}^2 + {\delta_p}^2 + {\delta_c}^2} = \sqrt{0.026^2 + 0.06^2 + 0.05^2 + 0.02^2} = 0.085 \tag{3.17}$$

Measured average ACS is known with confidence to within $\pm 8.5\%$ (Equation 3.17). However, for differentiating between the ACS of individual subjects, the uncertainty due to the efficiencies of the antennas can be discounted, as those will be constant. The uncertainty is then given by Equation 3.18.

$$\delta = \sqrt{{\delta_i}^2 + {\delta_p}^2 + {\delta_c}^2} = \sqrt{0.026^2 + 0.05^2 + 0.02^2} = 0.060 \tag{3.18}$$

The confidence interval when comparing ACS measurements, to the nearest 0.5 %, is 6.0 %.

3.6 Comparison of the initial and optimised measurement techniques

3.6.1 Comparing the stepped and stirred measurements

Before using the optimised continuous stirring methodology for further experiments, it is necessary to verify that the technique gives the same results in practice as does the old, stepped technique used in Campaign 1. To this end, measurements were run on both the spherical phantom and a human subject – the experimenter, who weighed 76.0 kg at this time and did not eat, drink or toilet between measurements. Measurements were taken using both the old and the new techniques, with two alterations to the old: measurements were taken with a 2 MHz frequency resolution rather than the 5 MHz resolution used in Campaign 1, and the antennas were left in the position used in the new technique, at the far end of the chamber as shown in Figure 3.14, rather than being moved to the positions used in the Campaign 1 measurements. This allowed all measurements to be run using a single calibration, removing the possibility of introducing calibration errors. Throughout these measurements, the subject and the phantom were seated on a polystyrene block that had recently been acquired and was thought to provide an electrically transparent seat, and which can be seen in Figure 3.46. In order to check for calibration drift, the first measurement of the day was repeated at the end of the session; the two measurements of the sphere are shown in Figure 3.47. No significant calibration drift is apparent between these two measurements, therefore the other measurements taken in the session can be compared directly.

Figure 3.46: Experimenter seated on polystyrene block for Campaign 2 measurements

To control for differences between the two measurement techniques, measurements were taken with both the old and new techniques (with the exceptions noted at the start of this section), using the polystyrene block as a seat. The results of these measurements are shown in Figure 3.48, from which it can be seen that the two techniques give results that are indistinguishable within the accuracy of the measurement.

These results do, however, present a problem: the shape of the curve appears to be different from those taken in Campaign 1 – there is less of a 'dip' at the minimum from 4 to 7 GHz. It

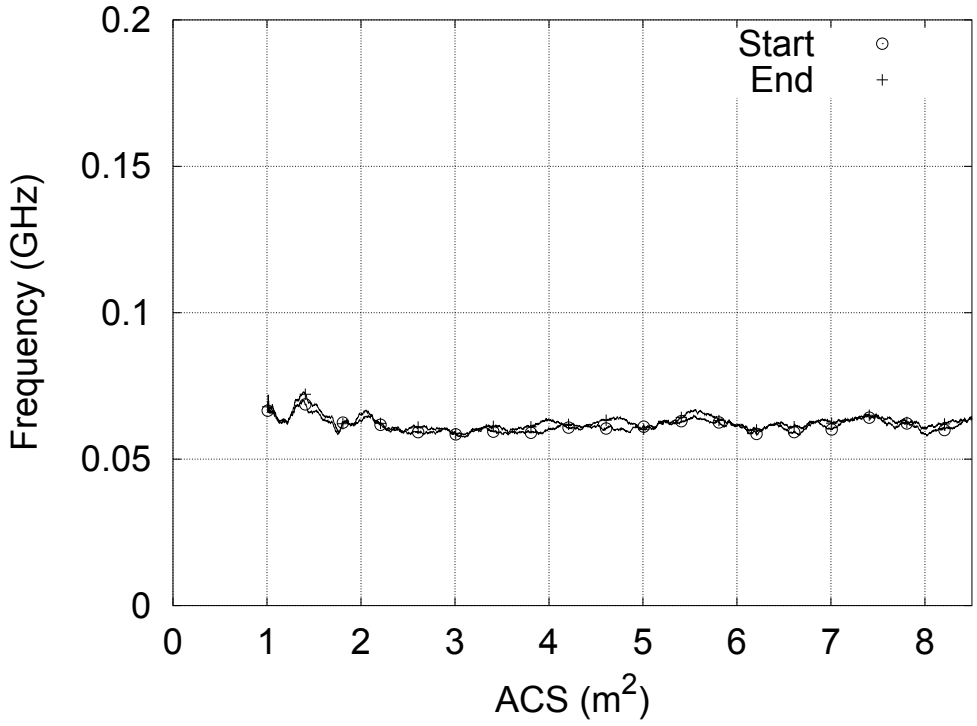

Figure 3.47: ACS of the sphere at the start and end of the day, to check for calibration drift.

is theorised that the reason for this could be the stool used in the January 2012 measurements. This was made of wood, which is lossy [103]. The stool could therefore prevent penetration into the buttock area by waves, which would also be reciprocally shielded from penetrating into the top surface of the stool. Absorption in both the buttocks and the stool would therefore be attenuated, which would reduce the difference between the energy lost in the empty chamber and in the loaded chamber, thus reducing the measured average ACS of the subject. Another potential confounding factor is that subjects were told to sit with their feet on the stool's cross-bar, to keep them within the stirred volume of the chamber. The stool's legs then forced the subject's legs together to some extent, which could cause the subject's legs to shadow each other. These effects would not have been present in the more recent measurements using the polystyrene block.

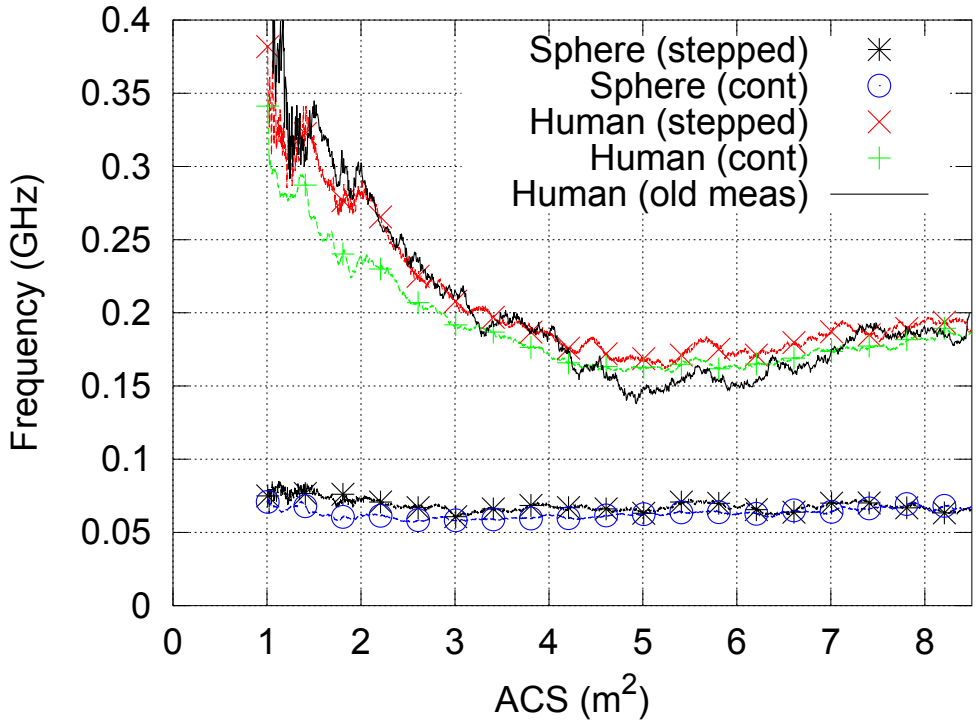

Figure 3.48: ACS of sphere and experimenter on polystyrene block, measured using stepped and continuous stirring and compared to measurement from Campaign 1

3.6.2 Controlling for the stool

The stool and the polystyrene block were first measured versus a completely empty chamber to obtain their ACS values, which are shown in Figure 3.50. The block's average ACS is within $\pm 0.005\text{m}^2$, i.e. within the uncertainty of the measurement, over the whole spectrum: this justifies the assumption that the block is electrically transparent at the frequencies of interest. The stool's average ACS starts at 0.03m^2 at 1 GHz and rises to just over 0.1m^2 at 15 GHz. This large – within the same order of magnitude as the ACS of a human body – so the stool may indeed be a source of error. The stool is not a convex object and parts of it could shadow each other, especially at low frequencies, which may explain why its $\langle ACS \rangle$ increases with frequency. The stool's extremely non-convex shape invalidates Cauchy's relation of $G_s = SA/4$, hence the calculated absorption efficiency Q_a should not be regarded as an accurate value. However, for future reference the stool's surface area was measured with a tape measure as 0.68m^2.

The experimenter's average ACS was then measured while sitting on the stool and on the block. When on the stool his legs were deliberately held together, whereas they were placed further apart when on the block. The results of these two measurements, shown in Figure 3.49, show that the measured average ACS of both the spherical phantom and the human subject is lower when using the stool than when using the block. Figure 3.51 shows the percentage difference between the two measurements: the average ACS of the spherical phantom on the stool is on average 81 % of its value when on the block, and the average ACS of the experimenter on the stool with legs together is 76 % of his average ACS when seated on the block with legs apart. This is more than enough to explain the difference in Figure 3.48 – the problem is now to explain why the C1 trace in Figure 3.48 is as high as it is, excepting the dip from 4 – 7 GHz.

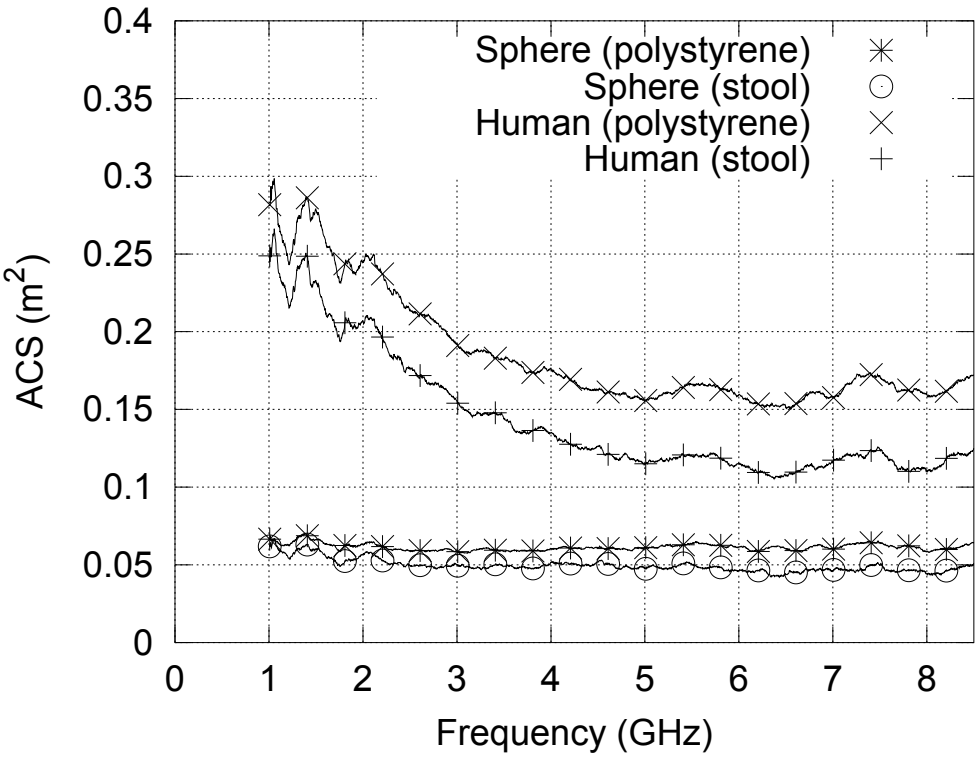

Figure 3.49: ACS of sphere and experimenter, measured using continuous stirring, seated on wooden stool used in Section 3.2 measurements and on polystyrene block

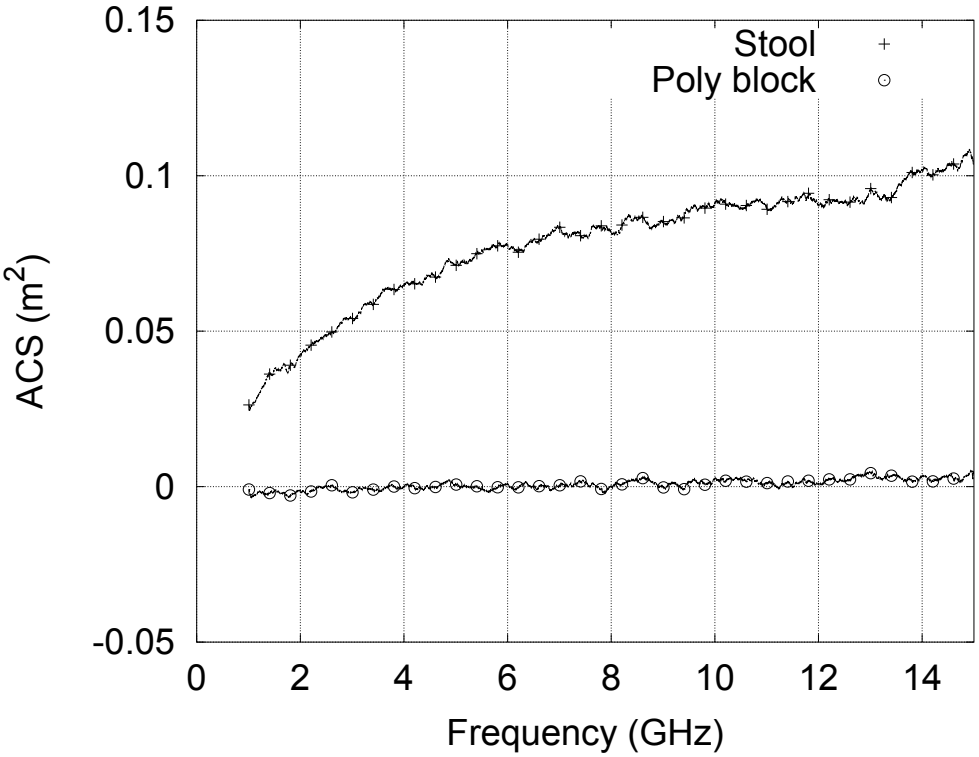

Figure 3.50: ACS of the stool and polystyrene block used in human ACS measurements, measured here versus a completely empty chamber

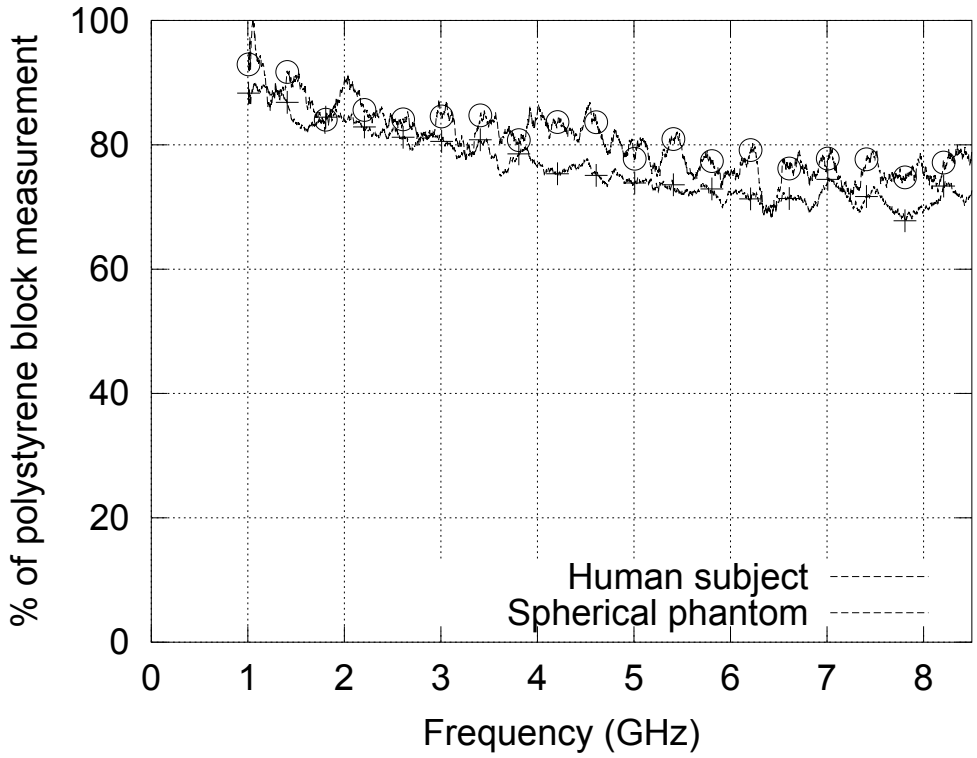

Figure 3.51: $\langle ACS \rangle$ of experimenter and spherical phantom on stool (experimenter with legs held together) as a percentage of $\langle ACS \rangle$ when seated on polystyrene block

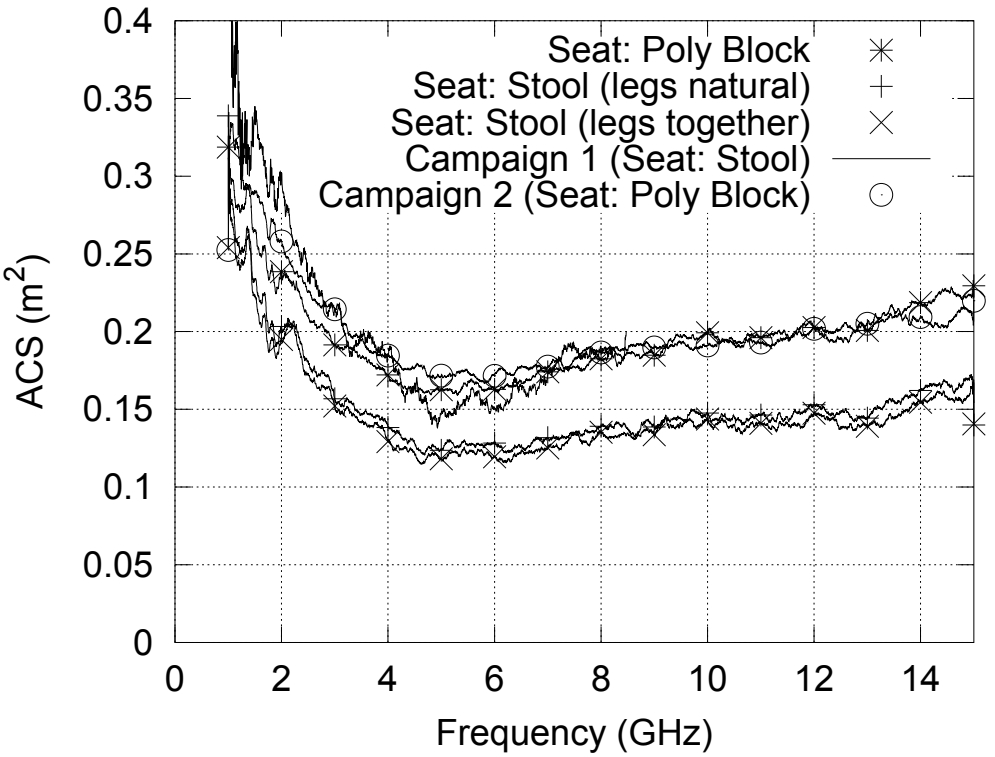

Figure 3.52: New measurements of experimenter $\langle ACS \rangle$ seated on the polystyrene block and the stool, compared to C1 and C2 measurements

3.6.3 Controlling for the change in antenna position

A difference between Campaigns 1 and 2 was that the antenna positions were changed in between the two campaigns. In Campaign 1 they were arranged with one antenna pointing into the stirrer from the side, while the other antenna was placed on the same side as the subject, and directed so as to bounce waves off the chamber wall and into the stirrer. Figures 3.1, 3.2 and 3.3 show a diagram and a two photographs of this setup. As part of the optimisation process between Campaigns 1 and 2, the antennas were moved in order to allow the use of shorter cables and hence faster sweep times. The NA was moved to the opposite end of the chamber and both antennas were placed on the opposite side of the stirrer from the subject, both pointing into the stirrer. A diagram can be seen in Figure 3.14 and a photograph can be seen in Figure 3.35.

It is hypothesised that in the C1 antenna position, waves may be transmitted from the near-side antenna, reflected off the chamber wall (on the left in the photo) and absorbed directly into the subject, without either reaching either the stirrer or the other antenna. This direct absorption would skew the proportion of transmitted to reflected energy at that antenna, and thus the calculated average ACS of the subject. The C2 measurement technique, with the antennas on the opposite side of the stirrer from the subject, should not suffer this problem to the same extent. To test for this effect, we would ideally inspect the four S parameters on each measurement. However, the C2 measurements recorded only a single S parameter in order to reduce measurement time. Therefore, we shall examine the effect of loading the chamber on three properties, for both the C1 and the C2 measurement setups. These properties are: the K-factor of the chamber, the backscattering factors of the antennas and the change in average ACS resulting from a subtraction of unstirred energy. These shall be used to investigate whether either or both of the two conflicting (C1 and C2) measurements have discoverable flaws that explain the differences between them.

Change in K-factor

Here we shall observe the change in K-factor when the chamber is loaded, for both antenna configurations. This is not a direct measurement: the effects of any direct absorption are hard to measure, as directly absorbed energy will never reach the receiving antenna, and so will not be included in either the stirred or the unstirred energy that are ratioed to calculate K-factor. However, the measurement with the lower K-factor will be the better-stirred and hence more reliable measurement. Also, in the C1 measurement, because one antenna is on the same side of the stirrer as the subject, energy that is stirred during the empty chamber measurement can be directly absorbed when the subject is placed in the chamber. However, because the C2 measurement setup has the antennas on the opposite side of the stirrer from the subject, the only energy that can be directly absorbed is energy that would be unstirred in both the loaded and unloaded cases - because the energy has to pass through the stirrer before it can be absorbed. The C2 K-factor will therefore set a limit on the proportion of the energy that could be directly absorbed by the subject.

Figure 3.53 shows the K-factors for the unloaded cases of two measurements: one is a measurement of the experimenter from Campaign 1. The other is a stepped measurement taken on 26/04/2013 of the experimenter sitting on the polystyrene block, using the C2 antenna setup, 100 mechanical stirrer positions, a 100 MHz frequency stirring window and a 2 MHz frequency step. This was the measurement used to compare stepped to continuous stirring in Section

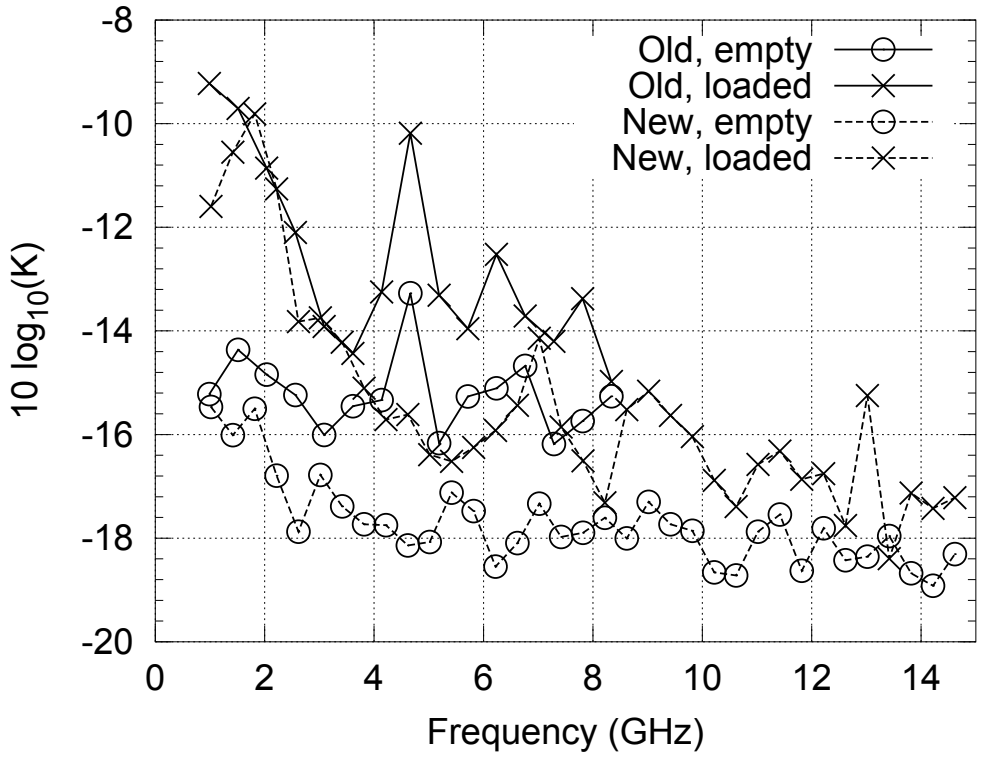

Figure 3.53: Loaded and unloaded Rician K-factors for the old and new antenna placements

3.6.1 – the 2 MHz frequency step and polystyrene block were used for consistency with the continuously stirred measurement in that experiment.

Figure 3.53 shows that the K-factor was lower for the empty case in both measurements. It also shows that the C2 measurement setup gives lower K-factors for both the empty and loaded cases across most of the frequency range. There are two exceptions to this, just below 2 GHz and near 7 GHz but apart from that, the loaded K-factor is smaller for the C2 than for the C1 antenna setup, and above 2 GHz, the unloaded K-factor remains below -17 dB for the C2 setup. Also notable are the spikes in the C1 K-factors around 5 GHz. This is the point at which the two ACS measurements diverge by the largest margin, so the discovery that the C1 measurement has a large unstirred energy component around this frequency is indicative of a possible explanation of this discrepancy.

Change in the effect on ACS of subtracting unstirred energy

To quantify the effects of the change in K-factor caused by altering the antenna setup, average ACS was calculated for the measurements in the previous section, both with and without the use of the vector-average subtraction (VAS) technique described in Section 3.2.2. The technique is designed to remove the effects of the unstirred energy in the chamber by subtracting the vector average of the chamber transmission coefficient over all stirrer positions, individually, from each individual measurement It thus re-centres the spread of complex transmission coefficients around the origin, as would be expected from a well-stirred measurement.

The change in the average ACS when VAS is applied shows the change in the $\langle ACS \rangle$ that can be effected by the unstirred energy in the chamber, and thus the margin for error due to the presence of this energy. Figure 3.54 shows the ACS of the sphere, calculated both with and with

out VAS for both measurements. As can be seen, VAS makes a difference to each measurement, but a lesser difference to the measurement that uses the C2 antenna configuration. The same calculation was also performed for the human load, but is omitted for plotting clarity.

The data in Figure 3.54 can be seen more clearly if the differences made to average ACS, rather than the ACS values themselves, are plotted. Figure 3.55 thus plots the percentage difference made to average ACS by the application of VAS, for both the sphere and the human load, for both the C1 and C2 antenna setups. This shows that the C1 measurement is altered by up to 5 % for the sphere and up to 15 % for the human load. On the other hand, the difference made to the C2 setup by VAS is much smaller, $\leq$2 % over all frequencies and $\leq$1 % above 4 GHz for the sphere, even less for the human load.

From this, we can conclude that over most frequencies – and notably over the frequencies of interest, where the C1 and C2 measurements disagree between 4 GHz and 7 GHz – that unstirred energy in the C2 measurement is only making a 1 % difference to the average ACS. The C1 measurement, on the other hand, is changed by up to 15 % by the presence or absence of unstirred energy – and the figure is indeed 15 % at 5 GHz where the greatest discrepancy between average ACS values is seen. A change of 15 % would be enough to make the C1 and C2 measurements agree. However, this does not entirely explain the discrepancy: while the C1 measurement can certainly be said to be the poorer measurement, our hypothesis was that transmitted energy was being absorbed or reflected by the subject before encountering the stirrer. We can now confidently state that this could make a maximum 2 % difference to the C2 measurement (because due to the antenna positions, it would require a pathologically convoluted path for energy to be directly absorbed in the subject, that would otherwise interact with the stirrer). However, the C1 measurement has an antenna on the same side of the stirrer as the subject, so both previously-stirred and previously-unstirred energy could interact directly with the subject.

The relatively larger difference made by VAS to the C2 measurement of the smaller load (the sphere) in Figure 3.55 is not surprising: in Equation 2.46, Carlberg shows that the greater the difference made to the G-factors by the introduction of a load, the more accurate the measurement will be. What is notable is that in the C1 measurement, VAS makes a $\leq$7 % difference to the sphere's ACS ($\leq$5 % above 4 GHz) but a larger, $\leq$15 % difference to the average ACS of the human load. This is not what would be expected were the inaccuracies in the C1 measurement solely due to the effects of unstirred energy. This suggests that the measurement is being skewed by a further effect, such as the posited direct absorption. To investigate this, it is necessary to investigate the backscattering factors of the antennas in each measurement.

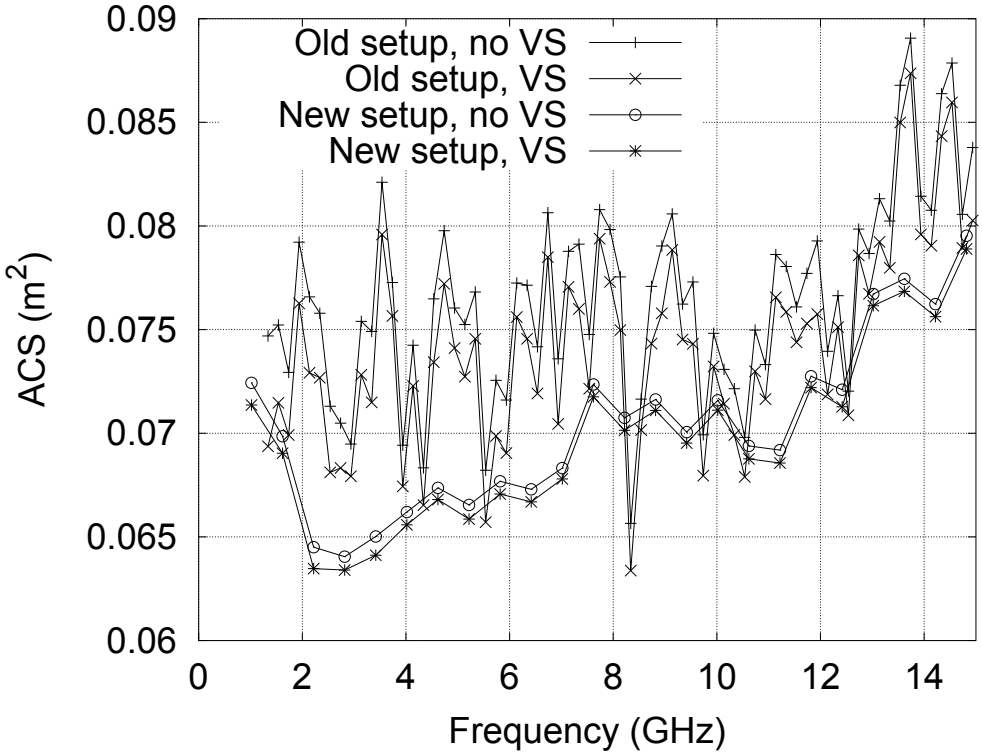

Figure 3.54: ACS measurements of the sphere, with and without vector average subtraction, using the C1 and C2 measurement techniques

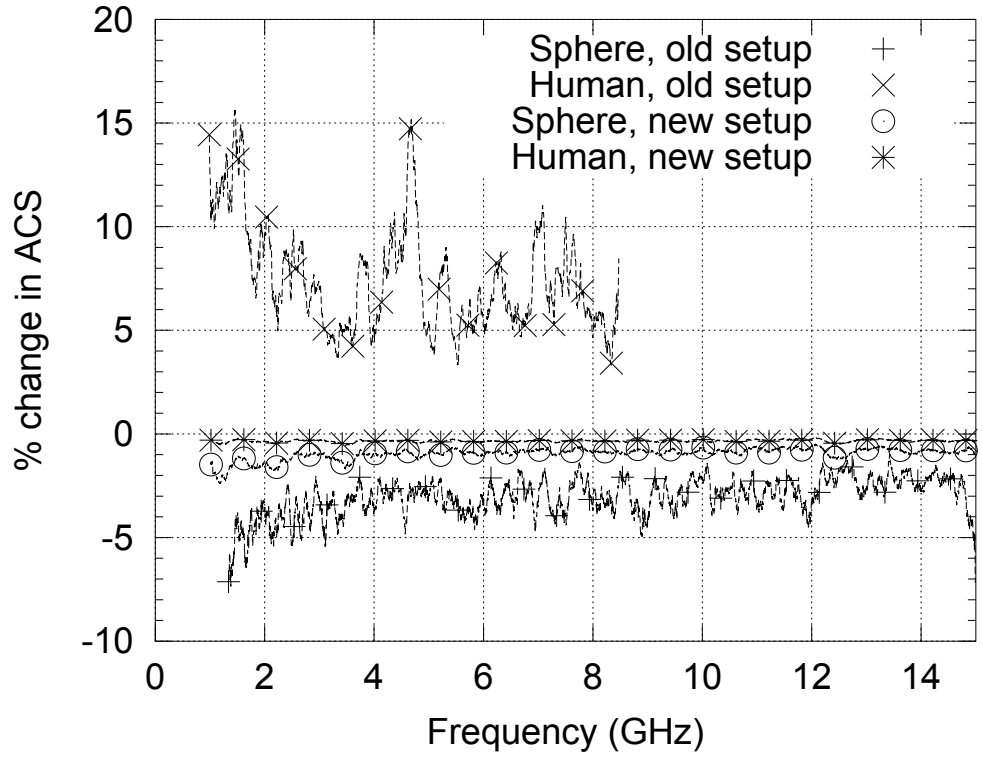

Figure 3.55: % change in $\langle ACS \rangle$ when vector average subtraction is applied to sphere and human measurements, using both C1 and C2 measurement techniques. The 8.5 GHz limit of one dataset is the limit of the Agilent NA.

Change in backscattering factors

The backscattering factor (BS) of an antenna is the ratio of the stirred components of the reflection and transmission coefficients in a two-port measurement, as defined in Section 2.3.4. The investigations in Section 3.4.4 showed that it is sensitive to changes in the loading of the chamber. The backscattering factor will be increased by either an increase in the stirred component of $\langle|S11|^2\rangle$, or else by a decrease in the stirred component of $\langle|S21|^2\rangle$. The introduction of a load to a chamber should therefore affect the backscattering factors of both antennas equally if the chamber is well stirred, because the two transmission coefficients and the stirred components of the two reflection coefficients should be attenuated by equal amounts. Investigations in Section 2.3.4 showed the backscattering factors to be raised when the chamber was loaded, indicating that the attenuation of the transmission coefficient was the larger effect. Why this should be the case is not well-understood – possibly due to coherence effects, similar to the reasoning provided for a positive backscattering factor [87]. However, it follows from reverberation chamber theory that within the stirred volume of a well-stirred chamber, provided both antennas are interacting with the chamber correctly (i.e. the electric field magnitudes follow Rayleigh statistics in the vicinities of both antennas), the effect on both the reflection and the transmission coefficients should be similar for each antenna.

To investigate this, the same two measurements were used as in previous sections: one of the C1 measurements of the experimenter, plus the 26/04/13 stepped measurement of the same, using the C2 antenna setup. Backscattering factors were calculated for both, these are shown in Figures 3.56 and 3.57 respectively. Each port shows four traces: the backscattering factors for each antenna, for both the loaded and unloaded chamber.

Figure 3.57 shows that in the measurement with the C2 antenna setup, the backscattering factors behave largely as predicted. The two antennas have different backscattering factors below 2 GHz where the stirring is known to be less effective, and also above 10 GHz. However, both are affected in substantially the same way by the insertion of the human load: they are increased by a value that ranges from 0.5 dB or less at low frequencies, to around 2 dB at the high frequencies. The insertion of the load is having a very similar, if not quite the same effect on each antenna.

Figure 3.56 shows that for the C1 measurement, on the other hand, C_{BS1} hardly changes at all when the load is inserted – it is in fact marginally decreased, never by more than 0.2 dB above 2 GHz, and by even less above 5 GHz. C_{BS2} changes by far more – it is increased by a fairly constant 0.5-0.6 dB above 2 GHz. This shows that the two antennas are interacting with the load in different ways, with the fields at the port 2 antenna affected much more than the presence of the load than those at the port 1 antenna. This behaviour is not consistent with a reverberation chamber that is working properly, so to investigate further, the individual S parameters are plotted in Figure 3.58.

Figure 3.58 shows the change in all four S parameters when the human load is introduced to the chamber, for both the C1 and C2 antenna setups. Note that the transmission coefficients are averaged over all stirrer positions, while the reflection coefficients first have their vector averages subtracted before being averaged themselves. This is because the vector average of an antenna's reflection coefficient in a well-stirred chamber is equal to the free space reflection coefficient of the antenna. This is therefore subtracted to leave the component of Sxx that is due to reflection from the chamber itself.

In the measurement with the C2 antenna setup, the two transmission coefficients are atten-

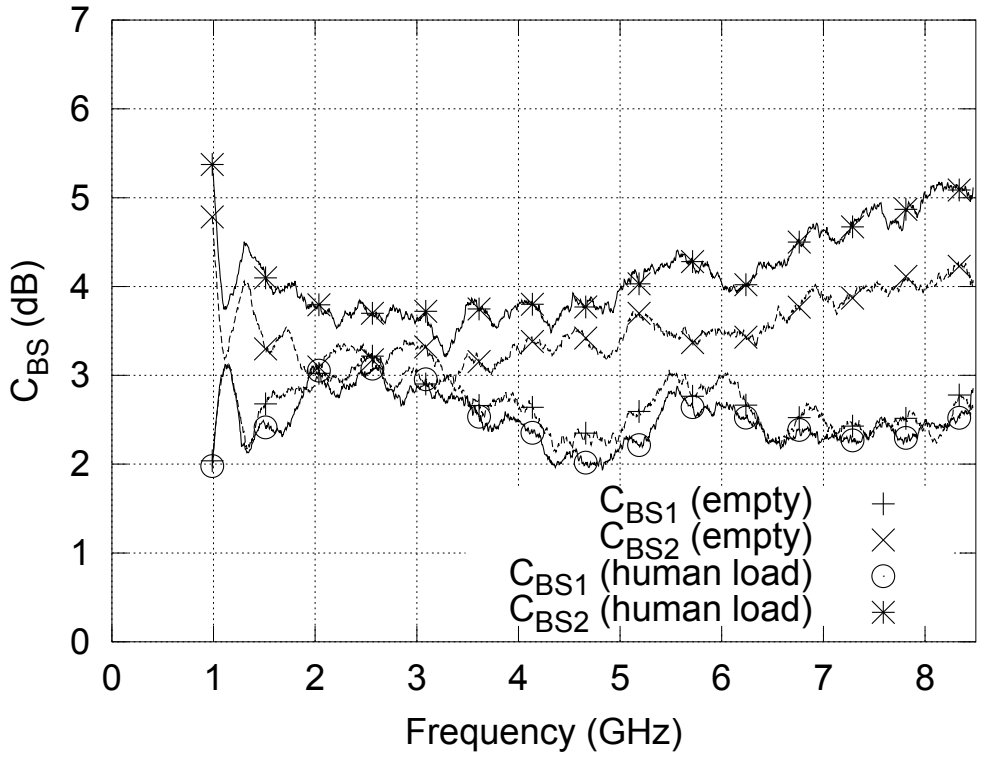

Figure 3.56: Backscattering factor on each port in a Campaign 1 measurement of the experimenter's $\langle ACS \rangle$, for both the loaded and unloaded chamber - note the maximum frequency is 8.5 GHz, as with other C1 measurements.

uated by almost exactly the same amount when the chamber is loaded: just under 5 dB for frequencies above 6 GHz, more at lower frequencies. They are always within 0.4 dB of each other, usually closer. The reflection coefficients for this measurement also behave very similarly: although the gap between them reaches 0.8 dB around 11.5 GHz, the difference between the attenuations of the reflection coefficients is small compared to the attenuations themselves, and enough to clearly distinguish the behaviours of the reflection coefficients as a separate pair from the behaviours of the transmission coefficients.

In the C1 measurement, $\langle |S11 - \langle S11 \rangle|^2 \rangle$ and both transmission coefficients are all attenuated by very similar amounts when the load is introduced to the chamber: about 3 dB above 5 GHz. All are attenuated less than any of the S parameters in the other measurement, possibly due to the different equipment used in Campaign 2: the new NA used a higher stimulus power of 6 dBmW and also might have had a more sensitive detector. $\langle |S22 - \langle S22 \rangle|^2 \rangle$ is the sole exception, being attenuated by up to 0.8 dB less. This is the cause of the asymmetric behaviour of the backscattering factors in Figure 3.56: C_{BS1} is affected so little by the loading of the chamber because $\langle |S11 - \langle S11 \rangle|^2 \rangle$ is attenuated by almost the same factor as $\langle |S21|^2 \rangle$. $\langle |S22 - \langle S22 \rangle|^2 \rangle$ behaves more as has been observed in other experiments, being attenuated by a lesser amount. This suggests a direct absorption effect on the Port 1 antenna, which would explain not only the anomalous drop in $S11$ when the chamber is loaded, but also the unexpectedly high $\langle ACS \rangle$ readings for subjects measured in Campaign 1, given that average ACS should have been under-read due to absorption in the stool.

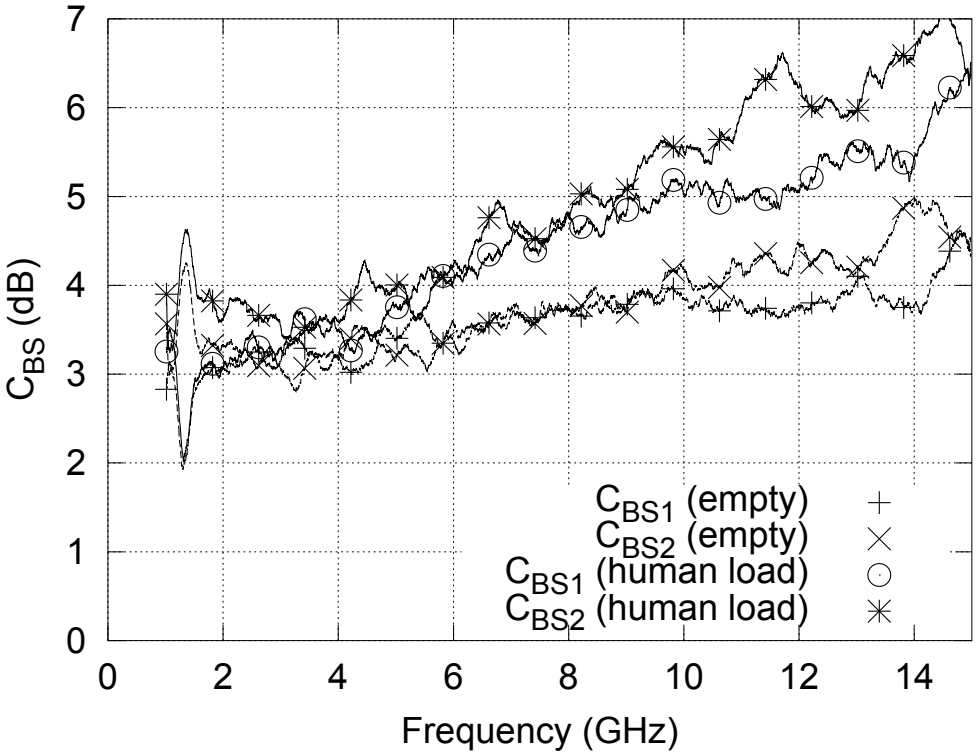

Figure 3.57: Backscattering factor on each port, for both the loaded and unloaded chamber, in a stepped *ACS* measurement with antennas in the C2 configuration – both on the opposite side of the stirrer from the subject.

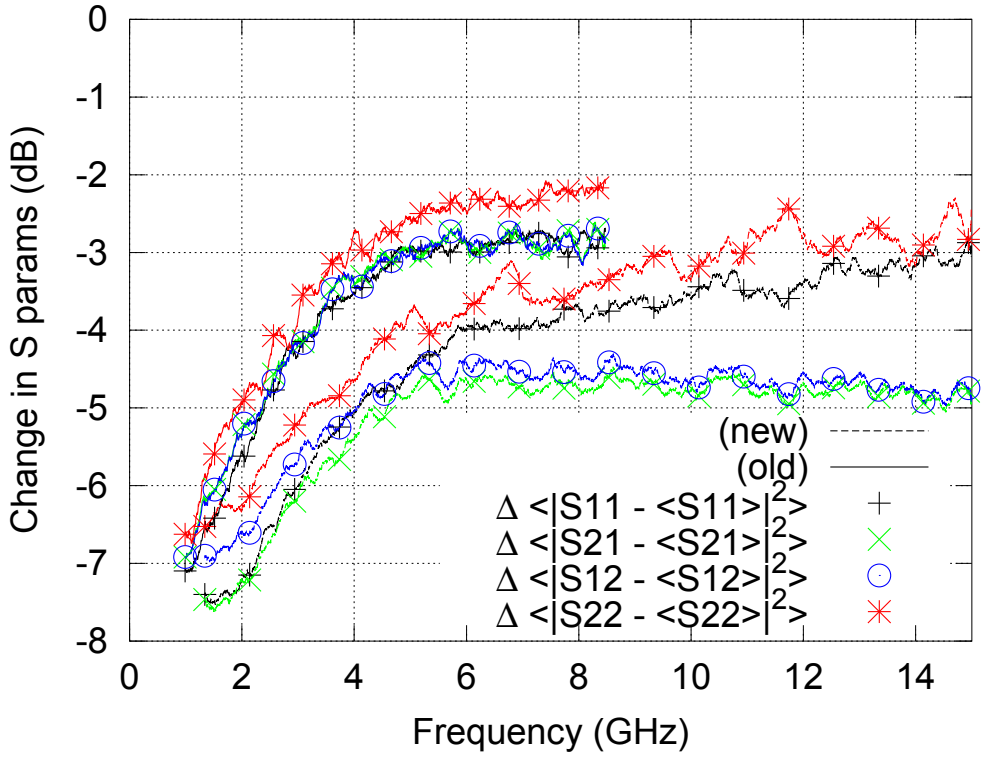

Figure 3.58: Change in S parameters when the RC is loaded with the experimenter, for a C1 measurement plus a more recent measurement with antennas in the C2 positions

3.6.4 Conclusions of the comparison between measurements

The comparison of the initial and optimised measurement techniques has led to these conclusions:

- Continuous stirring produces equivalent results to those from stepped stirred measurements. Continuous stirring is appropriate for use in future measurements.
- The wooden stool used in Campaign 1 is lossy, which therefore leads to under-reading of average ACS due to mutual shielding of the stool and the subject. The polystyrene block has been found to be electrically transparent at the frequencies of interest, therefore it should not distort results and is a superior seat for human ACS measurement.
- After accounting for the stool, results from Campaign 1 were found to have a different level and shape from those taken using the finalised methodology.
- The Campaign 1 measurements were found to be inadequately stirred, with a variation in average ACS of up to 15 % due to unstirred energy.
- Furthermore, the antennas in the Campaign 1 measurements were affected very differently by the introduction of the subject to the chamber. It is thought that this is due to direct absorption by the subject of energy from one of the antennas in the initial measurements.
- Together, these two effects are enough to account for the discrepancy in results between the Campaign 1 measurements and those taken with the finalised methodology.
- The repositioning of the antennas for the optimised measurements has greatly reduced this problem, as less than 1 % of energy transmitted is able to interact with the subject without first passing through the stirrer.

3.7 Summary

In this section, a methodology has been developed for accurate measurement of the average ACS of a live human subject. Initially, a stepped-stirred reverberation chamber measurement was used, which utilised the theory described by Carlberg *et al.* [83]. This method was found to be inadequate, chiefly due to the slow speed of data acquisition, which prevented the gathering of sufficient data to give accurate results within the time a subject could reasonably be expected to sit in the chamber. The method also displayed some problems with an excessive proportion of the energy in the chamber remaining unstirred and skewing the results.

Several approaches were taken to improving the measurement method. New, faster equipment was purchased. Measurement with one antenna was considered but the idea was not used, as it was difficult to control. The two-antenna technique was kept but the antennas were moved to the opposite side of the paddle stirrer from the subject. Continuous stirring was introduced to accelerate the measurement, and *in situ* measurement of antenna reflection parameters was replaced by pre-measurement of free-space reflection. Coherence in the chamber was examined across both the frequency and the mechanical stirring axes, and optimised to reduce runtime while giving enough measurement samples for accurate measurement across the maximum possible frequency spectrum. The stool used during measurements was replaced with an electrically transparent polystyrene block. Measurements were taken examining the effect of subject posture, clothing and position within the reverberation chamber, from which guidelines

were developed that could be given to subjects, to control for these properties. The optimised measurement reduced measurement time to under eight minutes, while reducing the intrinsic confidence limit of the measurement to $\pm 2.6 - 2.8\%$.

A test case was developed, in the form of a spherical phantom with an ACS that could be computed using a two-layer Mie scattering algorithm. The optimised measurement was compared to this, and found to agree. The optimised measurement was also compared to the initial measurement. Discrepancies were discovered, investigated and found to be due to inadequate stirring plus poor antenna placement, which encouraged direct interaction between transmitted energy and the subject's body.

The optimised measurement was tested with the spherical phantom and found to be repeatable to within its confidence limit. For the human measurement, other factors (subject posture and clothing) broadened the confidence limit to $\pm 4.4\%$. Absolute values are further affected by losses in the antennas; attempts to control for this effect met with limited success but did give some indicative results, which informed estimates that allowed for some improvement of the data. If antenna loss is included, the measurement's confidence limit is $\pm 8\%$, but the antenna losses will be proportionally constant between measurements, so for differentiating between the average ACS of different subjects, this is inapplicable so long as the same antennas are used.

The issues in the initial measurement have been addressed and improved. The optimised measurement is now sufficiently developed that it can be used in a second measurement campaign, to study the absorption cross sections of a wider range of human subjects, over a wider frequency range and with greater accuracy than has previously been accomplished.

Chapter 4

Results of the ACS Measurement

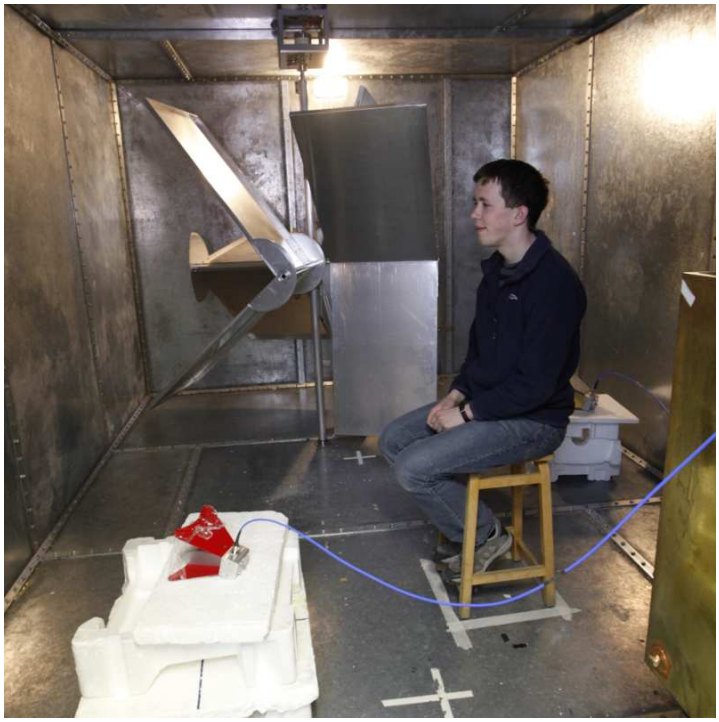

Figure 4.1: Live measurement inside the reverberation chamber, Jan-Feb 2012

4.1 Overview

This research program included two major measurement campaigns, in which ACS data was gathered across a sample population of human volunteers. These two campaigns were undertaken at either end of 2012, and are referred to as Campaigns 1 and 2, or C1 and C2. Between the two campaigns, the experimental methodology was adapted to improve the speed and accuracy of measurement and to solve several problems that manifested themselves during the first campaign. This process is recorded in Chapter 3; the current chapter presents the data gathered during the two campaigns.

4.2 Campaign 1

The first measurement campaign of this research program was undertaken in January-February 2012. Figure 4.1 shows the experimenter undergoing measurement during this campaign.

4.2.1 Apparatus and measurement protocols

This measurement campaign used the methodology developed in Section 3.2 to measure the ACS of nine volunteer subjects.

The measurements of different subjects took place on different days, so different cables were sometimes used, subject to availability. A full list of the equipment used can be found in Appendix B.

4.2.2 Sample population

The biometric parameters of the nine subjects measured in Campaign 1 are recorded in Table 4.1. The sample population consisted of six men and three women, aged between 20 and 48 years old. Masses ranged from 38.1 to 112.2 kg and heights ranged from 1.54 to 1.95m.

Table 4.1: Biometric parameters of subjects taking part in January 2012 ACS experiment

SN	D	S	A	M	H	Clothes
1	25/1	M	48	101.0	1.89	shirt, jumper, trousers, leather shoes
2	∗	M	26	∗	1.81	∗
3	25/1	F	21	84.1	1.65	shirt, cardigan, skirt, tights, leather boots
4	25/1	M	20	101.5	1.76	t-shirt, polyester jumper, trousers, shoes (steel toecaps)
5	21/1	M	39	67.8	1.75	shirt, trousers, leather shoes
6	31/1	F	24	38.1	1.54	t-shirt, jeans, jumper, leather boots
7	02/2	M	22	59.3	1.81	t-shirt, corduroys, trainers
8	02/2	F	30	52.8	1.72	t-shirt, wool jumper, corduroys, leather boots
9	10/2	M	25	112.2	1.95	t-shirt, polyester jumper, jeans, trainers

Key:
SN: Subject Number
D: Date (all January 2012)
S: Subject sex
A: Subject age in years
M: Subject mass in kilograms
H: Subject height in metres
∗: See Table 4.3

4.2.3 Error analysis: measurement of physical parameters

During the ACS experiments, subject mass was measured using a pair of Salter Electronics electronic bathroom scales. To check the accuracy of these scales, they were compared to the scales in the university's post room - a set of floor scales manufactured by MK Scales Ltd. Two human subjects were measured using each set of scales, the results are shown in Table 4.2. Without access to any further means of calibration, the better quality, more expensive set of scales that were used for professional purposes, were the best standard available by which to validate the Salter set. As can be seen, the Salter scales under-read subject mass compared to the post room's scales by 300 g and 350 g, or 0.25 % and 0.46 % respectively.

The height measurement was taken to the nearest cm by measuring subjects against the side of the reverberation chamber. As such, it had a resolution of 1 cm. The mass measurement, according to the post-room's scales, was under-reading by up to 350g.

Table 4.2: Mass in kg of two subjects, measured using two sets of scales

	Subject A	Subject B
ACS Scales	75.1	89.0
Post room scales	75.45	89.30

4.2.4 Results of Campaign 1 measurements

To investigate the repeatability of the technique, Subject 2 was measured 5 times over the course of the measurement campaign. These measurements were on three different days and the equipment was recalibrated between each measurement. The subject did not wear the same clothes each time, and was able to do such things as eat, drink and go to the toilet between measurements – he also exercised heavily between January 25th and 31st – all of which could account for the differences in mass between the five measurements, recorded in Table 4.3. The statistical uncertainty in the measured ACS, estimated from Figure 3.6 and excluding the effects of systematic errors, is 6-7 % above 2 GHz. In the 1 to 2 GHz band the higher statistical uncertainty is due to the lower number of independent samples available in the chamber. The results of these five measurements are shown in Figure 4.2 and indicate that the measurement procedure is robust, as the five measurements are all within the confidence band of the measurement.

Table 4.3: Physical characteristics of Subject 2 for 5 measurements in January 2012 ACS experiment

SN	D	S	A	M	H	Clothes
2 (1)	25/1	M	26	75.7	1.81	t-shirt, thin polyester jumper, jeans trainers
2 (2)	25/1	M	26	76.5	1.81	t-shirt, thin polyester jumper, jeans, trainers
2 (3)	31/1	M	26	75.1	1.81	t-shirt, jeans, trainers
2 (4)	02/2	M	26	74.7	1.81	t-shirt, polo shirt, jeans, trainers
2 (5)	02/2	M	26	74.7	1.81	t-shirt, polo shirt, jeans, trainers

Figure 4.3 shows ACS versus frequency for all nine subjects. From this, the body's absorption performance can be divided into two ranges: below roughly 5 GHz its ACS is strongly frequency-dependent, whereas above this point it varies much less with frequency. The ACS can also be seen to vary with subject mass: heavier subjects have larger absorption cross sections. Whether this is the largest correlation will be examined in Chapter 5. However, the large uncertainty in the measurement limits the ability to resolve the differences in ACS between the subjects.

The measurements of ACS show good agreement with values from the literature, shown in Section 1.4.

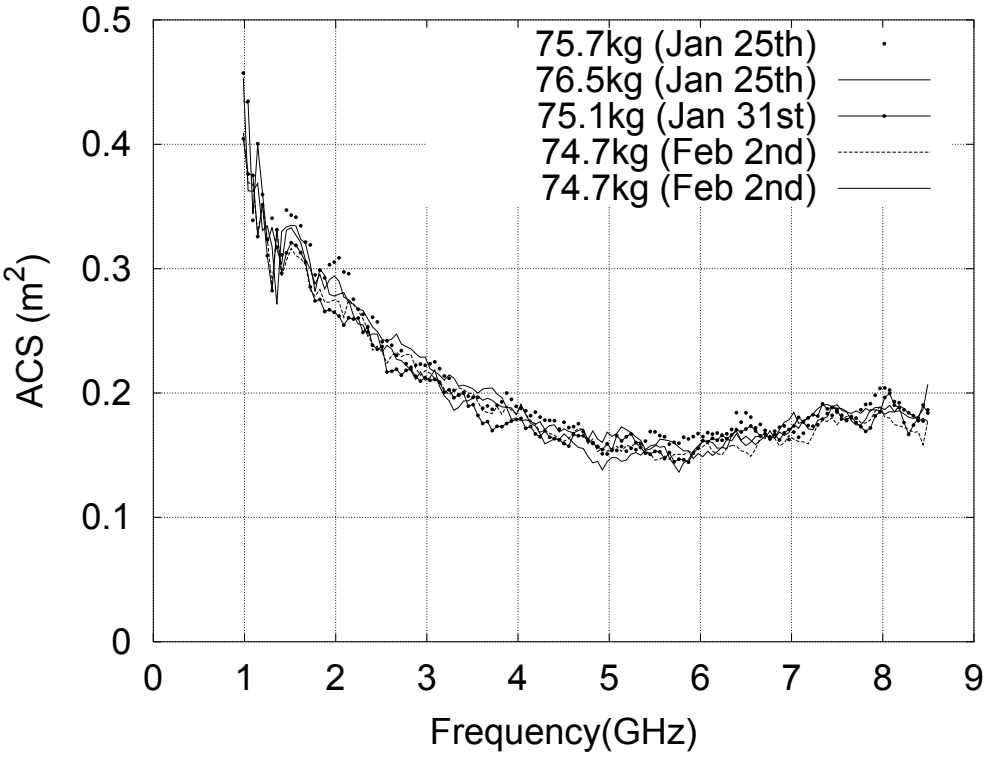

Figure 4.2: Five measurements of Subject 2 ACS, Jan-Feb 2012

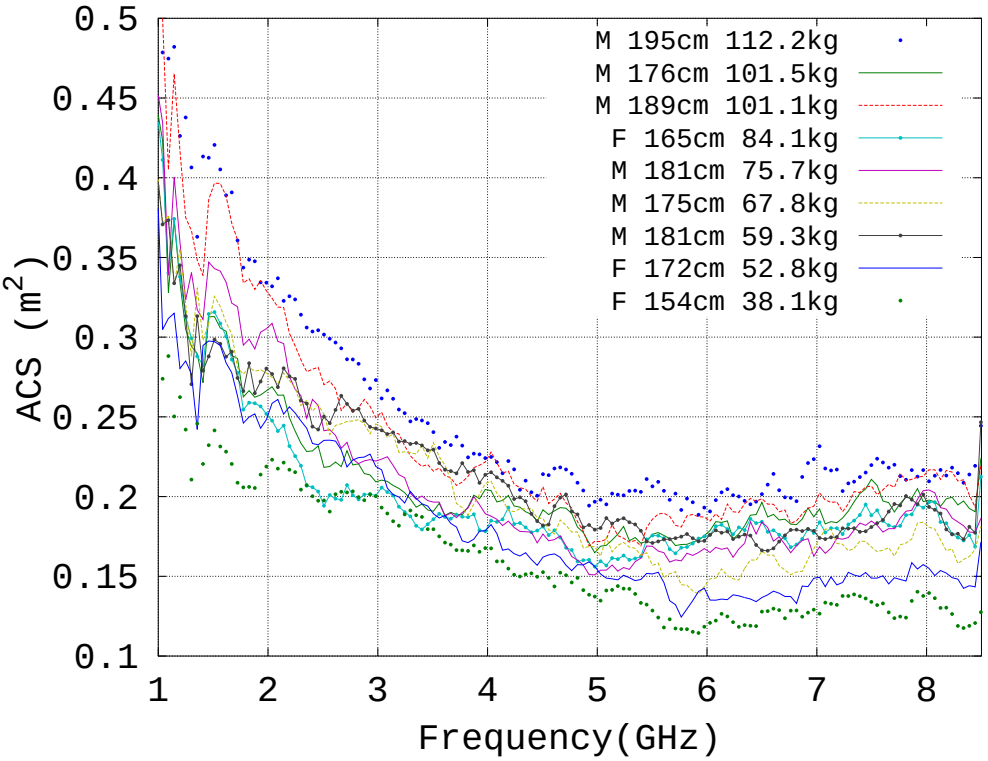

Figure 4.3: Measured ACS of 9 human subjects, Jan-Feb 2012

4.3 Campaign 2

4.3.1 Measurement protocols

The second measurement campaign of this PhD was undertaken over five consecutive days, from December 3rd-7th 2012. This used the methodology developed in Section 3.4 and described in Section 3.5 to measure the ACS of 65 locally-recruited volunteer subjects from 1-15 GHz.

The schedule of a day was as follows:

- Arrive, switch on NA to warm up for at least 30 minutes (if it was not left on overnight)
- Calibrate system
- Empty chamber measurement
- Sphere measurement
- Morning: live measurements
- Sphere measurement
- Lunch
- Re-calibrate system
- Sphere measurement
- Afternoon: live measurements
- Sphere measurement
- End of day

Upon arrival at the lab for their timetabled slot, experimental subjects were asked to read an information sheet and sign a consent form, in accordance with the protocol stated when ethical approval was applied for. This also recorded a subject number, which was used to identify the subject on all other forms - the consent form was the only document to contain a subject's name.

Subjects had been asked when recruited to wear a single layer of cotton clothing. They were now asked to remove shoes and extra clothes, along with the contents of their pockets and any jewellery they were wearing. They were then weighed using the same Salter scales that were used for Campaign 1. Their height was measured against a scale marked on the side of the reverberation chamber and their waist circumference was measured using a tape measure. These parameters were recorded, along with the subject's age and sex, their clothing, the date and any relevant miscellaneous information, on a record sheet identified by subject number. This information is given in Table 4.4. They were shown the interior of the reverberation chamber, asked to sit still for the duration of the measurement and given an opportunity for further questions. After this, they were ready to be measured in the reverberation chamber.

4.3.2 Apparatus

The experimental equipment was as follows:

NA Port 2 → Unmarked SMA-N cable (1m) → N Bulkhead 1 → Cable MW05 (N-SMA) (1m) → *calibration point* → SMA-N adapter → 3117 Antenna

3117 Antenna → N-SMA Adapter → *calibration point* → Cable MW02 (1.5m) → N Bulkhead 5 → Cable MW17 (1.5m) → NA Port 1

N-SMA adapters were attached to the horn antennas on the afternoon of December 2nd, the day before measurements started. A free space measurement was taken to determine the reflection coefficient of each antenna: the equipment was taken to the outer door of the lab, the antenna (on cable MW25) was pointed at the sky and its reflection coefficient was measured. This was done several times with the antenna pointing in different directions; if the reflection coefficient displayed on the NA screen remained constant, it was recorded. The SMA adapters were then left in place throughout the entire measurement period, as they contributed to the reflection performance of the antenna.

Data from Subjects 1 – 7 was discarded due to measurement problems. Subjects 2 and 3 were re-measured later, but Subjects 1, 4, 5, 6 and 7 do not appear in further results or analysis.

4.3.3 Error analysis: measurement of physical parameters

Measurement of subject height, mass and waist circumference were conducted as in Campaign 1; as such, their accuracy is as is discussed in Section 4.2.3. Surface area is calculated using mass and height using the Tikuisis formula, as discussed in Section 3.5.1. To calculate the amount by which this will affect ACS measurement, Figure 4.4 shows the variation in the Tikuisis calculation of surface area for each subject, resulting from variation in the height and mass parameters.

In order to calculate the uncertainty in the Tikuisis calculation of BSA due to measurement errors, bounds were set on the parametric measurements and fed into the Tikuisis formula. The lower and upper bounds for subject height were measurement ± 0.5 cm. The lower and upper bounds for the mass were 0.0 kg below and 0.4 kg above the value measured by the scales – these values were chosen due to the comparison with the postal scales in Table 4.2, where the Salter scales under-read by 300 and 350g. Surface area was then calculated using all four combinations of these values - the variation between the highest and lowest is here plotted as a percentage of the lowest value. Figure 4.4 shows that uncertainty in the measurement decreases with increasing subject surface area - which is unsurprising as constant errors will become smaller proportions of increasing body sizes. In fact, the correlation is nearly inverse, as is shown by the second plot in Figure 4.4. Even for the smallest subject (45.8 kg, 1.64 m tall), the variation in calculated BSA due to the uncertainties in mass and height is well under 1 %. We can therefore assume all uncertainty due to height and mass measurements to be $< 1\%$.

4.3.4 Subjects common to both measurement campaigns

Four subjects were measured during both measurement campaings. These were Subjects 1, 2, 8 and 9 in Campaign 1, who were marked as Subjects 24, 64, 20, 16 respectively in Campaign 2. Figure 4.5 plots both results for each subject against each other. These differ in the manner

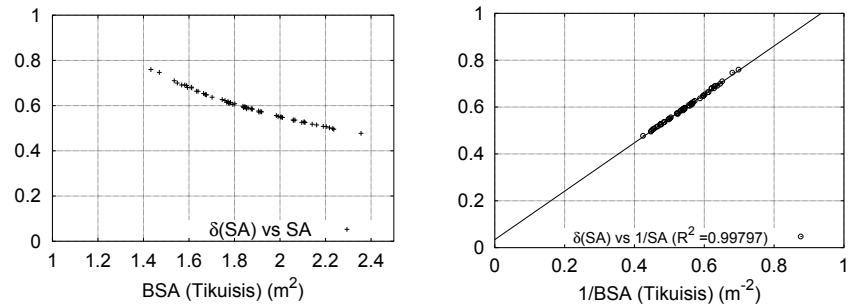

Figure 4.4: Variation in Tikuisis calculation of subject body surface area for all subjects, when subject height and mass are varied by the confidence interval of those measurements (0.4 kg and 0.01 m), plotted directly and reciprocally against subject mass. Y axes are proportional variation in BSA.

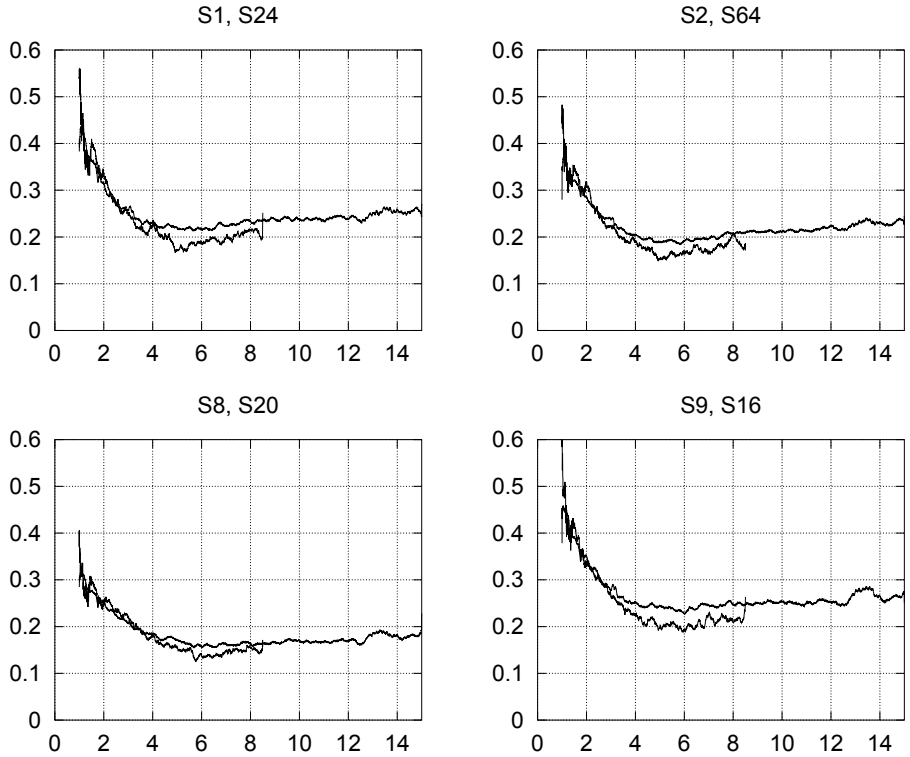

Figure 4.5: ACS of subjects who were measured in both campaigns. Y axes are ACS (m^2), X axes are frequency (GHz)

that was investigated and explained in Section 3.6, with the characteristic dip around 5 GHz and low reading at higher frequencies, due to poor stirring and direct absorption in the C1 measurement.

4.3.5 Physical characteristics of the experimental sample

In total, 24 female and 36 male subjects were successfully measured. Their biometric parameters are shown in Table 4.4.

Table 4.4: Physical Characteristics of subjects taking part in December 2012 ACS experiment

SN	D	E	Sp	S	A	M	H	W	SA	Clothes
02	03	3	3	M	49	72.8	1.80	0.9	1.91	T-shirt, cord trousers
03	03	2	2	M	45	67.2	1.65	0.83	1.75	T-shirt, thin (poly?)cotton trousers
08	03	3	3	M	46	96.2	1.85	1.07	2.19	T-shirt, jeans
09	03	3	3	F	51	62.1	1.65	0.78	1.70	Shirt, trousers
10	03	3	3	M	21	75.3	1.89	0.88	1.99	T-shirt, jeans
11	03	3	3	M	23	79.8	1.84	0.82	2.01	T-shirt, jeans
12	03	3	3	F	20	45.8	1.64	0.63	1.47	Strappy top, jeans
13	03	3	3	M	31	56.5	1.64	0.81	1.61	T-shirt, jeans
14	03	3	3	M	26	79.0	1.84	0.89	2.00	T-shirt, thin trousers
15	03	3	3	M	23	92.0	1.79	1.04	2.11	T-shirt, jeans
16	03	3	3	M	26	109.5	1.90	1.16	2.36	Shirt, jeans
17	03	3	3	M	28	91.4	1.85	0.98	2.14	T-shirt, jeans
18	03	3	3	F	26	57.2	1.57	0.74	1.59	Shirt, jeans
19	03	3	3	M	31	68.4	1.79	0.88	1.85	Shirt, trousers
20	03	3	3	F	31	51.3	1.70	0.73	1.58	T-shirt, shirt, jeans
21	03	3	3	M	22	92.6	1.97	0.87	2.24	T-shirt, jeans
22	03	3	3	M	22	89.7	1.83	0.84	2.11	T-shirt, cotton trousers
23	03	3	3	F	31	55.7	1.56	0.75	1.57	Jeans, thin (poly?) jumper
24	04	4	4,5	M	49	96.8	1.90	1.06	2.23	T-shirt, chinos
25	04	4	4,5	M	62	67.6	1.73	0.84	1.80	Shirt, cord trousers
26	04	4	4,5	M	71	72.4	1.70	0.89	1.84	Shirt, cotton trousers
27	04	4	4,5	M	19	68.3	1.80	0.79	1.85	LS t-shirt, jeans
28	04	4	4,5	F	27	69.9	1.74	0.81	1.85	T-shirt, LS t-shirt, jeans
29	04	4	4,5	F	46	64.9	1.70	0.72	1.77	Polo shirt, jeans
30	04	4	4,5	F	19	58.4	1.69	0.68	1.68	T-shirt, leggings
31	04	4	4,5	M	50	96.8	1.88	1.00	2.22	T-shirt, jeans
32	04	4	4,5	M	41	92.8	1.78	1.03	2.11	T-shirt, jeans
33	04	5	4,5	F	20	74.9	1.62	0.83	1.84	T-shirt, jeans
34	04	5	6,7	F	23	47.4	1.52	0.61	1.43	LS t-shirt, jeans
35	04	5	6,7	M	28	69.0	1.82	0.78	1.87	T-shirt, jeans
36	04	5	6,7	M	20	99.7	1.82	1.02	2.20	SS shirt, jeans
37	04	5	6,7	M	47	84.1	1.84	0.98	2.06	Shirt, trousers
38	04	5	6,7	F	31	59.3	1.67	0.78	1.68	LS t-shirt, jeans
39	04	5	6,7	F	30	90.0	1.62	1.01	2.01	Tights, skirt, light jumper
40	04	5	6,7	M	24	54.3	1.65	0.74	1.59	T-shirt, jeans
41	04	5	6,7	M	21	66.6	1.82	0.75	1.84	T-shirt, trousers
42	04	5	6,7	F	45	68.9	1.66	0.82	1.79	T-shirt, trousers

Continued on next page

Continued from previous page

SN	D	E	Sp	S	A	M	H	W	SA	Clothes
43	04	5	6,7	M	45	67.7	1.66	0.89	1.76	LS t-shirt, jeans
44	04	5	6,7	F	24	58.6	1.61	0.79	1.63	Shirt, trousers
45	05	6	8,9	M	21	67.6	1.70	0.82	1.78	T-shirt, MTB shorts
46	05	6	8,9	M	55	71.5	1.78	0.91	1.88	Shirt, trousers
47	05	6	8,9	M	31	72.0	1.83	0.87	1.92	T-shirt, jeans
48	05	6	8,9	F	24	78.1	1.67	0.61	1.91	Jeans, jumper
49	05	6	8,9	F	27	54.7	1.55	0.71	1.55	LS t-shirt, jeans
50	05	6	8,9	M	27	88.1	1.79	1.00	2.07	T-shirt, jeans
51	05	6	8,9	M	23	83.1	1.86	0.82	2.06	T-shirt, jeans
52	05	6	8,9	F	26	64.0	1.74	0.74	1.78	LS t-shirt, jeans
53	05	6	8,9	M	26	76.0	1.70	0.86	1.88	Thin ls top, jeans
54	06	7	10,11	M	54	72.7	1.73	0.89	1.86	Shirt, jeans
55	06	7	10,11	M	28	67.2	1.69	0.83	1.77	LS t-shirt, chinos
56	06	7	10,11	F	20	50.6	1.63	0.68	1.54	T-shirt, jeans
57	06	7	10,11	F	28	59.8	1.65	0.73	1.67	LS t-shirt, jeans
58	06	7	10.11	F	26	55.8	1.69	0.72	1.64	T-shirt, jeans
59	06	7	10,11	M	48	94.7	1.83	1.07	2.16	T-shirt, walking trousers
60	06	7	10,11	F	19	56.8	1.71	0.68	1.66	Dress, tights
61	06	7	10,11	F	21	64.2	1.73	0.75	1.77	Dress, tights
62	06	8	12,13	M	19	54.1	1.69	0.69	1.61	T-shirt, jeans
63	06	8	12,13	F	22	93.4	1.70	0.96	2.10	Strappy top, jog pants, leggings
64	06	8	12,13	M	27	73.4	1.81	0.79	1.92	T-shirt, jeans
65	07	9	14	F	48	89.9	1.59	1.11	1.98	T-shirt, cord trousers

Key:

SN: Subject Number

D: Date (all December 2012)

E: Relevant empty chamber measurement

Sp: Relevant sphere measurements

S: Subject sex

A: Subject age in years

M: Subject mass in kilograms

H: Subject height in metres

C_w: Subject waist circumference in metres

SA: Subject surface area in m^2, estimated using the Tikuisis equation [94]

Notes:

All subjects except 30, 38, 39, 42, 60 and 61 also wore socks.

Subject 14 had 6 surgical pins and 2 surgical plates in his back.

Subject 26 had two artificial half-knees.

Subject 39 was wearing a wedding ring.

End of table

4.3.6 Results of the Campaign 2 measurements

Figure 4.6 shows the ACS of a range of the subjects measured, from the lightest to the heaviest. It shows that the ACS behaves as in previous measurements, starting at its highest value at 1 GHz, dropping until a low point at 5-6 GHz (slightly higher for smaller subjects with lower ACS values) and then rising gradually with increasing frequency. There are prominent features above 12.5 GHz. These can also be seen on the spherical phantom measurements taken during that week, but not in other measurements taken at other times. They are therefore not a feature of the human body's true ACS but an artefact of the measurement. This was discovered part-way through the measurement campaign, and left constant for the remainder of the measurements.

The legend on Figure 4.6 shows the masses of the subjects plotted, where it can be seen that their masses are not evenly spaced, and that the spacing in mass does not always correlate with the spacing in ACS, eg. there is a 3.9 kg difference between Subjects 55 and 46, then a nearly identical 3.8 kg difference between Subjects 46 and 10, but certainly in the high frequency regime, the gap in ACS between Subjects 46 and 10 is much larger than that between Subjects 55 and 46. First, Figures 4.7 and 4.8 show plots of ACS vs mass for every subject, at frequency points at 1.1, 3, 5, 7, 9, 11, 13 and 14.9 GHz (the 1.1 and 14.9 points were moved in from 1 and 15 GHz to prevent any problem with the 100 MHz frequency stirring window). They also show least squares fit line for the points at each frequency, plus the coefficient of determination R^2 for the fit to each line.

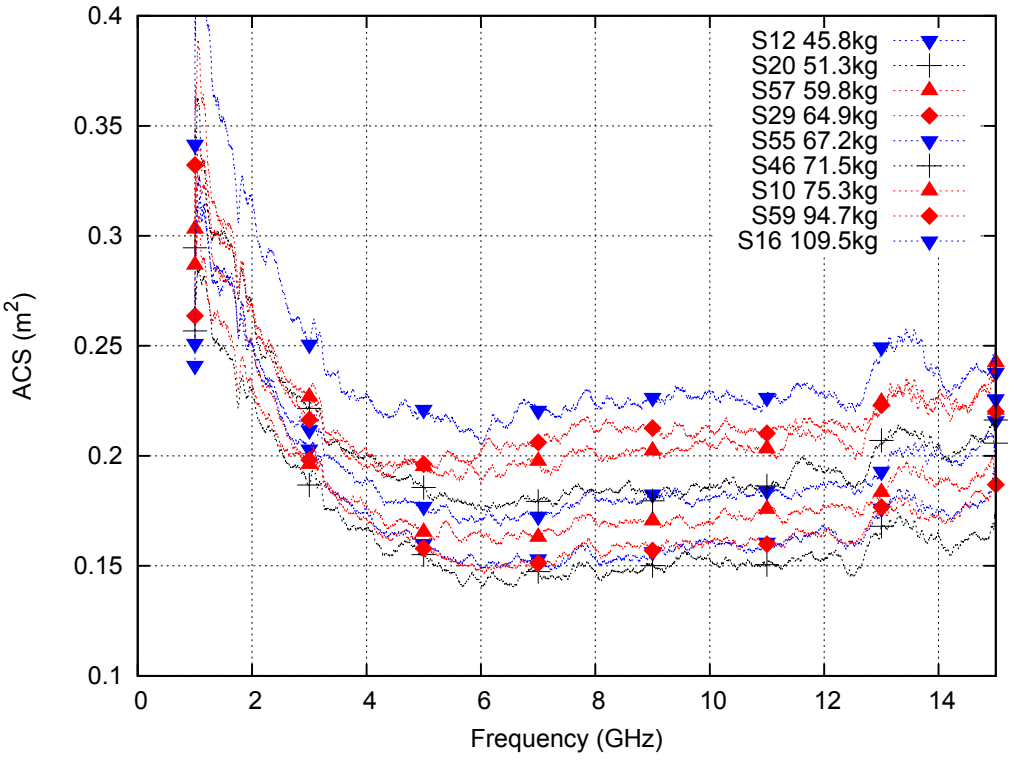

Figure 4.6: ACS vs frequency for a range of subjects

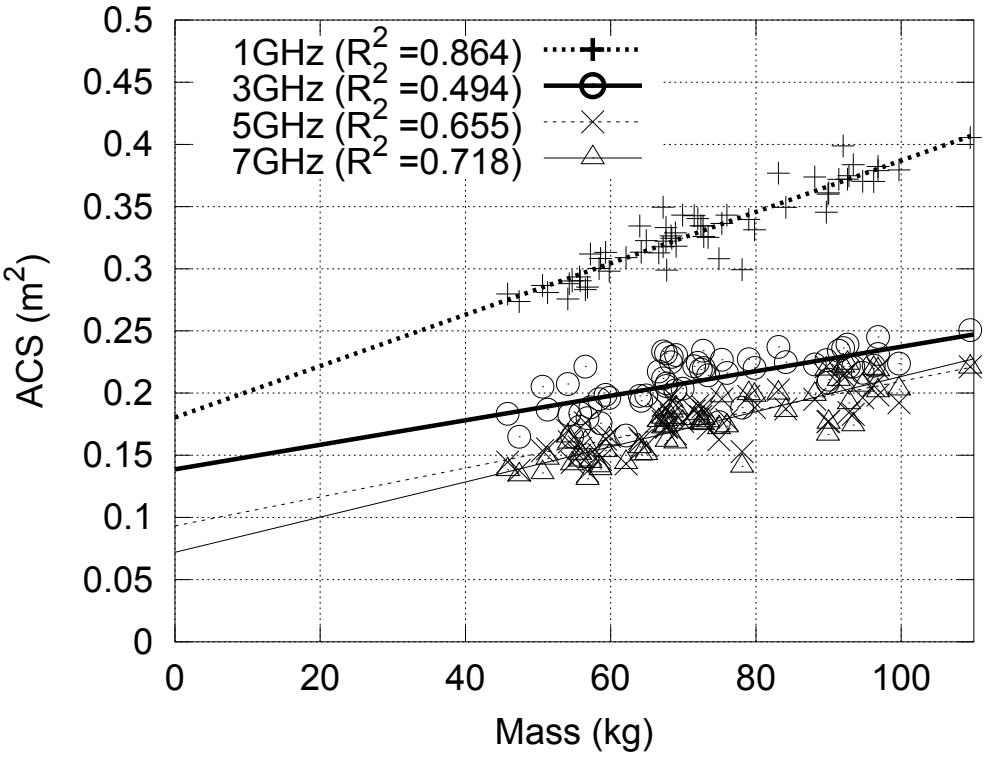

Figure 4.7: ACS vs mass at frequency points 1-7 GHz

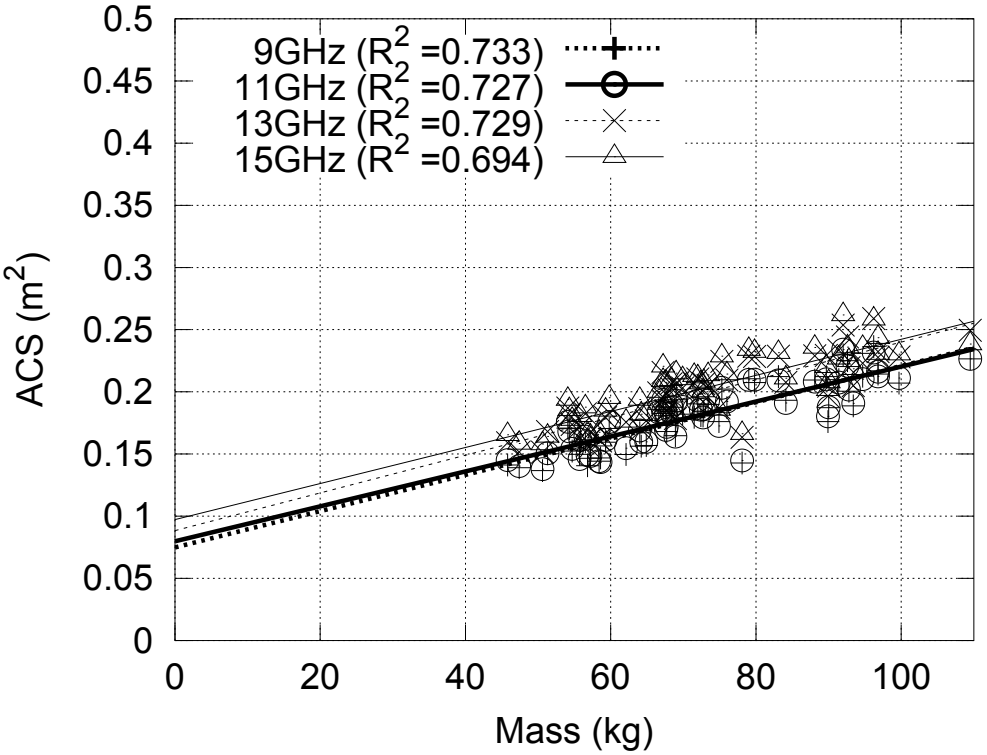

Figure 4.8: ACS vs mass at frequency points 9-15 GHz

4.3.7 Correlation of windowed ACS with biometric data

Figures 4.7 and 4.8 show ACS at point frequencies, plotted against subject mass. As measured ACS is variable over small changes in frequency, averaging ACS over windows around the same frequency points will provide values that are less susceptible to statistical variation. A 100 MHz window was therefore applied to the same data around the same points. The results are shown, plotted against all three measured physical characteristics (mass, height, waist circumference) and the Tikuisis calculation for surface area, in Figures 4.9 to 4.16.

Figures 4.9 to 4.16 again show the frequency response of human ACS: towards the top of the frequency band, the data points become increasingly clumped as ACS changes less with frequency. To determine the goodness of fit of ACS to each biometric parameter, these figures also provide two main metrics: the R^2 coefficient of the data, and the closeness with which the linear fits pass the origin. A fit line should pass through the origin, as otherwise it suggests that a zero-size absorber would give a positive or negative ACS, which is clearly false. The more realistic interpretation is that the property under investigation does not have a first order relationship with ACS, but rather a higher order fit is required. Higher order fits shall be investigated further in Chapter 5, for now we are looking for first order fits. The BSA fit is clearly superior as regards the proximity with which it passes the origin, as above 3 GHz the fits all reach 0m^2 BSA within $\pm 0.02\text{m}^2$ ACS, far closer than is the case for the other parameters: mass and waist circumference are next closest, with ACS within $\pm 0.1m^2$ when the parametric data is zero. The R^2 coefficients show that there is correlation with each parameter, with BSA again providing the best correlation.

These correlations and their significance shall be discussed further in the analysis chapter: Chapter 5. For now, it is sufficient to note that human ACS has been measured for a sample population of size N=60. The results are consistent with the measurements from the previous campaign, and show positive correlations with several parameters of the subjects' bodies.

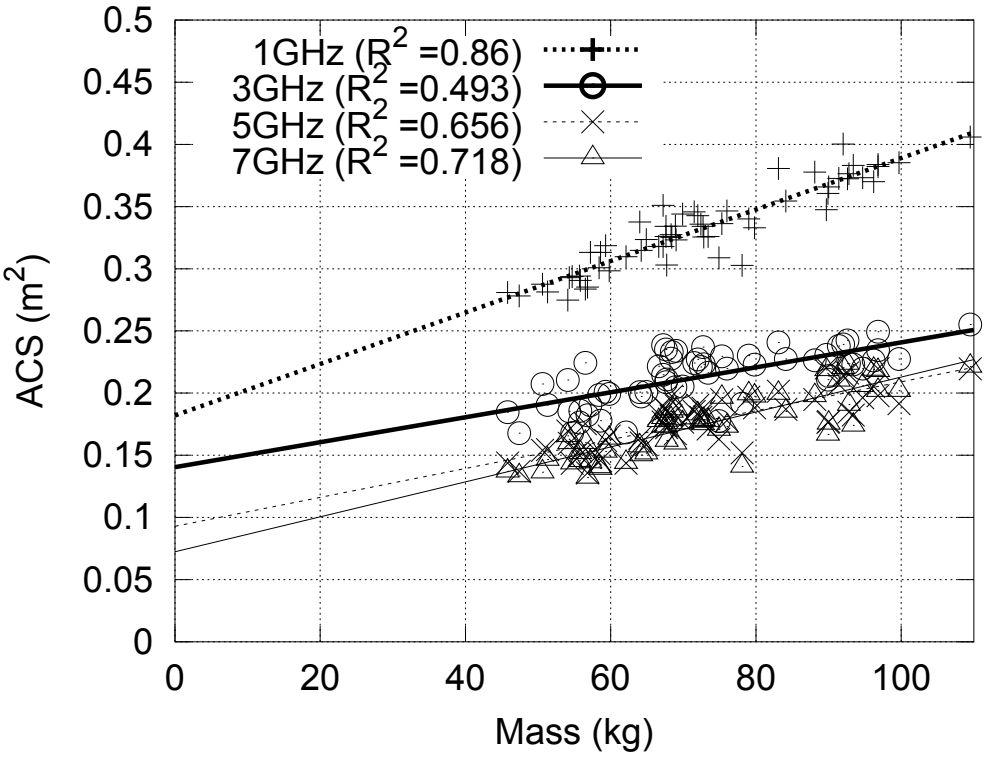

Figure 4.9: ACS vs mass, 100 MHz window at frequency points 1-7 GHz

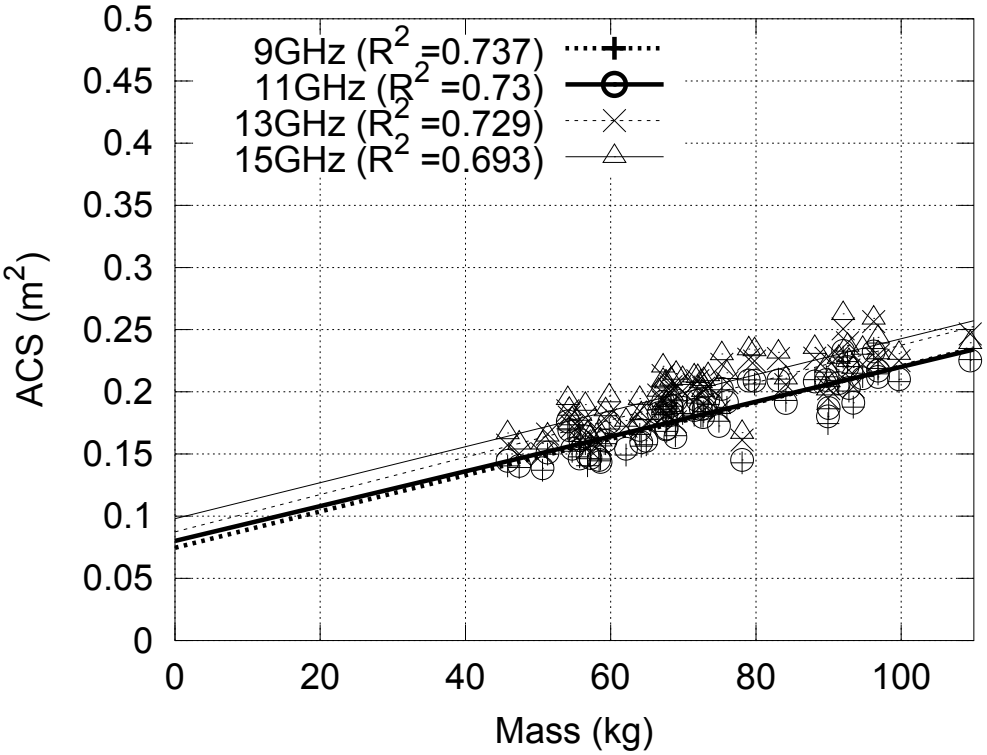

Figure 4.10: ACS vs mass, 100 MHz window at frequency points 9-15 GHz

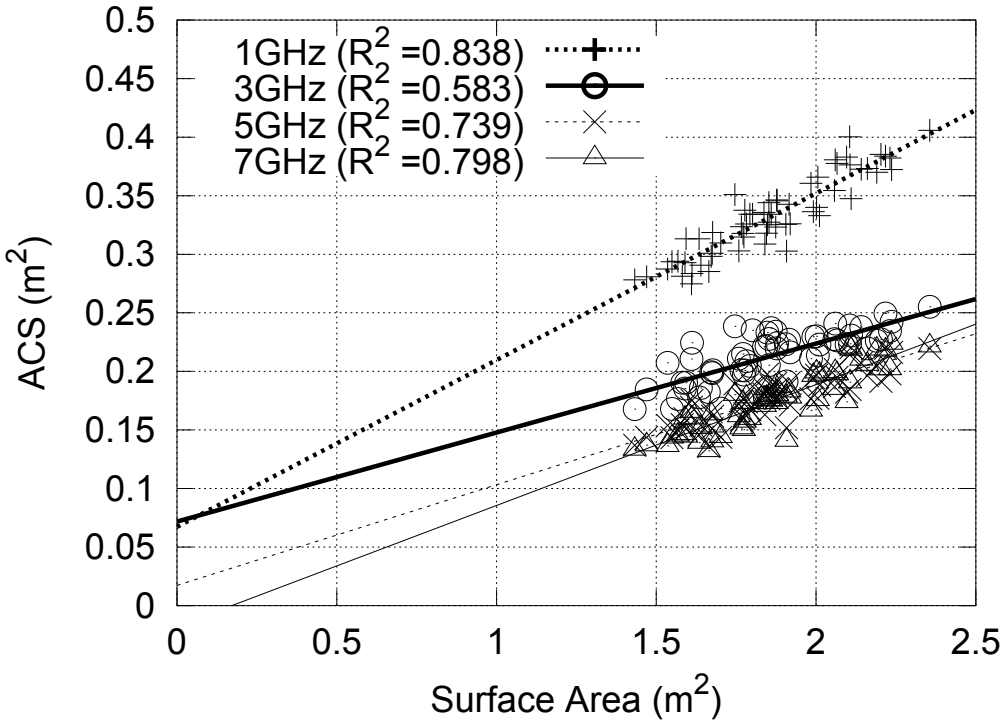

Figure 4.11: ACS vs BSA (Tikuisis), 100 MHz window at frequency points 1-7 GHz

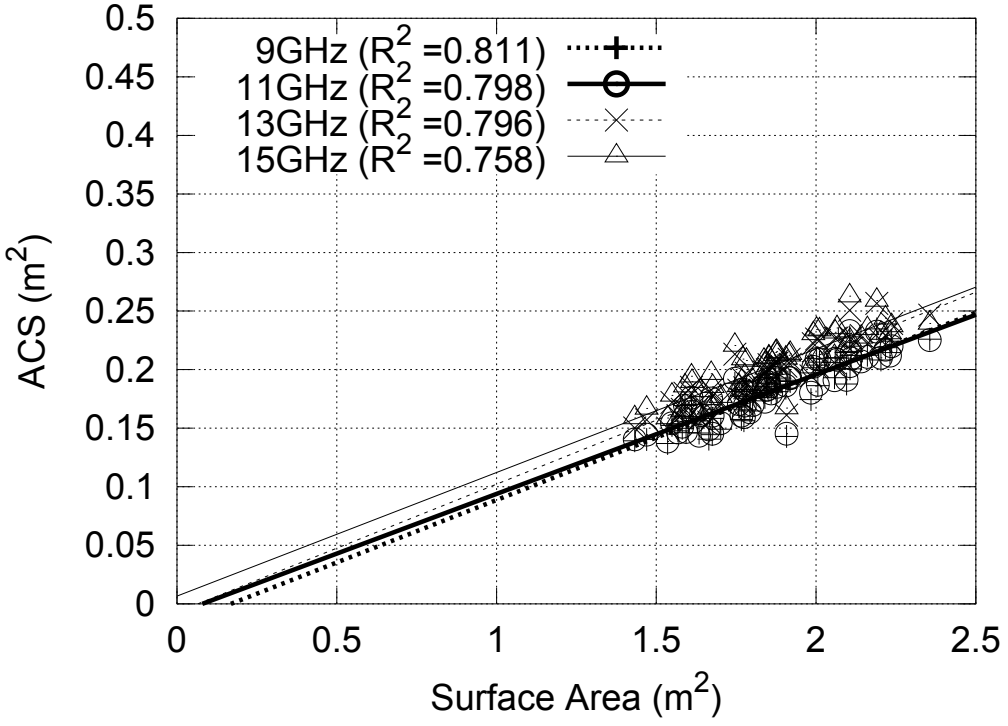

Figure 4.12: ACS vs BSA (Tikuisis), 100 MHz window at frequency points 9-15 GHz

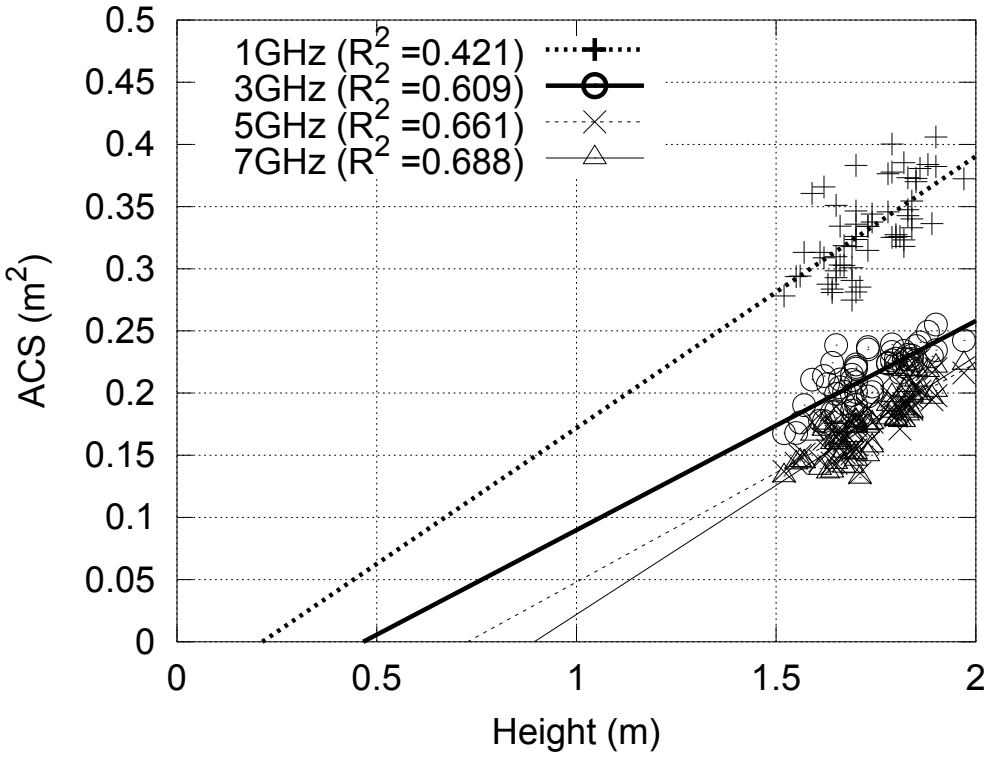

Figure 4.13: ACS vs height, 100 MHz window at frequency points 1-7 GHz

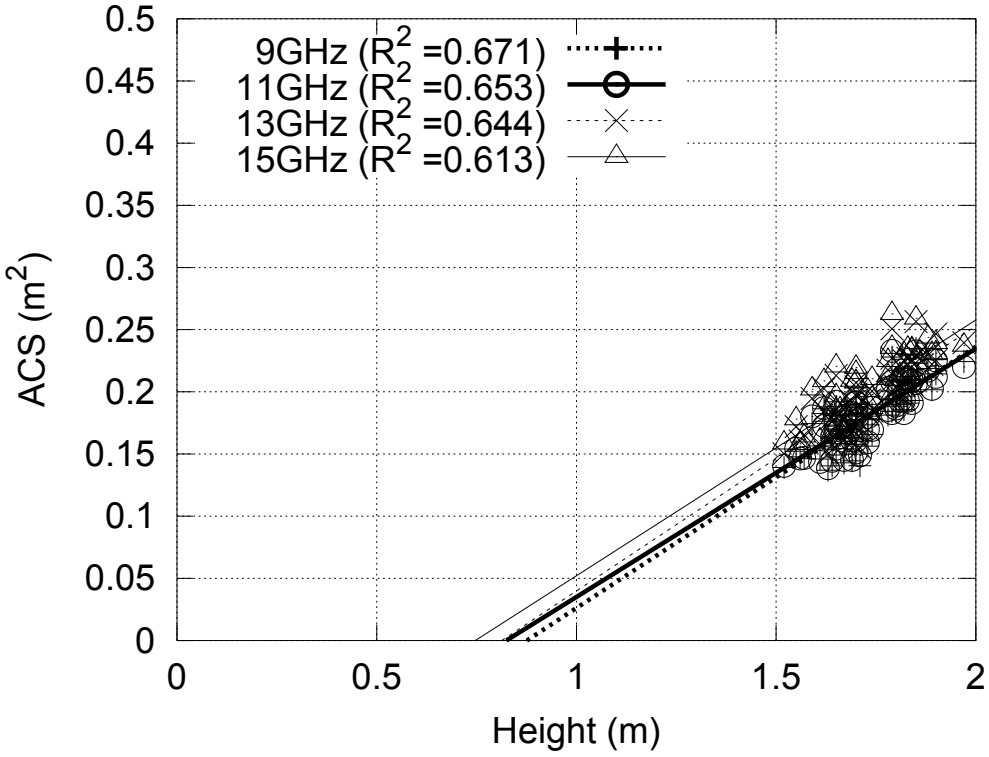

Figure 4.14: ACS vs height, 100 MHz window at frequency points 9-15 GHz

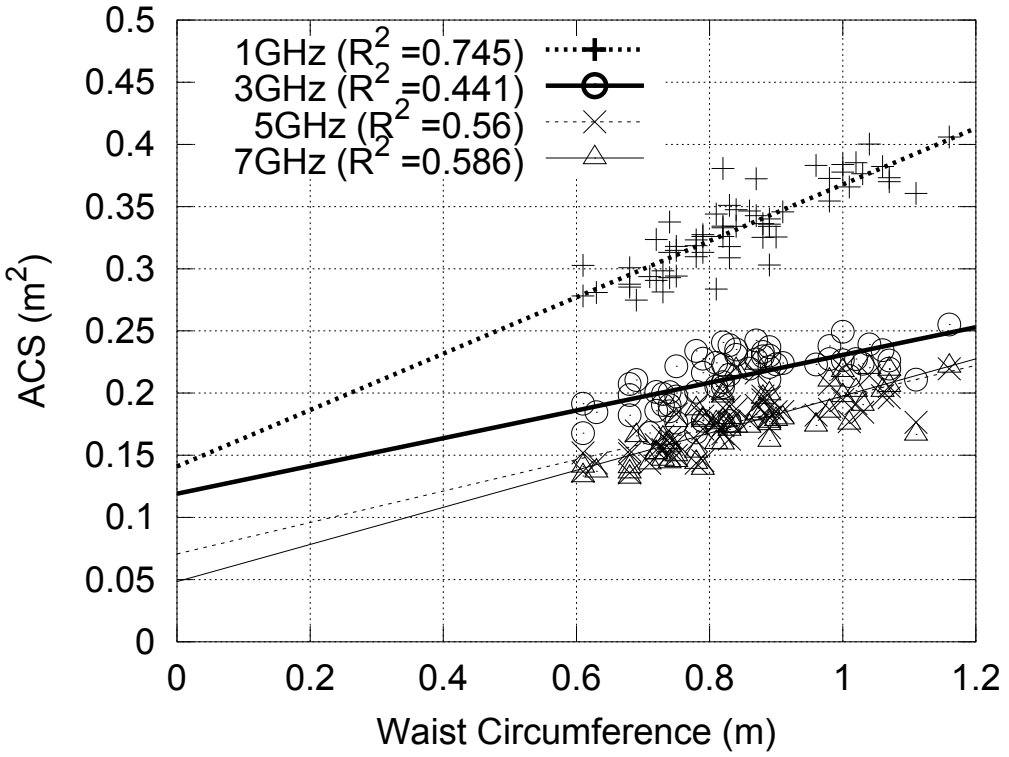

Figure 4.15: ACS vs waist circumference, 100 MHz window at frequency points 1-7 GHz

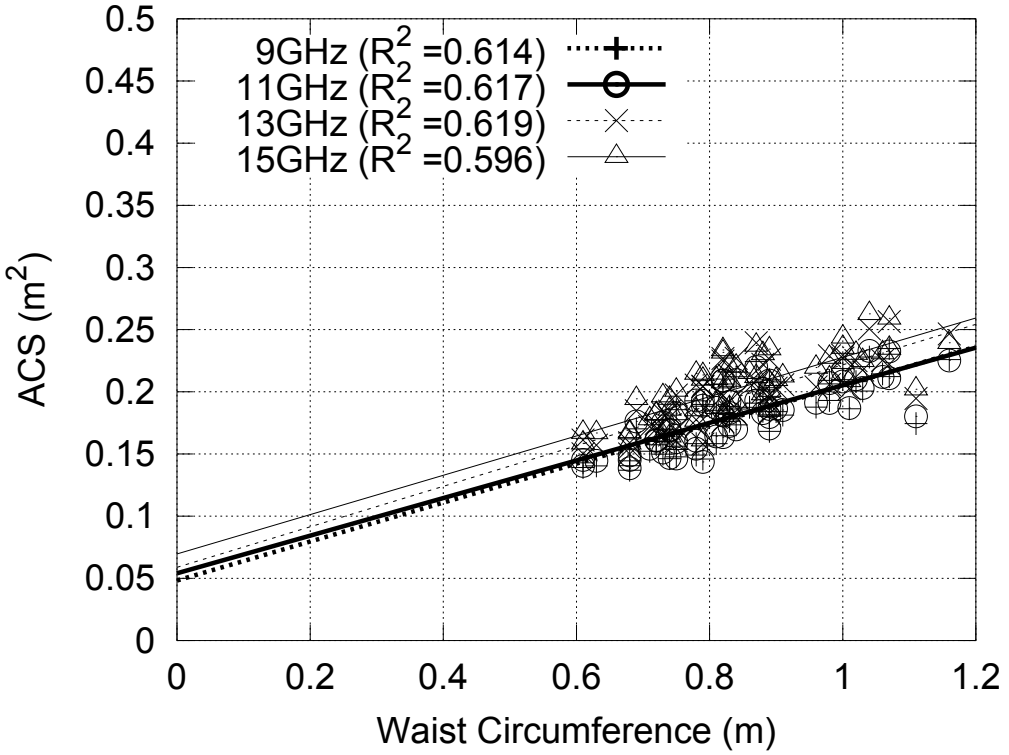

Figure 4.16: ACS vs waist circumference, 100 MHz window at frequency points 9-15 GHz

Chapter 5

Data Analysis

5.1 Overview

In this chapter, the data displayed in Chapter 4 is analysed further, to look for correlations between electromagnetic absorption and the biometric parameters of the body. First, the biometric parameters of the experimental sample are compared to the English population statistics, to check the representativeness of the sample, and also with each other, to establish the extent of each parameter's independence. The determination coefficients for the correlations between ACS and mass, BSA, height and waist circumference are then plotted in the frequency domain, allowing the relative goodness of fit of the parameters to be compared across the spectrum.

It is established that BSA has the strongest correlation with ACS across most of the measured frequency range. BSA is then normalised out, to give average absorption efficiency $\langle Q_a \rangle$. This is plotted against the four previously measured biometric parameters, plus computed values for body mass index (BMI), average subcutaneous fat thickness (D_{SF}), and total body water as a percentage of mass (%TBW). Analysis of these results finds small yet significant correlations to several of these parameters, as will be discussed.

Finally, the ACS model of the human body is applied to a power balance model of an airliner's passenger cabin, to calculate the effect of a full complement of passengers on the cabin's Q-factor. This shows how the data gathered by this research program can be applied to model the effects of human occupants on a modern EMC-critical situation.

5.2 Population Analysis

5.2.1 Campaign 1 sample

The experimental sample group which had their ACS measured comprised nine adult volunteers, six male and three female, drawn from friends and colleagues of the experimenter. In order to provide the average passenger ACS in this calculation, six were selected and their ACS was averaged. These were subjects 1, 2, 3, 5, 6 and 8 - three male and three female. The average ACS of the sample is reproduced in Figure 5.1, while the sample's biometric parameters are shown in Table 5.1, where they are compared to data from the 2003 NHS health survey for England [104], which gives the following data for the English population:

All of the parameters are less than 1.96 standard deviations of the population mean (i.e. the level for 95 % confidence), hence the experimental sample population can be considered to be a random sample taken from the English population as a whole. However, a sample size of nine subjects is not large enough to give this experiment statistical power, as any one outlier (e.g. Subject 6, mass 38.1 kg) can have a large effect on the values of μ and σ. The C1 results may be used for indicative purposes, and used to inform the development of the C2 measurement.

5.2.2 Campaign 2 sample

The sample population for the second measurement campaign was formed of adult volunteers, drawn from friends, associates and colleagues of the experimenter, and from advertisement around the university's physics and electronics departments. The means, standard deviations and standard errors of the means of the physical parameters of the sample are shown in Table 4.4, and are compared to the English population values in Table 5.2. The population values are taken from the 2003 Health Survey for England [104], which took measurements of 11,408 adults (age 16+) during nurse visits to private households (i.e. not institutions). Households were

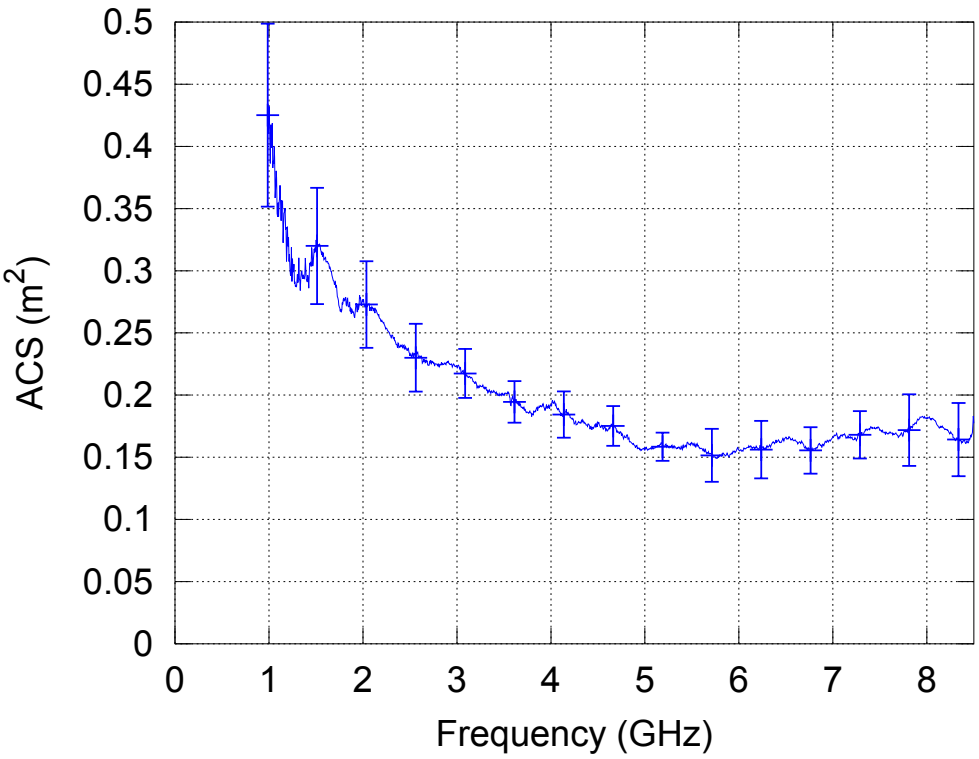

Figure 5.1: Mean 1σ variation in ACS of a representative subset of the C1 sample population (Subjects 1,2,3,5,6,8)

randomly selected from postcode data, and the demographic of the co-operating households was judged to be sufficiently close to that of the general population that response weighting was not necessary.

The experimental subjects are on average 3.5 kg lighter and 5 cm taller than the English population. The men are 4.1 kg lighter than the national mean, which is 1.8 standard errors of the sample mean, while the women are 5.8 kg lighter, which is 2.2 standard errors of the sample mean. The women in the experimental sample are 4.0 cm taller than the English mean, which is 2.9 standard errors of the sample mean, while the women are 3.5 cm taller, or 2.7 standard errors of the sample mean. The mass and height distributions of the experimental population can be seen in Figure 5.2. Modelling the sample as being normally distributed, the population means all fall within 1.96 standard deviations of the sample mean, so regarding the measured characteristics, the C2 sample can also be considered to be a random sample of 60 people taken from the English population without bias.

The subjects' various biometric parameters may also be compared to each other. Figures 5.3 and 5.4 show the correlation of the measured parameters, plus the Tikuisis calculation of BSA [94], with Table 5.3 showing the R^2 values.

This shows that mass and surface area are highly correlated. A line through these points would not pass through the origin, but the points could fit a curve, which would make sense if mass is proportional to volume and thus to the 3/2rd power of BSA, as is the case for the volume of a sphere. Conversely, height is poorly correlated to mass and particularly to waist circumference, two properties which are themselves well correlated.

Table 5.1: Biometric parameters of C1 subjects vs English adult population (n/s = not stated in the literature)

	Age	Mass (kg)	Height (m)
Subject mean	28.5	68.5	1.74
Subject SD	10.1	22.8	0.13
Subject male mean	32.0	78.7	1.84
Subject male SD	14.0	21.0	0.05
Subject female mean	25.0	58.3	1.64
Subject female SD	4.58	23.5	0.09
England male mean	n/s	82.6	1.75
England male SD	n/s	17.2	0.086
England female mean	n/s	69.6	1.61
England female SD	n/s	17.1	0.0789

Table 5.2: Biometric parameters of C2 subjects vs English adult population (n/s = not stated in the literature)

	Age	Mass (kg)	Height (m)	Waist (m)	BSA (m^2)	BMI (kg/m^2)
Subject mean	32	72.64	1.73	0.84	1.86	24.0
Subject SD	12	15.24	0.10	0.13	0.22	3.89
Subject mean (M)	34	78.53	1.79	0.90	1.96	24.4
Subject SD (M)	14	13.76	0.08	0.11	0.19	3.07
Subject SE (M)	n/s	2.294	0.014	0.018	n/s	
Subject mean (F)	28	63.82	1.65	0.77	1.72	23.5
Subject SD (F)	8.8	13.12	0.01	0.12	0.17	4.91
Subject SE (F)	n/s	2.678	0.013	0.024	n/s	
England mean (M)	n/s	82.6	1.75	0.965	n/s	26.9
England SD (M)		17.2	0.086	n/s	n/s	5.41
England SE (M)		0.22	0.0011	0.0022	n/s	0.07
England mean (F)	n/s	69.6	1.61	0.864	n/s	26.7
England SD (F)	n/s	17.1	0.078	n/s	n/s	5.89
England SE (F)	n/s	0.209	0.0009	0.0021	n/s	0.07

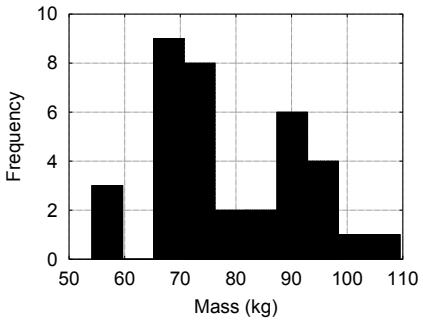

(a) Histogram to show mass distribution of the male experimental population (n=36)

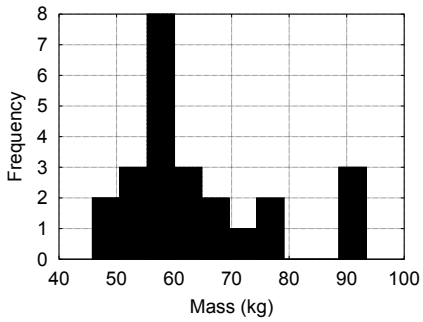

(b) Histogram to show mass distribution of the female experimental population (n=24)

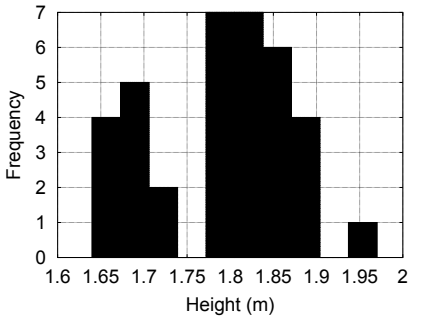

(c) Histogram to show height distribution of the male experimental population (n=36)

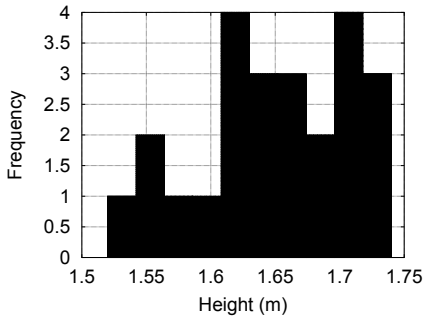

(d) Histogram to show height distribution of the female experimental population (n=24)

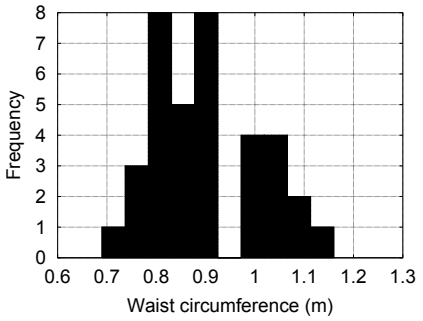

(e) Histogram to show waist circ. distribution of the male experimental population (n=36)

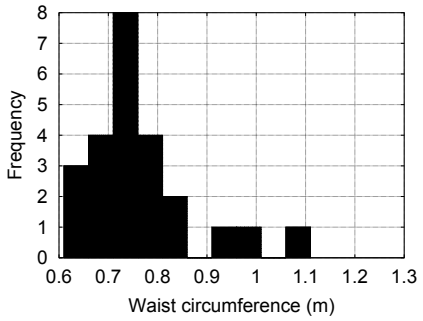

(f) Histogram to show waist circ. distribution of the female experimental population (n=24)

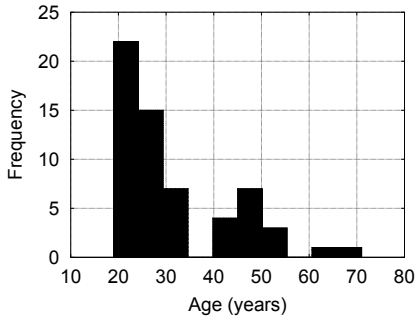

(g) Histogram to show age distribution of the experimental population (n=60)

Figure 5.2: Histograms to show the distribution of physical parameters in the experimental population (N=60)

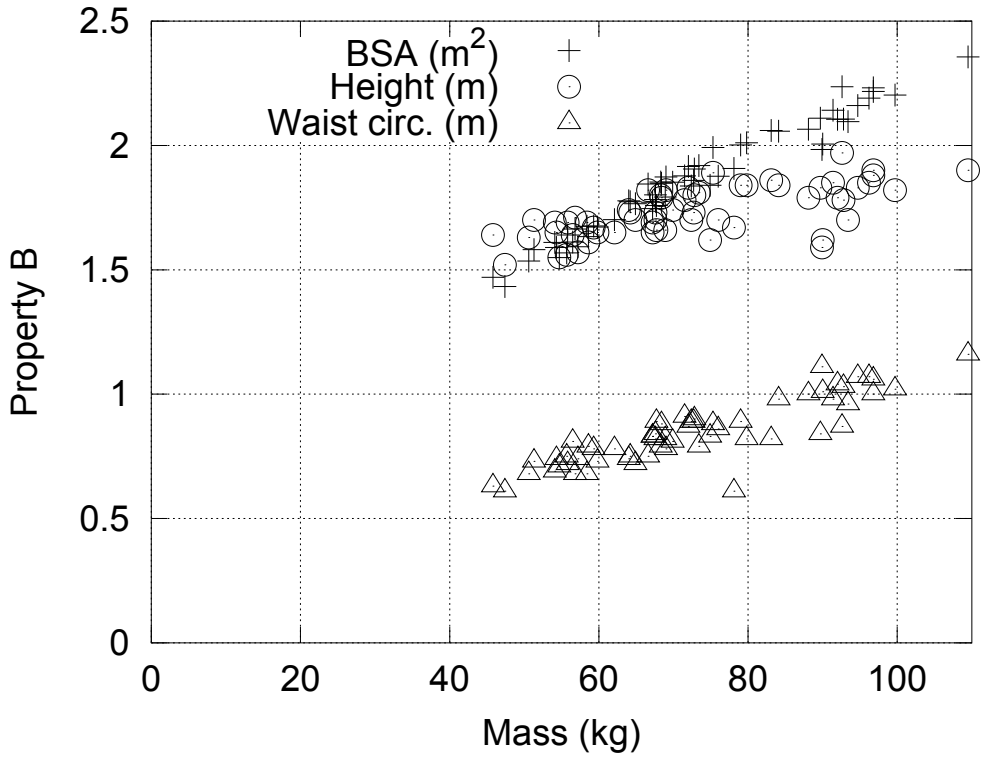

Figure 5.3: Mass vs other biometric parameters of experimental subjects

Table 5.3: Determination Coefficients of subject biometric parameters to each other

R^2	Mass	SA(D)	Height	Waist
Mass	1	0.93	0.45	0.87
SA(D)		1	0.71	0.66
Height			1	0.27
Waist				1

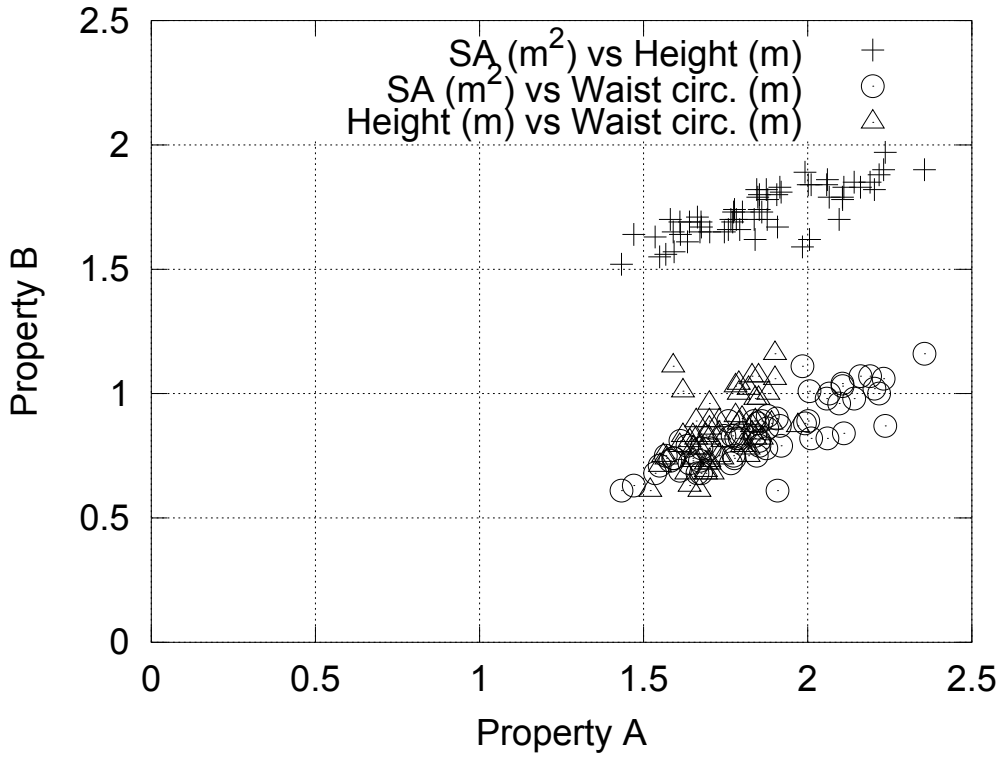

Figure 5.4: Comparison of biometric parameters of experimental subjects

5.3 Comparison of measured ACS to literature values

The ACS values measured in Campaign 1 are slightly low compared to the available literature values. To recap from Section 1.4.3, Table 5.4 gives these values.

Table 5.4: Literature values for ACS of the human body

Authors	f (GHz)	Method	Subject	ACS (m^2)
Andersen et al. [48]	3 – 8	Exp.	Several	0.33
Bamba et al. [49]	2.4 & 3.0	Exp.	Several avg 70 kg 175 cm	0.34 & 0.36
Harima [45]	1 – 4	Exp.	70.6 kg male	0.33 – 0.11
Hirata et al. [50]	2	FDTD sim.	Japanese adult & child	0.4 – 0.5
Hurst & Ellingson [47]	2.1	Not stated	Unknown	0.4
Robinson et al. [46]	0.91	TLM sim.	thin boundary models	0.25
Uusitupa et al. [40]	0.9 – 5	Sim.	VF Male (72.2 kg)	0.4 – 0.25
Findlay & Dimbylow [39]	1 – 2	FDTD sim.	NORMAN (73.0 kg)	0.35 – 0.3
Kientega *et al.* [42]	2.4	FDTD sim.	Thelonius (1.17m, 19 kg)	0.06 – 0.14

Our subjects' ACS values range from 0.3 – 0.44 m^2 at 1 GHz, 0.18 – 0.28 m^2 at 3 GHz, 0.16 – 0.25 m^2 at 5 GHz and 0.15 – 0.25 m^2 from 7 GHz – 11 GHz. At 13 GHz and 15 GHz some ACS values of up to 0.29 m^2 are recorded, but these results cannot be treated with the same level of confidence: see the discussion in Section 4.3.6. These give a wider range of values than are found in the literature, which is a logical reflection of the wider range of subject physiologies examined in our experiments than in the studies cited. The high values of ACS measured at 1 GHz may be the tail end of the whole-body's resonance at sub-GHz frequencies [17]. It would have been interesting to investigate below 1 GHz to attempt to detect this peak; unfortunately this was prevented by equipment limitations. The slight rise in ACS from around 5 GHz upwards might be due to the body tissues' dielectric constants falling with increasing frequency [20].

Figure 5.5 shows a direct comparison of Subject 59 in Campaign 2, mass 73.4 kg, alongside Uusitupa's FDTD simulations of the VF Male phantom, mass 72.2 kg, re-weighted to compensate for the lack of a simulation using a wave incident from the head down in Uusitupa's original study [105]. The measured ACS is within the range of ACS values calculated by Uusitupa, and the re-weighted mean ACS is very close in value to the measured result. The averaged ACS from Uusitupa's simulations do not display such a large resonant peak below 1 GHz as might be inferred from the rise in the measured ACS at low frequency; this is however speculation and since the antennas are not specified below 1 GHz, it cannot be easily investigated.

5.4 Variation of ACS with Biometric Parameters

Figure 5.6 shows the goodness of fit to the measured ACS values of the first order regressions for each physical parameter, plotted at each 300 MHz frequency step from 1.1-14.9 GHz, using the coefficient of determination R^2 as a metric (values are taken at 1.1-14.9 GHz rather than 1.0-15.0 GHz because of the 100 MHz frequency averaging window, which requires 50 MHz of data both above and below the nominal sampling point). This is not the only metric when searching for a linear correlation: it has previously been noted that an important property when investigating for a directly proportional relationship is the proximity with which the line of fit passes the origin. It has also been noted that BSA is the property which performs best by this metric, as shown in Figures 4.9 – 4.16. Notwithstanding this, R^2 is an important property when investigating linear correlations.

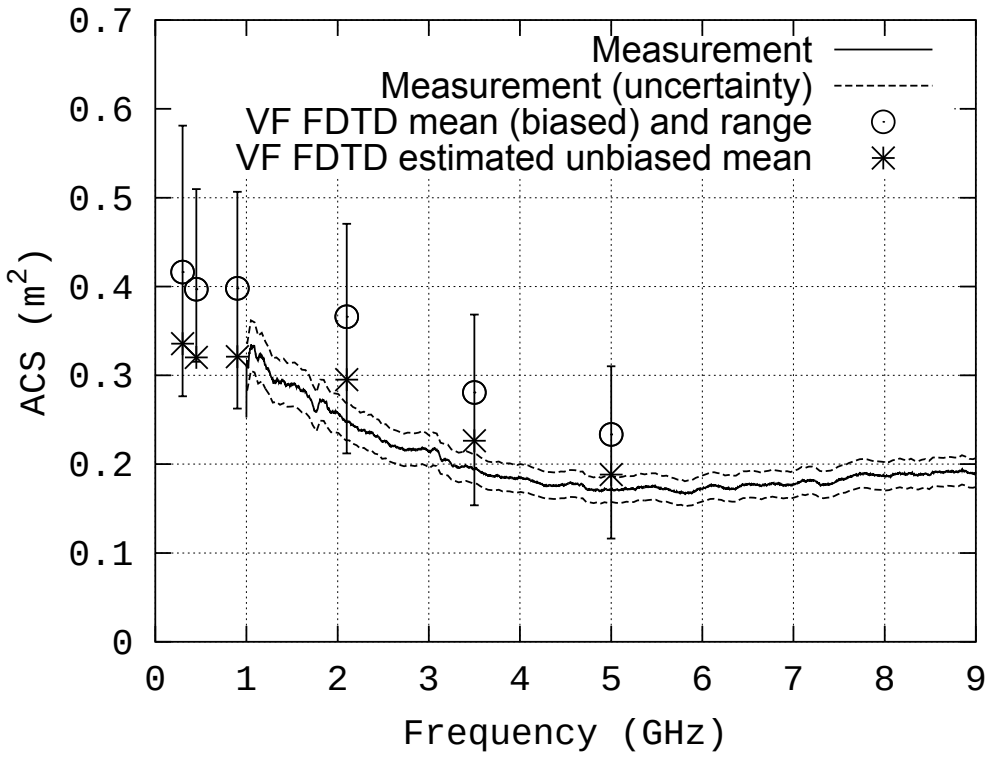

Figure 5.5: C2 measurement of Subject 59 (73.4 kg) ACS vs mean and range of Uusitupa simulations of the 72.2 kg VF Male phantom

Figure 5.6 also shows the effect of averaging ACS across a 100 MHz frequency window about each point: solid lines show ACS at point frequencies, dashed lines show windowed ACS. While R^2 is slightly higher for some of the windowed fits, this is not a large improvement.

Figure 5.7 compares the R^2 values of the linear regression ACS fits to 2nd order polynomial fits to the same (windowed) data. As can be seen, the waist fit is the only one that is improved noticeably by using a 2nd order fit. Figure 5.8 then does the same with a 3rd order fit - here, R^2 increases slightly for the height and waist fits, but not for the mass or surface area fits. This should not be surprising: waist circumference and height are linear dimensions, which are related to the surface area and the volume (and hence mass, assuming constant density) of three-dimensional solids, respectively by square and cubic powers. As ACS appears so far to be most closely proportional to surface area and then to mass, it makes sense that the waist and height fits can be improved by raising them to these powers. Since m and BSA display the best correlations to ACS, and since these are not substantially improved by the use of higher order fits, first order fits shall continue to be used for the rest of this study.

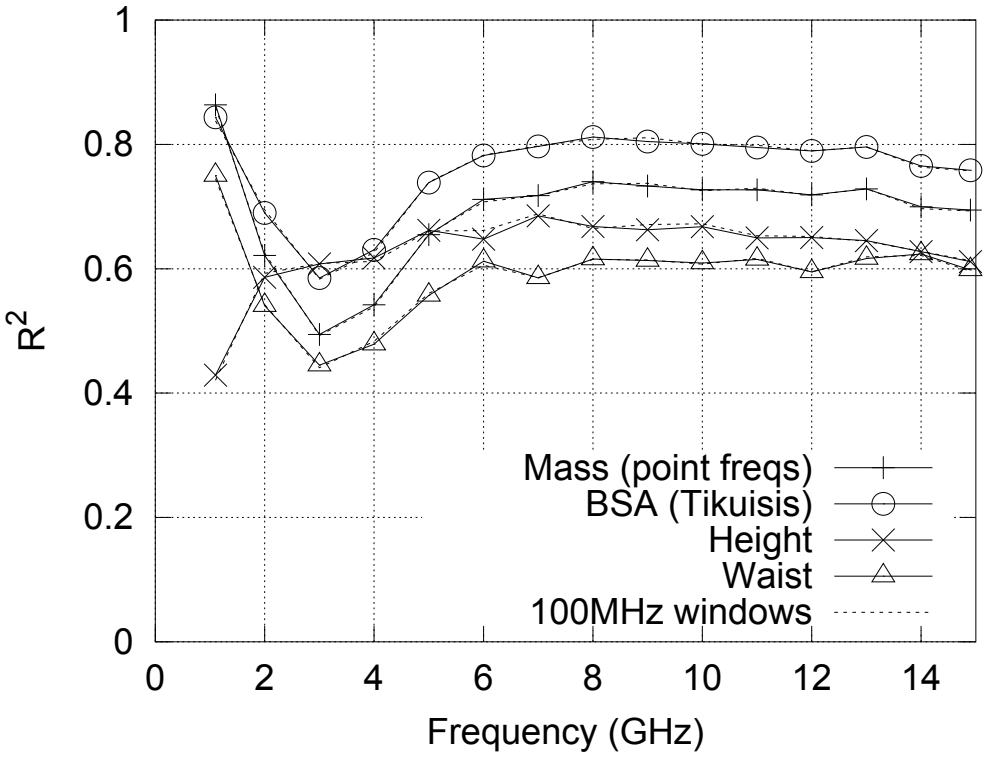

Figure 5.6: R^2 of 1st order ACS fits to biometric parameters, 1.1-14.9 GHz

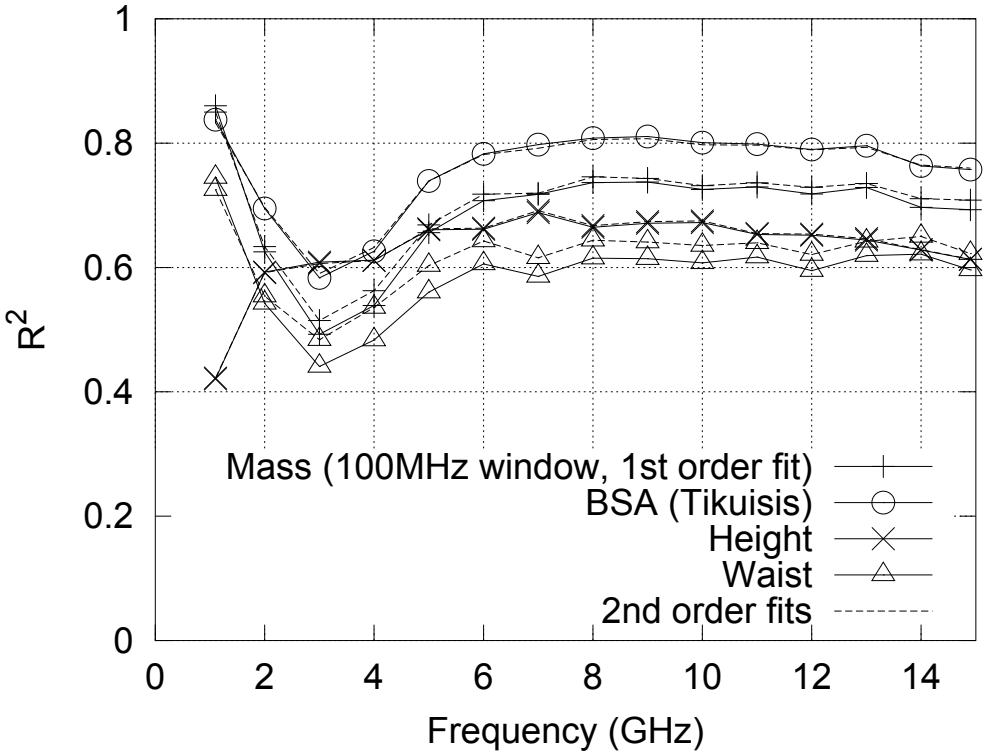

Figure 5.7: R^2 of ACS to biometric parameters: 1st vs 2nd order polynomials

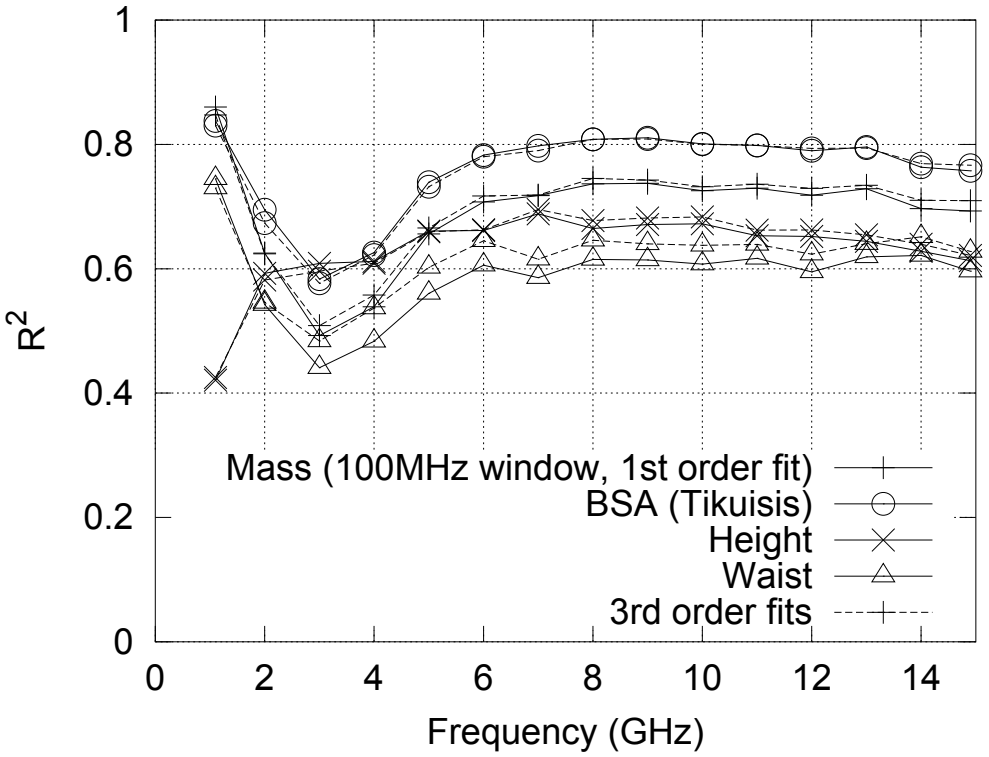

Figure 5.8: R^2 of ACS to biometric parameters: 1st vs 3rd order polynomials

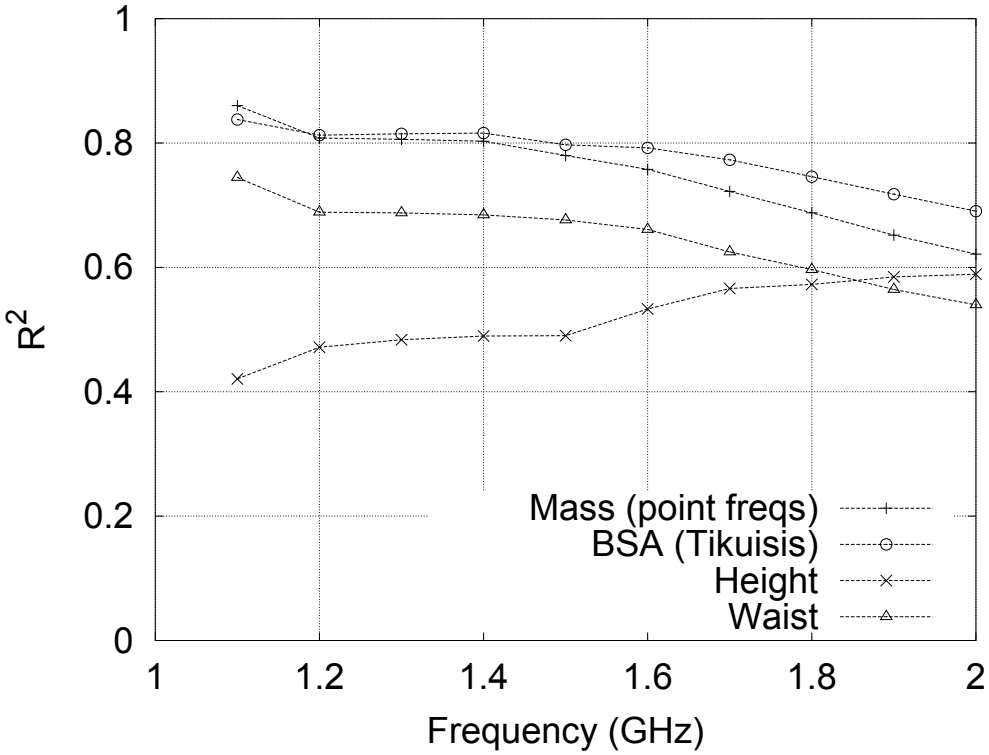

Figure 5.9: R^2 of ACS to biometric parameters: 1.1-2.0 GHz, 1st order polynomials

f (GHz)	1.1	1.2	1.3	1.4	1.5	1.6	1.7	1.8	1.9	2.0
R^2 (BSA fit)	0.84	0.81	0.82	0.81	0.80	0.79	0.77	0.74	0.72	0.69
R^2 (Mass fit)	0.86	0.80	0.81	0.80	0.78	0.76	0.72	0.69	0.66	0.62
R^2(M)$-R^2(BSA)$	0.02	0.01	-0.01	-0.02	-0.02	-0.04	-0.05	-0.06	-0.07	-0.07

Table 5.5: R^2 for 1st order fits to mass and BSA (Tikuisis) 1.1-2 GHz

Figures 5.6 - 5.8 show that over nearly all of the frequency range, surface area is the best predictor of ACS. Above 4 GHz it is so by a large margin: at 5 GHz, R^2= 0.74 for the first order surface area fit while the next best fit, mass, has R^2= 0.65. Below this frequency, none of the single parameters provide such good predictions of ACS, and the order is more mixed. At the very low end of the frequency range, mass is the best predictor of ACS, although by a very small, probably insignificant margin. Figure 5.9 zooms in on this end of the spectrum, plotting windowed ACS at 100 MHz intervals from 1.1-2.0 GHz. The values for surface area and mass are also shown in Table 5.5. This shows that mass and BSA correlate almost equally closely with ACS up to roughly 1.5 GHz, after which the coefficients diverge, BSA providing the higher R^2.

5.5 Absorption Efficiency

To recap from Section 2.1.3, absorption efficiency is defined by Equation 5.1 where $\langle Q_a \rangle$ is absorption efficiency, σ_a is ACS and G_s is the silhouette area of the absorbing object in the plane normal to the incident wave. In a reverberant environment, where waves are incident equally from all directions, it is necessary to use the average cross-sectional area of an absorber. For convex solids, this is equal to 1/4 of the surface area (i.e. Equation 5.2). A human body is not a simple convex solid, but with legs together this is hopefully a sufficiently close approximation to use. $\langle Q_a \rangle$ is therefore calculated here using Equation 5.3.

$$\langle Q_a \rangle = \frac{\langle \sigma_a \rangle}{G_s} \tag{5.1}$$

$$G_s = \frac{BSA}{4} \tag{5.2}$$

$$\langle Q_a \rangle = \frac{\langle \sigma_a \rangle}{G_s} = \frac{4 \cdot \langle \sigma_a \rangle}{BSA} \tag{5.3}$$

Previous plots (e.g. Figure 5.7) have shown that BSA is a good predictor of ACS at most frequencies in our range. Plotting in terms of $\langle Q_a \rangle$ normalises for the surface area of experimental subjects, so if BSA and ACS were directly proportional, a plot of $\langle Q_a \rangle$ vs ACS at any one frequency would show flat lines with no correlation whatsoever. It would then be possible to plot $\langle Q_a \rangle$ against other biometric parameters, to examine the residual correlations with these characteristics once BSA had been normalised out.

In order to check for residual correlations on nearly-flat trends, it will be necessary to calculate the confidence interval of the correlation coefficient R, which will show whether or not a correlation is significant. The standard error of R is denoted S_p and is given by Equation 5.4, where N is the total sample size. S_p gives the range into which will fall 68 % of correlation coefficients calculated from representative samples of a normally-distributed population with correlation coefficient R_t. As with standard deviation, 1.96 standard errors will enclose 95 % of

the sample correlations, so it can be stated with 95 % confidence (i.e. statistical significance) that the true correlation coefficent $R_t = R \pm 1.96S_p$. If $-1.96S_p \leq R \leq 1.96S_p$, i.e. if the 95 % confidence band of R includes the value 0, there is no significant correlation between the two properties.

$$S_p = \frac{1}{\sqrt{\mathrm{N}-1}} \tag{5.4}$$

Figure 5.10 shows the relation between estimated $\langle Q_a \rangle$ and estimated BSA for all experimental subjects. This tests the accuracy of the ACS measurement, the calculation of BSA using Tikuisis *et al.*'s formula and the calculation of G in Equation 2.14: if the estimates are perfect, a plot of $\langle Q_a \rangle$ vs BSA will vary with ACS at each frequency but will remain constant (i.e. show no correlation) for all subjects at any one frequency. The correlation coefficient R is therefore listed, including its 95 % confidence band.

Figure 5.10 shows that $\langle Q_a \rangle$ does indeed decrease (like ACS) from 1.1 – 5 GHz, where it levels out and increases slightly towards the top end of the spectrum. It also shows a significant correlation – a slight decrease of $\langle Q_a \rangle$ with increasing BSA – at 1.1 GHz and 3 GHz, whereas at all higher frequencies, there is no significant correlation. The purpose of calculating Q_a was to normalise out the effects of BSA, so this correlation of Q_a with BSA at low frequency suggests that the approximations used to calculate BSA and/or $\langle Q_a \rangle$ are imperfect and hence some effects of BSA remain (this is certainly true for BSA, especially at low frequency: see Figure 4.11), and/or people with a larger surface area really do absorb less energy per unit of surface area around 1-3 GHz.

Figure 5.11 shows the absorption efficiency of each subject, plotted against frequency. It has 60 lines, one for each subject. The lines are most clustered in the middle of the group, and less dense at either side, with a longer tail at lower values, as shown in the accompanying histogram in Figure 5.12. There is then the one significant outlier, which is Subject 56. S56 was measured on December 6th at 10am, during the session that used the empty measurement 7 and the spherical phantom measurements 10 and 11. She was female, 20 years old, 1.63 m tall and weighed 50.6 kg, with a waist circumference 0.68 m and a BMI of 19.04 kg/m^2. She wore a cotton t-shirt, jeans and socks. Other subjects were measured before and after her on the morning of December 6th, none of which show anomalous results on this plot, so the measurement is not likely to be at fault here. The recorded details of her physique do not explain this result: her BMI is low but it is not the lowest recorded: Subjects 12, 20 and 62 have BMIs of 17.03, 17.75 and 18.94 kg/m^2. One possible explanation is that several of the experimental subjects were recruited from the university's cycling club: were the subject one of these, she might be expected to have an abnormally low level of body fat, which might cause the change in $\langle Q_a \rangle$ seen here. As the data is anonymised, there is no way of telling whether this is the case, so this outlier remains unexplained.

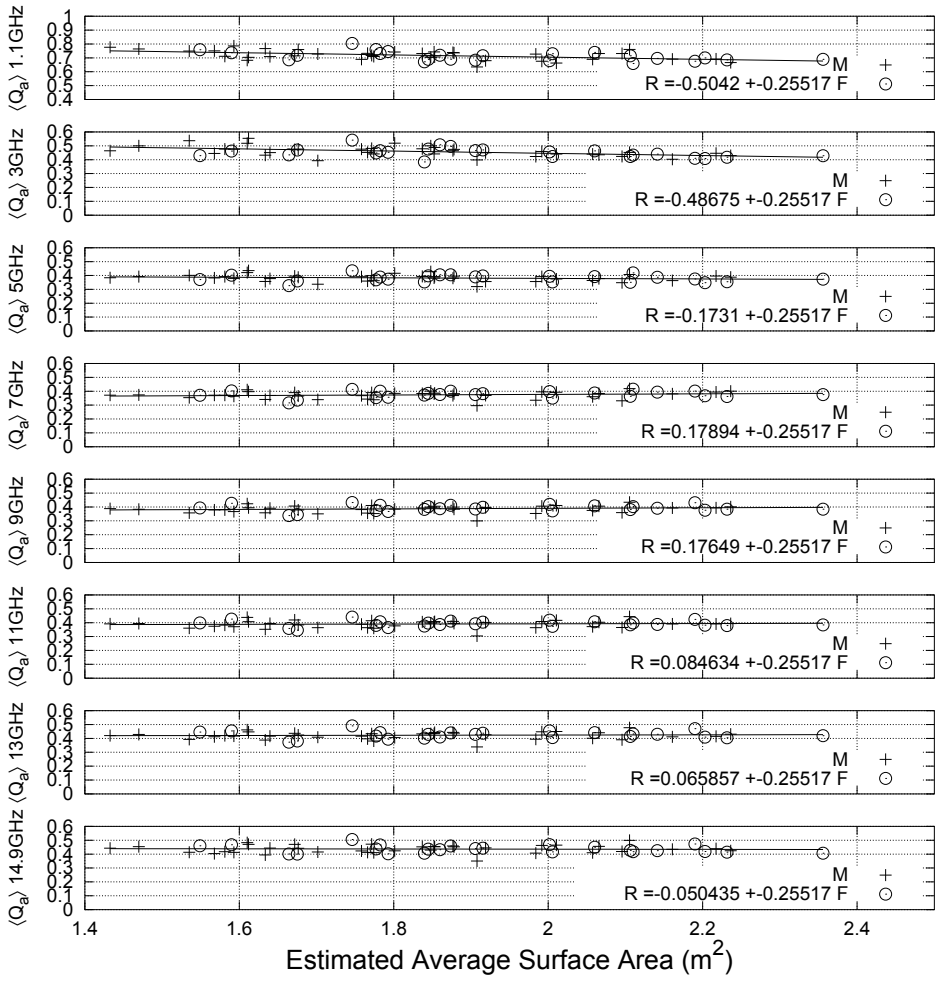

Figure 5.10: $\langle Q_a \rangle$ of human subjects, calculated using ACS averaged over 100 MHz windows, 1.1 - 14.9 GHz

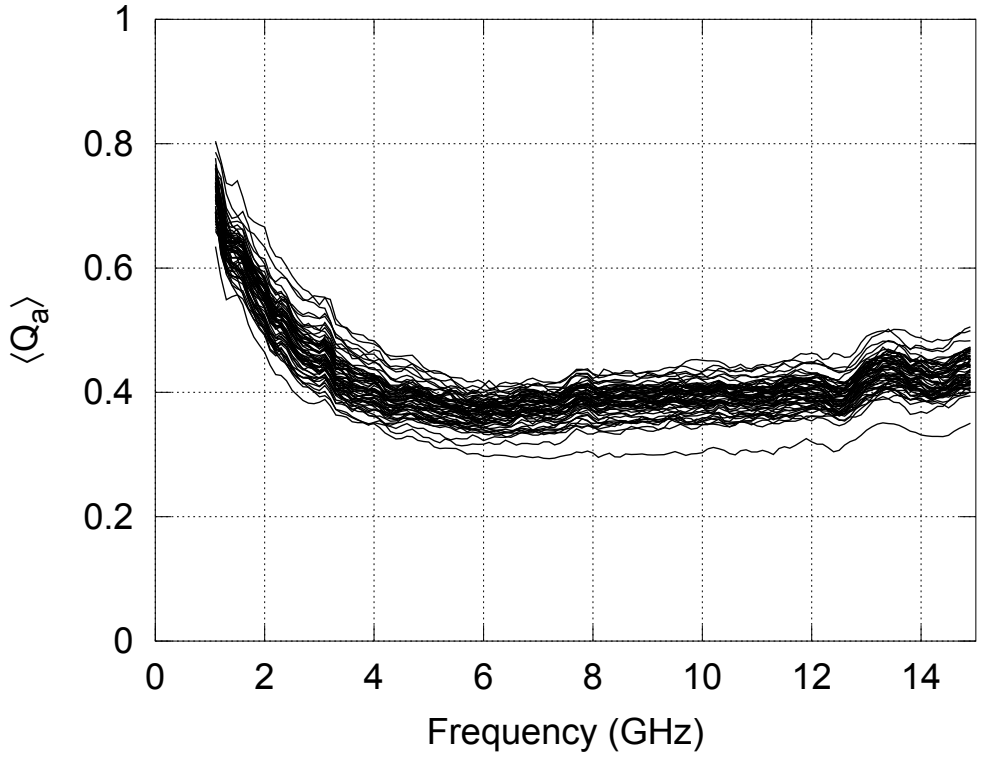

Figure 5.11: $\langle Q_a \rangle$ vs frequency for all subjects

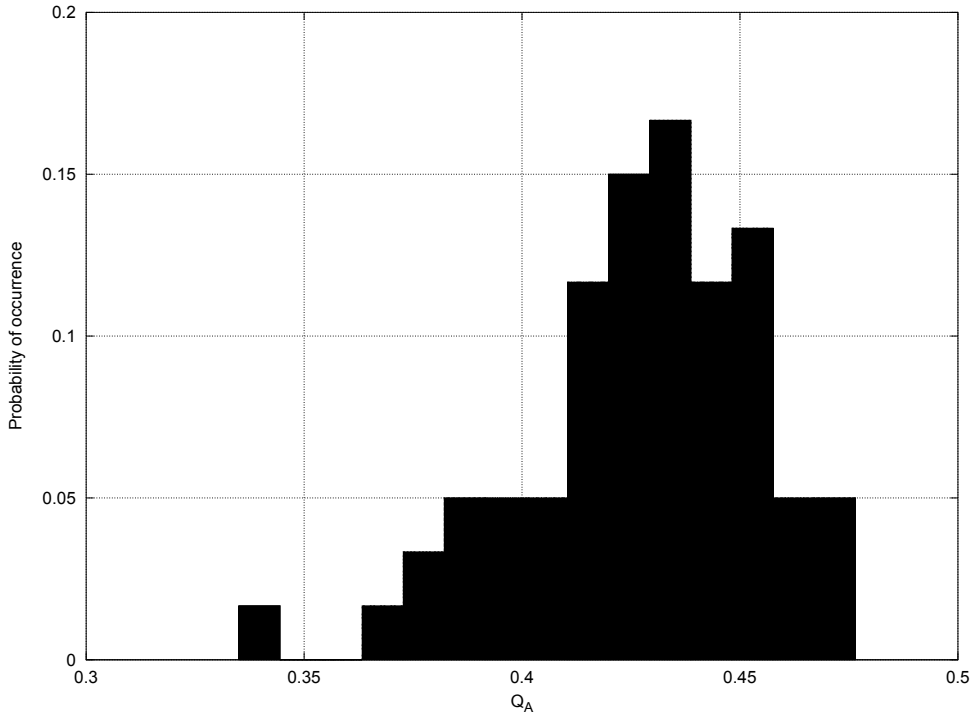

Figure 5.12: Distribution of $\langle Q_a \rangle$ over subjects at 8 GHz

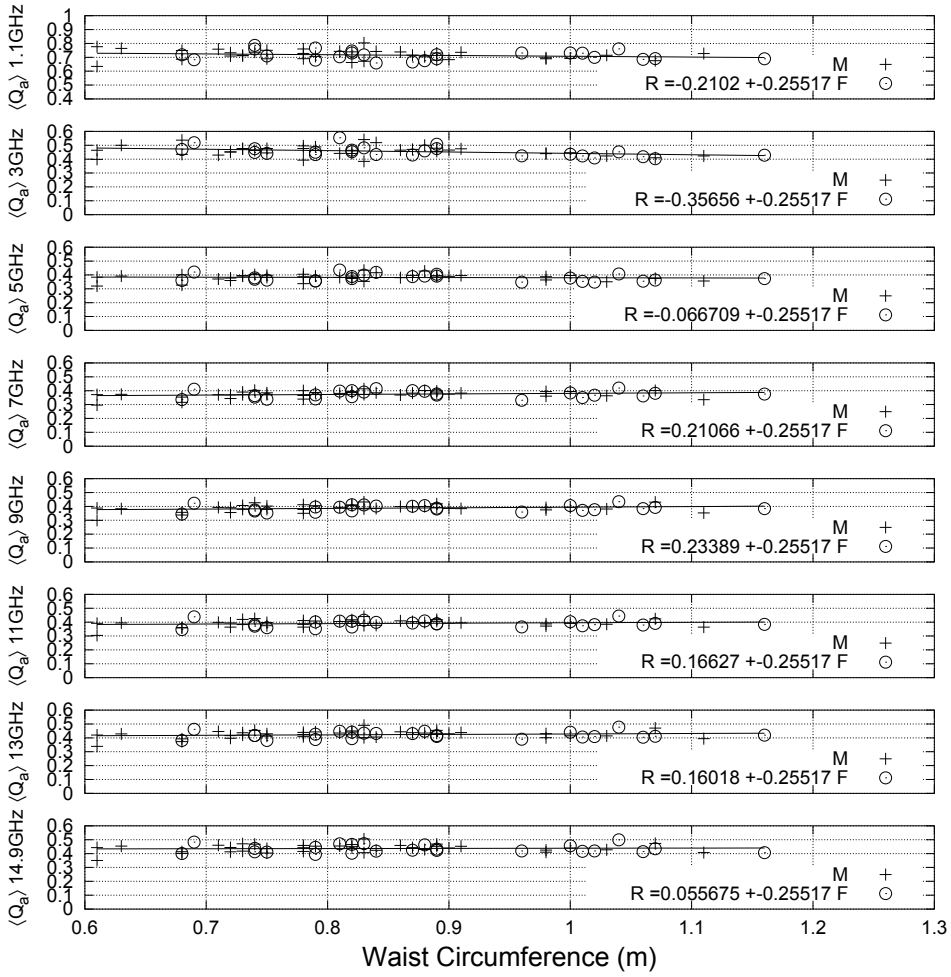

Figure 5.13: $\langle Q_a \rangle$ versus waist circumference of human subjects

Now that the main effect (BSA) has been normalised out by plotting $\langle Q_a \rangle$, it is possible to look for residual correlations with other characteristics. If, as predicted from Figures 5.6 - 5.9, human ACS is related to the thickness of the outer, fatty layers of the body, a correlation might be expected between $\langle Q_a \rangle$ and the thickness of this layer. Figures 5.13 - 5.14 therefore plot $\langle Q_a \rangle$ versus the two properties that might be correlated with the thickness of the subcutaneous fat layer: waist circumference and BMI.

Figure 5.13 shows a significant correlation between $\langle Q_a \rangle$ and waist circumference at 3 GHz only, not at any other frequency. Figure 5.14 shows a significant correlation between $\langle Q_a \rangle$ and BMI at 3 GHz and 5 GHz. Recalling the regression fits of several biological parameters to ACS, it was at these frequencies that the most complex behaviour was observed, before BSA emerged as clearly the best predictor of ACS from around 5 GHz upwards. Over 1-5 GHz, the EM penetration ('skin') depth of fat ranges from 15 cm to 2.5 cm and that of both skin and muscle ranges from 2 cm to 8 mm [22], as shown in Figure 2.1.2. As discussed in Chapter 2 of this thesis, this variation in penetration depth should take absorption in the body from a volumetric to a superficial regime, so it is therefore not surprising that it is in this range where

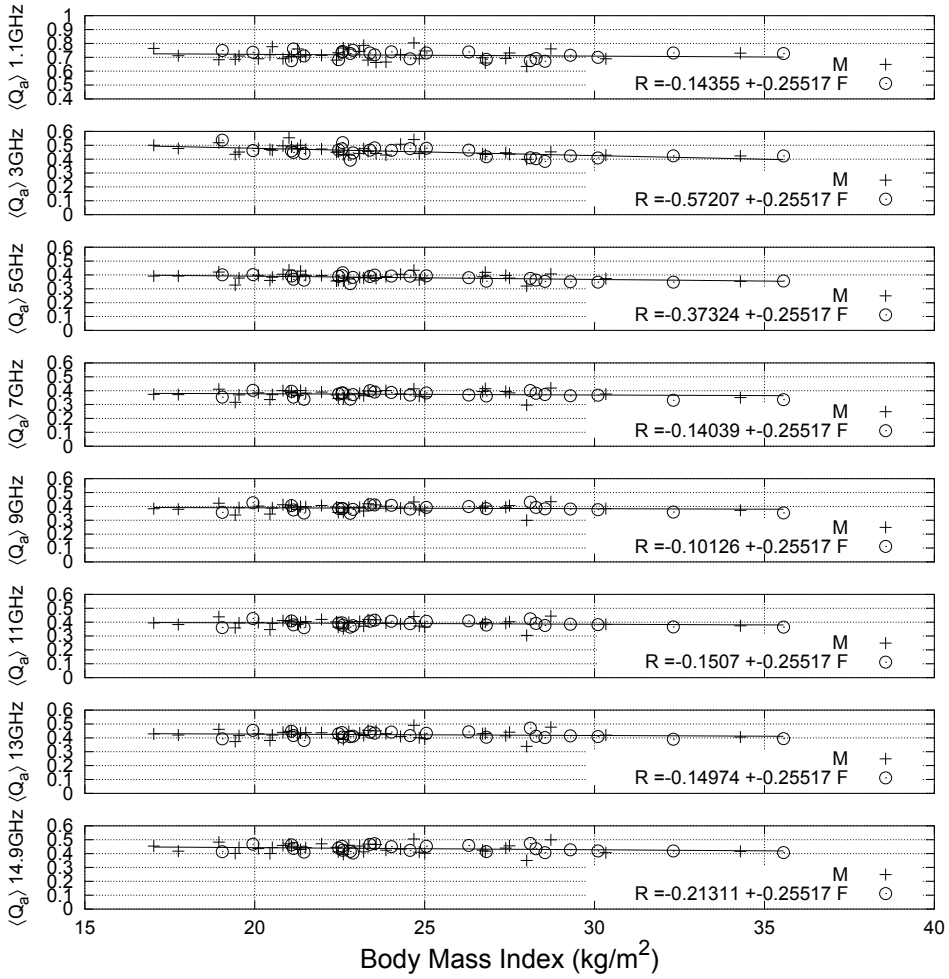

Figure 5.14: $\langle Q_a \rangle$ versus Body Mass Index of human subjects

$\langle Q_a \rangle$ is seen to be dependent on parameters that possibly relate to the composition of the outer layers of the body.

It is possible to estimate [106] the average thickness of the body's layer of subcutaneous fat, D_{SF}. To do this, the subcutaneous fat mass of the body (V_{SF}) is divided by the BSA, as in Equation 5.5.

$$\langle D_{SF} \rangle = \frac{V_{SF}}{BSA} \tag{5.5}$$

V_{SF} is calculated by using Equation 5.6, an emprical formula that gives the proportion by mass (ζ_{BF}) of fat in the body, taken from dual X-ray absorptiometry scans [107]. Here, E is ethnicity (1 for asian ethnicity, 0 for other ethnicity, i.e. all subjects in our study), Y is age in years and G is sex (1 for male, 0 for female).

$$\zeta_{BF} = 0.76 - 0.206G + \frac{1.54G + 0.95E - 10.978}{BMI} + 0.34G - 0.44E + 0.00053Y \tag{5.6}$$

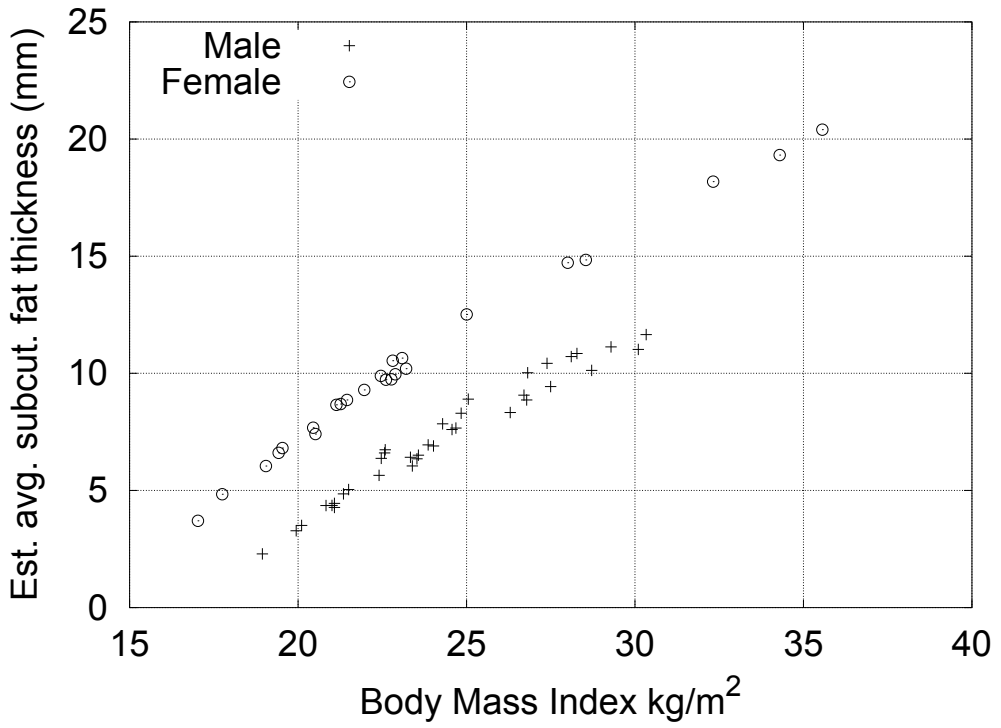

Figure 5.15: Estimated Average Subcutaneous Fat Layer Thickness vs Body Mass Index

It is then possible to calculate the total volume of subcutaneous fat V_{SF} using Equation 5.7, where ρ_{fat} is the average density of body fat, which has been estimated at 900kgm^{-3} [108], and ζ_{SF} is the proportion of fat that is subcutaneous, and has been estimated as 0.85 [109]. Note that V_{SF} and therefore $\langle D_{SF} \rangle$ is directly proportional to ζ_{SF}. Variations in ζ_{SF} will therefore not affect the strength of the correlation with Q_a, only the angle of slope - which will vary in proportion with the value for ζ_{SF}. A large variation between subjects in the proportion of total body fat that is subcutaneous could alter the fit of the regression line. However, Figure 5.15 shows a correlation between D_{SF} and BMI for both males and females, suggesting that D_{SF} has been accurately calculated and that ζ_{SF} is not a highly variable parameter.

$$V_{SF} = \frac{M}{\rho_{fat}} \cdot \zeta_{BF}\zeta_{SF} \tag{5.7}$$

As expected, D_{SF} correlates strongly with BMI, as shown in Figure 5.15. The effect of the sex terms in Equation 5.6 can be seen with the two linear correlations, one for men and the other for women.

Having estimated D_{SF}, it is then plotted against $\langle Q_a \rangle$ in Figure 5.16. This shows small yet significant correlations of $\langle Q_a \rangle$ with D_{SF} across the entire frequency range from 3 GHz upwards; only at 1.1 GHz is the correlation not significant. We can therefore conclude that the absorption efficiency of the human body, and hence its ACS, depends not only on the body's surface area, but also on the thickness of the body's layer of subcutaneous fat. Nevertheless, any future research should aim to directly measure D_{SF}, and will then be able to comment on the accuracy of this calculation.

The amount of water in the body (%TBW) is expected to correlate with absorption efficiency. Not only will the presence of water itself change the average dielectric properties of the

body by its presence, but it is also linked to the amount of fat in the body and %TBW has been approximated as 73 % of fat-free mass [64]. %TBW could therefore be proxy for fat content, so comparing the graphs for the two properties will be informative. Technology exists to measure %TBW in in a resonant cavity [64,65] but as this data was not collected at measurement time, it can be estimated using the equations in Section 2.1.3, which take subject height and mass as inputs.

Figure 5.17 shows the correlation of Q_a and %TBW. As with D_{SF} there is no significant correlation at 1 GHz, but then significant correlations are present from 3 GHz upwards. Unlike D_{SF} where the correlations are negative, all these correlations are positive. This is as expected: if %TBW really does increase as the proportion of fat decreases, we would expect to see a positive correlation in one and a negative correlation in the other – although note that D_{SF} only accounts for subcutaneous fat and not for fat in the interior of the body. In further experiments, it would be interesting to measure TBW at the same time as ACS, in order to further investigate the relationship between the two properties, and also between %TBW and D_{SF} and the body's total fat content.

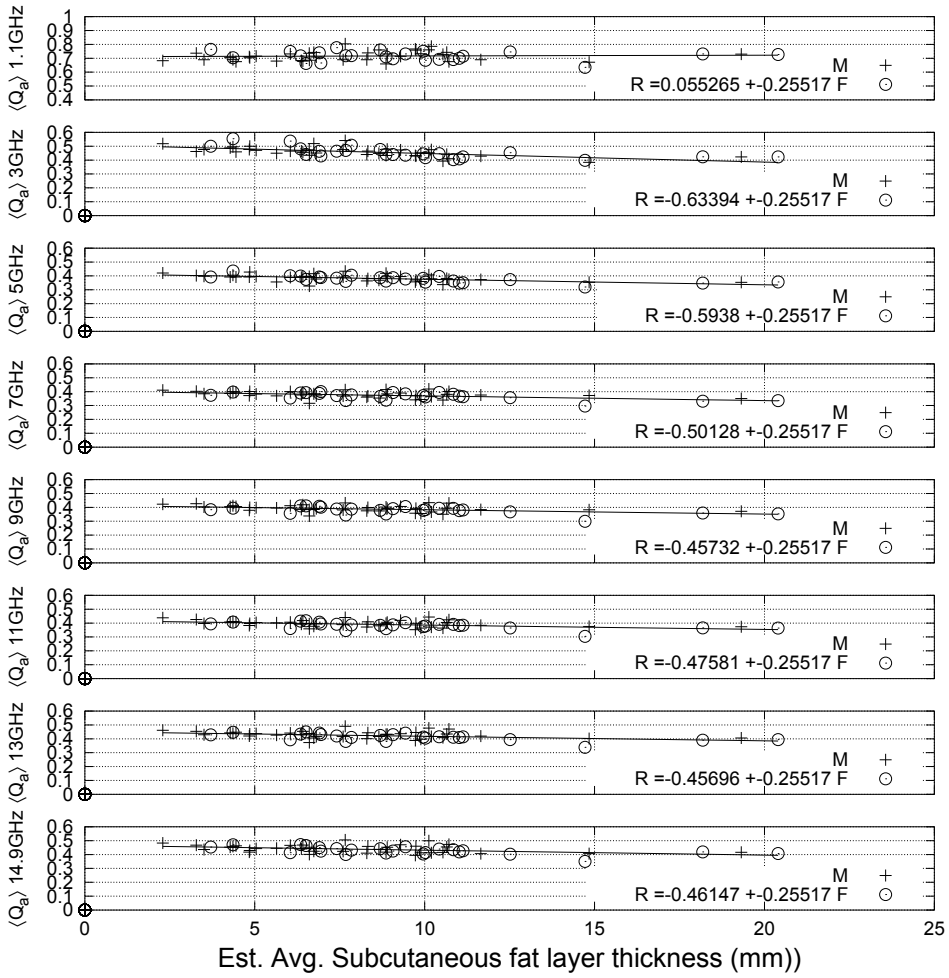

Figure 5.16: $\langle Q_a \rangle$ versus Estimated Average Subcutaneous Fat Layer Thickness of Human Subjects

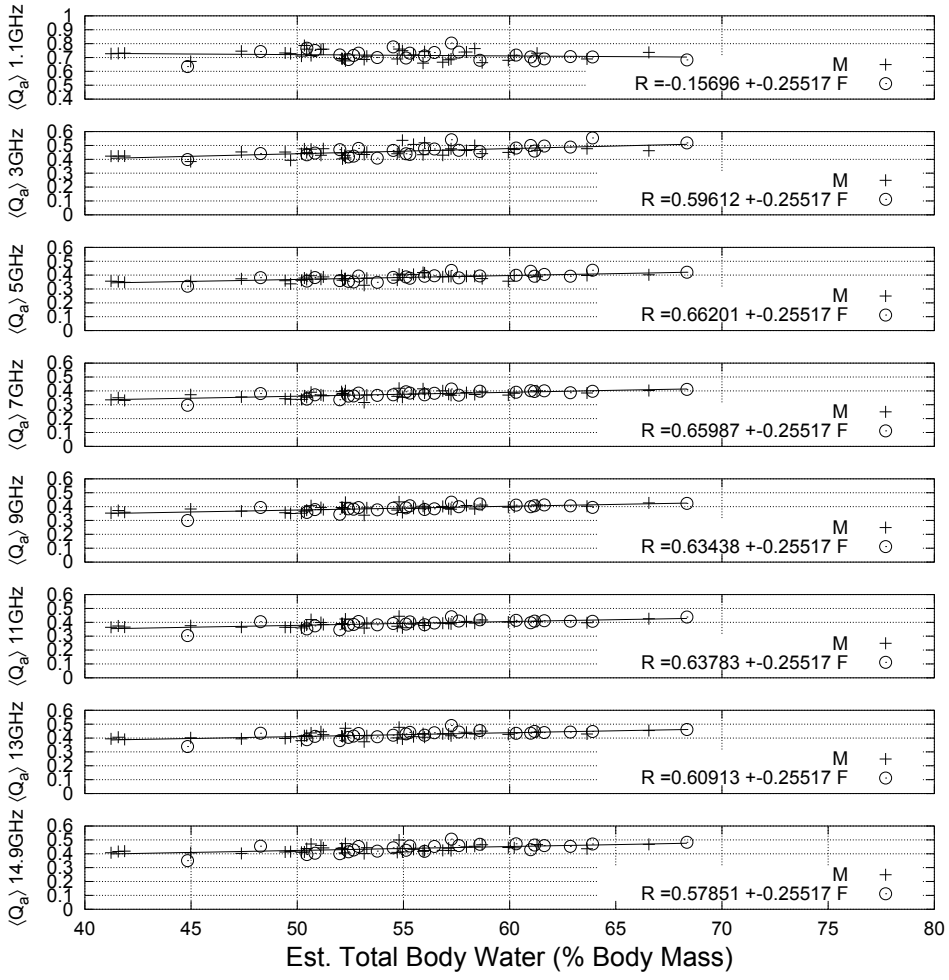

Figure 5.17: $\langle Q_a \rangle$ versus Estimated Total Body Water of Human Subjects (% body mass)

5.6 The aircraft cabin: An example of the effects of human absorption on the Q-factor of an enclosed environment

Armed with a knowledge of the average ACS of the human body, it is possible to calculate the damping effects of humans on the cavity resonances in a modern EMC-critical scenario. As an example, these calculations have been run to compute the change in the Q-factor of a wide bodied airliner's cabin, due to the presence of a full complement of passengers. In addition to to the fact that an aircraft's vulnerability to EMI provides a clear motivation for large-scale EMC simulation [110], the many electronic systems on board a modern passenger aircraft emit radiation at many different frequencies, supporting a pseudo-reverberant environment that makes them suitable for power balance modelling [3].

The cabin itself can be modelled as a cavity using Hill's power balance equation [75], described in Section 2.3.2. Here, different loss mechanisms are added in reciprocal to give the overall cavity Q-factor. For this approach to be valid, certain conditions must be met: firstly, the absorbant effects of the different passengers must be independent, i.e. Equation 5.8 must apply. This is discussed in Section 2.2.3.

$$\langle ACS \rangle 1 + \langle ACS \rangle 2 = \langle ACS \rangle (1 + 2) \tag{5.8}$$

For this to be true, passengers should be sitting far enough apart that their total ACS is given by a linear sum – if they are too close together, shadowing effects could confound this approximation. The variation of ACS with spacing of human subjects in a reverberation chamber is a subject for further research.

Secondly, in order for Hill's power balance equations to apply, it is necessary to model an aircraft as a reverberant environment, and it must be an appropriate model to use. Figure 5.18 shows the mode density in the cabins of three aircraft. This was calculated using the Helmholtz equation, shown and discussed in Section 2.2.3. The Helmholtz equation models the cabins as cuboids - so these results are indicative rather than precisely accurate. The aircraft dimensions used were estimated from technical drawings for the two smaller aircraft, whereas those for the 747 are the passenger cabin dimensions given in the aircraft's airport manual [111]. All dimensions are given in Table 5.6

Table 5.6: Passenger cabin dimensions (m) of three aircraft

Aircraft	Length	Width	Height
Boeing 747-8	57.64	6.50	2.41
Learjet 85	7.54	1.85	1.85
Bell Jet Ranger	4.5	1.45	1.45

Figure 5.18 shows that at 1 GHz, the 747 cabin supports several hundred modes per MHz, while the Learjet supports 15 and the Bell supports 5. The cabins are not perfect cuboids, so some of these modes will not be supported, and the lowering of the cabin Q-factors loss mechanisms such as passengers, windows and equipment will damp the cabin to the point where some of the weaker modes will not resonate to a detectable (and hence useful) level. However, this graph suggests that at 1 GHz, there are enough excess modes that all aircraft are likely to have at least 1 mode per MHz at all points above this frequency.

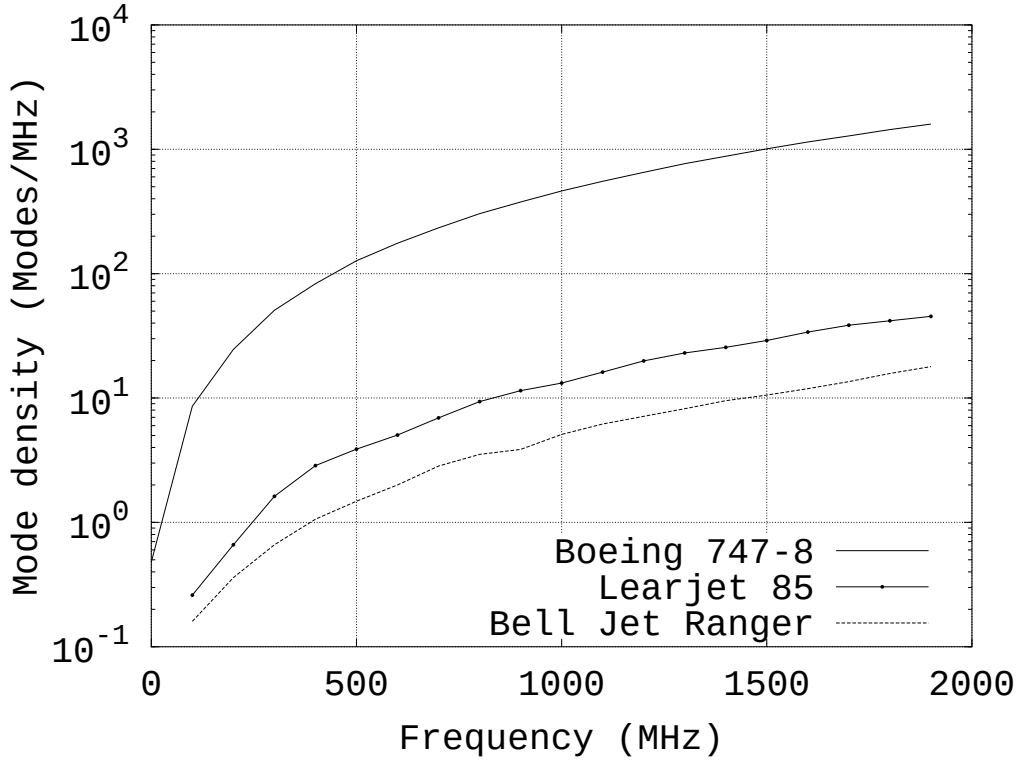

Figure 5.18: Mode density in three aircraft

The 747 cabin supports many more modes at this frequency. Taking a resonance bandwidth of 3 MHz, which will be justified in Section 5.6.1, the number of modes within this bandwidth is plotted in Figure 5.19 at our frequencies of interest, i.e. 1 GHz upwards. It shows that for the Helmholtz empty cabin case, over 700 modes are excited for all frequencies above 1 GHz, the reverberant environment model is therefore appropriate for this aircraft at these frequencies.

5.6.1 Q-factor of an airliner cabin

Measured data is available for the Q-factor of an empty Boeing 707 cabin [112]. Unfortunately, no data is available for more modern aircraft. However, [112] includes a photograph of the cabin as measured: this shows that the cabin contained no seats. Assuming there are no other significant lossy objects in the cabin, loss mechanisms can be limited to loss through the windows and absorption in the cabin walls, (including any wiring looms concealed within the walls).

A knowledge of the dimensions of the aircraft's dimensions allows these factors to be scaled. Data was primarily taken from the airport planning manuals [111, 113] with some data taken from aviation sites [114].

The Boeing 707 has 97 passenger windows of 9 x 12.5 inches, giving a total window area of 10912.5 square inches or 7.04m^2. According to Hill, aperture losses are frequency-independent if the aperture is electrically large. At 1 GHz, $\lambda = 0.3$m so this assumption is valid at our frequencies of interest. The partial Q is then given by Equation 5.9

$$Q_3 = \frac{4\pi V}{\lambda \langle \sigma_l \rangle} \tag{5.9}$$

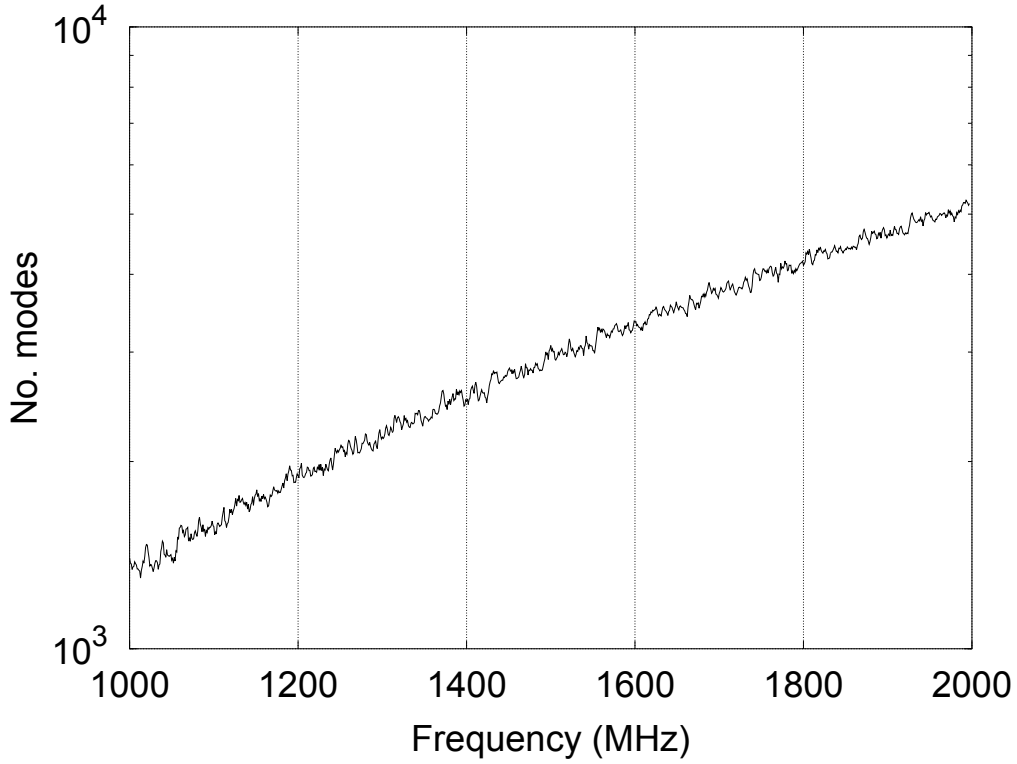

Figure 5.19: Modes excited within the resonance bandwidth of an empty 747 passenger cabin

where V is the chamber volume and $\langle \sigma_l \rangle$ is the aperture ACS averaged over all angles of incidence, which can be assumed to be equal to the aperture area for zero reflectivity and square incidence. The 707's window losses can now be calculated. Since our model holds all losses not due to the windows as being due to the walls, it is now possible to calculate these losses. Equation 5.10 gives the losses in walls, where S is wall surface area, δ is the wall skin depth and other symbols take their usual meanings.

$$Q_1 = \frac{3V}{2\mu_r S\delta} \tag{5.10}$$

From the airport manual, we can calculate $V = 211.1\text{m}^3, S = 357.6\text{m}^2$. This gives enough information to rearrange Equation 5.10 into Equation 5.11, and define X as the penetration depth multiplied by the permeability of a Boeing airliner wall, i.e. the factor affecting wall loss that is not immediately obtainable by measuring the physical dimensions of the aircraft cabin.

$$X = \mu_r \delta = \frac{3V}{2Q_1 S} \tag{5.11}$$

Assuming only that X remains similar between different Boeing airliners, their wall losses can now be calculated, given their cabin dimensions. Taken from the airport manual for the latest model, the 747-8, these are $V = 741.1\text{m}^3, S = 864.4\text{m}^2$. The 747-8 has 184 passenger windows, which are larger than on older 747 models, but are similar to the 777 windows. These have dimensions 27 x 38 cm, giving a total window area 18.88m^2. The window and wall losses of the 747-8 passenger cabin can now be estimated, and thus its Q-factor *sans* passengers and seats can be calculated.

The main sources of inaccuracy in these calculations are:

- Losses due to any wiring looms in the cabin walls will scale with length, rather than surface area.
- The cabin volume and wall surface area were calculated using a hemicylindrical approximation for cabin shape. The cabins are not perfect hemicylinders, so this will not be completely accurate.

However, assuming that the Q-factors of other airliner cabins will be similar to that of the 707, due to their similar construction, Johnson's 707 measurements can be used in the absence of model-specific data.

5.6.2 Addition of seats and passengers

Nguyen et al. [115] have measured the ACS of several Boeing 757 passenger seats in various configurations, finding them to have an average ACS of 0.04m^2 each. Assuming that changes in seat design have not significantly altered the ACS of the seats, this value can be used for the 747 model.

For the passengers, average ACS was taken to be the frequency-dependent average of all 60 subjects in the C2 sample. Section 5.2 discusses the representativeness of this sample, which is found to be slightly lighter, taller and younger than the English average, but still representative of a sample arbitrarily drawn from the English population. Due to the international nature of air travel, the passengers of a long-haul airliner are anyway unlikely to represent only one nationality, it was therefore not felt necessary to remove passengers to gain closer resemblance of the English population as a whole. Also, some of the passengers on a flight will be children, who will reduce the average size and ACS of the passenger group as a whole.

The partial Q factors relating to losses in the walls, seats, passengers and windows on a 747-8 cabin are shown in Figure 5.20. The effect on the total cabin Q factor of adding seats and passengers is then shown in Figure 5.21, which shows that while the addition of seats attenuates the cabin Q-factor by approximately 15 %, the addition of passengers has a more substantial effect, reducing Q by around 35 % across the frequency range. This is a significant effect, which vindicates the decision to study this problem.

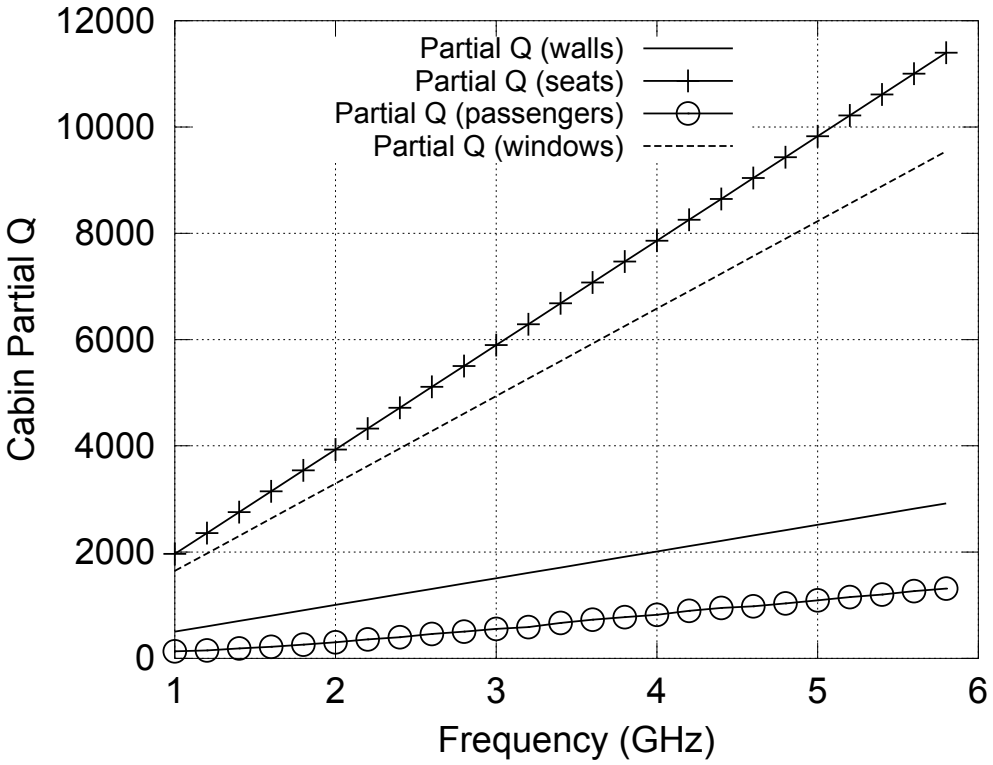

Figure 5.20: Partial Q-factors in a 747 cabin with 400 seats and passengers

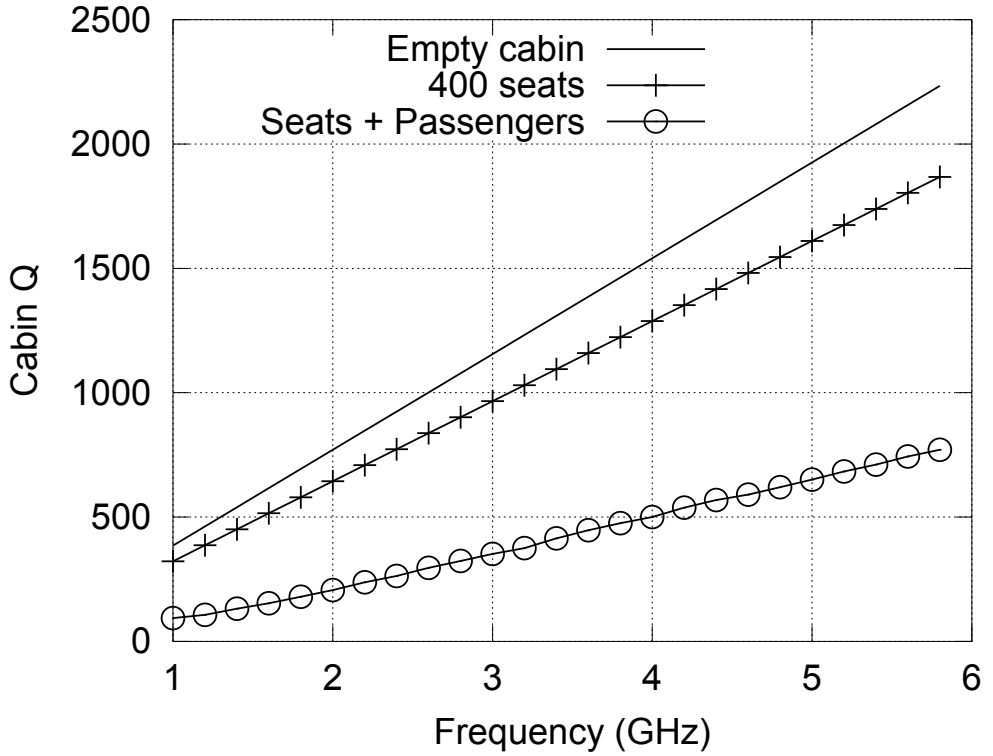

Figure 5.21: Q-factor of a 747 cabin: empty, loaded with 400 seats, and loaded with 400 seats and passengers

5.7 Summary

In this chapter, the data from Chapter 4 is further analysed to determine the parameters on which a person's ACS depends. The C2 sample, which is large enough that statistical analysis can be applied, is found to differ from the English population in height and mass, being on average younger and lighter than the average English resident. However, the sample can be considered an arbitrary sample of the English population, as the differences are too small to support any other conclusion with statistical significance. In any case, none of this affects the appropriateness of deriving relationships between the ACS and the biometric parameters of the experimental subjects. These parameters are themselves analysed and found to depend on each other, as expected. The ACS is compared to values in the literature. These are either individual values for individual subjects at point frequencies, or else were conducted with the intent of studying properties other than ACS, such as the bandwidth of communications channel bandwidths in aircraft. Some agreement is found: the ACS values measured in this research program are slightly lower than those in the literature, but these differences are adequately explained by the previously-mentioned differences, and by the comparative lightness of the C2 sample population. The ACS from a simulation of the VF Male phantom is compared to the measured ACS of one subject of similar biometric parameters; good agreement is found.

First, second and third order fits are examined, and it is concluded that the data is best fitted to first order regression lines. The determination coefficients of the different biometric parameters are examined, and it is shown that subject mass provides a good correlation with ACS from 1 – 1.5 GHz (i.e. the lower end of the frequency range), and that between 2 – 5 GHz, all of the correlations are relatively weak, which indicates that as predicted, reflections between the layers of tissue in this range generate complex relationships between ACS and the body's parameters. However, the main finding is that BSA provides the strongest correlation with ACS across almost the entire spectrum, and especially above 4 – 5 GHz, which is consistent with the prediction that absorption would enter a superficial regime at these frequencies.

BSA is then normalised out to give absorption efficiency $\langle Q_a \rangle$. This is plotted against the four previously measured biometric parameters, plus computed values for body mass index, average subcutaneous fat thickness, and total body water. A small residual correlation is found between BSA and $\langle Q_a \rangle$ at the lower end of the spectrum, which disappears at the higher end – this is consistent with the measurement being less accurate at lower frequencies, as was discovered and discussed in Chapter 3. Waist circumference displays a significant (negative) correlation with $\langle Q_a \rangle$ only at 3 GHz, and BMI displays significant correlations at 3 and 5 GHz, again both negative. On the other hand, a significant correlation was observed across the entire spectrum for estimated average subcutaneous fat thickness: positive at 1 GHz, negative at all other frequencies. A significant positive correlation is seen at all frequencies from 3 GHz upwards for estimated %TBW. These two correlations are highly interesting, as they show how the absorption of electromagnetic energy by the human body depends on the composition of the body's outer layers. Both, however, are based on population estimates of these parameters; a further study would ideally measure TBW and subcutaneous fat thickness in tandem with ACS, in order to provide more reliable data.

Finally, the data is used to model the effects of a full complement of passengers on the Q-factor of a Boeing 747's passenger cabin. The passengers are found to attenuate the Q by around 35 % from 1-6 GHz. This shows a use for this data, and also the importance of accounting for the effects of humans on EMC scenarios such as this.

Chapter 6

Conclusions

6.1 Development of an Experiment to Measure Human Absorption

The aims of this research project, as stated in Chapter 1, were to measure the electromagnetic energy absorbed by the bodies of a large sample of live human subjects, to investigate the relationships between the energy absorbed by subjects and the biometric parameters of their bodies, and to integrate the results of the measurements into a larger simulation of a complex EMC problem. To fulfil these criteria, a methodology was developed to measure the absorption cross section (ACS) of a loading object in a reverberation chamber, and an initial study was conducted using a sample of 9 adult volunteers. This highlighted several areas in which the methodology required improvement: chiefly the acceleration of the measurement to the point where gathering sufficient data for experimental accuracy did not take longer than a subject was prepared to sit motionless in the chamber. To this end, new equipment was purchased and the stepped stirring in the initial study was replaced with continuous stirring. The antennas were repositioned inside the chamber, in order to allow shorter cables to be used and also to provide better stirring. The radiation efficiencies were estimated based on experimental work, and a technique for measuring ACS using only one antenna was investigated. This relied on the use of coherent backscattering in the reverberation chamber, but the backscattering factor B_c was found to be too variable to allow its use for ACS measurement.

The number of independent data samples available in the reverberation chamber were measured, in order to adjust the parameters of the mechanical and frequency stirring and hence to optimise the measurement for both accuracy and speed by extracting all available data from the chamber. Decreasing the sampling bandwidth B_s of the measurement provided extra samples across the entire frequency range, up to the point where the B_s was finer than the coherence bandwidth B_c of the chamber. Increasing the frequency stirring window size also increased the number of samples available from frequency stirring, but at a cost of smoothing out features of the measurement. Increasing the number of mechanical stirrer positions provided more samples, up to the point where no more samples were available in the chamber. Increasing the number of stirrer positions and decreasing B_s both adversely affected (i.e. increased) measurement time.

It was found that setting B_s at 2 MHz extracted nearly all the data available from frequency stirring across the whole frequency range. With regard to mechanical stirring, the chamber was found to support relatively few (circa 60) samples at the bottom of the frequency range, but thousands at the top, so increasing the number of stirrer positions would only provide extra samples at high frequencies. The final measurement protocol therefore used only 300 mechanical stirrer positions, which allowed maximal use of the frequency stirring with $B_s = 2$ MHz, while keeping measurement time to under 8 minutes.

The finalised measurement provided average ACS data with a statistical accuracy of $\pm 2.6 - 2.8\%$. Further investigations were conducted to determine the errors in the experiment due to the clothing worn and the postures adopted by the experimental subjects, results of which are shown in Figure 6.1. The effect of adding outdoor clothing on top of the indoor clothing initially worn by the subject was to increase ACS by up to 10.5 %, while removing the indoor clothing reduced ACS by up to 5.5 %. The subject's posture was found to have a greater effect on their ACS, which was raised by up to 17 % when the subject moved from a seated position to a 'star jump' position designed to maximise surface area, while a move from a seated to a 'foetal' position reduced ACS by up to 24 %.

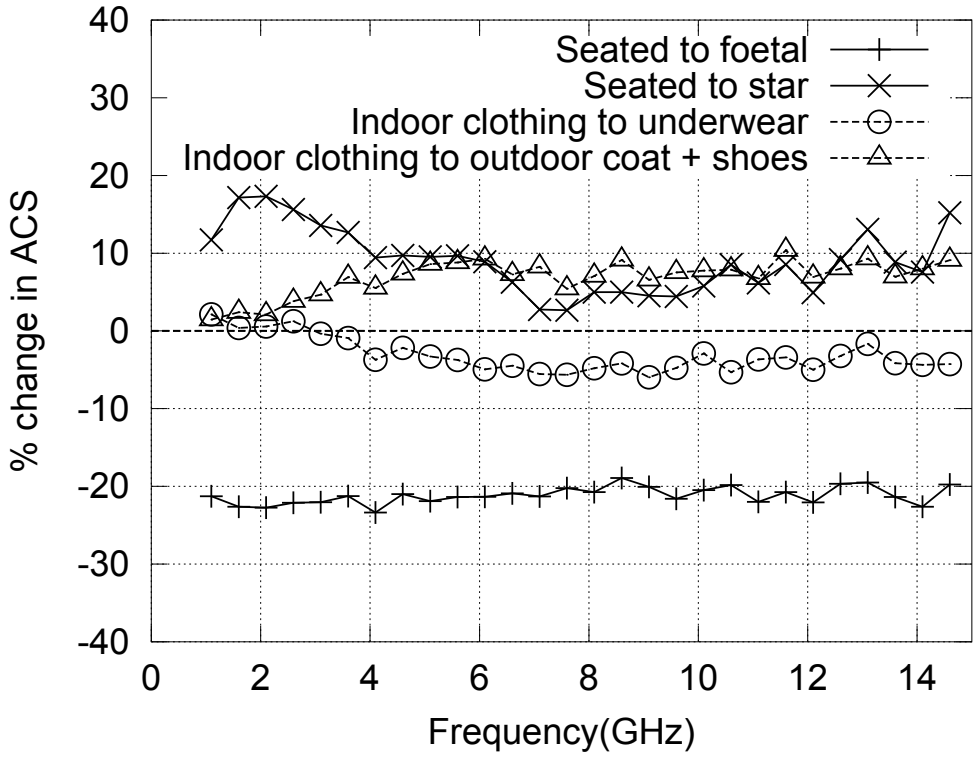

Figure 6.1: Change in ACS due to a subject's posture and level of clothing

6.2 Measurement of Absorption by a Sample Population of Human Subjects

A second measurement campaign was mounted, using a sample of 65 adult volunteers with masses ranging from $45.8 - 109.5$kg, heights from $1.52 - 1.97$m, waist circumferences from $0.61 - 1.16$m and ages from $19 - 71$ years. Their ACS was found to vary from $0.28 - 0.45\text{m}^2$ at 1 GHz, dropping to $0.15 - 0.23\text{m}^2$ at 6 GHz and then gradually rising to $0.18 - 0.27\text{m}^2$ by 15 GHz, as shown in Figure 6.2. Subjects were instructed how to dress and how to sit for the duraction of the measurement – it was nevertheless calculated that adding uncertainties due to subject posture and clothing to the statistical measurement uncertainty meant that results were accurate to within $\pm 6\%$. Adding in uncertainties due to the estimation of the antenna efficiencies raised this to $\pm 8.5\%$ for absolute values of ACS, though since the same antennas were used for all measurements, $\pm 6\%$ is the correct figure when considering the variations in average ACS between experimental subjects.

It was hypothesised that the nature of the frequency-dependence of ACS, shown in Figure 6.2, was due to the reduction of electromagnetic penetration depth δ with increasing frequency and the consequent change from a volumetric to a superficial absorption regime. It was also hypothesised that at an intermediate frequency, the nature of the absorption would become complicated, not obviously dependent on any one single parameter, due to the changing level of interaction with the layers of tissue near the body's surface as part of this regime change. To test for this, ACS was correlated with measurements of subject height, mass and waist circumference, and also with an empirically-based approximation for subject surface area (BSA). First order fits were found to describe the relationships between these properties and ACS as

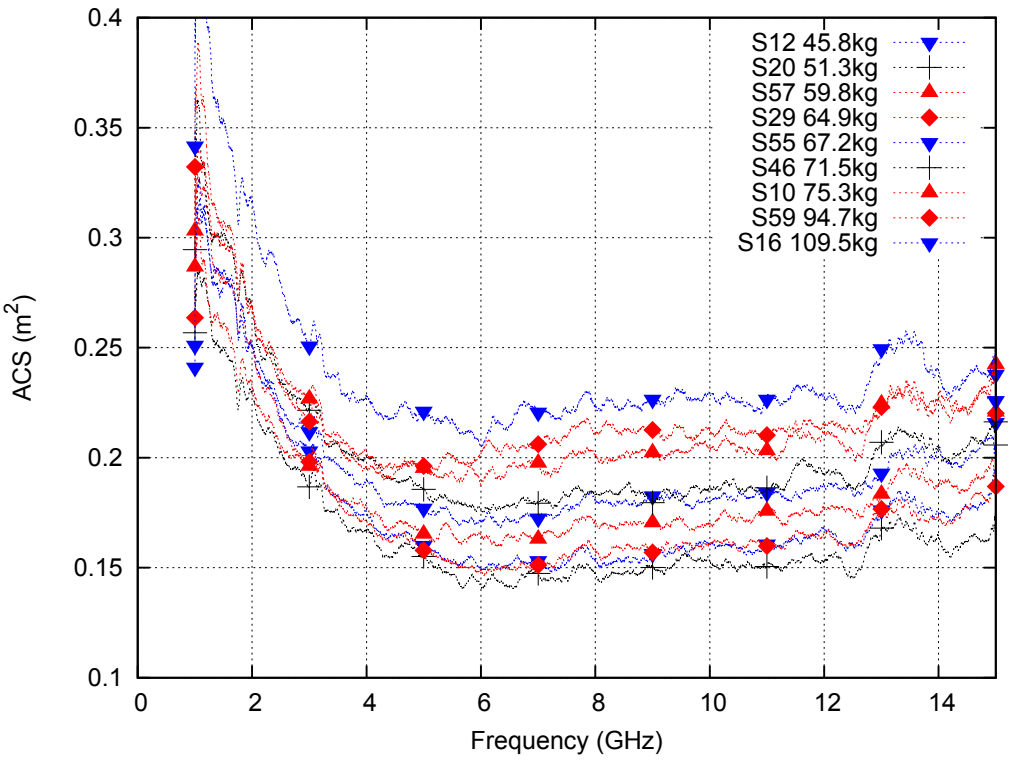

Figure 6.2: ACS vs frequency for several human subjects with a range of physiques

well as second or third order fits, based on the proximity with which they passed the origin, and also the value of their determination coefficient R^2. The latter is shown in Figure 6.3, in which it can be seen that BSA is clearly the parameter most closely related to ACS over most of the frequency range, although subject mass provides an equivalent correlation below 1.5 GHz. This is consistent with the predictions of volumetric absorption at low frequencies and superficial absorption at high frequencies, as is the lack of any clear correlation with any individual parameter from 2 – 5 GHz.

6.3 Absorption Efficiency of the Surface of the Body

The ACS data was next normalised with respect to BSA, in order to look for residual relationships once this dominant correlation had been removed. Dividing out BSA allowed the average absorption efficiency $\langle Q_a \rangle$ of the body's surface to be inspected; it was expected that this would depend on the fat content of the body, as the dielectric parameters of fat are different to those of both skin and muscle. Body mass index, somewhat surprisingly, did not correlate well with $\langle G_s \rangle$: assuming the approximations, the measurement and the theory are correct, this would show that BMI, whatever else it is used for, is not a good predictor of the depth of fat below the skin. Another model of subcutaneous fat thickness was applied to give a statistically significant negative correlation at all frequencies above 1 GHz.

The amount of water in the body (%TBW) was also known to be linked to the level of fat, so this quantity was also estimated from emprical formulae in the literature. The percentage of the body's mass that is water is known to decrease with increasing fat content, so it was no surprise that the %TBW was positively correlated with $\langle G_s \rangle$ at all frequencies above 1GHz:

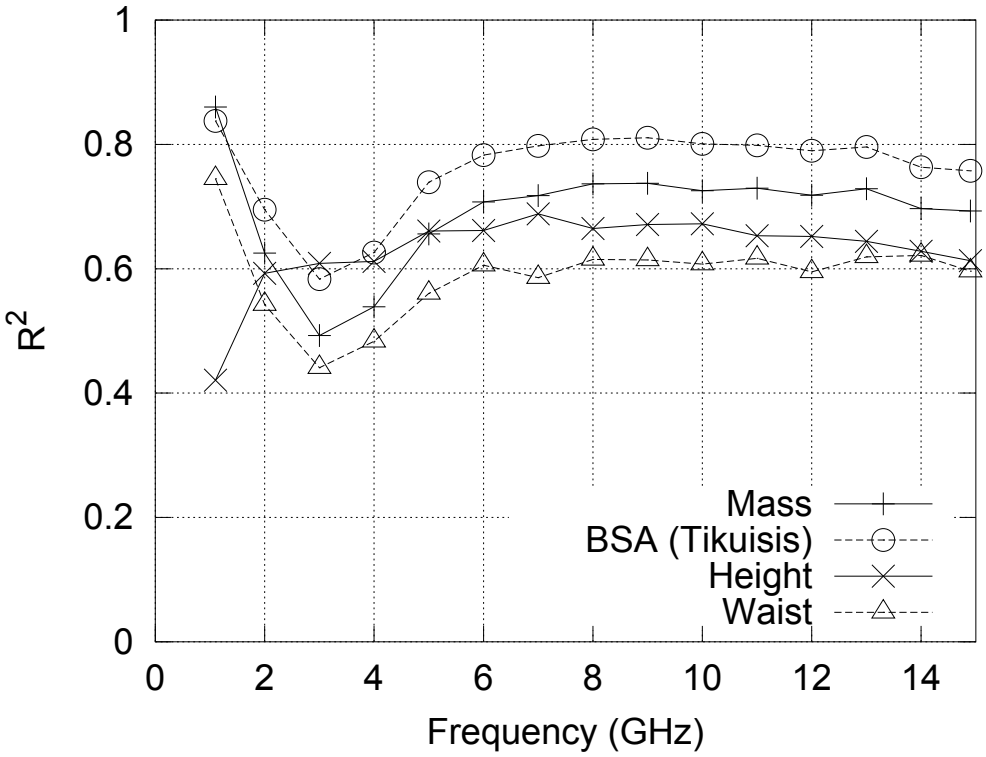

Figure 6.3: R^2 coefficients of ACS 1st order fits to biometric parameters of subjects' bodies

this was the inverse of the ACS:D_{SF} relationship.

6.4 Example Application: Passengers on an Aircraft

The ACS data from this measurement campaign was then input to a power balance model of a modern EMC-critical context: the passenger cabin of a Boeing 747-8. The effects of a full complement of passengers on the Q-factor of the cabin were calculated, and are shown in Figure 6.4. The addition of passengers was found to attenuate the Q-factor of the cabin by 75 % at 1 GHz, and by 60 % at 6 GHz. Absorption by passengers is therefore shown to make a substantial difference to the electromagnetic characteristics of a large passenger aircraft, absorbing over half of the EM energy in the passenger cabin. Absorption by passengers should therefore be considered when constructing EM models of aircraft, whether that be for the purposes of EMC, for modelling the performance of passengers' communication devices or for designing wireless aircraft. More generally, this shows the importance of considering absorption by humans wherever a large population is juxtaposed with complex and/or mission-critical electromagnetic systems and transmissions.

To summarise: The body's absorption cross section has been measured and found to vary between 0.2 – 0.4 m^2 for an average-sized adult. Apart from the effects of the clothes they are wearing and the position they adopt, that person's ACS depends mainly upon the size of their body's surface area, although body mass provides a reasonable correlation at the bottom of the frequency spectrum. If BSA is normalised out, the strongest remaining correlation is with the estimated thickness of the body's subcutaneous fat layer, which is possibly due to the differing dielectric parameters of fat compared to other tissues.

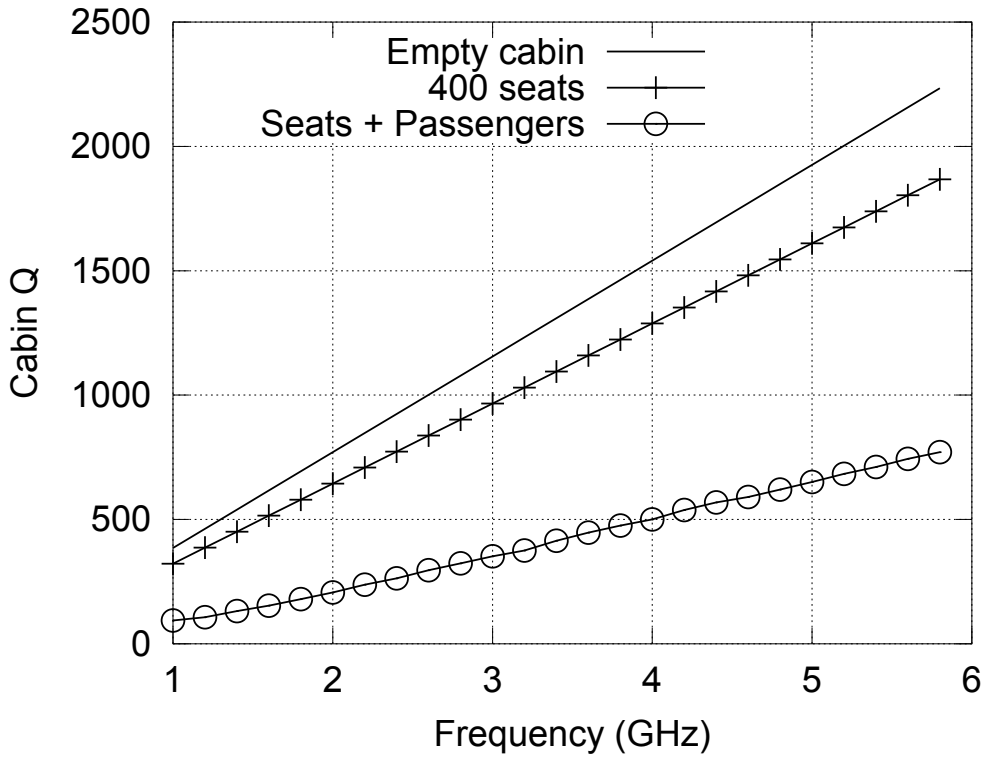

Figure 6.4: A power balance simulation of the effect of seats and passengers on the Q-factor of a Boeing 747 passenger cabin

6.5 Further Work

As always, the conclusions of this research raise further questions. Before answering these, it would however be advantageous to further improve the measurement methodology. The current measurement is sensitive to the calibration and positioning of the antennas; a fixed measurement setup inside the chamber, using rigid cables, would allow a future experimenter to perform measurements more quickly and easily, yet still gain robust and repeatable results. Different antennas and a larger RC could allow measurement below the current lower frequency limit of 1 GHz; the behaviour of the body's ACS at frequencies approaching this limit has varied greatly, so investigation at lower frequencies could produce highly informative results. Further research into the factors affecting backscattering in a reverberation chamber could also prove to be useful and informative, deepening our understanding of reverberation chamber measurements and also opening up the possibility of taking ACS measurements using only one antenna.

Whichever antennas are used, an accurate measurement of their efficiency would reduce the uncertainty in the absolute, values of the measured ACS. Uncertainty in the relative values of each subject's ACS could be reduced by better understanding the effects on ACS of subject posture. Currently, these have only been measured for one subject and for three postures – these were selected as extremes, in order to put an envelope on uncertainty due to posture. To understand the relationship between posture and ACS would require measurements not only of subjects in several different postures but of several subjects of differing physiques, to check the posture effects remained constant for each.

Once the ACS measurement is of satisfactory quality, the ACS of multiple bodies could

be usefully investigated. Characterizing the relationship between the ACS of a number of bodies and subject spacing should inform our understanding of the effects of electromagnetic shadowing between bodies. This data could then be used to construct predictive models – the ACS of an individual could be predicted on the basis of their biometric data, while the ACS of a population could be predicted as in Figure 6.4 but more accurately, taking into account the effects of the spacing between occupants in the simulation.

Investigations into the human body's absorption efficiency proved highly interesting, and offered the possibility of developing a new method for studying the composition of the body's outer layers and the relationship between the fat and water content of the body. This research was, however, limited by the accuracy of the estimates used for average silhouette area $\langle G_s \rangle$, total body water content $\%TBW$ and average subcutaneous fat thickness D_{SF}. Measurement techniques already exist for $\%TBW$, so this data could be gathered by measuring both quantities either simultaneously or consecutively. Measurement techniques for $\langle G_s \rangle$ and D_{SF} – such as skin fold tests – should be researched, so that the next study of human absorption can provide a more accurate characterization of the relationship between $\langle Q_a \rangle$, D_{SF} and $\%TBW$, and can thus further enhance our understanding of the interaction of electromagnetic waves with the human body.

Appendix A

Terminology and Conventions for modelling Electromagnetic Systems

A.1 Perfect Dielectrics

The permittivity of a material is its ability to polarize and thus sustain an electric field across it. To understand permittivity, let us start by considering a capacitor.

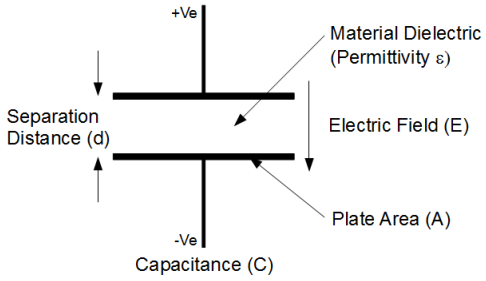

Figure A.1: A parallel plate capacitor.

The ability of the capacitor to store charge is its capacitance C, defined in Equation A.1, where Q is electric charge and V is voltage.

$$C = \frac{Q}{V} \tag{A.1}$$

The capacitance is the charge stored per Volt of potential difference between the plates. Recall the definition of potential difference in Equation A.2: The voltage between two points is the energy required (a.k.a. the work done, W) to move 1 Coulomb of charge between those points.

$$V = W/Q \tag{A.2}$$

Capacitance is therefore the amount of charge stored in a field, divided by the energy taken to move that charge across the gap. Capacitance is measured in Farads (F): A 1 Farad capacitor will require a potential difference of 1 Volt to store 1 Coulomb of charge. Still considering the capacitor, the electric field E between the plates can be defined as the potential difference between the plates, divided by the separation between the plates. It is measured in Volts/metre.

$$E = Q \times \frac{1}{4 \times \pi \times r^2} \times \frac{1}{\epsilon_0} \tag{A.3}$$

However, there is another way of measuring E field. Equation A.3 shows the electric field E produced by a point charge in free space, where r is the radius from that point charge: A charged particle will have an electric field around it, proportional to the charge on that particle, such that if another charged particle is placed in that field, it will experience a force. Multiplying Equation A.3 by the charge on the second hypothetical particle will give the force experienced by this second particle; E field thus gives the force to charge ratio F/q. E field can therefore also have units of Newtons/Coulomb. In fact, the two units are equivalent, as stated in Equation A.4

$$1\text{V/m} \equiv 1\text{N/C} \tag{A.4}$$

To recap: a capacitor stores charge in an electric field, the strength of which can be though of as the force experienced by a unit charge placed in the field, or as the gradient of potential difference across the field.

In Equation A.3, the $1/4\pi\text{r}^2$ term simply related to the surface area of the sphere around the charged particle. The ϵ_0 term, however, remained unexplained. It is the permittivity of free space, defined in Equation A.5

$$\epsilon_0 = 8.854 \times 10^{-12}\text{F/m} \tag{A.5}$$

Permittivity is measured in Farads per metre. If a capacitor was constructed of two square $1\text{m} \times 1\text{m}$ plates separated by a 1m gap, and if this capacitor was filled with a dielectric with permittivity $\epsilon = 1\text{F/m}$, the capacitor would have a value of 1 Farad, so a potential difference of 1V could store a 1C charge. Doubling the area of the plates would double the capacitance whereas doubling the separation distance would halve the capacitance. As area has the unit of m^2 and separation has the unit of m, hence the units of permittivity: Farads per metre. Capacitance can now also be written as in Equation A.6, where A = plate area and d = separation distance

$$C = \epsilon \times \frac{A}{d} \tag{A.6}$$

Capacitance is the ability of a medium to store charge in response to a potential difference across that medium. Permittivity is the property of a medium to sustain a field across it and thus store charge. This is possible by means of the material becoming polarized by one of several mechanisms, which shall be discussed shortly.

As stated in Equation A.5, free space has its own permittivity (also known as 'vacuum permittivity'). If a polarizing material has a permittivity greater than this, it is said to have a relative permittivity as defined in Equation A.7

$$\epsilon = \epsilon_0 \times \epsilon_r \tag{A.7}$$

ϵ_r is a dimensionless property, known also as a material's dielectric constant. In engineering, ϵ_r is frequently just written as ϵ, so it is important to watch for which value is in use.

A.1.1 Refractive Index

The speed of light in a vacuum is the universal constant $c_0 = 299792458$m/s, which also places a universal limit on speed of travel, as the Lorenz factor γ approaches infinity as an object's speed approaches c_0. However, in a dielectric medium light will travel at a speed v which is determined by the refractive index n, as given in Equation A.8. It is possible for particles to travel faster than this lower limit, while still travelling slower than c_0.

$$v/c_0 = n = \sqrt{\mu_r \epsilon_r} \tag{A.8}$$

n is a real refractive index; a complex refractive index is represented as $n^* = n - jk$. The dielectric constant is the square of the refractive index. So in a lossy dielectric:

$$\epsilon^* = (n - jk)^2 \tag{A.9}$$

A.2 Lossy Dielectrics

In a perfect dielectric, the only current flow is displacement current, which is caused by the polarization of the material in response to an electric field. While this will not transmit a current at DC, AC current can pass (hence the placement of capacitors in high pass filters). A lossy dielectric, however, will carry some charge by means of conduction current. A lossy dielectric therefore has both a permittivity ϵ and a conductivity σ.

A.2.1 Complex Permittivity

ϵ_r and σ can be written as a single complex permittivity ϵ^*. This complex permittivity is defined as in Equation A.10, where ω takes its usual meaning of angular velocity. The real part of the permittivity represents the reactive property of the dielectric – the energy that can be temporarily stored (such as in a capacitor) but which is not lost. Lossless dielectrics therefore have real permittivities, because the imaginary part of a complex permittivity represents a loss of energy. This is the opposite of impedance in circuit theory, where a real impedance represents a resistive load and imaginary impedance represents a reactive load.

$$\epsilon^* = \epsilon' - j\epsilon'' = \epsilon' - j\frac{\sigma}{\omega} \tag{A.10}$$

Separating real and imaginary parts gives:

$$\epsilon_r = \epsilon', \ \sigma = \epsilon'' \epsilon_0 \omega \tag{A.11}$$

The complex permittivity of a medium is a frequency-dependent property. The frequency response need not be linear, since several different conduction methods can be effective at different frequencies. For a more detailed explanation of these phenomena, see [20].

A.2.2 Loss Factor and Loss Tangent

The imaginary part ϵ'' of a complex permittivity ϵ^* is known as its loss factor. The real part of the permittivity can then be expressed as the dielectric constant. The same information about a lossy dielectric can also be written as a real relative permittivity (a.k.a. dielectric constant) and a loss tangent. Consider an Argand diagram: the real permittivity is plotted on the x axis and the imaginary permittivity is plotted on the y axis. The loss tangent is then given by Equation A.12

$$\tan(\delta) = \frac{\epsilon''}{\epsilon'} \tag{A.12}$$

The loss tangent is therefore simply the ratio of the imaginary to the real parts of the complex permittivity at a given frequency. A large loss tangent indicates a highly lossy material.

A.2.3 Complex Propagation Constant

The complex propagation constant γ is a measure of the amplitude of a wave at any given point in the material relative to its amplitude when it entered the material. α is the real part of γ and is known as the attenuation constant and is measured in Nepers per metre (N/m). The imaginary part β (also referred to as k) is the phase constant and is measured in radians per metre. Despite its name, note that the complex propagation 'constant', being calculated from ϵ^*, is highly frequency dependent.

Appendix B

Equipment used in Campaign 1

MW01, MW09, MW15, MW21 and MW24 are coaxial cables. The N) is an Agilent E5071B. The ETS Lindgren 3115 and 3117 are double ridged waveguide antennas.

Table B.1: Equipment to measure the ACS of each subject in Campaign 1

Subject	Date	Equipment used
1	25th Jan	NA Pt 1 → MW21 → Chamber Pt A → MW01 → 3115 3117 → MW15 → Chamber Pt B → MW24 → NA Pt 2
2 (i)	25th Jan	NA Pt 1 → MW21 → Chamber Pt A → MW01 → 3115 3117 → MW15 → Chamber Pt B → MW24 → NA Pt 2
2 (ii)	25th Jan	NA Pt 1 → MW21 → Chamber Pt A → MW01 → 3115 → MW15 → Chamber Pt B → MW24 → NA Pt 2
2 (iii)	31st Jan	NA Pt 1 → MW21 → Chamber Pt A → MW01 → 3115 → MW15 → Chamber Pt B → MW24 → NA Pt 2
2 (iv)	2nd Feb	NA Pt 1 → MW21 → Chamber Pt A → MW15 → 3117 → MW09 → Chamber Pt B → MW24 → NA Pt 2
2 (v)	2nd Feb	NA Pt 1 → MW21 → Chamber Pt A → MW15 → 3117 3115 → MW09 → Chamber Pt B → MW24 → NA Pt 2
3	25th Jan	NA Pt 1 → MW21 → Chamber Pt A → MW01 → 3115 3117 → MW15 → Chamber Pt B → MW24 → NA Pt 2
4	25th Jan	NA Pt 1 → MW21 → Chamber Pt A → MW01 → 3115 3117 → MW15 → Chamber Pt B → MW24 → NA Pt 2
5	31st Jan	NA Pt 1 → MW21 → Chamber Pt A → MW01 → 3115 3117 → MW15 → Chamber Pt B → MW24 → NA Pt 2
6	31st Jan	NA Pt 1 → MW21 → Chamber Pt A → MW01 → 3115 3117 → MW15 → Chamber Pt B → MW24 → NA Pt 2
7	2nd Feb	NA Pt 1 → MW21 → Chamber Pt A → MW15 → 3117 3115 → MW09 → Chamber Pt B → MW24 → NA Pt 2
8	2nd Feb	NA Pt 1 → MW21 → Chamber Pt A → MW15 → 3117 3115 → MW09 → Chamber Pt B → MW24 → NA Pt 2
9	10th Feb	NA Pt 1 → MW21 → Chamber Pt A → MW15 → 3117 3115 → MW09 → Chamber Pt B → MW24 → NA Pt 2

Bibliography

[1] *Psalm 139:14, New Revised Standard Version.*

[2] S. B. Heymsfield, Z. Wang, R. N. Baumgartner, and R. Ross, "Human body composition: Advances in models and methods," *Annual Review of Nutrition*, vol. 17, no. 1, pp. 527–558, 1997. PMID: 9240939.

[3] I. Junqua, J. Parmantier, and F. Isaac, "A network formulation of the power balance method for high-frequency coupling," *Electromagnetics*, vol. 25, no. 7,8, pp. 603–622, 2005.

[4] T. Hondou, "Rising level of public exposure to mobile phones: Accumulation through additivity and reflectivity," *Journal of the Physical Society of Japan*, vol. 71, no. 2, pp. 432–455, 2002.

[5] T. Hondou, U. Takenori, S. Yasuhiro, T. Nobuto, S. Tetsu, K. Taizo, and I. Kesuke, "Passive exposure to mobile phones: Enhancement of intensity by reflection," *Journal of the Physical Society of Japan*, vol. 75, no. 8, pp. 084801:1–5, 2006.

[6] J. Ferrer, L. Fernandez-Seivane, J. Hernando, L. Castan, M.B. Andarcia, and J. Vazquez, "On the exposure to mobile phone radiation in trains," *Applied Physics Letters*, vol. 86, p. 224101, 2005.

[7] T. Hikage, L. Harris, T. Nojima, S. Aly, and S. Wtanabe, "Estimations for implantable cardiac pacemakers EMI from cellular radios in narrow space multi reflection environments," in *19th International Zurich Smposium on Electromagnetic Compatibility*, 2008.

[8] Y. Kawamaura, T. Hikage, T. Nojima, A. Simba, and S. Watanabe, "Effects of losses due to human phantoms on 3-dimensional electromagnetic field distribution in elevators," in *PIERS Proceedings, Beijing, China,*, pp. 23–27, 2009.

[9] T. Schafer and W. Wiesbeck, "Simulation of radiowave propagation in hospital based on fdtd and ray-optical methods," *IEEE Transactions on Antennas and Propagation*, vol. 53, no. 8, pp. 2381–2388, 2005.

[10] "http://www.hirf-se.eu."

[11] ICNIRP, "Guidelines for limiting exposure to time-varying electric, magnetic, and electromagnetic fields (up to 300GHz)," *ICNIRP Guidelines*, 1998.

[12] I. C. on Non-Ionizing Radiation Protection, "Fact sheet on the guidelines on limits of exposure to static magnetic fields," *Health Physics*, vol. 96, no. 4, pp. 504–514, 2009.

[13] H. Zaidi and B. Tsui, "Review of computational anthropomorphic anatomical and physiological models," *Proceedings of the IEEE*, vol. 97, pp. 1938–1953, Dec. 2009.

[14] M. Caon, "Voxel-based computational models of real human anatomy: a review," *Radiation and Environmental Biophysics*, vol. 42, pp. 229–235, 2004. 10.1007/s00411-003-0221-8.

[15] J. Hand, "Modelling the interaction of electromagnetic fields (10 MH - 10 GHz) with the human body: methods and applications," *Physics in Medicine and Biology*, vol. 53, pp. R243–286, 2008.

[16] P. Barber, O. P. Gandhi, M. J. Hagmann, and I. Chatterjee, "Electromagnetic absorption in a multilayered model of man," *Biomedical Engineering, IEEE Transactions on*, vol. BME-26, no. 7, pp. 400–405, 1979.

[17] O. P. Gandhi, "State of the knowledge for electromagnetic absorbed dose in man and animals," *Proceedings of the IEEE*, vol. 68, no. 1, pp. 24–32, 1980.

[18] R. Kramer, J. W. Vieira, H. J. Khoury, F. R. A. Lima, and D. Fuelle, "All about MAX: a male adult voxel phantom for monte carlo calculations in radiation protection dosimetry," *Physics in Medicine and Biology*, vol. 48, no. 10, p. 1239, 2003.

[19] W. Snyder, M. Cook, E. Nasset, L. Karhausen, G. P. Howells, and I. Tipton, *Report of the Task Group on Reference Man, ICRP Publication 23*. Pergamon, 1975.

[20] C. Gabriel, S. Gabriel, and E. Corthout, "The dielectric properties of biological tissues: I. literature survey," *Physics in Medicine and Biology*, vol. 41, no. 11, p. 2231, 1996.

[21] S. Gabriel, R. W. Lau, and C. Gabriel, "The dielectric properties of biological tissues: II. measurements in the frequency range 10 hz to 20 GHz," *Physics in Medicine and Biology*, vol. 41, no. 11, p. 2251, 1996.

[22] S. Gabriel, R. W. Lau, and C. Gabriel, "The dielectric properties of biological tissues: III. parametric models for the dielectric spectrum of tissues," *Physics in Medicine and Biology*, vol. 41, no. 11, p. 2271, 1996.

[23] ICRP, *ICRP Publication 89: Basic Anatomical and Physiological Data for Use in Radiological Protection: Reference Values*. Pergamon, July 2003.

[24] O. Ghandi and C. Furse, "Millimeter-resolution mri-based models of the human body for electromagnetic dosimetry from elf to microwave frequencies," in *Proc. Int. Workshop on Voxel Phantom Development*, 1995.

[25] G. H. Kramer, L. Burns, and L. Noel, "The brmd bomab phantom familydevelopment," *Health Physics*, vol. 61, no. 6, pp. 895–902, 1991.

[26] M. Ackerman, "The visible human project," Mar. 1998.

[27] X. Xu, T. Chao, and A. Bozkurt, "VIP-man: An image-based whole-body adult male model constructed from color photographs of the visible human project for multi-particle monte carlo calculations," *Health Physics*, vol. 78, no. 5, pp. 476–486, 2000.

[28] I. G. Zubal, C. R. Harrell, E. O. Smith, Z. Rattner, G. Gindi, , and P. B. Hoffer, "Computerized three dimensional segmented human anatomy," *Medical Physics*, vol. 21, p. 299, 1994.

[29] P. J. Dimbylow, "FDTD calculations of the whole-body averaged SAR in an anatomically realistic voxel model of the human body from 1 MHz to 1 GHz," *Physics in Medicine and Biology*, vol. 42, no. 3, p. 479, 1997.

[30] P. Ferrari and G. Gualdrini, "An improved MCNP version of the NORMAN voxel phantom for dosimetry studies," *Physics in Medicine and Biology*, vol. 50, no. 18, p. 4299, 2005.

[31] P. Dimbylow, "Development of the female voxel phantom, NAOMI, and its application to calculations of induced current densities and electric fields from applied low frequency magnetic and electric fields," *Physics in Medicine and Biology*, vol. 50, no. 6, p. 1047, 2005.

[32] P. J. Dimbylow, T. Nagaoka, and X. G. Xu, "A comparison of foetal SAR in three sets of pregnant female models," *Physics in Medicine and Biology*, vol. 54, no. 9, p. 2755, 2009.

[33] M. Zankl and A. Wittmann, "The adult male voxel model golem segmented from whole-body CT patient data," *Radiation and Environmental Biophysics*, vol. 40, pp. 153–162, 2001. 10.1007/s004110100094.

[34] A. Christ, W. Kainz, E. G. Hahn, K. Honegger, M. Zefferer, E. Neufeld, W. Rascher, R. Janka, W. Bautz, J. Chen, B. Kiefer, P. Schmitt, H.-P. Hollenbach, J. Shen, M. Oberle, D. Szczerba, A. Kam, J. W. Guag, and N. Kuster, "The virtual family - development of surface-based anatomical models of two adults and two children for dosimetric simulations," *Physics in Medicine and Biology*, vol. 55, no. 2, p. N23, 2010.

[35] T. Nagaoka, S. Watanabe, K. Sakurai, E. Kunieda, S. Watanabe, M. Taki, and Y. Yamanaka, "Development of realistic high-resolution whole-body voxel models of Japanese adult males and females of average height and weight, and application of models to radio-frequency electromagnetic-field dosimetry," *Physics in Medicine and Biology*, vol. 49, pp. 1–15, Jan. 2004.

[36] A. Lee, W. Choi, M. Chung, H. Choi, and J. Choi, "Development of Korean male body model for computational dosimetry," *ETRI Journal*, vol. 28, no. 1, pp. 107–110, 2006.

[37] S. Choi, C. Lee, S. Cho, M. Chung, S. Na, and C. Kim, "Construction of a high-definition 'Reference Korean' voxel phantom for organ and tissue radiation dose calculation," *IFMBE Proceedings*, vol. 14, no. 6, pp. 4204–4207, 2007.

[38] J. Keshvari, R. Keshvari, and S. Lang, "The effect of increase in dielectric values on specific absorption rate (SAR) in eye and head tissues following 900, 1800 and 2450 MHz radio frequency (rf) exposure," *Physics in Medicine and Biology*, vol. 51, pp. 1463–1477, Mar. 2006.

[39] R. Findlay and P. Dimbylow, "Calculated SAR distributions in a human voxel phantom due to the reflection of electromagnetic fields from a ground plane between 65 MHz and 2 GHz," *Physics in Medicine and Biology*, vol. 53, no. 9, p. 2277, 2008.

[40] T. Uusitupa, I. Laakso, S. Ilvonen, and K. Nikoskinen, "SAR variation study from 300 to 5000 MHz for 15 voxel models including different postures," *Physics in Medicine and Biology*, vol. 55, no. 4, p. 1157, 2010.

[41] E. Conil, A. Hadjem, A. Gati, M.-F. Wong, and J. Wiart, "Influence of plane-wave incidence angle on whole body and local exposure at 2100 MHz," *Electromagnetic Compatibility, IEEE Transactions on*, vol. 53, no. 1, pp. 48–52, 2011.

[42] T. Kientega, E. Conil, A. Hadjem, E. Richalot, A. Gati, M. Wong, O. Picon, and J. Wiart, "A surrogate model to assess the whole body sar induced by multiple plane waves at 2.4 GHz," *annals of telecommunications - annales des tlcommunications*, vol. 66, no. 7-8, pp. 419–428, 2011.

[43] D. Chiu, S. Michelson, "Effect of human presence on UWB radiowave propagation within the passenger cabin of a midsize airliner," *IEEE Transactions on Antennas and Propagation*, vol. 58, no. 3, pp. 1–11, 2009.

[44] P. J. Dimbylow, A. Hirata, and T. Nagaoka, "Intercomparison of whole-body averaged sar in european and japanese voxel phantoms," *Physics in Medicine and Biology*, vol. 53, no. 20, p. 5883, 2008.

[45] K. Harima, "Estimation of power absorbed by human body using reverberation chamber," in *Electromagnetic Compatibility (EMC), 2012 IEEE International Symposium on*, pp. 39–43, 2012.

[46] M. Robinson, J. Clegg, and A. Marvin, "Radio frequency electromagnetic fields in large conducting enclosures: effects of apertures and human bodies on propagation and field-statistics," *IEEE Transactions on Electromagnetic Compatibility*, vol. 48, pp. 304–310, May 2006.

[47] K. Hurst and S. Ellingson, "Path loss from a transmitter inside an aircraft cabin to an exterior fuselage-mounted antenna," *Electromagnetic Compatibility, IEEE Transactions on*, vol. 50, no. 3, pp. 504–512, 2008.

[48] J. Andersen, K. L. Chee, M. Jacob, G. Pedersen, and T. Kurner, "Reverberation and absorption in an aircraft cabin with the impact of passengers," *Antennas and Propagation, IEEE Transactions on*, vol. 60, pp. 2472 –2480, May 2012.

[49] A. Bamba, W. Joseph, J. B. Andersen, E. Tanghe, G. Vermeeren, D. Plets, J. O. Nielsen, and L. Martens, "Experimental assessment of specific absorption rate using room electromagnetics," *Electromagnetic Compatibility, IEEE Transactions on*, vol. PP, no. 99, pp. 1 –11, 2012.

[50] A. Hirata, Y. Nagaya, F. Osamu, A. Nagaoka, and S. Watanabe, "Correlation between absorption cross section and body surface area of human for far-field exposure at GHz bands," in *EMC 2007. IEEE International Symposium on Electromagnetic Compatibility*, pp. 1–4, July 2007.

[51] A. E. Habachi, E. Conil, A. Hadjem, E. Vazquez, G. Fleury, and J. Wiart, "Identification of factors influencing the whole body absorption rate using statistical analysis," in *Proceedings of the The joint meeting of the Bioelectromagnetics Society and the European Bioelectromagnetics Association (BioEM'09)*, 2009.

[52] A. E. Habachi, E. Conil, A. Hadjem, E. Vazquez, M. F. Wong, A. Gati, G. Fleury, and J. Wiart, "Statistical analysis of whole-body absorption depending on anatomical human characteristics at a frequency of 2.1 GHz," *Physics in Medicine and Biology*, vol. 55, no. 7, p. 1875, 2010.

[53] Y. Feldman, A. Puzenko, and Y. Ryabov, *Dielectric Relaxation Phenomena in Complex Materials*, pp. 1–125. John Wiley & Sons, Inc., 2005.

[54] B. Pevzner, "Transport and dielectric properties of thin fullerene films," Master's thesis, Massachusetts Institute of Technology, 1995.

[55] Y. Feldman, A. Puzenko, and Y. Ryabov, *Dielectric Relaxation Phenomena in Complex Materials*, pp. 1–125. John Wiley & Sons, Inc., 2005.

[56] C. Polk and E. Postow, *Handbook of Biological Effects of Electromagnetic Fields (Second Edition)*. CRC Press, 1996.

[57] D. Kelley, T. Destan, and R. Luebbers, "Debye function expansions of complex permittivity using a hybrid particle swarm-least squares optimization approach," *Antennas and Propagation, IEEE Transactions on*, vol. 55, no. 7, pp. 1999–2005, 2007.

[58] J. Clegg and M. P. Robinson, "A genetic algorithm used to fit debye functions to the dielectric properties of tissues," in *WICI*, 2010.

[59] S. W. Smye, C. J. Evans, M. P. Robinson, and B. D. Sleeman, "Modelling the electrical properties of tissue as a porous medium," *Physics in Medicine and Biology*, vol. 52, no. 23, p. 7007, 2007.

[60] S. Ramo, J. R. Whinnery, and T. V. Duzer, *Fields and Waves in Communication Electronics*. Wiley, 1965.

[61] D. Sjoberg, "Electromagnetic wave propagation lecture 10: Multilayer structures 1," Lund University, Sweden, 2013.

[62] E. Conil, A. Hadjem, F. Lacroux, M. F. Wong, and J. Wiart, "Variability analysis of SAR from 20 MHz to 2.4 GHz for different adult and child models using finite-difference time-domain," *Physics in Medicine and Biology*, vol. 53, no. 6, p. 1511, 2008.

[63] A. L. Cauchy, *Mémoire sur la rectification des courbes et la quadrature des surfaces courbes*. 1832.

[64] M. P. Robinson, J. Clegg, and D. A. Stone, "A novel method of studying total body water content using a resonant cavity: experiments and numerical simulation," *Physics in Medicine and Biology*, vol. 48, no. 1, p. 113, 2003.

[65] D. A. Stone and M. P. Robinson, "Total body water measurements using resonant cavity perturbation techniques," *Physics in Medicine and Biology*, vol. 49, no. 9, p. 1773, 2004.

[66] P. E. Watson, I. D. Watson, and R. D. Batt, "Total body water volumes for adult male sand females estimated from simple anthropometric measurements," *American Journal of Clinical Nutrition*, vol. 33, pp. 27–39, January 1980.

[67] C. Christopolous, "Full-wave volume modelling techniques," in *EMC Europe 2010: Young Scientists Program*, 2010.

[68] J. F. Dawson and S. J. Porter, "Chapter 3: The finite-difference time-domain method," in *Time Domain Computational Electronics*, The University of York, 2005.

[69] L. N. Ng, *Manipulation of Particles on Optical Waveguides*. PhD thesis, The University of Southampton, September 2000. Chapter 3 on Mie scattering.

[70] M. Kerker, P. Scheiner, and D. D. Cooke, "The range of validity of the Rayleigh and thomson limits for lorenz-mie scattering," *J. Opt. Soc. Am.*, vol. 68, pp. 135–137, Jan 1978.

[71] P. Chýlek, "Large-sphere limits of the Mie-scattering functions," *J. Opt. Soc. Am.*, vol. 63, pp. 699–706, Jun 1973.

[72] O. Pena and U. Pal, "Scattering of electromagnetic radiation by a multilayered sphere," *Computer Physics Communications*, vol. 180, no. 11, pp. 2348 – 2354, 2009.

[73] C. Matzler, "Matlab functions for Mie scattering and absorption," tech. rep., University of Bern, 2004.

[74] A. Stogryn, "Equations for calculating the dielectric constant of saline water (correspondence)," *Microwave Theory and Techniques, IEEE Transactions on*, vol. 19, pp. 733 – 736, Aug. 1971.

[75] D. Hill, M. Ma, A. Ondrejka, B. Riddle, M. Crawford, and R. Johnk, "Aperture excitation of electrically large, lossy cavities," *IEEE Transactions on Electromagnetic Compatibility*, vol. 36, no. 3, pp. 169–178, 1994.

[76] R. Xia, J. Dawson, I. Flintoft, A. Marvin, and S. Porter, "Use of a genetic algorithm in modelling small structures in airframes," in *Electromagnetic Compatibility (EMC EUROPE), 2012 International Symposium on*, pp. 1–5, IEEE, 2012.

[77] J. Parmantier and P. Degauque, *Modern Radio Science*, ch. Topology Based Modeling of Very Large Systems, pp. 151–176. Oxford Science Publications, 1996.

[78] C. L. Holloway, D. A. Hill, J. M. Ladbury, and G. Koepke, "Requirements for an effective reverberation chamber: Unloaded or loaded," *Electromagnetic Compatibility, IEEE Transactions on*, vol. 48, pp. 187–194, feb. 2006.

[79] F. Leferink, "Mode stirred chambers (reverberation chambers)," in *EMC Wroclaw 2010, Young Scientists Program*, 2010.

[80] J. Clegg, A. Marvin, J. Dawson, and S. Porter, "Optimization of stirrer designs in a reverberation chamber," *Electromagnetic Compatibility, IEEE Transactions on*, vol. 47, pp. 824 – 832, Nov. 2005.

[81] C. Holloway, D. Hill, J. Ladbury, P. Wilson, G. Koepke, and J. Coder, "On the use of reverberation chambers to simulate a Rician radio environment for the testing of wireless devices," *Antennas and Propagation, IEEE Transactions on*, vol. 54, no. 11, pp. 3167–3177, 2006.

[82] K. Madsen, P. Hallbjorner, and C. Orlenius, "Models for the number of independent samples in reverberation chamber measurements with mechanical, frequency, and combined stirring," *Antennas and Wireless Propagation Letters, IEEE*, vol. 3, pp. 48 –51, Dec. 2004.

[83] U. Carlberg, P.-S. Kildal, A. Wolfgang, O. Sotoudeh, and C. Orlenius, "Calculated and measured absorption cross sections of lossy objects in reverberation chamber," *IEEE Transactions on Electromagnetic Compatibility*, vol. 46, pp. 146 – 154, May 2004.

[84] J. Ladbury and D. Hill, "Enhanced backscatter in a reverberation chamber: Inside every complex problem is a simple solution struggling to get out," in *Electromagnetic Compatibility, 2007. EMC 2007. IEEE International Symposium on*, pp. 1 –5, July 2007.

[85] M. Piette, "Antenna radiation efficiency measurements in a reverberation chamber," in *Radio Science Conference, 2004. Proceedings. 2004 Asia-Pacific*, pp. 19 – 22, Aug. 2004.

[86] H. Wheeler, "The radiansphere around a small antenna," *Proceedings of the IRE*, vol. 47, no. 8, pp. 1325–1331, 1959.

[87] C. Holloway, H. Shah, R. Pirkl, W. Young, D. Hill, and J. Ladbury, "A three-antenna technique for determining the total and radiation efficiencies of antennas in reverberation chambers," *Antennas and Propagation Magazine, IEEE*, vol. 54, pp. 235 –241, Feb. 2012.

[88] C. Holloway, H. Shah, R. Pirkl, W. Young, D. Hill, and J. Ladbury, "Reverberation chamber techniques for determining the radiation and total efficiency of antennas," *Antennas and Propagation, IEEE Transactions on*, vol. 60, no. 4, pp. 1758–1770, 2012.

[89] B. Riddle, J. Baker-Jarvis, and J. Krupka, "Complex permittivity measurements of common plastics over variable temperatures," *Microwave Theory and Techniques, IEEE Transactions on*, vol. 51, pp. 727 – 733, Mar 2003.

[90] U. Kaatze, "Complex permittivity of water as a function of frequency and temperature," *Journal of Chemical & Engineering Data*, vol. 34, no. 4, pp. 371–374, 1989.

[91] R. . Schwarz, "Vector network analyzer R&S ZVB datasheet," tech. rep., Rohde & Schwarz, 2007.

[92] M.-I. Andries, P. Besnier, and C. Lemoine, "On the prediction of the average absorbing cross section of materials from coherence bandwidth measurements in reverberation chamber," in *Electromagnetic Compatibility (EMC EUROPE), 2012 International Symposium on*, pp. 1–6, Sept.

[93] S. Takai and S. Shimaguchi, "Are height and weight sufficient for the estimation of human body surface area?," *Human biology*, vol. 58, no. 4, pp. 625–638, 1986.

[94] P. Tikuisis, P. Meunier, and C. Jubenville, "Human body surface area: measurement and prediction using three dimensional body scans," *European Journal of Applied Physiology*, vol. 85, pp. 264–271, 2001.

[95] D. DuBois and E. F. DuBois, "A formula to estimate the approximate surface area if height and weight be known," *Arch. Intern. Med.*, vol. 17, pp. 863–871, 1916.

[96] G. Haycock, G. Schwartz, and D. Wisotsky, "Geometric method for measuring body surface area: A height-weight formula validated in infants, children, and adults," *The Journal of Pediatrics*, vol. 93, pp. 62–66, July 1978.

[97] J. Verbraecken, P. V. de Heyning, W. D. Backer, and L. V. Gaal, "Body surface area in normal-weight, overweight, and obese adults. a comparison study," *Metabolism*, vol. 55, no. 4, pp. 515 – 524, 2006.

[98] C.-Y. Yu, Y.-H. Lo, and W.-K. Chiou, "The 3d scanner for measuring body surface area: a simplified calculation in the chinese adult," *Applied Ergonomics*, vol. 34, no. 3, pp. 273 – 278, 2003.

[99] B. J. R. Bailey and G. L. Briars, "Estimating the surface area of the human body," *Statistics in Medicine*, vol. 15, no. 13, pp. 1325–1332, 1996.

[100] S. G. E.A. Gehan, "Estimation of human body surface area from height and weight," *Cancer Chemotherapy Reports*, vol. 54, no. 4, pp. 225–235, 1970.

[101] E. Boyd, *The growth of the surface area of the human body*. Greenwood Press, 1935.

[102] J. Coder, J. Ladbury, C. Holloway, and K. Remley, "Examining the true effectiveness of loading a reverberation chamber: How to get your chamber consistently loaded," in *Electromagnetic Compatibility (EMC), 2010 IEEE International Symposium on*, pp. 530–535, 2010.

[103] G. Torgovnikov, "Interaction between the electromagnetic field and wood. main features of dielectric properties of wood," in *Dielectric Properties of Wood and Wood-Based Materials*, Springer Series in Wood Science, pp. 1–19, Springer Berlin Heidelberg, 1993.

[104] N. C. f. S. R. Joint Health Surveys Unit, "Health survey 2003."

[105] G. Melia, M. Robinson, I. Flintoft, A. Marvin, and J. Dawson, "Broadband measurement of absorption cross section of the human body in a reverberation chamber," *Electromagnetic Compatibility, IEEE Transactions on*, vol. (Pre Press), pp. 1–8, 2013.

[106] I. D. Flintoft, "Models for the absorption cross-section of the human body from 100 MHz to 100 GHz." 2013.

[107] D. Gallagher, S. B. Heymsfield, M. Heo, S. A. Jebb, P. R. Murgatroyd, and Y. Sakamoto, "Healthy percentage body fat ranges: an approach for developing guidelines based on body mass index," *The American Journal of Clinical Nutrition*, vol. 72, no. 3, pp. 694–701, 2000.

[108] S. Heymsfield, T. Lohman, Z. Wang, and S. Going, *Human Body Composition*. Human Kinetics Publishers, 2nd ed., April 2005.

[109] E. L. Thomas, N. Saeed, J. V. Hajnal, A. Brynes, A. P. Goldstone, G. Frost, and J. D. Bell, "Magnetic resonance imaging of total body fat," *Journal of Applied Physiology*, vol. 85, no. 5, pp. 1778–1785, 1998.

[110] B. Grishenko and N. Simonova, "Common vulnerabilities to electromagnetic interference among modern transport aircraft," *Russian Journal of Avionics*, vol. 23, pp. 134–140, 1995.

[111] Boeing, *Boeing 747 Airplane characteristics for airport planning*, 2012.

[112] D. M. Johnson, M. O. Hatfield, and M. Slocum, "Phase ii demonstration test of the electromagnetic reverberation characteristics of a large transport aircraft," 1998.

[113] Boeing, *Boeing 707 Airplane characteristics for airport planning*, 2012.

[114] "http://www.airliners.net."

[115] T. Nguyen, "RF loading effects of aircraft seats in an electromagnetic reverberating environment," in *Digital Avionics Systems Conference, 1999. Proceedings. 18th*, vol. 2, pp. 10.B.5–1 –10.B.5–7 vol.2, 1999.